

UC Berkeley

UC Berkeley Electronic Theses and Dissertations

Title

A Spectroscopic Investigation of Photoelectrochemical Reactions at the Semiconductor - Electrolyte Interface for Artificial Photosynthesis

Permalink

<https://escholarship.org/uc/item/0hv2b3kx>

Author

Herlihy, David Michael

Publication Date

2016

Peer reviewed|Thesis/dissertation

**A Spectroscopic Investigation of Photoelectrochemical Reactions at the
Semiconductor - Electrolyte Interface for Artificial Photosynthesis**

by

David Michael Herlihy

A dissertation submitted in partial satisfaction of the
requirements for the degree of
Doctor of Philosophy

in

Chemistry

in the

Graduate Division
of the
University of California, Berkeley

Committee in charge:

Professor Charles B. Harris, Chair
Professor Richard J. Saykally
Professor Jonathan Wurtele

Fall 2016

**A Spectroscopic Investigation of Photoelectrochemical Reactions at the
Semiconductor - Electrolyte Interface for Artificial Photosynthesis**

Copyright 2016
by
David Michael Herlihy

Abstract

A Spectroscopic Investigation of Photoelectrochemical Reactions at the Semiconductor - Electrolyte Interface for Artificial Photosynthesis

by

David Michael Herlihy
Doctor of Philosophy in Chemistry
University of California, Berkeley
Professor Charles B. Harris, Chair

Abstract: The mechanism of water oxidation to molecular oxygen at the surface of strontium titanate, a representative transition-metal oxide photocatalyst, was investigated using ultrafast pump-probe spectroscopy and accompanying characterization methods. The dependence of the rate of initial charge transfer on applied potential was investigated with transient absorption spectroscopy, revealing a phenomenological transfer coefficient for this single step of the multi-step water oxidation reaction. Time resolved infrared spectroscopy provided the first direct evidence of the molecular character of the first intermediate to be a titanium-bound oxyl radical, and revealed interfacial Fano coupling between the electrolyte, surface species, and catalyst electronic continuum. Further work combining both transient absorption and time-resolved mid-infrared spectroscopy exposed a minimum of three distinct surface states at the strontium titanate surface, providing insight into the rich chemistry mediated at the catalyst surface. These results highlight the intricacies of charge transfer at the surface of these promising materials, provide insight into an important but difficult reaction necessary for any artificial photosynthetic system, and offer a generalizable paradigm for considering heterogeneous photochemistry. Finally, preliminary groundwork was done to uncover the mechanism of the carbon dioxide reduction half reaction in a novel inorganic-biological bacterial system with potential to produce green chemicals such as carbon-neutral liquid fuels.

I would like to dedicate this work to my parents Liuba and Maurice, and to my sister Anna.

Contents

List of Figures	v
List of Tables	vii
1 Introduction	1
2 Theory of Semiconductor Photo-Electrochemical Water Oxidation	6
2.1 Foundations of Semiconductor Electrochemistry	7
2.1.1 Semiconductor Electronic Structure	7
2.1.2 Electrolyte Electronic Structure	10
2.1.3 Semiconductor - Liquid Junctions	11
2.1.4 Semiconductor Electrochemistry in the Dark	14
2.1.5 Semiconductor Electrochemistry Under Illumination	15
2.2 The Mechanism of Photo-Electrochemical Water Oxidation On Semicon- ductor Electrodes	16
3 Experimental Methods	19
3.1 Ultrafast Pump-Probe Spectroscopy	20
3.1.1 Overview	20
3.1.2 Excitation Pulses	20
3.1.3 Mid Infrared Spectrum Probe Pulses	24
3.1.4 Data Collection	26
3.1.5 Design of Attenuated Total Reflection Experiments	28
3.2 Electrochemistry	30
3.2.1 Cyclic Voltammetry and Mott-Schottky Analysis	30
3.3 In-Situ Spectro-Electrochemical Reaction Cells	31
4 Surface Hole Potential Dependence of Carrier Dynamics at the SrTiO₃- Electrolyte Interface During Photoelectrochemical Water Oxidation	33
4.1 Original Publication	34
4.2 Introduction	34
4.3 Results	36

4.3.1	Quantum Efficiency of Oxygen Evolution	36
4.3.2	Band Edge Position in the Dark	38
4.3.3	Band Edge Movement with Applied Bias and Laser Illumination . .	40
4.3.4	Helmholtz Potential Drop and Thermodynamic Overpotential . . .	42
4.3.5	Ultrafast Charge-Transfer Rates at Open Circuit	42
4.3.6	Ultrafast Charge-Transfer Rates with External Bias	44
4.4	Discussion	45
4.5	Conclusions	47
4.6	Sample Characterization	47
4.7	Acknowledgements	49
5	Detecting the Oxyl Radical of Photocatalytic Water Oxidation at an n-SrTiO₃/Aqueous Interface by its Sub-Surface Vibration	58
5.1	Original Publication	59
5.2	Introduction	59
5.3	Results	60
5.3.1	An Interfacial Ti-O Dipole that Reports on the Oxyl Radical	62
5.3.2	Line Shape Analysis Reports on Coupling Nearby Continua	69
5.3.3	Theory of Interfacial Ti – O• and its Surface Modes	77
5.4	Discussion	91
5.5	Sample Characterization	91
5.6	Acknowledgements	94
6	Surface State Dynamics at the Aqueous Electrolyte / Strontium Titanate Interface	96
6.1	Introduction	97
6.2	Results	98
6.2.1	Polarization Dependence	98
6.2.2	H-D Electrolyte Exchange	100
6.2.3	Fluence and Roughening	103
6.2.4	Oxyl Radical Potential Dependence	106
6.3	Discussion	107
6.4	Conclusions	108
6.5	Sample Characterization	109
6.6	Acknowledgements	109
7	Spectroscopic Elucidation of Energy Transfer in Hybrid Inorganic-Biological Organisms for Solar-to-Chemical Production	111
7.1	Original Publication	112
7.2	Introduction	112
7.3	Results and Discussion	114
7.3.1	Biochemical Characterization	114

7.3.2	TA Spectroscopy	116
7.3.3	TRIR Spectroscopy	120
7.4	Discussion	125
7.4.1	Proposed e^- Transfer Mechanism of <i>M. thermoacetica</i> -CdS	125
7.5	Conclusions	125
7.6	Methods and Materials	127
7.6.1	Preparation and Biochemical Characterization of <i>M. thermoacetica</i> -CdS	127
7.6.2	TA Spectroscopy	127
7.6.3	TRIR Spectroscopy	128
7.7	Acknowledgements	128
Bibliography		129
A Derivation of Attenuated Total Reflection Signals		147
A.1	Evanescent Fields at Multiple Interfaces	148
A.1.1	Internal Reflection Equations	148
A.1.2	Equations for Multiple Absorbing Interfaces	149
A.2	Differential Measurements Using ATR	152
A.2.1	General Equations	152
A.2.2	Weak Absorption Approximation	152
A.2.3	Evanescent Wave Decay	153
A.2.4	Surface Sensitivity	154
A.2.5	Quantitative Determination of Changes of κ and n	155

List of Figures

2.1	Density of States of Metals and Semiconductors	8
2.2	Band Diagram of Semiconductors in a Vacuum	10
2.3	Band Diagram of Semiconductors in Electrolyte	12
2.4	Semiconductor Electrochemistry in the Dark	13
3.1	Pump-Probe Experimental Setup	21
3.2	Third Harmonic Generation Setup	22
3.3	Autocorrelation of Stretched Fundamental	24
3.4	OPerA Solo Layout	25
3.5	Experimental Geometry	29
4.1	Quantum Efficiency Versus Wavelength, Doping, and Applied Potential. . .	36
4.2	Quantum Efficiency Versus pH, and Ellipsometry Measurements	37
4.3	Helmholtz Model of the Interface Capacitance	38
4.4	Photovoltage and Mott-Schottky Measurements	39
4.5	Differential Capacitance in the Dark and Under Illumination	41
4.6	Calculated Helmholtz Potential as a Function of Fluence and Applied Bias	50
4.7	Kinetic Traces at Open Circuit in Hydroxide and Thiocyanate Electrolyte .	51
4.8	Kinetic Traces with Applied Bias	52
4.9	Kinetic Traces with Applied Bias Continued	53
4.10	Energy Level Diagram of the Semiconductor-Electrolyte Interface	54
4.11	Hole-Transfer Rate with Respect to Applied and Helmholtz Potentials . .	55
4.12	SEM of Damaged SrTiO ₃ Surface	56
4.13	CV of SrTiO ₃ Under Xe Illumination	57
5.1	Molecular Origin of Infrared Activity of the O _{xyl} Radical	61
5.2	Investigating the Ti – O [•] O _{xyl} Signature of n-SrTiO ₃	63
5.3	Transient Infrared Spectra from 675 – 1070 cm ⁻¹	64
5.4	Specular Reflectance and Attenuated Total Reflection of SrTiO ₃	65
5.5	The Photoinduced Absorption and the Photocurrent are Correlated	67
5.6	Fano line shapes tuned by doping, electrolyte, H/D exchange, and pH . . .	70
5.7	Attenuated Total Reflection of Liquid H ₂ O and D ₂ O	71
5.8	Full Spectra of Variously Doped Samples in Air and Electrolyte	74

5.9	Full Spectra in Different pH and pD Electrolytes	75
5.10	DFT Derived PDOS and Activity of Surface-Related Modes	78
5.11	Calculated Bulk and Slab Geometries	82
5.12	Calculated Bulk and Slab Electronic and Vibrational Properties	83
5.13	Projected Densities of States and IR Absorbance of Slab Configurations . .	85
5.14	Theory Calculations of the Effect of O ₁₆ /O ₁₈ Isotope Exchange on IR Absorbance	89
5.15	SrTiO ₃ Q.E. Under Pulsed Laser Irradiation	92
5.16	Direct Measurement of O ₂ Evolution	94
6.1	Pump and Probe Polarization Dependence for 800 nm Dynamics	99
6.2	Affect of Isotopic Exchange on 800 nm Dynamics	100
6.3	Affect of Electrolyte pH on 800 nm Dynamics and Photovoltage	101
6.4	Evolving Spectra and Fano Parameters in Isotopically Exchanged Electrolyte	102
6.5	Hole Concentration Affects on the Open Circuit Dynamics 800 nm Species	104
6.6	Hole Concentration Affects on the Closed Circuit Dynamics of the 800 nm Species	105
6.7	Ultrafast Dynamics of the Oxyl Radical with Applied Bias	106
6.8	ICP-AES Finds No Significant Photo-Decomposition of SrTiO ₃	110
7.1	Schematic of <i>M. thermoacetica</i> -CdS Photosynthetic Charge Transfer	113
7.2	Biochemical Assays of <i>M. thermoacetica</i> -CdS	114
7.3	H ₂ ase Activity of <i>M. thermoacetica</i> -CdS with Varying [H ₂]	115
7.4	TA Spectroscopy of <i>M. thermoacetica</i> -CdS	116
7.5	TA Spectroscopy of <i>M. thermoacetica</i> -CdS: Extended time scale	118
7.6	TA Spectra of <i>M. thermoacetica</i> -CdS	119
7.7	TRIR Spectra of <i>M. thermoacetica</i> -CdS	121
7.8	Standard Error of TRIR Spectra	122
7.9	TRIR Kinetic Data	123
7.10	TRIR Kinetic Data (Continued)	124
7.11	Proposed Dual Pathway of Charge and Energy Transfer in <i>M. thermoacetica</i> -CdS	126
A.1	Attenuated Total Reflection Experimental Setup	150
A.2	Differential Absorbance for ATR Spectroscopy	153

List of Tables

5.1	Fano Parameters Obtained for Different Dopings	75
5.2	Fano Parameters Obtained for Different Electrolytes	76
5.3	Calculated and Experimental Bulk SrTiO_3 Structural Parameters	84
7.1	Tri-Exponential Fitting Data for TA Spectra	117

Acknowledgments

I would like to thank everyone who defined my experience in graduate school. Throughout my time at Berkeley the people here have consistently stood out as the best and brightest part of being here.

First and foremost I would like to thank my research advisors, Professor Cuk and Professor Harris. I would like to thank both of them for their guidance, support, and for the opportunity to perform such interesting research. In much the same way I would like to thank Dr. Waagele for helping me through my first three years of graduate school, and beyond. I would not have made it through without your help and what's more, I would not have enjoyed it anywhere near as much. I would also like to thank my undergraduate research advisor at Brown University, Professor Christoph Rose-Petruck, and my graduate student mentor Dr. Brian Ahr, for introducing me to research and the field of physical chemistry. Thank you all.

I would also like to thank my labmates, the friends at my back, who made every day an exciting adventure. Stephanie, Hoang, Kevin, Xihan, Jon, and Son - thank you. In particular, I would like to thank Xihan for sharing our projects from the outset, and for working with me despite what might be termed a somewhat difficult beginning. I have enjoyed working with you, learning from you, and struggling through all the challenges of research with your help. I want to thank Stephanie for consistently being an endless source of knowledge, support and guidance both in general and on our x-ray projects. I also owe Son a deep well of gratitude for training me and sharing his research projects with me when I joined the Harris group.

In my various research projects I have had the privilege of working with several collaborators who generously shared their time, expertise and creativity in pursuit of scientific discovery. I would like to thank Das Pemmaraju, Nick Kornienko, Kelsey K. Sakimoto, David Prendergast, Adam M. Schwartzberg, Professor Paul Alivisatos, and Professor Peidong Yang.

Beyond my research group, the friends I made in graduate school have undoubtedly made the difference between merely surviving graduate school and enjoying my time here: Sean, Danie, Daniel, Laura - I am so glad to have met all of you. And of course, I undoubtedly owe my entire graduate school career to my Thriving in Science peer group for your support: Sahar, Varsha, and Heidi - there are no words, so thank you will have to do.

Finally, I need to highlight the love and support my parents, my sister, and the rest of my family provide every day. From taking my phone calls in the middle of the night to driving me to the airport at four in the morning, their support is the foundation for everything I will ever achieve.

Chapter 1

Introduction

The use of renewable energy to meet domestic power consumption has grown dramatically in the past decade. As of 2014, U.S. renewable electricity had grown to 13.5% of total electricity generation but only 3.1% of total domestic consumption (9.83 quadrillion British thermal units) [1] because of mismatch between spatial and temporal characteristics of generation and consumption. The main sources of U.S. renewable electric energy capacity: biomass, geothermal, and hydropower (representing over 66% of U.S. renewable energy capacity) all remained at the same levels from 2000 to 2014 [1]. The growing sources of renewable energy are photovoltaics and concentrated solar power (CSP), which grew from zero to 6% of renewable capacity and 0.5% of the total energy produced nationally. However the use of renewable energy in transportation, which represents 28% of domestic energy use, is limited to 5%, primarily in the form of first-generation biofuels [2]. Even as renewable sources of electricity spread, the weight-to-power ratio, reliability, and safety requirements for transportation limit the adoption of both current and projected battery technology required for electric vehicles. The most widespread currently available renewable methods for generating liquid fuels use biological sources (plants and algae) to harness solar energy, which typically have efficiencies between 3 and 6 percent [3]. In contrast commercially available single-junction semiconductor photovoltaics already achieve 20% efficiency [4], with a theoretical efficiency up to the Shockley-Queisser limit of 30% [5].

Artificial photosynthesis, the direct conversion of solar energy to chemical fuels, provides an alternative form of energy storage with particular benefits in the transportation sector. The primary commercial product derived from a working artificial photosynthetic system would be a so-called “drop-in” fuel that integrates with existing equipment without the need for costly new infrastructure and vehicle upgrades. The two chemical processes making up artificial photosynthesis can be categorized as (1) the oxidation of water to reform molecular oxygen (O_2) and (2) a reduction of water and/or carbon dioxide to form an energy dense fuel. I address both halves of the overall reaction in the following chapters. Although the fuel material serves as the potential commercial product (oxygen being relatively abundant and freely available), it is the oxygen evolution reaction that provides a large endothermic and kinetic barrier to efficient use of solar energy. Therefore the majority of the work presented herein focuses on that half reaction. The challenge of producing not merely a chemical fuel, but specifically one that can be used with existing infrastructure motivates my investigation into novel inorganic-biological hybrid systems that attempt to couple the solar efficiency of semiconductors with the chemical product control of biology.

One route to renewable chemical fuels is the use of metal electrodes to drive the oxygen evolution reaction (OER), exemplified by coupling an electrolyzer to a photovoltaic array or other renewable source. In this way intermittent energy can be used at will to separate energy capture from energy consumption from the electrical grid, or can be used in transportation applications. However, recently the research community has shifted focus to finding an integrated photoelectrochemical (PEC) material that combines energy capture (absorption of solar irradiation, charge separation, bulk charge transport) and

chemical synthesis (fuel generation, OER) into a single monolithic device. The shift has been driven by economic analyses that concluded a simple PEC system made of cheap, earth-abundant materials was the only viable solution in light of the constraints imposed by the scale required to impact global energy use and the per-unit costs required to compete with conventional fossil fuels [6, 7]. Transition-metal oxides with semiconductor properties provide a possible route to a low-cost (earth abundant) stable (corrosion resistant) and efficient PEC material.

Despite their promise, these materials have proven difficult to optimize. The water oxidation reaction is highly endothermic, kinetically slow, and even the best-known photocatalysts cannot keep up with the fluence of solar photons reaching the surface during peak hours. Materials with appropriately tuned band-gap and band-edge position have turned out not to be chemically stable in operational conditions. A detailed understanding the mechanism of water oxidation is therefore required to drive the rational design of a photocatalyst that achieves the material properties required for industrial applications.

At the outset of this work, the research community had a limited understanding of the reaction mechanism driving water oxidation. Three general mechanisms for the reaction had been proposed. Early work [8, 9, 10] theorized outer sphere hydroxide radical formation, essentially formation of a highly reactive species free in solution. The hydroxide radical was thought to traverse a spontaneous reaction path to form hydrogen peroxide, which subsequently released molecular oxygen through catalyzed decomposition. Later workers attributed early supporting evidence for this pathway to systemic experimental error [11] and found the mechanism contributed below 1% of the overall experimental yield [12]. Two competing mechanisms have since been developed, derived from seemingly contradictory results based on work done on different PEC materials. The first potential mechanism progressed through the formation of highly oxidized metal centers serving as activated catalytic sites. This was based on the range of oxidation states available to molecular metal centers previously known to catalyze chemical reactions [13]. The second potential mechanism is unique to heterogeneous catalysts and arises from their ability to generate high densities of single-charge-transfer species on their surfaces. Rather than localizing multiple holes at highly oxidized metal centers, single holes could potentially self-trap at molecular states at the surface. These surface species could then diffuse freely on the surface until encountering another such species, wherein they react to form activated complexes above the catalyst metal centers. This mechanism was originally put forth to explain the catalytic activity of titanates (among other materials), catalysts composed of already highly oxidized metal centers (Ti^{4+}) where the formation of multiply oxidized metal sites is thermodynamically inaccessible [14].

While both mechanisms involve formation of a O-O bond and eventually molecular oxygen, the molecular species at play in the earliest stages are molecularly distinct. To reconcile the conflicting mechanisms I set out to identify the molecular species involved in the earliest steps of the water oxidation mechanism. The primary reason for this knowledge gap is that the important steps of these reactions occur at interfaces, historically very difficult regions to probe, and on ultrafast timescales. Moreover, although previous

workers in the extensive field of surface science have examined pristine surfaces in vacuum, actual catalysis occurs at so called “buried interfaces”, between the solid catalyst and liquid electrolyte. The analogy between the vacuum interface and the liquid one can be quite tenuous as the presence of a solvent plays a defining role in chemical reactions in the condensed phase [15].

The difficulty in detecting intermediates at buried interfaces is best demonstrated by considering that if 10% of a catalyst surface is occupied by reactant molecules (e.g. 10^{14} molecules/cm²) and is probed through 1 micrometer of electrolyte (10^{18} molecules/cm²) then the molecules of interest represent only 1 in 1,000 (0.01%) of the total number being probed. To track the molecular transformations driven by photo-generated charge-carriers from the very outset of the reaction I chose ultrafast pump-probe spectroscopy. Time resolved infrared and optical spectroscopy provided the unparalleled spectral and temporal sensitivity required to detect sub-monolayer species with extremely low absorption cross-sections, and to do so quantitatively. I chose to investigate the surface of strontium titanate, a representative transition metal oxide photocatalyst, because of its uniquely high quantum efficiency, quantum yield, and photochemical stability.

Chapter 2 presents a theoretical basis for discussing the solid-liquid interface and water oxidation photo-electrochemistry, followed by a review of the existing literature addressing the mechanism of water oxidation on semiconductor electrode surfaces.

Chapter 3 presents the experimental methods and instrumentation designs that I built while pursuing the challenging research questions presented here. I describe the overall ultrafast laser system, excitation- and probe-pulse generation, the experimental design including detection methodology, and finally the spectroscopic electrochemical cells that enabled the in-operando work of chapters 4, 5 and 6.

Chapter 4 presents experiments using optical spectroscopy to track the hole dynamics at the surface before the critical rate-determining step to understand how charges transform into chemical moieties at the surface. The dynamics with respect to applied bias were investigated to report the charge-transfer coefficient, a metric used to understand the symmetry of the potential energy surface at the first transition state. The work described in this chapter was previously published as Matthias M. Waegele, Xihan Chen, David M. Herlihy, and Tanja Cuk, *Journal of the American Chemical Society*, **2014**, 136 (30), 10632 [16].

Chapter 5 presents experiments using infrared spectroscopy to identify the molecular characteristics of the charges at the surface, and led to the discovery of sub-surface vibrations that are characteristic of an oxyl radical, the initial molecular species present at the surface. Line shape distortions are discussed and revealed to inform on the coupling between electrolyte, catalyst, and intermediate. This work was previously published as David M. Herlihy, Matthias M. Waegele, Xihan Chen, C. D. Pemmaraju, David Prendergast, and Tanja Cuk, *Nature Chemistry*, **2016**, 8, 549-555 [17].

Chapter 6 presents a combination of optical and infrared results with the added dimension of the temporal evolution of the signals identified in earlier chapters. I discuss the nature and dynamics of the surface states that are present during the critical first

nanoseconds of the reaction.

Chapter 7 presents my latest work applying the technique of ultrafast infrared spectroscopy to understand mechanistically how artificial photosynthetic systems work at a molecular level. I studied a novel biological-inorganic hybrid system developed by my collaborators [18, 19], designed to perform both water oxidation and CO₂-reduction to synthesize useful chemicals and renewable liquid fuels. These preliminary results suggest a successful coupling of the inorganic charge-separation mechanics to the biological protein-mediated synthesis capabilities present within the bacteria. This novel design promises to combine the high quantum efficiency of semiconductors (30-80%) with the unique chemical specificity and C-C bond activation ability of biological systems. The work presented in this chapter has been published previously as: Nikolay Kornienko¹, Kelsey K. Sakimoto¹, David M. Herlihy, Son C. Nguyen, A. Paul Alivisatos, Charles. B. Harris, Adam M. Schwartzberg, and Peidong Yang, *Proceedings of the National Academy of Sciences*, **2016** (in press).

¹Authors contributed equally

Chapter 2

Theory of Semiconductor Photo-Electrochemical Water Oxidation

Chapter 2 presents a theoretical basis for discussing semiconductor photochemistry followed by a review of the existing literature addressing the mechanism of water oxidation on semiconductor electrode surfaces.

In Section 2.1 I present a brief overview of the underlying mechanics of semiconductor electrochemistry. The theoretical background and vocabulary introduced here is commonly used when discussing the molecular mechanism of water oxidation chemistry in detail. I describe the electronic structures of the electrode and the electrolyte, as well as the unique aspects of the semiconductor-electrolyte interface that play a role in mediating photochemistry. The framework concludes with how semiconductor electrodes operate in the dark and under illumination. Any reader interested in a more detailed framework is directed to Bard and Faulkner’s *Electrochemical Methods* [20] and in particular chapter 18, which addresses semiconductor electrodes, and chapter 3, which addresses microscopic theories of charge transfer.

Section 2.2 presents the current established theories regarding the mechanism of photocatalytic water oxidation. The principal question of how water oxidation progresses is framed in its historical context and the latest discoveries in the field, mine included, are summarized.

2.1 Foundations of Semiconductor Electrochemistry

2.1.1 Semiconductor Electronic Structure

Solid state material electronic structure is the result of atomic orbitals mixing between atoms in extended periodic lattices. The resulting electronic orbitals can be described by band theory, an approximation that uses the periodicity of the lattice to explain some of the unique properties of solids. The orbital mixing gives rise to so-called electronic “bands”. These bands are characterized by their continuous distribution of states with a certain density per unit energy and unit volume. The unique properties of band-like electronic structure is what gives rise to the high conductivity, among other properties, associated with some solid state materials.

The relative occupation and density of these bands define a material as a conductor, an insulator, or a semiconductor. When the distribution of electrons is such that a band is partially occupied, the material is generally considered a conductor. When the distribution falls such that all bands are either completely full or empty (in the absence of thermal excitations), the material behaves as a semiconductor or insulator. To characterize materials quantitatively, the energy distribution of an electron population at equilibrium is first described by the Fermi-Dirac distribution function, Equation 2.1, which assumes a Boltzmann distribution of electron energies at equilibrium [21]. The energy where a hypothetical state would be 50% occupied is known as the Fermi Energy (E_F). Combining the effective density of states of the material with Fermi-Dirac population statistics allows us

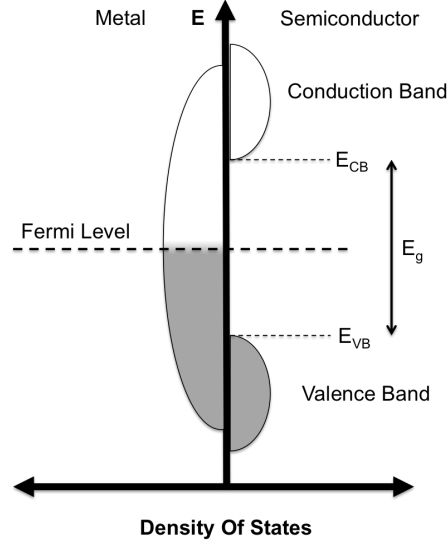


Figure 2.1: Density of States (DOS) of a typical metal and semiconductor. The Fermi level (E_F) falls within a band for a metal, and between bands for a semiconductor. The bands above and below the Fermi level in a semiconductor are known as the conduction and valence bands, respectively. The energy separating the bottom of the conduction band (E_{CB}) and top of the valence band (E_{VB}) is known as the band-gap, and is usually represented as E_g .

to calculate the occupation of conduction band states (Equation 2.2) and vacancies in the valence band states (referred to as valence band “holes”, Equation 2.3) in the material. For intrinsic semiconductors i.e. those without any dopants, the Fermi level lies in the middle of the band gap. The density of states (DOS) with respect to electron energy (E) for a typical metal and semiconductor are shown in Figure 2.1. The population of thermally excited electrons and holes in intrinsic semiconductors drops off exponentially for materials with band gaps larger than the thermal energy kT (approximately 26 meV at 300K). For wide band gap materials such as SrTiO_3 ($E_g = 3.2$ eV), with typical effective density of states $N_C \approx 10^{19} \text{ cm}^{-3}$ [22], the intrinsic population of electrons and holes is 10^{-9} cm^{-3} , effectively zero.

$$f(E) = \frac{1}{1 + \exp \left[\frac{E - E_F}{kT} \right]} \quad (2.1)$$

$$n(E) = N_C \exp \left[-\frac{E - E_F}{2kT} \right] \quad (2.2)$$

$$p(E) = N_V \exp \left[-\frac{E - E_F}{2kT} \right] \quad (2.3)$$

Non-stoichiometric impurities can be introduced into intrinsic semiconductors that give rise to a finite density of states within the band-gap region, where previously the density of states was zero. Doping of SrTiO_3 is achieved by substitution of Ti atoms with p-type electron deficient atoms (e.g. Fe), n-type electron donating atoms (e.g. Nb), or by controlling lattice defect concentrations. Oxygen deficiencies in the lattice have been shown to introduce excess electrons in the material [23]. Introduction of an occupied state just below the conduction band serves to move the Fermi level from the middle of the band gap to half way between the occupied dopant state and the unoccupied conduction band edge (CBE). If the new Fermi level is within kT of the CBE then the dopant states can be thermally excited, *donating* their electrons to the conduction band and leaving behind unoccupied states. Semiconductors doped in this way are known as n-type, and at room temperature are commonly assumed to have conduction band electron density equal to the donor dopant density (i.e. 100% of donor states are ionized at room temperature). In the same manner, introducing unoccupied dopant states close to the valence band edge (VBE) moves the Fermi level to within several kT of the VBE where these states *accept* thermally excited electrons from the VBE, leaving behind holes. Semiconductors with significant valence band hole populations due to dopant electron acceptors are referred to as p-type, with the hole population equal to the acceptor dopant concentration (N_A). It is important to note that at equilibrium, conduction band electrons and valence band holes feel a screened coulomb attraction and can react, transferring the high-energy electron to the lower, unoccupied hole state. Conservation of energy requires that the lost energy be re-emitted, e.g. as a photon (fluorescence), as phonons (heat) or transferred to an adjacent carrier (Auger processes). This equilibrium is described by Equation 2.4 for intrinsic semiconductors, where $n = p$ because the only method of generating conduction band electrons leaves behind a valence band hole. In n-type semiconductors the hole population is given by Equation 2.5, and is significantly smaller than the intrinsic concentration because even low concentrations of holes react with the increased population of electrons. In all semiconductors the dopant-induced carrier is referred to as the *majority carrier* because of its relatively enhanced population density and the other carrier is referred to as the *minority carrier*. In complete analogy, holes are the majority carrier in p-type semiconductors, electrons are the minority carrier, and the minority carrier density is given by Equation 2.6. The location of the dopant states and the resulting Fermi level shift for n- and p-type semiconductors is shown in Figure 2.2.

$$n = p = \exp \left[\frac{-E_g}{2kT} \right] \quad (2.4)$$

$$p = \frac{(n_i)^2}{n} = \frac{(n_i)^2}{N_D} \quad (2.5)$$

$$n = \frac{(n_i)^2}{p} = \frac{(n_i)^2}{N_A} \quad (2.6)$$

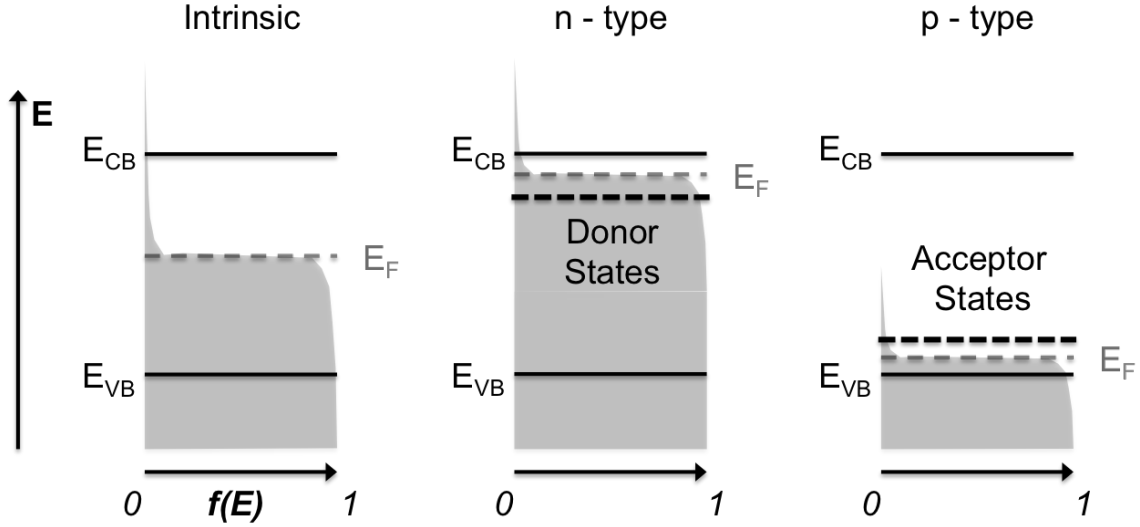


Figure 2.2: Band diagrams of the intrinsic, n-doped and p-doped semiconductors. The Fermi-Dirac distribution function for each material is overlaid in grey. The dopant states introduced close to the conduction band (n-type) or valence band (p-type) causes the Fermi level to shift, and results in an equilibrium population of the doping *majority carrier*.

2.1.2 Electrolyte Electronic Structure

Fermi Levels are Electrochemical Potentials

In order to perform electrochemistry a semiconductor electrode must be immersed in an electrolyte. Each phase has electrons occupying states with unique and unequal energies, which results in electron transfer directly upon contact. Before addressing this issue however it is important to highlight two different conventions used to describe the energy of electrons in the solid-state (Fermi level) and electrolyte (electrochemical potential). Unifying these two descriptions is in fact easy, as the Fermi level used to describe the occupation of the semiconductor states is the same as the electrochemical potential used in the electrochemistry literature [24] as shown by Equation (2.7).

$$E_F^\alpha = \bar{\mu}_e^\alpha = \mu_e^\alpha \pm e\phi^\alpha \quad (2.7)$$

In brief summary, the Fermi level in phase α is equal to the chemical potential of an electron μ_e in phase α with the additional potential $e\phi$ arising from any electric field present in α acting on the charged electron. The Fermi level, drawing from solid state conventions, is commonly referenced to the vacuum level ($E_{\text{vac}} = 0$) and is more negative at lower overall energy. In contrast the chemical potential, drawing from electrochemistry conventions, is often given in reference to the Standard Hydrogen Electrode ($\text{SHE} = 0$) and with more positive potentials associated with lower overall energy. The two standards

can be reconciled, finding $\text{SHE} = -4.5 \pm 0.1 \text{ V}$ with respect to a resting electron in the vacuum state [25, 20].

The active redox couple in solution defines the electrochemical potential (i.e. Fermi level) of the solution. The potential of the highest occupied molecular orbital (HOMO) defines the lower bound for an oxidation potential, and the lowest unoccupied molecular orbital (LUMO) defines the upper bound for a reduction potential, as shown in Figure 2.4a. The electrochemical potential is defined as the midpoint between the two electronic states. Although individual HOMO and LUMO are quite narrow, the ensemble sampled at finite temperature is inhomogenously broadened due to the range of solvation conditions arising from thermal fluctuations of the solvent surrounding the individual redox species. The effect of solvation can cause redox levels to broaden and shift the level energy by up to several eV.

2.1.3 Semiconductor - Liquid Junctions

By convention, systems that are in equilibrium are represented as having an equal Fermi level. As shown in Figure 2.3a, when two materials come in contact with each other the unique Fermi level of each material implies a thermodynamic driving force for electron transfer from the electrons in higher lying states (from the material with a higher Fermi level) to any unoccupied, lower lying states newly available at the interface (from the material with the lower Fermi level). For an n-type semiconductor such as niobium doped strontium titanate the transferred majority charge carriers (electrons), leave behind positively charged niobium donor atoms. These atoms are immobile within the material lattice. The coulomb interaction between the transferred electrons and ionized donors produces an electric field that eventually prohibits further charges from transferring. The charges transferred at the semiconductor interface leave behind a *depletion region* free of majority carriers.

The space charge region extends a finite distance W into the semiconductor due to the low charge density in semiconductors. Assuming that all donor atoms within the depletion region are ionized (the Schottky approximation) and solving Poisson's equation (Equation 2.8) gives the potential with respect to distance from the interface (Equation 2.9), which can be further rearranged to give Equation 2.10 for the depletion width [25, 26].

$$\frac{d^2U(z)}{dz^2} = -\frac{e^2N_D}{\varepsilon\varepsilon_0} \quad (2.8)$$

$$U(z) = -\frac{e^2N_D}{2\varepsilon\varepsilon_0}(z - \omega_0)^2 \quad (2.9)$$

$$W = \sqrt{\frac{e\varepsilon\varepsilon_0}{eN_D} \left(U_{SC} - U_{applied} - \frac{kT}{e} \right)} \quad (2.10)$$

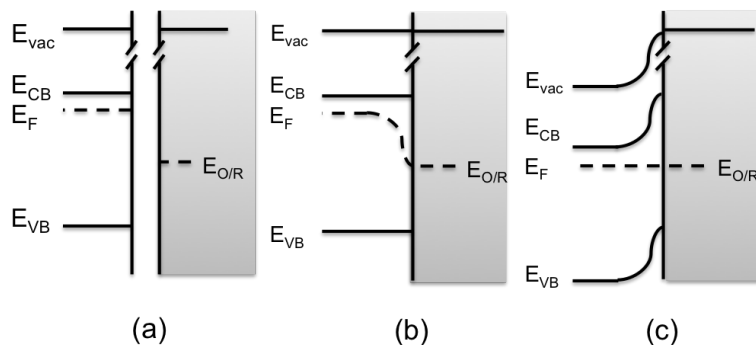


Figure 2.3: Band Diagram of energy levels for an n-type semiconductor, electrolyte interface. (a) Before equilibrating, the material Fermi levels are unique to each material. (b) Immediately after coming in contact, majority carriers (electrons) will begin to move to lower lying states now present at the interface. As they do so they leave behind the immobile donor atoms. (c) The coulomb interaction between the positive lattice charges and transferred electrons builds up until the driving force for electron transfer is balanced by the counter-acting electric field. The build-up of an interfacial electric field is not explicitly shown, but is represented by bending of the vacuum level.

Beyond the screening effects of ions in solution typically addressed for metal electrodes, semiconductor electrodes experience an additional potential drop within the space-charge region due to the immobilized charge carriers in the lattice. This has the effect of limiting the effect of an externally applied potential on the potential difference between carriers at the band edge and the redox potential of the species within the Helmholtz layer. To quantify the potential drop experienced between a redox species in solution and a band-edge carrier, an equivalent circuit can be constructed and assumptions to limit the number of unconstrained variables can be assembled based on reasonable approximations. Detailed work of this type is contained in Chapter 4 and Bard and Faulkner [20].

When applying a potential to a metal electrode the Fermi level shifts, and changing the energy of electrons transferred at the interface. In a semiconductor the applied potential drops over the depletion region as well as the Helmholtz layer. Potential that drops within the semiconductor does not change the band-edge potential relative to the redox species in the Helmholtz layer and therefore does not change the rate of reaction at the interface. A particular applied potential of interest is that which counters the contact potential between semiconductor and electrolyte, resulting in a semiconductor with no band bending. This potential is known as the flat-band potential. The flat-band potential can be extrapolated from experiment using a Mott-Schottky plot if mitigating assumptions regarding the role of surface states are made.

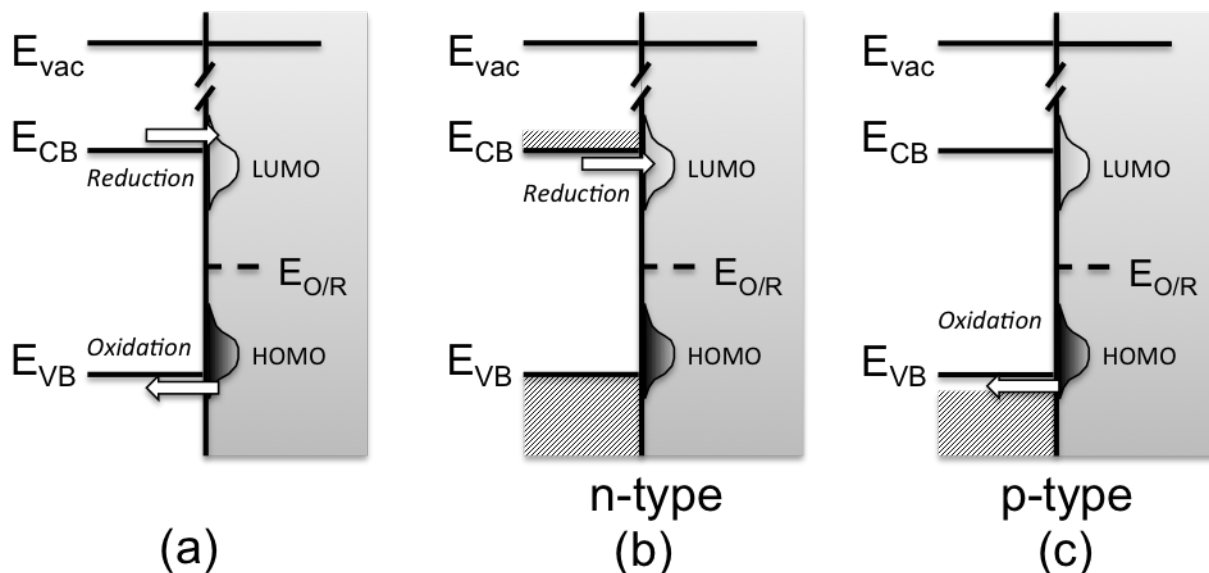


Figure 2.4: Band Diagram of energy levels for the semiconductor-electrolyte interface (band bending has been omitted for the sake of clarity). (a) For intrinsic semiconductors, during oxidation reactions electrons transfer out of the redox species' highest occupied molecular orbital (HOMO) and during reduction reactions electrons transfer into the redox species' lowest occupied molecular orbitals (LUMO). The electrolyte Fermi level is halfway between the highest occupied and lowest unoccupied level. The bulk conductivity of intrinsic semiconductors is typically extremely low. (b) For an n-type semiconductor in the dark the valence band is fully occupied and so oxidation cannot occur. Majority carriers in the conduction band are well positioned to participate in reduction reactions. (c) For a p-type semiconductor in the dark the conduction band is entirely unoccupied and so reduction reactions cannot occur. Majority carriers in the valence band however are well positioned to participate in oxidation reactions.

2.1.4 Semiconductor Electrochemistry in the Dark

At the metal-electrode / electrolyte interface the reactivity of the electrolyte phase is dominated by the species with a density of electronic states that enables electron transfer from (oxidation) or to (reduction) that species. Metal electrodes have a continuum of states above and below the Fermi Energy, so in general any unoccupied state below (or occupied state above) the Fermi Energy will react, and precise alignment of the Fermi Energy with the electrolyte state is unnecessary. In contrast, a semiconductor Fermi Energy lies between the valence band maximum and conduction band minimum so even if energetically an electron transfer were favorable, a complete lack of occupied states within the band gap would prevent charge transfer. In practice surface states on the semiconductor and solvent broadening of the redox couple electronic energy mean there is almost always some density of states present to enable a charge transfer reaction. In particular, the solvent reorganization energy plays a significant role in “smearing” the density of states associated with a well-defined redox couple in solution.

While metals at finite temperature effectively contain a simultaneous population of electrons and holes, undoped semiconductors in the dark have extremely low populations of either carrier and as a result show poor conductivity. Doping of the semiconductor produces a majority carrier population, either electrons or holes, which can now perform one type of redox chemistry. As shown in Figure 2.4b and Figure 2.4c, doped semiconductors can perform reductive (n-type) or oxidative (p-type) chemistry because of the presence of majority carriers in one of the two bands. Returning to the example of n-type strontium titanate, the near-zero valence band hole population is effectively unchanged by doping, and so the electrode cannot accept electrons from electrolyte species to perform oxidation chemistry. However, doping introduces a non-negligible electron population (as the majority carrier) at the conduction band edge that is energetically well positioned for reduction chemistry and which can be driven across the interface with sufficient applied bias. In effect, doped semiconductors in the dark exhibit metallic properties concerning the majority carrier chemistry, but as insulators concerning the minority carrier.

Restricting this discussion to the conditions where the redox couple lies within the band-gap and the applied potential remains positive (for n-type semiconductors) and negative (for p-type semiconductors) of the flat-band potential, the reaction rate for an n-type semiconductor can be described by Equation 2.11.

$$i = nFAk'_f n_{SC} C_0(x=0) \quad (2.11)$$

Both the conduction band electron population (n_{SC}) and the rate constant (k'_f) are affected by applied bias. The conduction band carrier concentration is described for an n-type semiconductor by Equation 2.12, and the rate constant for a single-electron transfer reaction (derived from transition-state theory) is described by Equation 2.13.

$$n = N_D \exp \left[-\frac{F(E - E_{fb})}{RT} \right] \quad (2.12)$$

$$k_f = k_0 \exp \left[\frac{-\alpha F (E - E_{fb})}{RT} \right] \quad (2.13)$$

The standard rate constant, k_0 , reflects the underlying rate constant defined by the material properties of the electrode and redox couple. The transfer coefficient, α , is a measure of the symmetry of the energy barrier [27, 20]. For semiconductors in the dark in this regime, the potential drop is predominantly weighted to occur within the semiconductor rather than over the Helmholtz layer, and as a result the transfer coefficient value is approximately unity. This is not true for the same regime under illumination. In the dark outside of the specific experimental conditions discussed, other phenomena such as the creation of an *inversion layer* can occur.

2.1.5 Semiconductor Electrochemistry Under Illumination

Given their low density of states relative to metal electrodes (and the corresponding lower exchange currents), semiconductors are rarely used as electrodes in traditional electrochemical cells. They have however found extensive use in photo-electrochemistry. Under illumination with photon energy larger than the band gap, semiconductors absorb photons, exciting an electron from the valence band into the conduction band. For n-type (p-type) semiconductors in contact with a redox couple below (above) the conduction (valence) band edge, the built-in electric field present within the space charge layer separates the electron-hole pair, shuttling the minority carrier to the surface and the majority carrier to the electrode bulk. Without this separation carrier pairs recombine (the electron returns to the unoccupied valence band state) through a number of mechanisms including direct recombination with accompanying photon generation, trap-state mediated recombination, Auger recombination and others. When the depletion width matches or is greater than the absorption depth of incident light the charge separation efficiency can approach unity. The dominant recombination mechanism is affected by the depletion-width, applied potential, material properties such as trap state density and carrier mobility, and illumination intensity. Minority carriers that reach the interface are capable of performing redox chemistry, transforming the energy imparted from the absorbed photon into chemical bonds. N-type semiconductors with upward band bending perform oxidation chemistry with an effective potential of the valence band edge, while p-type semiconductors with downward band bending can perform reduction chemistry with an effective potential of the conduction band minimum. When solar irradiance is used as the light source, semiconductor electrodes can serve as a mechanism for renewable energy stored as chemical fuels. As discovered by researchers in the field of photovoltaics [5] and now discussed in established photovoltaic literature [28], single band gap materials do not efficiently absorb sub-band gap light, and release excess photon energy beyond the band gap energy as heat. They are therefore limited in their efficient use of the solar spectrum to approximately 30% quantum efficiency. Several techniques to get around this limit have been proposed [26, 7, 29] with varying success. I will not discuss the schemes further

because although these schemes are of great interest when envisioning commercial applications, they primarily center on the photo-physics preceding the surface photochemistry and therefore are independent of the focus of this dissertation, specifically the mechanism of photoelectrochemical water oxidation chemistry on semiconductor electrodes.

2.2 The Mechanism of Photo-Electrochemical Water Oxidation On Semiconductor Electrodes

At the outset of my dissertation work the research community possessed a limited understanding of the reaction mechanism of water oxidation at semiconductor surfaces. Despite intense interest following the initial discovery of water oxidation by Fujishima and Honda in 1968 [30], published mechanistic work focused primarily on the rate-determining step that is experimentally accessible by “slow” probes such as electrochemistry and steady-state spectroscopies. No experimental evidence had been published on the reaction progression leading up to the rate-determining step.

Water oxidation at semiconductor valence band edges could reasonably be expected to progress through a similar mechanism whether the charge transfer at the interface is driven by valence band holes generated through photo-excitation or by an external bias [20, Ch. 18]. While there exist reaction mechanisms unique to photo-driven water oxidation (such as hot-electron transfer) these pathways are generally negligible ($< 3\%$ quantum yield) due to the short lifetime of the excited states involved [31]. As a result established theories regarding the electrochemical reaction mechanism at semiconductor and metal electrodes are often used as a basis for developing theories regarding the mechanism under photo-driven conditions.

Key mechanistic insights established at the outset of the project are available from review papers published at the time [32, 33] and include: the overall stoichiometry of the reaction is a four hole transfer and four step reaction [34], revealed by calibrated-fluence overall rate studies. The rate-determining step is not potential dependent [35]. The rate-limiting step is sometimes assigned to the initial charge transfer [35], O – O bond formation, or O₂-release [32].

Three popular mechanisms that have been proposed for water oxidation at PEC catalyst surfaces are: (1) outer-sphere electron transfer to form solvated hydroxide radicals, (2) sequential electron transfers at a single active site, and (3) single electron transfers at multiple sites followed by surface diffusion and combination.

Outer sphere hydroxide radical formation, essentially formation of a highly reactive species free in solution, was the initial hypothesis proposed to explain water oxidation at a TiO₂ electrode [8, 9, 10]. After the system was driven over the transition state barrier to form the hydroxide radical, the species was theorized to traverse a spontaneous reaction path to form hydrogen peroxide, which subsequently released molecular oxygen through photo-catalyzed or solution-catalyzed decomposition. Direct hydroxide radical production, while a primary mechanism in the oxidation of organic molecules in aqueous

solution [9], remains disputed as a mechanism for water oxidation. In particular, workers found that the surface-trapped holes on titania produce similar fluorescence signatures to the radical-traps used to identify the presence of the hydroxyl radical [11]. Other works found that while present, the percent-yield is in fact quite low [36] while recent (2013) work rules the mechanism out conclusively [12].

The two remaining proposed mechanisms for water oxidation are differentiated by how four charges (holes) are eventually localized on one molecular species. The first mechanism involves concentration of the charges on highly reactive metal centers with large formal oxidation state changes followed by nucleophilic attack by molecular water. These metal centers serve as the unique catalytic site that stabilizes the otherwise unfavorable co-localization of multiple charges. This mechanism is referred to as the Single-Site, Multiple-Oxidation (SS-MO) mechanism, the nucleophilic attack (NA) mechanism [37] mechanism, or the water nucleophilic attack (WNA) mechanism in molecular systems [38]. The second mechanism involves the accumulation of charges at single surface metal sites with single formal charge accumulations either on the metal center or residing on adsorbed molecular species. These singly oxidized species then diffuse on the surface until encountering another singly oxidized species to form an activated complex spontaneously. This mechanism is referred to as the Multi-Site, Single-Oxidation (MS-SO) mechanism, the redox photo-oxidation (RP) mechanism [37], or the radical coupling pathway (RC) in molecular systems [38]. Both mechanisms proceed from the activated complex to the potential-independent rate-determining step, likely O – O bond formation or O₂ release, after which ambient solvent adsorbs to the site, closing the catalytic cycle.

In 2011, Frei and workers [39] presented evidence for the first mechanism (SS-MO) on iridium oxide nanoclusters. The reaction mechanism identified by microsecond transient infrared spectroscopy progressed through Ir^{IV} → Ir^V → Ir^{III} cycles. From the publication itself [39]:

Specifically, the findings confirm the dominant role of nucleophilic attack of H₂O on an electrophilic oxo metal site in O – O bond formation over a possible alternative path of direct coupling of adjacent oxo metal sites ($M = O + O = M \rightarrow O_2 + M + M$) to liberate O₂.

Further evidence for a SS-MO mechanism was provided by x-ray studies on IrO₂ performing as an electrochemical catalyst rather than PEC catalyst. The results showed Ir^{III}, Ir^{IV}, and Ir^V intermediate states that appear only in the catalytic potential regime [40]. Beyond iridium-oxide systems, evidence for multi-valence catalytic sites in monometallic iron-based homogenous catalysts [41] have also been found, whereas for iron-based heterogeneous catalysts (i.e. with access to adjacent metal centers) the established evidence is less clear, but leans towards high-valence active sites [42, 37]. A recent review [43] and citations therein discuss MnO₂ systems and also present evidence for multiply oxidized metal centers (Mn²⁺, Mn³⁺, and Mn⁴⁺) playing a role during photocatalysis.

In a more muddled case, for Co₃O₄ – phosphate thin-film catalysts (Co – Pi) [44] a Co^{III} – OH and Co^{IV} – OH interaction was identified as an important step before the

rate-determining O – O bond formation. Existence of the Co^{IV} species was also identified by EPR [45] and XANES/EXAFS [46]. The experimental evidence does not reveal the origin of the Co^{IV} species, i.e. whether it is preferentially derived from the native Co^{II} or Co^{III} sites. However, whether the mechanism on these mixed-valance metals progresses through a multiply oxidized metal site or not, it does clearly involve the participation of an adjacent metal site.

Evidence for the second (MS-SO) mechanism is found on other materials. Cobalt-oxide mixed valence nanoparticle studies found multiple catalytic sites [47] including a fast site that operates through early formation of co-located oxo ($\text{Co} = \text{O}$) intermediates that react with water to form a peroxo-containing (O – O) intermediate. The critical step (judging by the build up of the precursor) follows formation of a radical peroxo-moiety and is likely the release of O_2 . The same work identified an early oxo species $\text{Co} = \text{O}$ as characteristic of a slow reactive site despite its similarity to the fast-site’s single-hole intermediate state. Subsequent theoretical calculations using DFT [48] reveal the energetics behind the multi-site/single-hole transfer mechanistic pathway on cobalt oxide. They report the Co_3O_4 mechanism involves surface hopping of single-charge-transfer species (an oxo) to reach adjacent sites before nucleophilic attack by water drives the catalytic cycle to completion.

Circumstantial evidence for an alternate (i.e. the multi-site, singly oxidized) mechanism arises from the high quantum efficiency of titanium-oxide PEC catalysts such as TiO_2 and SrTiO_3 as they only contain metal that are already in highly oxidized states. Oxidation of the Ti^{4+} metal center is thermodynamically inaccessible with band-gap illumination (requiring 57 eV [14, page E-63]) and such a species, if generated, would immediately extract an electron from the primarily O(2p)-composed valance band and return to the Ti^{4+} state. Qualitatively, the multi-site, singly oxidized mechanism appears to avert some of the coulomb repulsion expected from co-localizing multiple holes at a single metal center.

In Chapter 5 I present my work identifying the primary, nascent catalytic intermediate to be the titanium-bound neutral oxyl radical. This discovery resolved the discrepancy revolving around the titanium oxidation state (unchanged, as the charge is located on the surface hydroxide). The long lifetime of this species at the surface suggests the primary mechanism on strontium titanate could be through the multi-site, singly oxidized mechanism. Note the peroxo species that could have fallen in a similar spectral range is not expected to appear within the temporal range (1.5 ns) of the transient infrared experiments.

With the experimental setup completed, further studies can be done to extend the probe to a range of PEC materials. Comparison between the titanates (likely candidates for the MS-SO mechanism) and iridium oxide (expected to proceed through the SS-MO mechanism) would be of particular interest. Other attractive experiments for continuing this work would be extending my transient infrared probe to TiO_2 rutile and anatase catalysts to confirm the generality of the oxyl state and its sub-surface vibrational signature, as well as extending the temporal range of the method to observe later reaction intermediates.

Chapter 3

Experimental Methods

3.1 Ultrafast Pump-Probe Spectroscopy

3.1.1 Overview

As the third generation of graduate students in a new research lab, I had the privilege of constructing, in concert with our post-doc Dr. Matthias Waegele, the setup that enabled my research in ultrafast vibrational spectroscopy of molecular dynamics at the SrTiO₃ surface. The excitation and probe pulses derived from a regeneratively amplified Ti:Sapphire laser (Legend Elite HE, Coherent Inc.) that produced high power ultrafast pulses (125 fs, 800 nm) at a repetition rate of 1 kHz. The amplifier was seeded by $\approx 8 \mu\text{J}$ pulses at 80 MHz with a bandwidth of 100 fs from a Ti:Sapphire oscillator (Vitesse, Coherent Inc.) driven with internally maintained solid-state pump lasers. The amplifier crystal was pumped at 1 kHz by an internally up-converted Nd:YLF green pump laser (Evolution, Coherent Inc.) which produced 20 W of 532 nm light. Before injection into the amplifier cavity the seed pulse was first spectrally dispersed, passed through a mask to lower the bandwidth to 125 fs and then recollimated (“stretched”). This optimized the pulse length and bandwidth for mid-IR generation downstream. The output of this amplified system (125 fs, 800 nm, 5 mJ, 1 kHz) was split immediately after recompression, directing 60% (≈ 2.5 W) of the beam power to a commercially purchased white-light seeded two stage Optical Parametric Amplifier (OPerA Solo, Light Conversion, Vilnius, Lithuania) with integrated difference frequency generation using non-linear alignment to a AgGaS₂ and AgGaSe₂ crystal. The remaining light (≈ 2 W) was split further to power other experiments on the optical table. Approximately 300 mW was returned to the transient infrared experimental setup and passed through a computer controlled mechanical delay stage (MTM250CC1; Newport, Inc., Irvine, CA) before being converted to the 800 nm probe or 266 nm pump for the near-infrared and mid-infrared experiments, respectively.

3.1.2 Excitation Pulses

Third Harmonic Generation: Investigating the molecular dynamics that follow charge-transfer during the photochemical cycle required exciting the sample with a excitation pulse with photon energy above the band gap of strontium titanate. The band structure for strontium titanate has indirect and direct band gaps of $E_g = 3.25$ eV and $E_g = 3.75$ eV, respectively [49]. The third harmonic of our fundamental 800 nm light provided an easy route to 266 nm light, $E_{hv} = 4.66$ eV, sufficient to excite well beyond the valence and conduction band edges. The third harmonic was generated using a commercially purchased kit from Eksma Optics through their American distributor Altos Photonics. The product name was Femtokit Basic FK-800-200-M. The optics were designed for ultrafast pulses at 800 nm with a pulse duration of 200 fs. The kit consisted of four

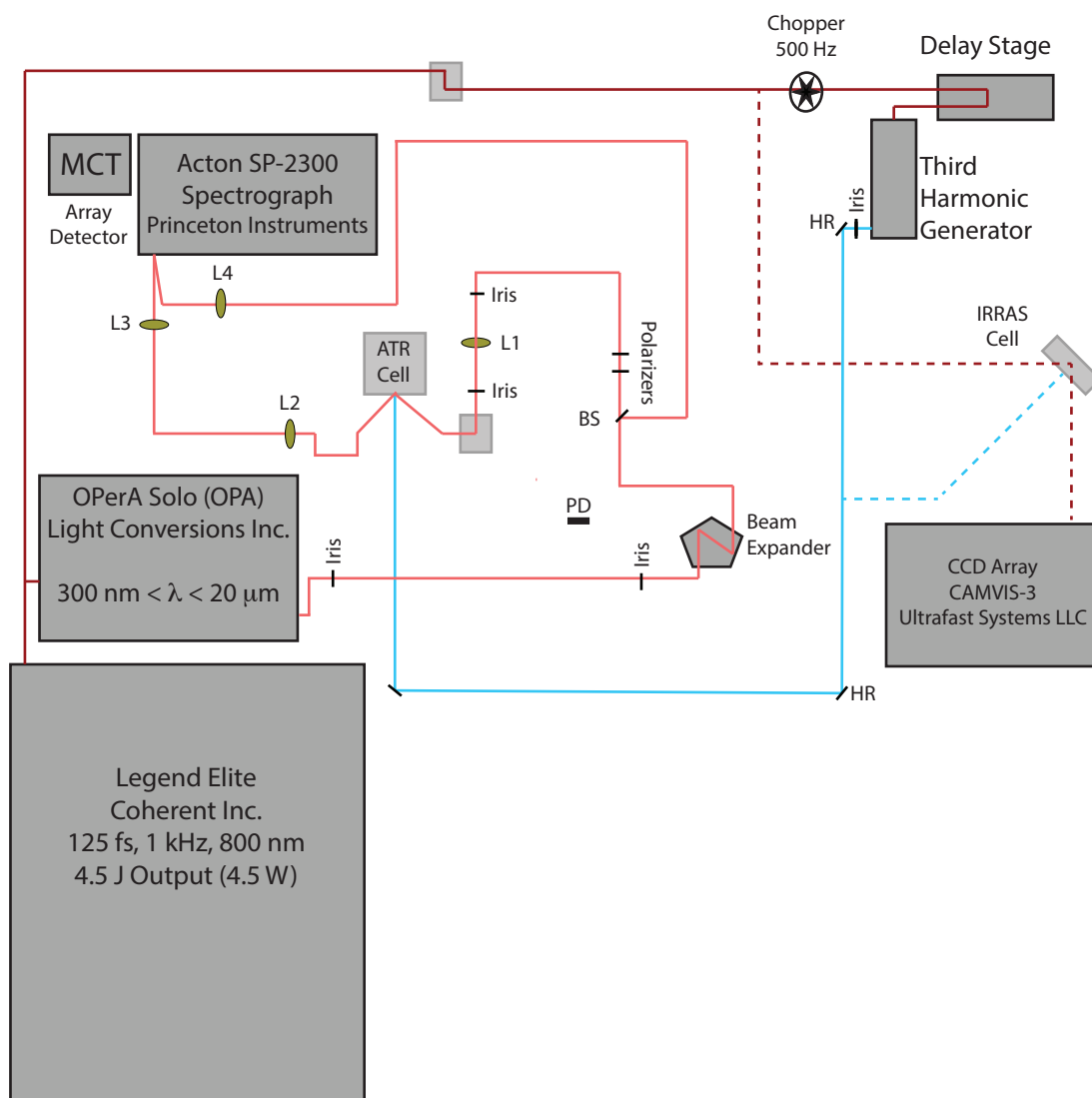


Figure 3.1: Pump-probe experimental setup: The pump line is shown in blue, the probe in red. The transient mid-infrared experiment beam path is shown as solid lines, the transient near-infrared (800 nm) experiment is shown as dotted lines.

Third Harmonic Generation

Input: 800 nm, 133 fs, 300 μJ , $\varphi = 0^\circ$

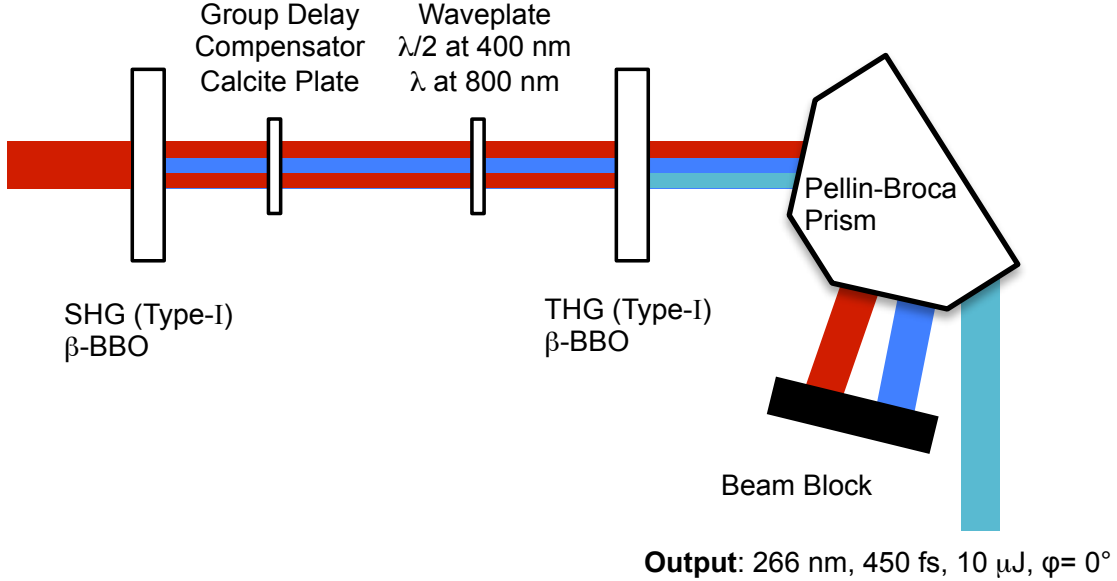


Figure 3.2: Third Harmonic Generation: SHG (type-I), GVD-correction, SH-waveplate, THG (Type-I)

optics. First, a type-I β -Barium Borate (BBO) crystal to accept the S-polarized 800 nm fundamental and generate a coherent, P-polarized pulse with the frequency of the second harmonic (SH) of the fundamental. Within the crystal the difference in propagation velocity for 800 nm and 400 nm pulses (GVM or “Group Velocity Mismatch”) introduced a quantifiable temporal walk-off of the two beams [50, 51]. To compensate for this walk-off a calcite crystal was placed after the first BBO crystal. The calcite birefringence introduced a negative group velocity mismatch between the S-polarized fundamental and P-polarized second harmonic. This negative group velocity mismatch compensated that introduced in the BBO. After the calcite plate the second harmonic beam was rotated back to S-polarization by use of a wavelength selective wave plate ($\lambda/2$ @ 400 nm, $\lambda = 800$ nm). Finally the third harmonic was generated by collinear alignment of the second harmonic and residual fundamental in a type-I BBO crystal. The physical process behind harmonic generation has been addressed in the literature[52, 53] and in modern textbooks[54].

Separation: The 266 nm, 400 nm, and 800 nm pulses were separated using a Pellin-Broca prism at Brewster’s angle. Numerous stray beams were blocked by an anodized-aluminum housing, and the correct wavelength was selected by positioning a large iris

and an exit port at the appropriate position. The pump wavelength purity was improved further by reflecting off of two dichroic mirrors with high ($>99\%$) reflectivity at 266 nm and high transmission ($>90\%$) at 400 nm and 800 nm. The overall conversion and separation process was approximately 10% efficient (250 mW of 800 nm fundamental can be converted to 20 mW of 266 nm light).

Characterization: Characterization of the third harmonic was done after wavelength separation. The fundamental and third harmonic beam diameters were measured using a knife-edge scan with a fresh razor blade and a micrometer actuated linear stage. The beam power was measured using a wavelength-calibrated power meter and scaled by the repetition rate (1 kHz) to calculate pulse energies. The pulse length of the fundamental beam was characterized by auto-correlation using type-I SHG in a 1-mm thick BBO crystal. The third harmonic pulse length was characterized by recording the photo-induced carrier rise-time in a solid sample of SrTiO_3 , probed with the previously characterized fundamental (133 ± 6 fs FWHM). This provided a lower bound for the third harmonic pulse length. By these techniques, an input beam with 9.0 mm $1/e^2$ diameter, $220 \frac{\mu\text{J}}{\text{pulse}}$ and 133 ± 6 fs FWHM was used to produce a third harmonic pump beam with 2.0 mm $1/e^2$ diameter, $17 \frac{\mu\text{J}}{\text{pulse}}$, and 350 fs FWHM duration. In daily operation the pump power was measured quickly and reliably using a flip mirror to redirect the beam to a calibrated photodiode (PD).

UV Pulse Stretcher: In ultrafast pump-probe spectroscopy short pulses are generally desired to maximize the experiment time-resolution. Additionally, second and third harmonic generation are non-linear processes that depend on high photon densities to overcome the inherently low conversion efficiency of multi-photon processes. However, high power femtosecond UV pulses were found to induce sample damage [16], in part due to their high peak power. As a result longer pulses can sometimes be desired. A 266 nm, 133 fs, transform-limited pulse, has a bandwidth ($\Delta\lambda$) of 0.7 nm, requiring a one-meter rod of UV grade fused silica to reach a chirped-pulse length of 1.5 ps using dispersion. Other UV transparent materials have similar group velocity delay values, typically 3.3 fs/mm. An alternate method [55] [also communicated privately by Coherent Inc.] takes advantage of birefringence in the UV-transparent alpha-barium borate crystal (α -BBO). In a crystal rotated 45° with respect to the incident polarization, a pulse will separate into two pulses due to the ordinary and extraordinary indices of refraction experienced for each polarization component. The pulse separation is related to the thickness of the α -BBO crystal and the difference in the ordinary and extraordinary indices of refraction. α -BBO birefringence produces an effective group velocity delay of ≈ 300 fs/mm for the two polarizations. Passing the beam through a series of progressively thicker crystals generates a longer pulse composed of the overlapping individual short pulses. A stretcher was constructed of six α -BBO crystals (thicknesses: 185 μm , 514 μm , 1027 μm , 2055 μm , 4109 μm , 8219 μm) to stretch the 266 nm pump, if desired. The 266 nm light cannot be measured in our home-built auto-correlator. To characterize the stretcher, the fundamental beam (800 nm, 133 fs) was measured before and after the stretcher. Dispersion due to the fundamental bandwidth was measured with the crystals oriented to

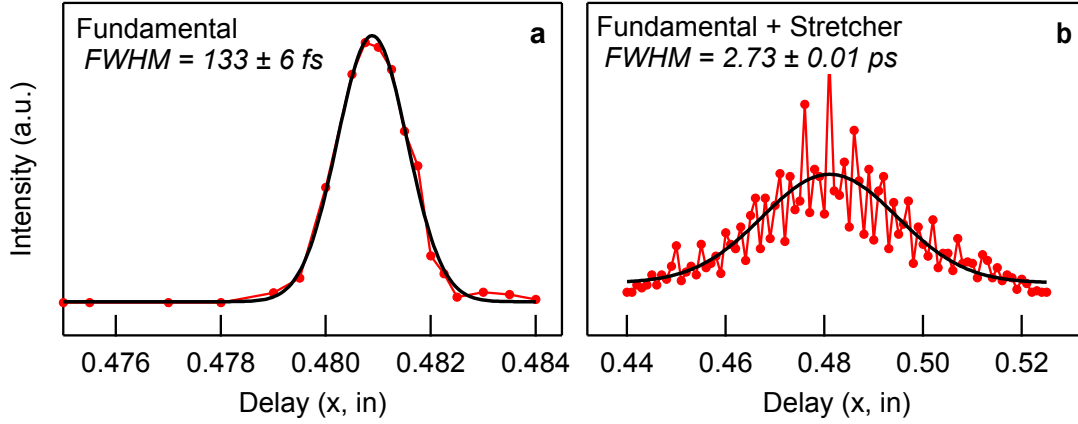


Figure 3.3: Autocorrelation of 800 nm fundamental before and after birefringent stretcher.

match the incident pulse, resulting in a 160 fs pulse FWHM (not shown). Figure 3.3 shows the autocorrelation measurement of the fundamental and the fully stretched pulse. The stretcher produced a 2730 fs pulse with a roughly gaussian envelope.

3.1.3 Mid Infrared Spectrum Probe Pulses

Optical Parametric Amplification: Ultrafast pulses of broad-spectrum mid-infrared light were generated using a commercially purchased white-light seeded two stage optical parametric amplifier (OPerA Solo, Light Conversion, Vilnius, Lithuania). The OPA layout is represented in Figure 3.4. Briefly, the input beam (≈ 2.6 W) was split 90:10 with 90% of the input light (≈ 2.34 W) reserved for pumping the second stage nonlinear crystal and 10% of the input light (≈ 260 mW) used to generate the initial signal and idler. Of that 10%, a further 90% was separated for pumping the first stage nonlinear crystal, and 10% was focussed into a calcium fluoride window to generate a stable white light continuum (“WLC”). The WLC and first stage pump were overlapped spatially and temporally in a β – BBO crystal labelled NC1 in Figure 3.4. The non-collinear alignment produced four easily separable beams representing the signal, idler, residual pump and WLC. The angle and relative phase delay of the pump beam with respect to the WLC beam was computer controlled and allowed for efficient selection of the desired wavelengths. The resulting signal and idler beams were passed to a second stage where they were amplified in a β – BBO crystal (NC2) pumped by the fundamental output that was split off at the earlier stage. From there, the signal and idler beams were separated, temporally delayed and recombined at a tunable angle in one of two nonlinear crystals optimized for difference frequency generation (DFG). The two DFG crystals were AgGaS_2 ($\lambda = 2.5 \mu\text{m} - 6 \mu\text{m}$) or AgGaSe_2 ($\lambda = 5 \mu\text{m} - 15 \mu\text{m}$) and could be rotated in place to maximize the phase matching condition required to optimize mid-infrared output. As in the first stage, the

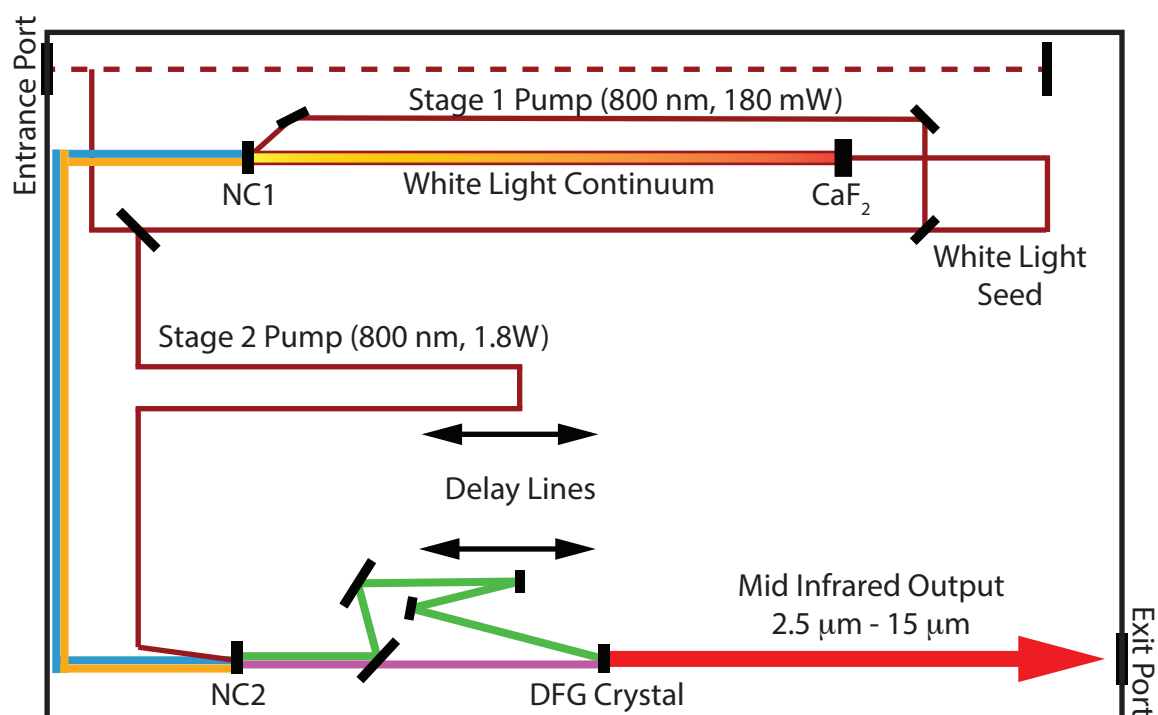


Figure 3.4: Optical Parametric Amplifier seeding non-collinear difference frequency generation to generate mid-infrared probe pulses for time-resolved vibrational spectroscopy experiments.

non-collinear geometry allowed easy separation of the remaining signal and idler beams from the mid-infrared beam. During far-infrared experiments Germanium plates were fixed over the OPA output and spectrometer slits to ensure that only the infrared probe pulse contributed to the detected signal.

Polarization control (Polarizer/Analyzer): Passing the beam through two consecutive ZnSe wire-grid polarizers controls the probe polarization and intensity. Each polarizer transmits a maximum of 70% of the IR light, and has a polarization selectivity extinction ratio in the IR of 150:1 at 3 μm and 300:1 at 10 μm . The second polarizer (“analyzer”) controls the probe polarization when it reaches the sample. The first polarizer can be used to either attenuate the beam to your desired intensity (if the incident and final polarization are the same) or is necessary to rotate the polarization of the light by $\theta/2$ before it reaches the analyzer (if a $\theta/2$ rotation is desired). Malus’s law describes the transmission of polarized light through polarization selective optics. With an initially linearly polarized incident beam, Equation 3.1 describes the transmitted probe power where θ_1 is the angle between the incident beam and the first polarizer, and θ_2 is the angle between the polarizer and analyzer.

$$I_T = I_0 \cos^2(\theta_1) \cos^2(\theta_2) \quad (3.1)$$

To rotate the P-polarized IR beam to an S-polarization, this method requires a minimum attenuation to 25% of the original power.

3.1.4 Data Collection

Taking Differential Measurements Using Alternating Laser Shots: The chopper modulates the pump pulse such that every other probe pulse is measuring an photoexcited and non-photoexcited condition. Calculating the difference between the probe intensity for the photoexcited and non-photoexcited sample using pulses that are only separated by 1 millisecond (the delay between laser shots) minimizes contributions to the signal that arise from drift in the laser intensity, or changes in other experimental conditions that occurs slower than over milliseconds. In contrast, measuring a thousand laser shots of one condition, followed by a thousand of another, can give rise to the same signal, but the reflectivity can have changed for other reasons, such as slow heating of the sample. This gives rise to a non-statistically random signal contribution (a background) that does not arise from the intended changes in the control variable.

Improving Data Quality through Signal and Reference Beams: To maximize our desired signal-to-noise ratio, another technique is applied to minimize a well known source of statistical noise: the shot-to-shot power fluctuations in the fundamental laser output. This source of noise introduces a random intensity change between two adjacent laser shots that correspond to our light-on and light-off conditions. To account for this, the probe is split using an anti-reflection coated ZnSe window into probe and reference beams. The probe light was directed and focused ($f = 150 \text{ mm}$) onto the aperture of a 45°

trapezoidal ATR element at an incident angle of 20° . After the sample, the probe beam was collimated ($f = 254$ mm) and focused ($f = 150$ mm) onto the entrance slit an Acton SP-2300 spectrograph (Princeton Instruments, Princeton, NJ), where it was spectrally dispersed and detected on the top row of a 64-element, dual-row array detector (MCT-12-64; Infrared Associates, Stuart, FL). Similarly, the reference beam was dispersed on the lower row of the detector. The reference beam intensity is always proportional to the fundamental laser shot energy and not to the sample condition. This allows us to normalize the probe intensity change to the initial laser shot energy, thereby removing contributions from the shot-to-shot laser fluctuations. This technique implies that even if two consecutive laser shots are dramatically different in energy then two adjacent laser shots can still be used to accurately measure the reflectivity change at different experimental conditions. This holds both for total energy or energy at each wavelength i.e. if the probe spectrum changes because both the signal and reference lines are spectrally dispersed and therefore normalized at all wavelengths independently.

Increasing Throughput by use of a Spectrograph and Array Detector: To increase the speed of full spectrum data collection, the infrared probe pulse is dispersed by a spectrometer (Acton SP-2300 Spectrograph, Princeton Instruments) at a dispersion angle to the detector that corresponds to 150 cm^{-1} spectral width, which matches the probe bandwidth ($\approx 200\text{ cm}^{-1}$). As mentioned above, both probe pulses (signal and reference) are dispersed and measured on two 32-element HgCdTe (“MCT”) arrays of the detector. A liquid-nitrogen Dewar in the detector cools the individual elements and minimizes thermally-derived noise. The Dewar is large enough to maintain detector operation for 10 hours. The detector is held at the focal spot of the spectrometer by a custom mount.

The signal from each element is amplified by variable preamplifiers built into the detector body before being transmitted to the box-car integrator (FPAS-6416; Infrared Systems Development, Winter Park, FL) through shielded cables. The integrator unit powers the detector, and passes each element’s signal as well as 8 “external channels” to four voltage-pot amplifiers that amplify each signal individually. Finally the Boxcar Integrator integrates the signal over a variable window of time (c.a. 2 ns) beginning after a controllable time delay triggered by a TTL signal derived from the Ti:Sapphire amplifier Pockel cells. The boxcar is set to record for an even number of trigger events, usually 1000, that is limited by the available memory of the personal computer storing the detected values. The data is then sent to a dedicated PCI card in the computer, where it can be accessed through company-provided Labview sub-VIs. The external channels carry a signal derived from a photodiode placed behind the chopper which allows the identification of the first pulse as either a “photo-excited” or “ground state” condition. To assist in selecting the correct integration parameters the pre-amplified signal from four elements (one from each quadrant, or chip) is passed directly to four BNC connectors in the back of the integrator. These can be compared with the integration-window out to visualize the relative timings.

Data Collection Software Framework: The experiment control software design is built around the boxcar sub-VI requirements for data collection. Specifically, the boxcar

must be “armed” with a full set of experimental parameters (integration window, integration delay, trims, gains, number of laser shots, etc.) before it will execute the described data collection in response to the Legend trigger signal. It cannot respond within the 10 nanosecond laser table traversal time to begin data collection in response to a trigger signal generated upstream by the same laser pulse. Instead, the boxcar integrator collects a series of laser shots beginning at an arbitrary trigger pulse. After the data is stored in on-board memory, the data is loaded into the computer memory along with an external channel that corresponds to the chopper phase (i.e. whether the probed condition was “photo-excited” or “ground state”). The software then calculates the signal/reference ratio, divides the “photo-excited” shots by the “ground state” shots, and averages all 500 remaining data points together. From there the software appends the new data to a running collection stored in memory, updates the software user-interface, delay stage and other variables, and waits for a one-second vibrational-damping period. Finally it sends the experimental parameters of the next step in the experimental series the boxcar integrator, restarting the process. At the end of a full time-trace it saves the data from the latest trace, as well as the average of all traces collected so far. The average data is saved in two formats so that professional data-visualization software such as Igor Pro can easily read the data as “absorbance vs. time” (traces at each wavelength) or “absorbance vs. wavelength” (spectra at each time point).

Data Analysis: All absorbance changes reported herein were calculated using Beer’s Law, i.e. $\Delta A = -\log(\Delta R/R_0)$, where ΔR is the time-dependent change in reflectance upon sample excitation and R_0 is the reflection before excitation. For transient mid-infrared spectroscopy, both ΔR and R_0 are normalized by the reference beam signal for each probe pulse detected. In all experiments, the pump beam was modulated by a mechanical chopper (3501; Newport, Inc., Irvine, CA) at a frequency of 500 Hz. The typical incident pump fluence was about $40 \mu\text{J}/\text{cm}^2$, corresponding to carrier densities on the order of 10^{19} cm^{-3} , or 7% of lattice sites at the surface. Using a lattice constant of 0.3905 nm, the surface site density was calculated to be $6.56 \times 10^{14} \text{ sites}/\text{cm}^2$. The excitation beam spot size was $\approx 900 \mu\text{m}$ (FWHM).

3.1.5 Design of Attenuated Total Reflection Experiments

The transient mid-infrared data was collected using the evanescent wave generated by total internal reflection at the diamond/electrolyte interface as a probe. The SrTiO_3 sample was then positioned (Figure 3.5a) within the evanescent wave which decays exponentially away from the supporting interface. Equation 3.2, describing the $1/e$ decay distance of the electric field, gives a value of $d_p \approx 3 \mu\text{m}$ for a 60° angle of incidence, at 800 cm^{-1} , for a diamond ($n_1 = 2.4$) electrolyte ($n_2 = 1.12$) interface.

$$d_p = \frac{\lambda}{2\pi\sqrt{n_1^2 \sin^2(\theta) - n_2^2}} \quad (3.2)$$

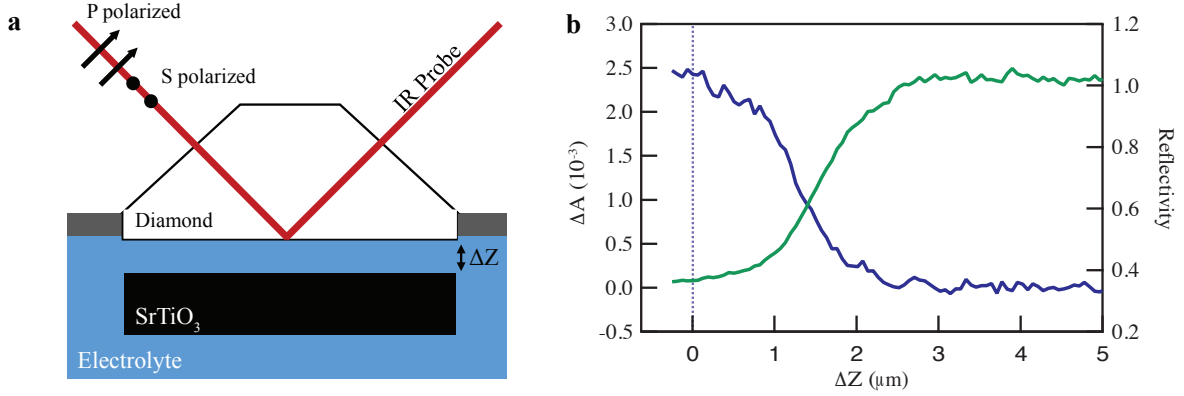


Figure 3.5: Experimental Geometry. **a**, The SrTiO_3 single crystal is positioned within the evanescent wave generated at the diamond – electrolyte interface. ΔZ ($0 - 10 \mu\text{m}$) is controlled using a piezo-electric stepper motor. **b**, When a 0.7% Nb doped SrTiO_3 sample is stepped towards the diamond, the magnitude of the transient signal (blue) grows as the sample enters the probe region. Conversely the light throughput (green) decays from its maximum value as the SrTiO_3 single-crystal attenuates the light. The dotted line indicates when the sample is considered pressed to the diamond surface.

Fine control over the electrolyte-filled gap between sample and diamond was achieved using a piezo-electric motor (Newport, Model 8302) providing 1-inch translation and 30 nm step resolution. The piezo motor does not include closed-loop feedback of the motor position, making the reported step distance approximate. Therefore, to repeatedly position the sample between experiments, I preceded each experiment by scanning the sample position as in Figure 3.5b, and then returned to the position with half the magnitude when pressed. This position is defined by the diamond, electrolyte, and angle of incidence, but is independent of the sample being probed. This provides the feedback required to reliably position the sample with respect to the diamond. Equation 3.3 governs the absorption change (for weakly absorbing samples) [56].

$$\Delta A = -\log \left[\frac{I_0 - I_0 \left(\frac{n_2^{ON} \kappa_2^{ON} |t_{12}|^2}{n_1 \cos \theta \sqrt{n_1^2 \sin^2 \theta - (n_2^{ON} + i\kappa_2^{ON})^2}} \exp \left(\frac{-2\Delta Z}{d_P} \right) \right)}{I_0 - I_0 \left(\frac{n_2^{OFF} \kappa_2^{OFF} |t_{12}|^2}{n_1 \cos \theta \sqrt{n_1^2 \sin^2 \theta - (n_2^{OFF} + i\kappa_2^{OFF})^2}} \exp \left(\frac{-2\Delta Z}{d_P} \right) \right)} \right] \quad (3.3)$$

Where n^{ON} , κ , n^{OFF} , κ^{OFF} represent the indices of refraction with light on and light off. Although the samples used in these experiments are not weak absorbers, the simplified relation serves to highlight an ATR-specific property; as the sample is positioned closer to the diamond there is greater overlap between the sample and the evanescent electric field, so more light is attenuated, and the reflectivity drops. Likewise in the differential

(pump-probe) signal, the displacement of the sample from the interface will lower the magnitude of the transient signal. This is accounted for by repeatable positioning of the sample as described above. Equation 3.3 shows that ΔA , probed by ATR, can change in a complex manner with n^{ON} , κ^{ON} , n^{OFF} , and κ^{OFF} . In the limits of weak absorption and where a continuum is not involved through n , the interpretation can be simplified to a purely absorptive change in κ . These experiments are performed in the strongly absorbing regime and also have two continua involved (the solid state plasmonic and liquid librational continua). This means that, while lineshapes that are well described by the Fano lineshape equation make it clear that the frequency dependence of an intrinsic matrix element of an absorptive change at the solid-liquid interface is observed, the sign and magnitude of the differential signal depends on the details of n and κ . Through the Kramers-Kronig relation that derives n from κ , changing the absorption cross section via κ^{ON} also modifies n^{ON} in the same spectral region. Furthermore, photoexcitation will change n , κ over a larger spectral range than is being measured. Therefore, to truly determine the absolute change in the absorptive cross-section ($\kappa^{ON} - \kappa^{OFF}$), the Kramers-Kronig relation for n and κ over a large frequency range should be consistently incorporated into the ATR equations. I do not attempt this here, as it requires taking data out to far infrared frequencies. Instead, I rationalize the sign of the signal used in the Fano line shapes analysis by the changes in reflectivity that occur with doping in the 700-1000 cm^{-1} spectral range being measured (see Figure 5.4).

3.2 Electrochemistry

3.2.1 Cyclic Voltammetry and Mott-Schottky Analysis

All electrochemistry experiments in this research were controlled and recorded by a potentiostat (CHI1140B, CH Instruments, Austin, TX). During spectro-electrochemical components of these transient spectroscopies a bias was applied to the n-SrTiO₃ working electrode with respect to an 3M KCl Ag/AgCl reference electrode (MF-2052; Basi, West Lafayette, IN). A platinum wire served as the counter electrode. Ohmic contact between the unpolished n-SrTiO₃ back side and teflon-coated gold wire was established using silver paste (Electron Microscopy Sciences, Hatfield, PA). During the transient absorption experiments only the polished front side of the crystal was exposed to electrolyte. All other surfaces were covered by an insulating lacquer or insulating epoxy (Loctite 615; Henkel North America, Rocky Hill, CT). The front surface areas of the 0.1% and 0.7% samples were ≈ 25 and ≈ 50 mm^2 , respectively.

For Mott-Schottky plots the electrode area exposed to electrolyte was restricted by lacquer to match the laser spot size of ≈ 1 mm^2 (Gaussian full-width at half-maximum). Differential capacitance measurements were carried out using AC voltammetry. The DC potential was swept from positive to negative applied potentials and the AC amplitude and frequency were 0.025 V and 100 Hz, respectively.

3.3 In-Situ Spectro-Electrochemical Reaction Cells

Transient Absorption Measurements

Transient absorption measurements (found in Chapter 4) were performed in a home-built three electrode spectro-electrochemical cell made of Teflon with CaF_2 windows (30 mm diameter, 3 mm thick). The cell contained a lid to hold the electrically-contacted sample in a consistent position roughly 1 mm from the window, with adjacent counter and reference electrodes. The cell was filled with degassed 0.1M NaOH electrolyte while exposed to air. The sample was excited by 300 nm pump pulses directed at the sample surface at $\theta = 0^\circ$ angle of incidence i.e. normal to the sample surface. The sample was probed by a small fraction of the 800 nm fundamental, directed to the sample surface at a $\theta = 45^\circ$ angle of incidence. The probe was focused on the sample surface with a $f = 150$ mm lens and then recollimated with the same before being focused into a fiber optic cable coupled to a spectrometer and CCD array (CAMVIS- 3; Ultrafast Systems, LLC, Sarasota, FL). The typical pump-induced light absorption ($\Delta A = -\log(\Delta R/R)$) was on the order of 0.8 mOD. The typical incident pump fluence was $\approx 45 \mu\text{J}/\text{cm}^2$ and generated carrier densities on the order of 10^{19} cm^{-3} . The excitation beam spot size was $\approx 500 \mu\text{m}$ (FWHM).

Transient Mid-Infrared Spectroscopy Cell Design

All mid-infrared reflectivity, electrochemical, and spectro-electrochemical measurements were performed in a custom built Teflon/stainless steel electrochemical cell designed to accommodate the requirements of in-operando photo-electrochemistry and mid-IR spectroscopy. The electrolyte used was a ≈ 1 M aqueous solution of sodium hydroxide unless otherwise noted. The electrolyte was degassed in vacuum ($\approx 10^{-4}$ torr) prior to use but remained in contact with the atmosphere during measurements.

These spectro-electrochemical cells went through iterative designs, the latest design providing important capabilities that made the transient infrared experiments possible. The sample is mounted within a watertight basin on an arm that can move on a translation stage, perpendicular to the cell wall with the diamond ATR crystal surface. A piezoelectric stepper motor with 30 nm steps controls the translation stage and therefore the diamond-sample displacement. The diamond and sample are mounted horizontally, to allow all laser beams to remain parallel to the optical table, while still providing an electrolyte environment to study electrochemical processes. The electrolyte volume incorporates a second chamber with the ability to mount a reference electrode tip within 2 cm of the working electrode surface.

The working electrode surface faces a high-purity (< 5 ppb N-atom doping) trapezoidal, single-crystal diamond mounted into the stainless steel wall (Special Order, Pike Technologies, Madison, WI). The high purity ensures no absorption of the 266 nm pump beam when the sample is excited through the diamond face. The opposite side of the stainless steel plate features a cut-away design that maintains physical support for the diamond in case the electrode contacts the diamond but simultaneously allows the infrared probe beam to enter and exit the diamond crystal. The diamond dimensions are carefully

chosen to produce a single bounce at the center of the diamond window, providing a single evanescent probe volume at the diamond-electrolyte interface. The 266 nm beam can pump through the top of the diamond to illuminate the probe volume. The cell is mounted on a magnetic mount for convenient removal, disassembly and sample changing, as well as easy replacement and repeatable laser alignment.

Chapter 4

Surface Hole Potential Dependence of Carrier Dynamics at the SrTiO₃-Electrolyte Interface During Photoelectrochemical Water Oxidation

4.1 Original Publication

The work described in this chapter was previously published as Matthias M. Waegle, Xihan Chen, David M. Herlihy, and Tanja Cuk, *Journal of the American Chemical Society* **2014**, *136* (30), 10632 [16].

4.2 Introduction

Water oxidation is important for any solar fuel cycle. Combustion of hydrogen and hydrocarbon fuels consumes molecular oxygen and produces water. For a renewable fuel to avoid the build up of waste products (e.g. CO₂) and the depletion of reactants (e.g. fossil fuels) the fuel must be regenerated from combustion products. Therefore, a renewable fuel generation system must regenerate water to molecular oxygen if it is to support combustion of either hydrogen or hydrocarbons. Transition metal oxides offer unique benefits regarding cost, scalability, and efficient use of absorbed solar energy. The space-charge region at the interface efficiently separates excited electrons and holes generated by solar radiation, minimizing energy loss through geminate or trap-assisted carrier recombination [28]. Understanding the chemistry that follows carrier separation is important and necessary to optimize the design of solar fuel systems. Strontium Titanate (SrTiO₃) is a highly efficient (quantum efficiency above 80%) and highly selective (100% chemical selectivity) catalyst for water oxidation under ultraviolet illumination. SrTiO₃ provides a model system that minimizes the convolution of the intended chemistry with loss to charge recombination, photodecomposition, and parallel reactions.

Despite extensive research the mechanism for water oxidation is poorly understood, and limited successes suggest that the mechanism on various materials can differ [57, 58, 59, 60, 42, 43, 47, 39]. The overall mechanism, Equation 4.1, is a four hole transfer reaction as required from net oxidation state balancing. Calibrated illumination studies [34, 61, 62] have corroborated a four-photon driven mechanism.



Here I present a bias-controlled study of the ultrafast charge transfer associated with the first step in the water oxidation process. The ultrafast reaction precedes the rate determining step of the reaction, and in doing so prepares the catalyst surface dynamically for that critical step. Ideally, sequential following of the elementary charge-transfer steps can eventually reveal the rate determining step and reveal general methods to improve photocatalyst efficiency. These time-resolved studies complement steady-state electrochemical and photoelectrochemical that use the relationship between product formation rates and free energy difference driving the reaction to extract activation-energy barriers [44, 63, 64]. Such studies provide mechanistic insight but are model dependent for multistep reactions [20, 65]. Uniquely, transient studies present the ability to measure the progression of a non-rate determining step, combined with control of the absolute hole

potential. This allows us to investigate the free energy dependence of the rate of the first steps of this multi-step reaction, rather than track an unknown intermediate- or net-reaction. The first step of the water oxidation reaction in basic solution is suggested to be hole transfer to a hydroxide ion, as in Equation 4.2.



The hydroxide ion is initially adsorbed or free in solution when it captures a hole, although it eventually forms the more stable surface-oxo ($Ti = O$) intermediate suggested by steady-state electrochemical studies [66, 44, 63, 64, 67, 68] and recently seen directly by millisecond time-resolved illuminated infrared studies [39, 47]. Previous ultrafast optical spectroscopy experiments have found time constants for charge transfer spanning six orders of magnitude, from 500 picoseconds [69, 70] to hundreds of milliseconds [34, 35] on other metal-oxide semiconductors such as $n\text{-Fe}_3\text{O}_4$ and $n\text{-TiO}_2$. However, these experiments were performed under experimental conditions where the quantum efficiency of O_2 evolution was as low as 0.1-5.0% [34, 71], highlighting the inherent difficulty in separating the charge-transfer process of interest from others such as carrier recombination, trapping, and photodecomposition. Without the ability to tune the free-hole potential at the interface these previous works tracked the charge transfer rate at a single electrochemical potential, defined by the valence band edge of the semiconductor in electrolyte [72, 73, 74, 75, 76]. Continuous control of the electrochemical potential of holes with an externally applied potential and laser irradiation [75, 77] provides the ability to track reaction kinetics as a function of the free energy difference between reactant and product. This, in combination with the high quantum efficiency of $SrTiO_3$ photoelectrodes even under laser irradiation, allows clear assignment of the kinetics to a single charge-transfer step of the reaction and detailed reporting of the nature of the activation barrier.

The kinetics of charge transfer are expected to depend on the free energy of the reaction as described and developed in Marcus Theory of electron transfer. In the following experiments, the free energy of reaction is tuned by application of an external bias. The applied bias drops across both the semiconductor space charge region and across the Helmholtz layer. Only the latter contributes to a change in the reaction free energy change. By modeling the interface potential distribution in combination with ultrafast transient-absorption measurements, this work provides an experimental probe of the relationship between the photoelectrode kinetics and the reaction free energy change.

This allows us to report the charge-transfer coefficient (α), a measure of how efficiently increasing the absolute potential of the hole decreases the activation barrier of the reaction. This is equivalent to investigating the curvature of the free energy surface traversed in this first step of the water oxidation reaction, and has not been done previously for photoelectrochemical reactions on transition metal oxide semiconductors. Additional information gleaned from these experiments include the rate of charge transfer when the free energy difference is zero, i.e. at the Nernstein potential. This is related to the intrinsic activation barrier for the reaction and found to be consistent with previous measurements

of the absolute potential for the $\text{OH}^-/\text{OH}^\bullet$ reaction in the gas phase. These experiments confirm the charge transfer rate follows an Arrhenius-type dependence with respect to applied bias. Finally, I am able to separate a distinct feature at longer time scales in keeping with a downstream or parallel intermediate of the water oxidation reaction.

4.3 Results

4.3.1 Quantum Efficiency of Oxygen Evolution

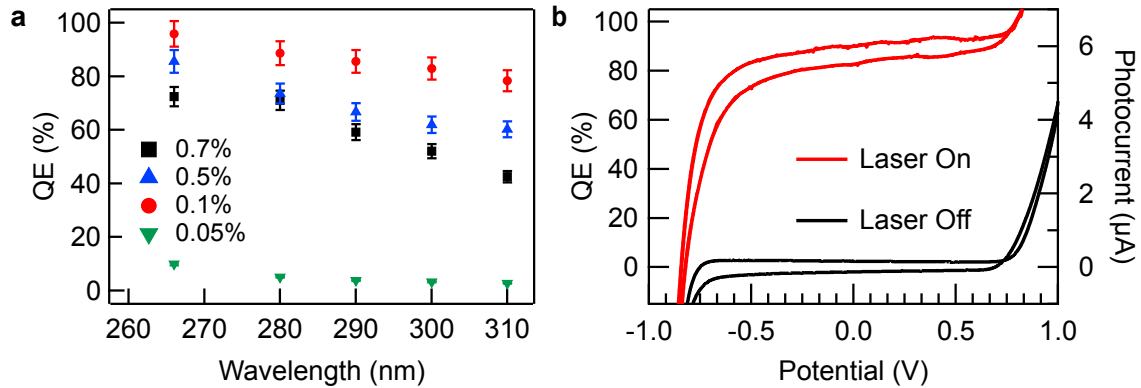


Figure 4.1: The absorbed-photon-to- O_2 quantum efficiency (QE) with respect to **a** excitation wavelength and niobium doping by weight-percent. **b** QE at a range of applied biases, referenced to a Ag/AgCl electrode. A quantum efficiency of 100% corresponds to a photocurrent of $10.7 \mu\text{A}$. Unless otherwise specified, experiments were performed at a fluence of 0.040 mJ/cm^2 , on 0.1% Nb SrTiO_3 , held at 0.0V vs Ag/AgCl in 1.0M NaOH aqueous electrolyte.

Strontium titanate has an exceptionally high absorbed-photon-to- O_2 quantum efficiency (QE). Figure 4.1a shows the quantum efficiency characterized with respect to excitation wavelength, applied bias, and sample doping. The highest quantum efficiency ($> 80\%$) was found for 0.1 weight-percent Nb doped SrTiO_3 after comparing to 0.7% Nb ($> 50\%$), 0.5% Nb ($> 60\%$) and 0.05% Nb ($\approx 5\%$). This 0.1% Nb doped SrTiO_3 samples are used for all experiments in order to preferentially track holes that contribute to water oxidation rather than recombine within the semiconductor. The excitation frequency was chosen to be $\lambda = 300 \text{ nm}$ in order to match the absorption depth (30 nm) to the depletion width at this doping.

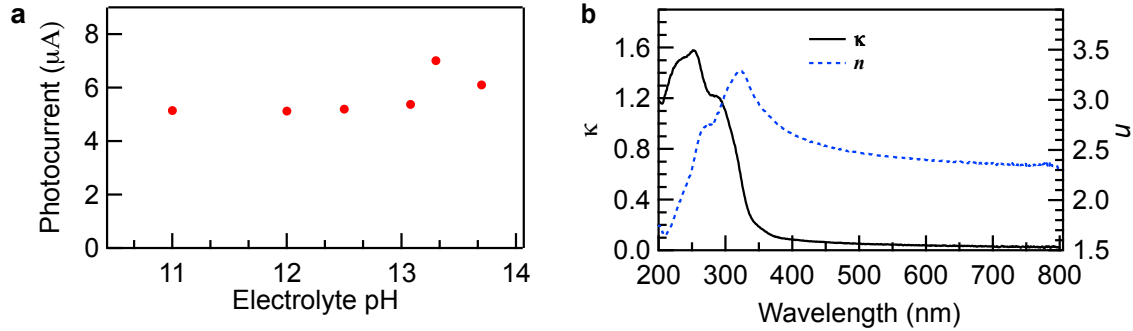


Figure 4.2: **a** The photocurrent generated in a range of electrolyte pH values. The experiment was performed in a 3-electrode cell with an electrically contacted 0.1% Nb doped SrTiO_3 sample held at 0.0V with respect to an Ag/AgCl reference electrode. The sample was illuminated with 300 nm laser pulses at a fluence of 0.04 mJ/cm^2 . **b** Ellipsometry measurements of the 0.1% Nb doped SrTiO_3 sample report the real and imaginary components of the index of refraction, n and κ respectively.

Figure 4.1b shows the quantum efficiency as a function of applied bias in a cyclic voltammetry experiment. The photocurrent, a measure of the overall (4 hole transfer) reaction rate, does not change significantly with applied bias within the range -0.8V to $+0.8\text{V}$. Additionally the photocurrent does not change with electrolyte pH (Figure 4.2a, for pH 11 - 14), indicating that the reaction is not mass transport limited. Together these confirm that the rate-determining step is not potential dependent. At applied biases more negative than -0.8V the semiconductor depletion width becomes smaller than the 300 nm photon absorption depth. As a result, the electric field no longer separates photoexcited electrons and holes and the photocurrent drops. At potentials more positive than 0.8V water oxidation chemistry occurs in the dark, as can be seen from the current onset in the dark.

To understand the high quantum efficiency of the sample and ultimately the charge dynamics at the interface it is important to have an understanding of the photo-physics that occur after excitation with above band-gap ($h\nu > E_g$) laser pulses. For a more detailed examination of the semiconductor-electrolyte interface see Chapter 2. Briefly, the interface can be considered to be made up of a depletion region within the semiconductor and layers of ions (both adsorbed and in solution) extending towards the bulk electrolyte (Gouy-Chapman-Stern model) [20]. The width of the depletion region is given, within the Schottky approximation, by Equation 4.3 [25, 26] where N_d , ϵ_0 , ϵ , e_0 , k_B , and T represent the doping density, the vacuum permittivity, the relative permittivity of the semiconductor, the electronic charge, Boltzmann's constant, and the absolute temperature, respectively. For $U_{SC} = 0.8\text{V}$ as measured from photovoltage measurements (Figure 4.4) the depletion width is 25 nm.

$$W = \sqrt{\frac{2\epsilon\epsilon_0}{|e_0| N_D} \left(U_{SC} - \frac{k_B T}{|e_0|} \right)} \quad (4.3)$$

The high quantum efficiency of the 0.1% sample under $\lambda = 300$ nm illumination is attributed to the match between the semiconductor depletion width ($W > 30$ nm) and the absorption depth, α_{abs} , given by Equation 4.4. For 300 nm light and $\kappa = 1.1$ as ascertained by ellipsometry measurements (Figure 4.2b), the absorption depth is also 30 nm. Ellipsometry measurements that measured the sample optical constants were performed on a Horiba Jobin- Yvon UVISEL Ellipsometer (Horiba, Edison, NJ). The spectra were taken in reflection mode in air at a 70° angle of incidence.

$$\alpha_{abs} = \frac{\lambda}{4\pi\kappa} \quad (4.4)$$

4.3.2 Band Edge Position in the Dark

The combination of the contact potential and any applied potential drops over both the semiconductor space charge region (U_{SC}) and the electrode double layer (U_H) [72, 73, 74, 75, 76]. I treat the double layer within the Helmholtz model, as represented by two capacitors in series [72, 73, 74] (Figure 4.3). This overestimates the potential drop over the Helmholtz layer by neglecting charge screening by ion rearrangement within the electrolyte diffuse layer [20]. For electrolyte spanning pH 7.5 to pH 13.5, the Debye length (Equation 4.5) and therefore the diffuse layer thickness changes by a factor of 10^3 .

$$\kappa^{-1} = \sqrt{\frac{\epsilon\epsilon_0 RT}{2F^2 C_0}} \quad (4.5)$$

As a result, the diffuse layer potential drop, approximated as a parallel plate capacitor where $U_{dl} \propto \frac{\epsilon\epsilon_0 A}{d}$, changes by a similar factor of 10^3 . The photocurrent (Figure 4.2a) is shown to be independent of electrolyte pH. This justifies a model that

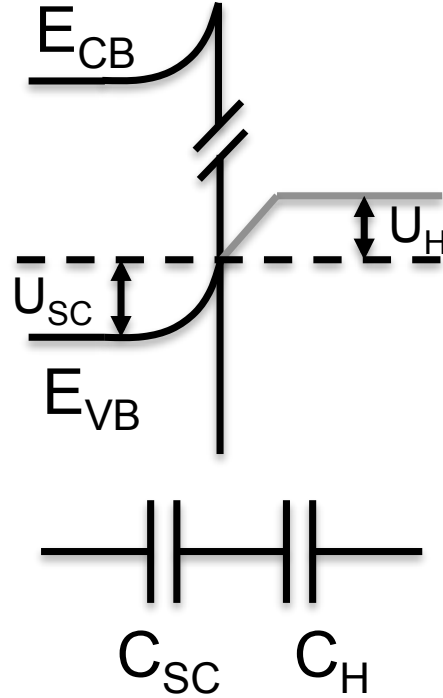


Figure 4.3: The Helmholtz model of the interface. The space charge capacitance (C_{SC}) and Helmholtz capacitance (C_H) are modeled as two parallel-plate capacitors in series. The combined contact potential (U_{fb}) and applied bias ($U_{applied}$) drops over each region in relation to their capacitance.

does not account for the diffuse layer potential drop as it is clearly negligible under these experimental conditions. Using that assumption, the total potential drop between bulk electrolyte and bulk semiconductor is given by the sum of the contact potential (U_{fb}) resulting from the chemical potential difference between the two materials, and any applied bias (U_{appl}). Together they give Equation 4.6 [73, 75].

$$U_{fb} - U_{applied} = U_{SC} + U_H \quad (4.6)$$

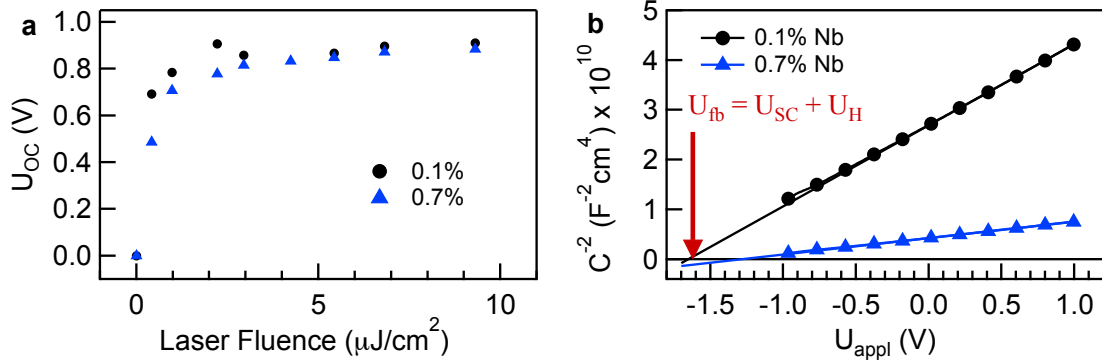


Figure 4.4: **a** Photovoltage measurements of 0.1% and 0.7% Nb SrTiO₃ in pH 13 electrolyte. **b** Mott-Schottky plot of 0.1% Nb SrTiO₃ in 0.1M NaOH electrolyte, in the dark.

The Helmholtz potential drop, U_H , represents the potential difference between the solution redox couple and the valence band edge. The theoretical framework for experimentally measuring the Helmholtz potential drop in the dark has been reported previously [73, 74], and has been applied with success recently for another metal oxide, Fe₃O₄ [78]. The photovoltage was measured for a range of fluences (Figure 4.4a) and shown to saturate above $\approx 2 \mu J/cm^2$ at 0.85V. This is a direct measurement of U_{SC} at open circuit, and gives $U_{OC} = 0.85V$. Using the Schottky approximation for space-charge, Equation 4.7, the depletion region charge q_{SC} can be calculated.

$$q_{SC} = \sqrt{2\epsilon\epsilon_0 e_0 N_D \left(U_{SC} - \frac{k_B T}{e_0} \right)} \quad (4.7)$$

Within the series-capacitor model of the semiconductor and Helmholtz layer interface the charge on each capacitor must equal the other, i.e. $q_{SC} = q_H$. This charge then helps defines U_H using Equation 4.8 in the case where $q_{photo} = 0$.

$$U_H = \frac{q_{sc} + q_{photo}}{C_H} \quad (4.8)$$

A direct measurement of C_H is complicated for a highly doped semiconductor such as 0.1% Nb SrTiO₃ because the measured capacitance has contributions from both the Helmholtz and space-charge capacitance, i.e. $\frac{1}{C} = \frac{1}{C_H} + \frac{1}{C_{SC}}$. To resolve this a Mott-Schottky plot (Figure 4.4b) was prepared, where the measured inverse-squared capacitance is described by Equation 4.9.

$$\frac{1}{C^2} = \frac{1}{C_H^2} \left[1 + \frac{2C_H^2}{\epsilon\epsilon_0 e_0 N_D} \left(U - U_{fb} - \frac{kT}{e_0} \right) \right] \quad (4.9)$$

The Mott-Schottky plot slope confirms the sample doping concentration ($N_D = 2.66 \times 10^{19} \text{ cm}^{-3}$), and the intercept (Equation 4.10), where $\frac{1}{C^2} = 0$, gives the flat-band potential U_{fb} . From Figure 4.4b, $U_{C^{-2}=0} = -1.65 \text{ V}$ and $U_{fb} = -1.52 \text{ V}$.

$$U_{fb} = U_{applied}^{C^{-2}=0} - \frac{k_B T}{e_0} + \frac{\epsilon\epsilon_0 e_0 N_D}{2C_H^2} \quad (4.10)$$

Equations 4.6, 4.8, and 4.7 involve four unknown variables, specifically U_{fb} , U_H , U_{SC} , and C_H . Algebraic manipulation of these Equations allows us to eliminate U_H , giving Equation 4.11.

$$U_{applied} - U_{fb} = U_{SC} + \left(\frac{q_{photo} + \sqrt{2\epsilon\epsilon_0 e_0 N_D \left(U_{SC} - \frac{k_B T}{e_0} \right)}}{C_H} \right) \quad (4.11)$$

For 0.1% Nb doped SrTiO₃ in 0.1M NaOH electrolyte $\epsilon = 300$, $\epsilon_0 = 1$, $e_0 = 2.1 \times 10^{19} \text{ C}$, $T = 298 \text{ K}$, and $k_B = 6.23 \times 10^{-34} \text{ Js}$. The saturated open-circuit potential (U_{OC}) is 0.85V. The Mott-Schottky intercept reveals $U_{applied}^{C^{-2}=0} = -1.52 \text{ V}$ and the slope reports $N_D = 2.66 \times 10^{19} \text{ cm}^{-3}$. Use of the Schottky approximation to calculate the interfacial charge returns $q_{SC} = 14.07 \mu\text{C}/\text{cm}^2$. Applying these together with Equation 4.11 requires noting that in the dark, at equilibrium, the only potential drop across the interface is U_{fb} , i.e. $U_{appl} = 0$. For these conditions, I find $U_H = 0.67 \text{ V}$ and $C_H = 21 \mu\text{F}/\text{cm}^2$. C_H is considered independent of applied bias for potentials below the electrolyte decomposition voltage [20].

4.3.3 Band Edge Movement with Applied Bias and Laser Illumination

The photovoltage measurements reveal that the semiconductor bands are flattened at a fluence well below that used in the experiments ($2 \mu\text{J}/\text{cm}^2$ saturation vs $45 \mu\text{J}/\text{cm}^2$ used experimentally). This implies that under experimental conditions excess photogenerated holes, and therefore charges, are introduced at the interface. When the photogenerated

holes outnumber the dopant-induced electron population a thin layer of p-type semiconductor is produced at the interface, called an inversion layer. This increases the semiconductor capacitance as shown in Figure 4.5a. The presence of the inversion layer is also indicated by the capacitance increase with more positive applied bias, an unexpected result for an n-type semiconductor in reverse-bias conditions but consistent with the presence of a p-type surface layer. Previous works have investigated inversion layers affect on the band edge, whether introduced via surface states [79] or illumination [77].

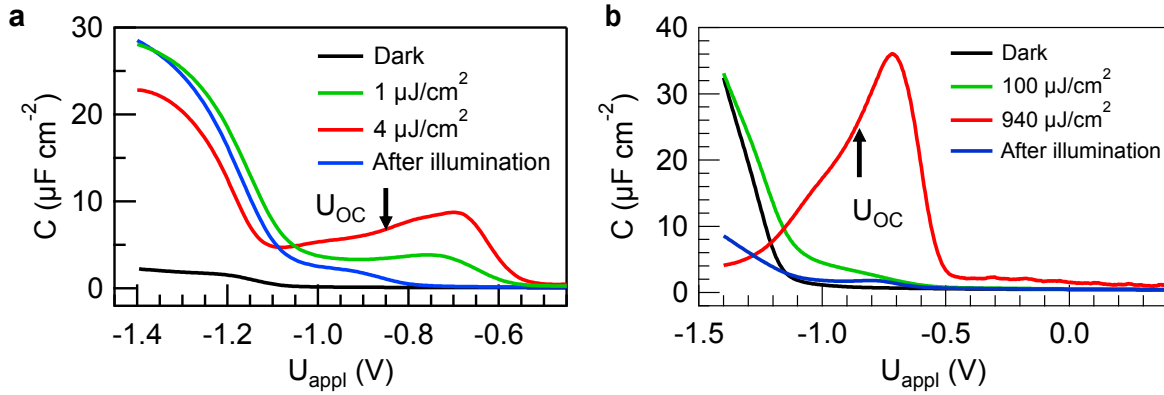


Figure 4.5: Differential capacitance for **a** the 0.1% Nb doped and **b** the 0.7% Nb doped SrTiO_3 samples in the dark and under laser illumination. The samples were prepared in 0.1M Na_2SO_4 aqueous solution, adjusted to pH 8.4 using solid NaOH. The photocurrent onsets at ≈ -0.85 V. The large change in capacitance observed for higher fluences results from the excess photoinduced holes producing a p-type inversion layer (when the concentration of holes is greater than the n-type dopant concentration) at the interface. The 0.7% Nb doped sample requires approximately 10x higher laser fluence to produce the inversion layer, as expected due to the higher doping density.

The increase in C_{SC} increases the relative potential drop over the Helmholtz layer under illumination compared to the potential drop in the dark. Equation 4.8 is used to quantify the potential drop over the Helmholtz layer, including photoinduced charges. This assumes a voltage-independent C_{H} , a generally accepted assumption for biases smaller than the electrolyte decomposition voltage which has been applied successfully previously [72, 80]. The values q_{sc} and q_{photo} are calculated using the Schottky approximation (Equation 4.7) and the measured laser fluence, respectively.

Once the laser fluence and Helmholtz capacitance in the dark are known, the Helmholtz potential drop under experimental conditions (illumination and applied bias) can be calculated using Equations 4.8, 4.6, and 4.7. The calculated values for the band-edge shift (U_{H}) with respect to laser fluence are shown in Figure 4.6a. At low fluences U_{H} has a similar value as in the dark, i.e. 45% of the total interfacial potential drops over the Helmholtz layer. As the fluence increases and the semiconductor bands flatten, U_{SC} ap-

proaches zero and the magnitude of U_H increases. At the fluence used in the experiment ($\approx 45\mu J/cm^2$) roughly 70% of the applied bias drops over the Helmholtz layer. Extended calculations for the range of applied potentials used in the transient experiments are shown in Figure 4.6b in the dark and with $45\mu J/cm^2$ and $65\mu J/cm^2$ laser fluences. While U_H is roughly linear for all conditions, the fraction of the applied bias that affects U_H (i.e. the slope) is strongly affected by illumination. A higher fluence is shown to demonstrate the uncertainty introduced by the uncertainty in the laser fluence.

4.3.4 Helmholtz Potential Drop and Thermodynamic Overpotential

While $U_H(U_{appl})$ reports on the valence band edge shift with applied potential, it can also be used to identify the free energy difference between the reactant state (VBE hole) and the charge-transfer state of the solution redox couple, by using as reference the absolute valence band potential. This is expressed in Equation 4.12. The electrochemical potential difference between the valence band edge and the overall thermodynamic product, Equation 4.13, is known as the thermodynamic overpotential (η) for the reaction.

$$\phi_{BE}(U_{appl}) = \phi_{BE}(U_{appl} = 0) - U_H(U_{appl} = 0) + U_H(U_{appl}) \quad (4.12)$$

$$\eta = \phi_{BE}(U_{appl}) - \phi_{OH^-/O_2} \quad (4.13)$$

$\phi_{BE}(U_{appl})$ was calculated using $\phi_{BE}(U_{appl} = 0) = 1.88V$ for pH 13, at open circuit, in the dark [81], $U_H(U_{appl} = 0) = 0.67V$ and the calculated $U_H(U_{appl})$ from Figure 4.6b. This neglects the small correction to the Helmholtz drop associated the pH surface equilibrium [76]. The overpotential shown in Figure 4.6b was calculated using the Nernstein potential at pH 13, $\phi_{OH^-/O_2} = +0.463V$ vs SHE.

4.3.5 Ultrafast Charge-Transfer Rates at Open Circuit

In this experiment high quantum efficiency for absorbed-photons-to- O_2 -evolution was achieved by matching the depletion width to the excitation absorption depth for the excitation pulse. In a similar vein, high interfacial sensitivity is achieved by probing in reflection, with a 45 degrees angle of incidence (AOI) from the surface normal, and using 800 nm light. The probe depth, a measure of the surface sensitivity, can be calculated by Equation 4.14 and gives 25 nm. Although this is significantly longer than the atomic layer thickness ($a = 3.905\text{\AA}$) constituting the interface, the region probed “behind” the interface is strictly that of the depletion region of the semiconductor where, after charge-separation, only photogenerated holes are present.

$$d = \frac{\lambda}{4\pi n} \quad (4.14)$$

The charge injection time for electrons into the bulk provides an estimate for the lifetime any expected electron signature. The estimate is based on the equations and framework for semiconductor devices [82]. Within the depletion region, the maximum electric field magnitude (by the Schottky approximation) is given by Equation 4.15 where N_d , e_0 , ϵ_0 , and ϵ are the doping density, the electronic charge, the vacuum permittivity and the semiconductor dielectric constant, respectively.

$$E_m = \sqrt{\frac{2e_0N_dU_{SC}}{\epsilon_0\epsilon}} \quad (4.15)$$

Plugging in $U_{SC} = 0.85V$ gives $E_m \approx 450 \text{ kV/cm}$. The maximum carrier drift velocity is given by $v_d = \mu E_m$. The carrier mobility for SrTiO_3 is $\mu = 5.5 \text{ cm}^2/\text{Vs}$ [83], which implies a maximum drift velocity of $v_d = 2.5 \times 10^6 \text{ cm/s}$. The electric field is linear within the depletion region, so the average hole drift velocity is approximately half of its maximum value. For a depletion width of 25 nm, the hole drift time out of the depletion region is $\approx 2 \text{ ps}$, and less for electrons. In light of this, signatures with lifetimes significantly longer than 2 ps are expected to derive from holes at the semiconductor-electrolyte interface.

This is confirmed experimentally through the introduction of a hole-scavenger, the thiocyanate ion. Figure 4.7a shows the pump-probe signal for the 0.1% and 0.7% doped samples at open circuit in 0.1M NaOH electrolyte. Both display a decrease in reflectivity (i.e. an increase in absorption of the 800 nm probe) that decays with a lifetime of 3 ns. For the 0.1% doped sample the feature decays three times faster in electrolyte with the thiocyanate ion. This is consistent with the lower Nernstein potential for hole-transfer to thiocyanate relative to the hydroxide ion [84]. The rate increase in response to the solution oxidation potential change confirms the assignment of these dynamics to interfacial holes. Absorbance of sub-band-gap optical frequencies ($h\nu < E_g$) is consistent with an increase in the free carrier concentration and has previously been assigned as such in SrTiO_3 [85]. The photo-induced absorption is therefore assigned to photogenerated holes, and the decrease in absorbance with time is assigned to holes leaving the sample through the electrolyte interface.

The interfacial sensitivity arises from careful matching of the excitation depth, the probe depth, and the sample depletion region. Comparing 0.1% and 0.7% doped samples at open circuit (Figure 4.7a and b, respectively) only the 0.1% doped sample responds to the solution oxidation potential. The 0.7% doped sample has a much narrower depletion width ($W = 9 \text{ nm}$), as calculated from Equation 4.3. The probe depth therefore extends significantly beyond the depletion region and no longer tracks interfacial charge transfer.

Illumination of the sample with above-band-gap light generates a potential difference across the Helmholtz layer, even without an externally applied bias (i.e. at open circuit). Photovoltage measurements at open circuit indicate that illumination flattens the semiconductor bands, applying the equivalent of -0.85 V and countering the built-in U_{SC} present in the dark. The charge-transfer kinetics measured at open circuit reflect a specific U_H by that photovoltage. There therefore should be a closed-circuit condition where

the applied potential similarly flattens the semiconductor bands (*i.e.* $U_{SC} = 0$) and produces the same U_H at the interface. Using Equation 4.6 and $U_{appl} = -0.85V$ returns $U_{SC} = 0$. Indeed, Figure 4.7c shows that both conditions have the same transient kinetics as expected for conditions with the same surface hole potential.

4.3.6 Ultrafast Charge-Transfer Rates with External Bias

With an understanding of how the valence band edge potential moves with applied bias the groundwork is now laid to investigate how the rate of hole-transfer across the interface depends on the electrochemical potential driving force, U_H . The reaction being probed is assigned to the first step of water oxidation, specifically Equation 4.16:



Figure 4.8 and Figure 4.9 present the photoinduced absorbance decay for potentials spanning -0.90 V to 0.70 V vs. Ag/AgCl over a two nanosecond window. The measured reflectivity change was converted to absorbance units using Beer's law, *i.e.* $\Delta A = -\log(\Delta R)$, the maximum at two picosecond was normalized to unity and time-zero was shifted by one picosecond for display on a logarithmic time scale. The absorbance change is well fit by a single exponential decay function, as expected for first-order kinetics. This suggests first that the reaction is first order in holes and second that the concentration of accessible hydroxides are not significantly altered by the extent of reaction. This "pseudo-first order" condition arises from our low experimental fluence. Extrapolating from the lattice parameter $a = 3.9\text{\AA}$, each laser shot generates holes at only $\approx 5\%$ of surface sites, so even after the full extent of reaction the surface hydroxide concentration is negligibly depleted.

The observed lifetimes range from 3 nanoseconds to 8 picoseconds from $-0.92V \leq U_{appl} \leq 0.7V$. The logarithm of the rate constants is linear with respect to applied potential (Figure 4.11a) as expected for an Arrhenius-like relationship between the transition state free energy, tuned through applied bias, and the overall rate. The efficiency with which the applied bias lowers the activation barrier energy is described by Equation 4.17 through a phenomenological constant, α , referred to as the charge-transfer coefficient.

$$k(U_{appl}) = k(U_{OC}) \exp\left(\frac{\alpha F (U_{applied} - U_{OC})}{RT}\right) \quad (4.17)$$

Here F , R and T represent Faraday's constant, the ideal gas constant, and the temperature in Kelvin, respectively. $k(U_{OC})$ is the rate observed at open circuit. As the first check of our previous findings, compare the kinetics at open circuit and $U_{appl} = -0.85V$, plotted in Figure 4.11c. The observed rates are equivalent, as expected from calculations of the Helmholtz potential based on Mott-Schottky plot analysis and open-circuit voltage measurements. These two approaches (electrochemistry and ultrafast spectroscopy) use different assumptions and experimental data to arrive at the same conclusion, indicating

we are in fact tracking the hole transfer rates following an Arrhenius-like relationship between applied potential and rate.

As developed in Section 4.3.3, the potential applied at the interface is U_H rather than U_{applied} due to the partial potential drop across the space-charge region. The potential difference relevant for the charge-transfer kinetics is therefore not U_{applied} as in Equation 4.17 but rather U_H as in Equation 4.18. This reflects the true applied potential when regarding only the interface, i.e. the potential experienced by charges moving from the valence band edge to species within the Helmholtz layer.

$$k(U_{\text{appl}}) = k(U_{OC}) \exp\left(\frac{\alpha F U_H}{RT}\right) \quad (4.18)$$

The relative energies of the materials electronic states are shown in Figure 4.10a, and an approximation of the reaction barrier is represented in Figure 4.10b. To extract the correct relationship between interfacial potential difference and rate, the $\log(k)$ values of Figure 4.11a are replotted in Figure 4.11b with respect to the calculated Helmholtz potential drop from Figure 4.6b. The primary error introduced by this rescaling arises from uncertainty in the applied fluence, $0.55 \pm 0.10 \text{ mJ/cm}^2$. The resulting relationship between $\log(k)$ and U_H is clearly linear, confirming Arrhenius kinetics. The charge-transfer coefficient, derived from the slope, is $\alpha = 0.24$ and $\alpha = 0.19$ for a fluence of 0.45 mJ/cm^2 and 0.65 mJ/cm^2 , respectively. Given the uncertainty in the fluence, the charge transfer coefficient is reported as $\alpha = 0.20 \pm 0.05$. The physical origin and implication of the transfer coefficient α is explored in Section 2.1.4 and below.

4.4 Discussion

The electrical energy applied to the catalyst is modified in two ways before being applied to improving the rate of this first step. Irrespective of illumination, any applied potential is distributed across both the Helmholtz layer and the depletion region. Only the potential drop across the Helmholtz layer as shown in Figure 4.10a contributes to lowering the activation barrier of the reaction. Even under illumination, where the semiconductor bands are flattened and the majority of the applied potential drops over the Helmholtz layer, only a fraction of U_H , specifically αU_H , has the effect of lowering the activation energy. An $\alpha = 0.20$ implies that 20% of the interfacial potential contributes to an increase in the reaction rate. This manifests in the reaction diagram in Figure 4.10b as asymmetry in the curvature of the initial and final states with respect to the charge transfer extent. The activation barrier change with applied potential, $\alpha e_0 \Delta U_H(U_{\text{appl}})$, is only equivalent to ΔU_H in the case where there is no curvature in the two states, an unrealistic condition for two states spatially separated across a dielectric such as the electrolyte of the Helmholtz layer. In a simplified model presented to illustrate a physical

origin for α [20], assume U_H drops across the full width of the Helmholtz layer. The charge-donating species however can lie within the Helmholtz layer, where only part of U_H has been screened. In this case the effective change in the electrochemical potential for charge transfer is only a fraction of U_H . The transfer coefficient is commonly assumed to be 0.5, in part due to the difficulty in quantifying it for multi-step reactions. This assumption is not necessarily true, and has important implications for efforts directed at increasing the effectiveness of electrochemical and photo-electrochemical reactions. Deviation from $\alpha = 0.5$ is predicted by Marcus theory, dependent on the relative magnitude of the applied overpotential and the solvent reorganizational energy per molecule of reactant at the solid/electrolyte interface [20]. The value of α found here implies a significant barrier to hole localization from the delocalized, O_{2p} band of the semiconductor to a localized hydroxide ion in solution. These data were collected in a regime of high overpotential, $1.3V < \eta < 2.1V$, where the early hole-transfer step probed is not rate limiting. This is understood from Figure 4.1b where changing the initial surface-hole potential does not change the steady-state photocurrent.

Transfer-coefficient was derived by reference to changes in U_H calculated from U_{appl} , in a regime where the reaction taking place does not change (indicated by a lack of features in the cyclic voltammetry curve of Figure 1b). As a result, the value derived is independent of the reaction taking place and independent of the absolute value of U_H . Nevertheless, the assignment of Reaction 4.16 is justified on the ultrafast timescales involved and the strongly basic conditions. U_H represents the potential screened by ions and solvent within the Helmholtz layer, and therefore is interpreted as the free-energy difference for the OH^-/OH^\bullet charge transfer reaction. The OH^- considered here is assumed to be localized beyond the inner Helmholtz plane, i.e. not adsorbed to the surface [72]. Starting from the absolute potential for the valence band edge [81] and adding the value for U_H calculated from these experiments, the absolute Nernstein potential for the OH^-/OH^\bullet reaction is found to be +1.21V vs SHE at pH = 13. This is in qualitative agreement with values derived from gas-phase photoemission measurements [86] of the same reaction at pH = 13 that report +1.41V, and consistent with the range of values reported by Hoare [87]. The assignment of this reaction to Reaction 4.16 is supported by the similar values found in the literature. Theoretical calculations have previously found the free energy difference driving a similar reaction on the $TiO_2(110)$ surface to be 0.57 V [88] similar to the value of $U_H = 0.67V$ found here. It is important to note that the TiO_2 surface calculations assumed a surface-bound hydroxide species. Our experiments do not offer conclusive evidence on this point, and the actual location of the reactive hydroxide must remain an open question.

A second value can be extrapolated from Figure 4.11b, specifically $k(U_{OC})$. $k(U_{OC})$ represents the forward reaction rate at the Nernstein potential when the net reaction rate is zero. In this case we considering this equivalent to when U_H , the thermodynamic driving force for the charge-transfer reaction, is zero. Normalized to the reactive area, this rate is equivalent to the exchange current density, a value recognized by electrochemists as important for characterizing the inherent reaction dynamics. The intercept gives a value

of $k(U_{OC}) = (6.76 \pm 1.5) \times 10^{-7} \text{ ps}^{-1}$, although reporting this value requires extrapolating Equation 4.18 to a regime of zero overpotential, where experiments cannot measure the kinetics directly. The value can be related to the activation barrier magnitude, and is required for calculating the current for a single step in the overall water oxidation reaction. At the time of publication, there were no other direct measurements of this value in the literature.

There are several other features present in the kinetic traces represented in Figures 4.8 and 4.9. The very fast decay ($\tau < 2 \text{ ps}$) observed at potentials $U_{appl} > 0.2 \text{ V}$ are tentatively assigned to hot-hole transfer. Beyond $\approx 200 \text{ ps}$ a long-lived negative absorption feature appears that extends past the limit of delay-stage range, i.e. $> 2 \text{ ns}$. This is consistent with the generation of a new species at the interface, and is attributed to another component of the multi-step reaction mechanism of water oxidation. Given the single-exponential decay of the early signal and the long-lived nature of the second, the ultrafast consumption of surface holes can lead to a surface population of long-lived single-oxidation products such as a surface oxo ($\text{Ti} = \text{O}$). Such a species was previously observed in steady-state infrared and Raman experiments [39, 47, 89] on metal-oxides, and transient optical studies have found new intermediates evolving on millisecond timescales [34, 35]. This work provided the motivation for extensive efforts to identify and characterize the subsequent nascent intermediate of the charge-transfer reaction at the SrTiO_3 -electrolyte interface. Those results have been published [17] and are reported in depth in Chapter 5.

4.5 Conclusions

The first step of water oxidation at the SrTiO_3 -electrolyte interface has been investigated and the rate for the first step has been quantified under a range of conditions. The results linking the applied potential to the interfacial potential drop across the interface were confirmed independently using two experimental techniques, linking steady-state and ultrafast measurements. For the first time, the activation barrier magnitude to a single step has been reported (through $k(U_{OC})$), and the curvature of that barrier has been quantified (through the transfer coefficient α). The Nernstein potential for this partial step was derived from experimental data and found consistent with the reaction $\text{h}^+ + \text{OH}^- \rightarrow \text{OH}^\bullet$ measured in the literature. Quantification of these values are important for electronic structure calculations that investigate the activation barrier and Nernstein potential for individual hole-transfer steps of the water oxidation reaction [90, 91, 92, 93, 94]. This method for identifying early steps of photoelectrochemical reactions is generalizable, and motivates further studies elaborated in the following chapters.

4.6 Sample Characterization

Single-crystal samples of strontium titanate, cut along the (100) plane were purchased from MTI Corp. of Richmond, CA. The samples were 0.5 mm thick with a polished front

side ($R_a \approx 5 \text{ \AA}$) and rough back side. The samples were provided with niobium doping concentrations of 0.7 and 0.08 weight-percent. The 0.08% doped sample is generally referred to as 0.1% for brevity.

Unless otherwise specified, spectroscopic and characterization experiments were performed in standard electrolyte of 0.1M $\text{NaOH}_{(\text{aq})}$ made from deionized water (resistivity $< 18\Omega$) and semiconductor grade sodium hydroxide pellets purchased from Sigma Aldrich (purity $> 99.99\%$, CAS 1310-73-2). Electrolyte was degassed under rough vacuum ($P = 10^{-3}$ torr) immediately prior to use in the electrochemical cell. This avoided bubble formation induced by the pump beam. The laser power used was insufficient to generate visible bubbles of oxygen gas. The bubbles are attributed dissolved air released by local heating of the SrTiO_3 lattice and adjacent electrolyte by above-band gap irradiation.

When illuminated by the pulsed laser excitation under closed circuit conditions a photocurrent is generated and the sample damages. The sample damage is shown in Figure 4.12 using a scanning electron microscope at three different magnifications. The images show randomly spaced pits in the sample surface with diameters $\phi \approx 5 - 10 \mu\text{m}$ covering $\approx 15\%$ of the surface. The pits indicate the material has been ablated. Such ablation is attributed to Coulomb explosion [95, 96] where sufficient photoexcited charge carriers are generated in the material to cause bond cleavage. A typical pump pulse produces $\approx 10^{19} \text{ holes}/\text{cm}^3$ within the depletion layer. If the same area is repeatedly excited by subsequent pulses and the holes have not been fully depleted by recombination or water oxidation the build up of holes would be sufficient to drive Coulomb explosion. To minimize the sample damage the sample was rastered during transient absorption experiments. The same data was collected at each location at open circuit and closed circuit conditions and the open circuit results were used to confirm that the sample damage did not affect the results. The source of the damage is further suggested to be physical (coulomb explosion) rather than due to photodecomposition of the sample by voltammograms taken before and after the experiment. The unchanged voltammogram confirms the catalyst is chemically stable under illumination. Previous experiments on n- SrTiO_3 with high current densities performed over many hours showed no photo-corrosion in basic conditions [97, 98].

The photochemistry was measured using a cyclic voltammogram under both ultrashort UV pulsed irradiation and steady-state, low intensity, broadband UV irradiation from a Xe lamp. The diode like behavior under pulsed laser irradiation is also seen under steady-state illumination, indicating the ultrashort laser pulses do not drive separate chemistry from the steady-state illuminated sample. The broader onset potential arises from the broadband illumination of the Xe arc due to the fact that each wavelength has a unique quantum efficiency, as found in Figure 4.1.

4.7 Acknowledgements

The project was conceived by Dr. Tanja Cuk. The experimental work presented in this chapter were led by Dr. Matthias M. Waagele with the participation of Xihan Chen and David M. Herlihy. Sample characterization was performed by Xihan Chen and David M. Herlihy. Analysis and interpretation was led by Tanja Cuk and Matthias M. Waagele with the participation of all authors.

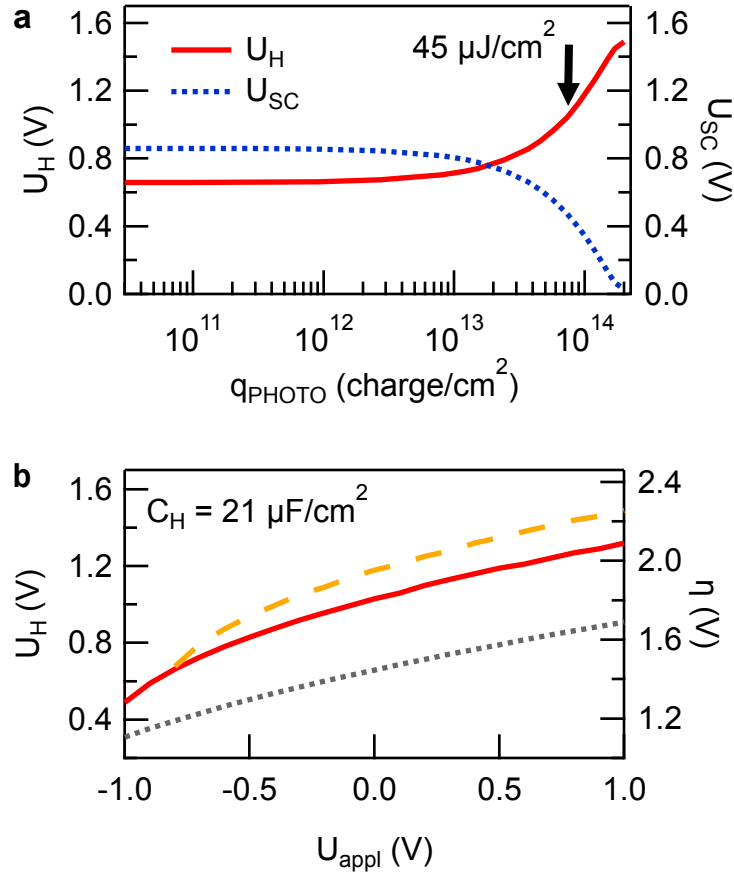


Figure 4.6: The potential drop over the Helmholtz layer (U_H) is affected by the laser fluence and the externally applied bias. **a** The calculated U_H at open circuit for a range of laser fluences. **b** The calculated U_H for the range of applied biases used. The experimental fluence, $45 \mu J/cm^2$, is shown in solid red, and a higher fluence, $65 \mu J/cm^2$, is shown in dashed yellow. The higher fluence demonstrates the uncertainty in U_H propagated from uncertainty in the fluence measurements. U_H in the dark is shown for reference in dotted grey.

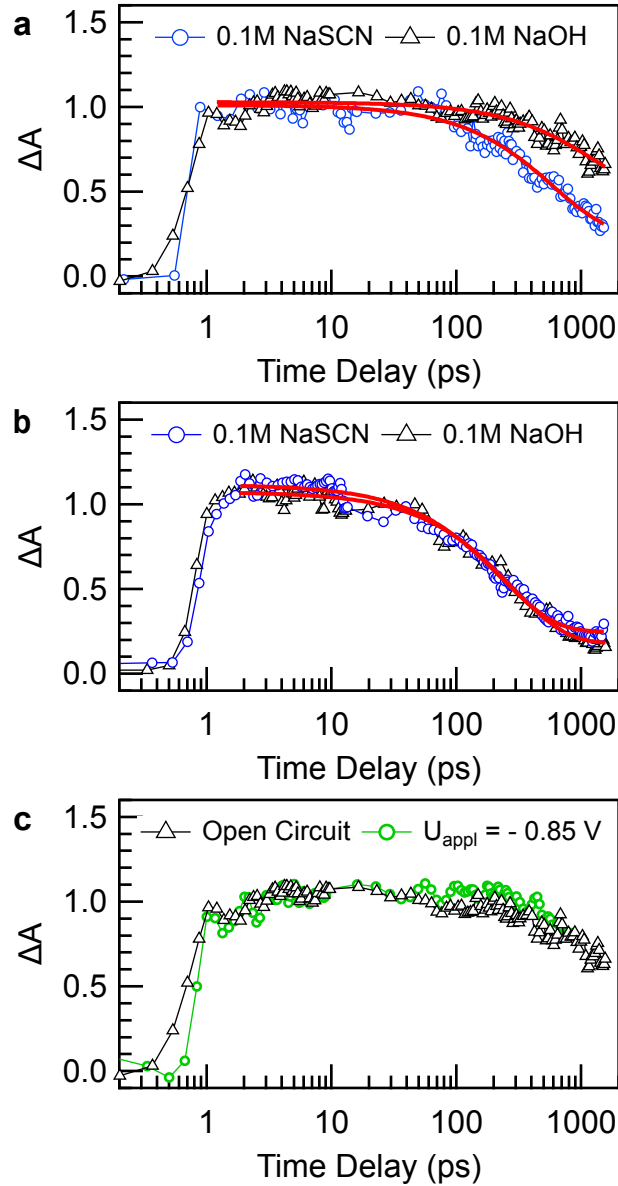


Figure 4.7: Normalized change in reflectance (plotted in absorbance units) at open circuit for **a** 0.1% Nb and **b** 0.7% Nb doped SrTiO_3 samples immersed in different electrolytes. Kinetics are well fit with single-exponential decays (red). For 0.1% doped samples the observed lifetime changes between 0.1M NaOH (black, $\tau = 3$ ns) and 0.2M NaSCN (blue, $\tau = 1$ ns) aqueous electrolyte. The faster signal decay in the presence of the thiocyanate ion, a hole scavenger, reveals the tracked species to derive from holes. The same change is not detected for the 0.7% doped sample ($\tau = 3$ ns), due to the smaller depletion width no longer matching the probe absorption depth. **c** The kinetics measured in 0.1M NaOH at open circuit (black) match those observed at $U_{\text{appl}} = -0.85$ V (green) because of the equivalent surface-hole potential. The time axis for all traces has been shifted by one picosecond for display on a logarithmic scale.

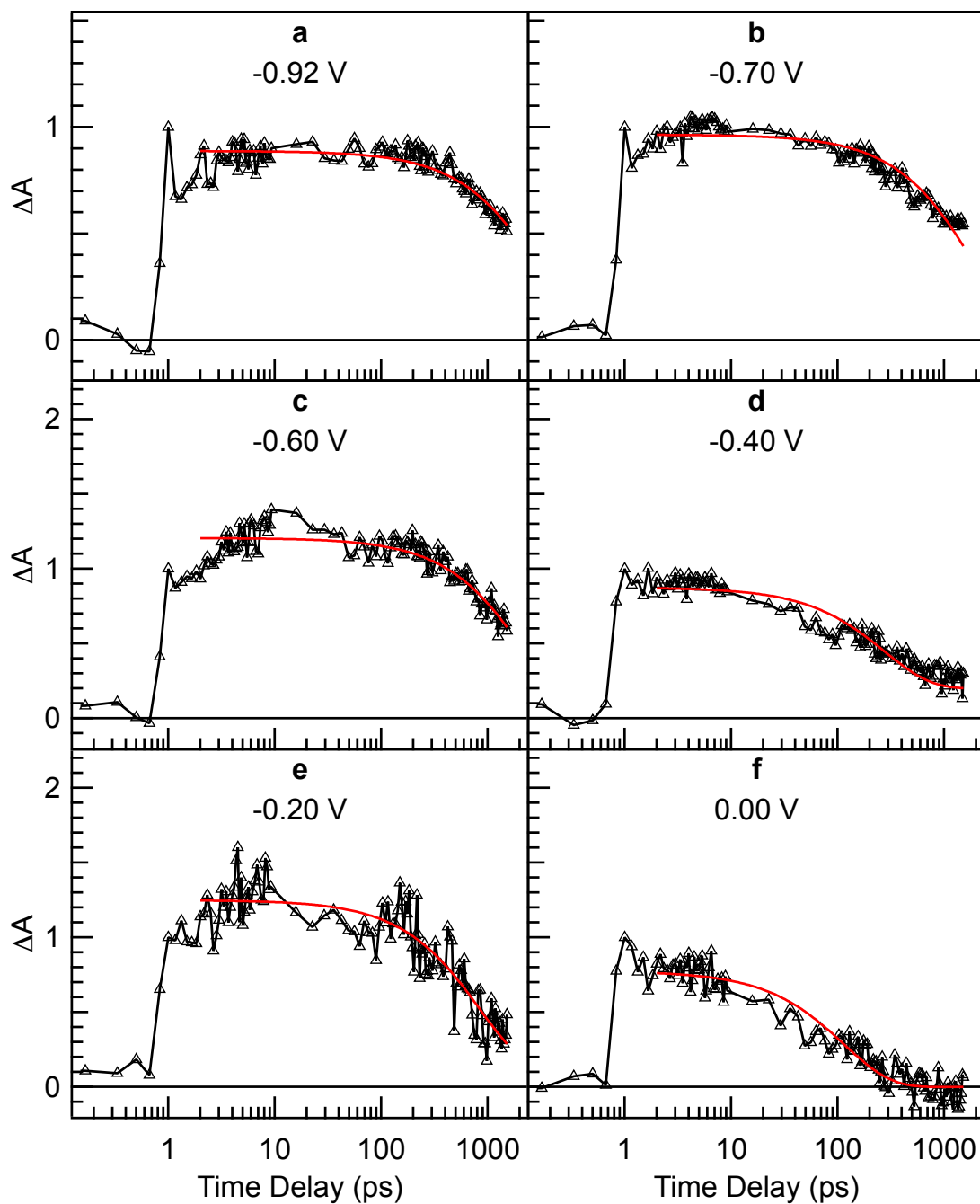


Figure 4.8: Normalized change in reflectivity (in absorbance units) of the sample after photoexcitation. This figure shows traces taken at applied potentials of **a** -0.92 V, **b** -0.70 V, **c** -0.60 V, **d** -0.40 V, **e** -0.20 V and **f** 0.0 V, all with respect to Ag/AgCl reference electrodes.

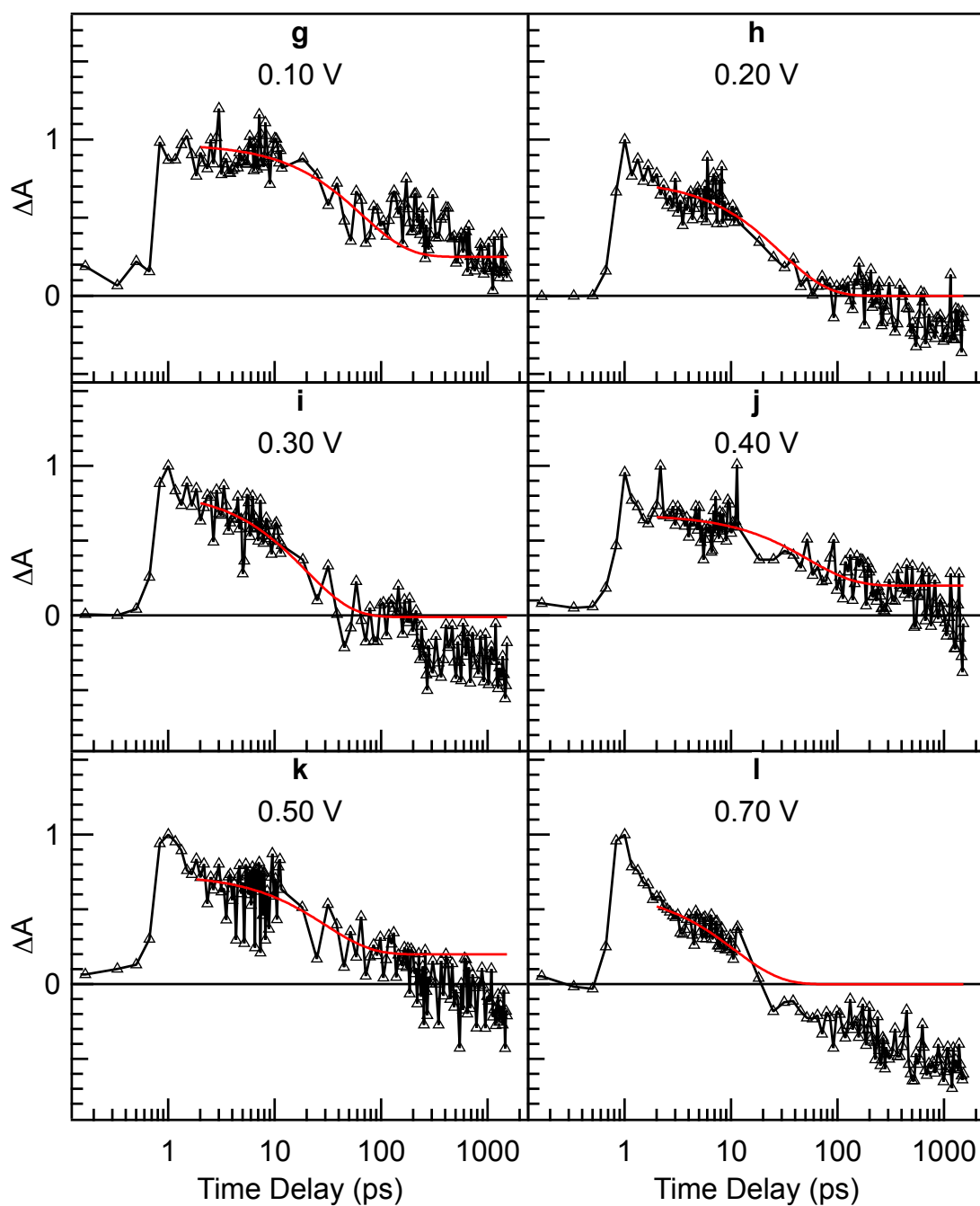


Figure 4.9: Normalized change in reflectivity (in absorbance units) of the sample after photoexcitation. This figure shows traces taken at applied potentials of **g** 0.10 V, **h** 0.20 V, **i** 0.30 V, **j** 0.40 V, **k** 0.50 V and **l** 0.70 V, all with respect to Ag/AgCl reference electrodes.

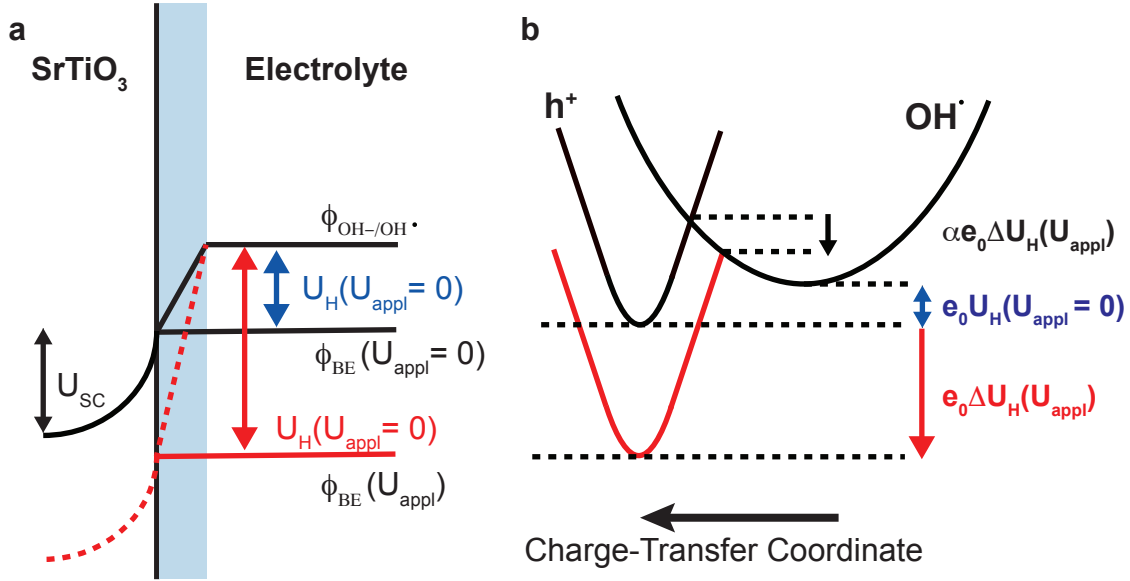


Figure 4.10: The rate of hole transfer from the valence band edge (VBE) is affected by the potential difference (U_{H}) from VBE of the solution redox species. **a.** A band diagram highlights that $\Delta U_{\text{H}} < U_{\text{appl}}$, since U_{appl} is distributed across both the depletion width in the semiconductor and over the Helmholtz layer (blue background). **b.** A free energy diagram of the two charge-transfer states with respect to the electron position in the Helmholtz layer. The Helmholtz drop with applied potential (red) does not apply fully to lowering the charge-transfer activation barrier (black). The curvature (slope) of the free energy of each state with respect to the charge-transfer coordinate means only part of U_{H} modifies ΔG^\ddagger . The fraction of U_{H} that affects the activation barrier is given by the charge transfer coefficient (α).

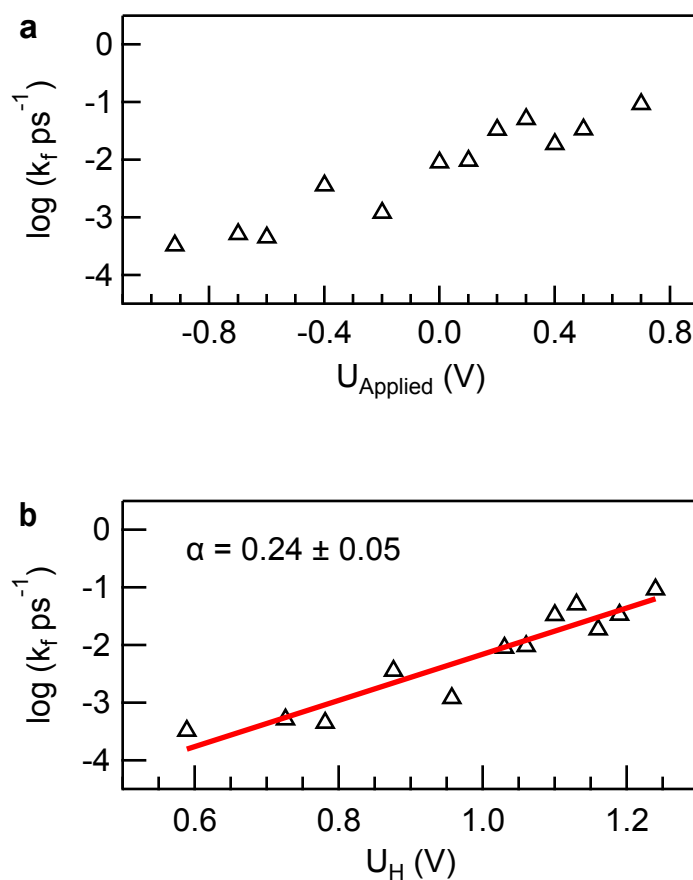


Figure 4.11: The fraction of the Helmholtz potential change (ΔU_H) that contributes to lowering the reaction activation barrier is referred to as the charge-transfer coefficient (α). **a** The rate with reference to the applied potential was measured experimentally. **b** The rate with reference to the Helmholtz potential (U_H). The rate change per change in U_H (i.e. the slope) equals $0.434 \frac{\alpha F}{RT}$. An α of unity implies lowering U_H perfectly translates to a lowering of the activation barrier, while $\alpha = 0.5$ implies the reaction activation barrier changed by half of the Helmholtz potential change.

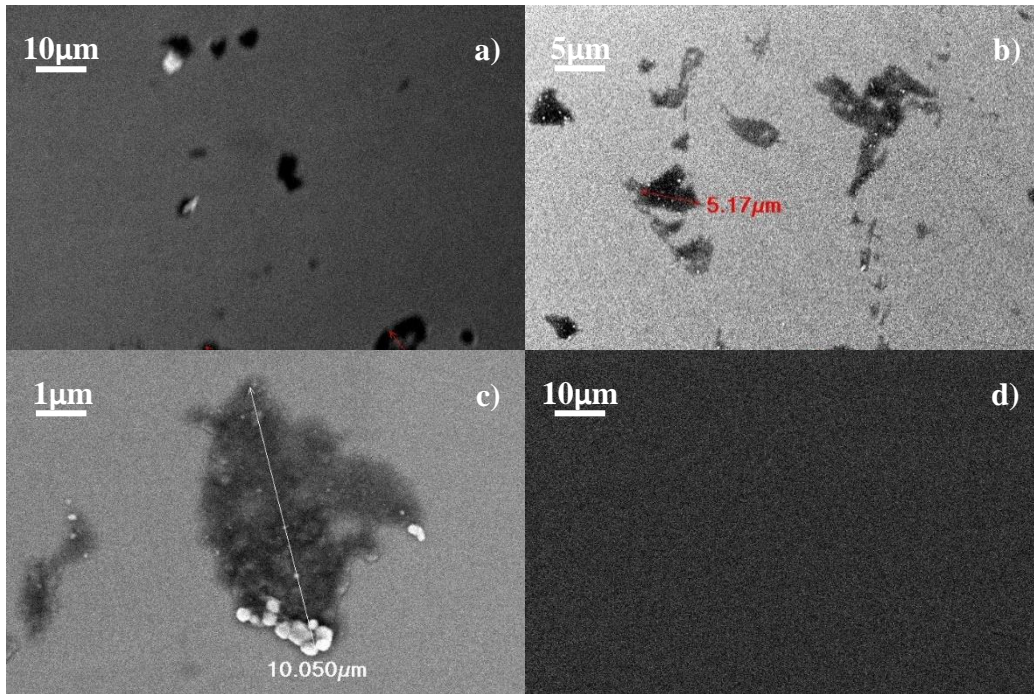


Figure 4.12: SEM images of 0.1% Nb doped SrTiO₃ sample before and after laser irradiation. **a** The photo-damaged surface at 1500x magnification. **b** A different location on the photo-damaged surface at 2500x magnification. **c** Two pits from image **b**, at 3500x magnification. **d** The undamaged surface at 1500x magnification.

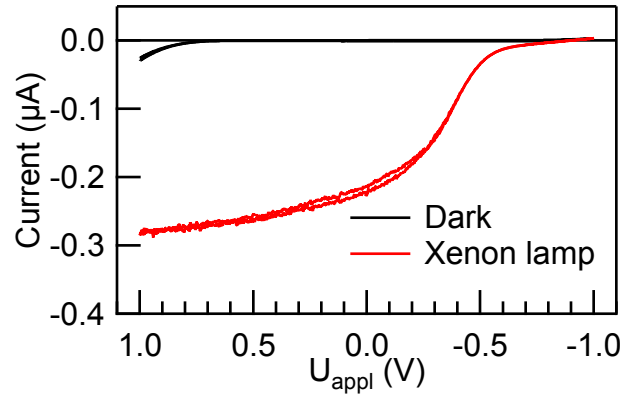


Figure 4.13: Cyclic voltammogram of the 0.1% Nb doped SrTiO_3 sample in 0.1M NaOH electrolyte. The photocurrent was measured under Xe lamp illumination (red, solid) and in the dark (black, dashed). The diode-like behavior is conserved between pulsed-laser and steady-state conditions. The onset potential under Xe illumination is not as sharp because the Xe source is a broadband source, and each wavelength produces a photocurrent at different efficiencies across a range potentials. The photocurrent magnitude is much larger for Xe illumination because the full sample area was illuminated ($A = 25 \text{ mm}^2$) while the laser spot size was much smaller ($A \approx 0.196 \text{ mm}^2$).

Chapter 5

Detecting the Oxyl Radical of Photocatalytic Water Oxidation at an n-SrTiO₃/Aqueous Interface by its Sub-Surface Vibration

5.1 Original Publication

This work was previously published as David M. Herlihy, Matthias M. Waagele, Xihan Chen, C. D. Pemmaraju, David Prendergast, and Tanja Cuk, *Nature Chemistry*, **2016**, 8, 549-555 [17].

5.2 Introduction

This chapter presents ultrafast infrared experiments that were motivated by the transient absorption studies described in Chapter 4. Those experiments identified ultrafast time-scales for transformation of photogenerated charge-carriers into new molecular species at the catalyst-liquid interface. I performed ultrafast infrared studies to identify the primary molecular signature of the surface-localized charge.

Water can be used as a feedstock for the conversion of solar energy into fuels, supplying the electrons needed to reorganize bonds and create energy-dense compounds through the water oxidation reaction [99, 100]. Central to the water oxidation reaction is the formation of the O-O bond that then leads to the evolution of O₂. Proposed reaction mechanisms of O-O bond formation within both biological and artificial photosynthetic systems over the decades have been used to differentiate O₂ evolution activity of especially transition metal oxide catalysts [101]. Directly resolving the sequence of catalytic intermediates that leads to the O-O bond and how they couple dynamically to their environment is a long standing goal that, if achieved, would guide catalyst design and provide a new paradigm for affecting catalytic cycles through their local surface environment [47, 102].

A charged transition-metal-oxygen species that accepts electrons should precede O-O bond formation. In the Mn₄O₄ complex of photosystem II [103, 104, 105, 106], the widely sought radical (either Mn(IV,V) – O or Mn – O•) has not yet been identified despite many transient IR [107], EPR [108], and recently ultrafast X-ray measurements [109]. At the heterogeneous transition metal oxide/aqueous interface, electrochemical and spectroelectrochemical studies [110, 42] find indirect evidence of such radicals. For titanate catalysts, the catalytic intermediate is thought to be the oxyl radical (e.g. Ti – O•), with some support for its identification from transient photocurrent/luminescence measurements and EPR under illumination [68, 66, 111, 112]. In oxides of later transition metals, electrochemical current-voltage studies that also employ X-ray absorption and EPR [46, 113], suggest an oxidized metal center such as Co(IV)=O/Mn(IV)=O or an oxyl Ni – O• radical [44, 63, 64, 114]. Illuminated infrared (FTIR) spectra observe the O–O bond within the photochemical cycle in TiO₂ [66] and IrO₂ [39], but not the transition metal oxide radical. A millisecond FTIR study of Co₃O₄ [47] upon light-excitation was the first to identify a photo-induced Co=O bond.

These steady-state and millisecond-resolved experiments are especially successful in detecting intermediates from later in the water oxidation cycle, when new bonds have already formed, but inherently have difficulty in differentiating the nascent, transition-

metal-oxide radical at the surface from localized charge in the bulk material (e.g., polarons [115, 116]) or other surface bonds/intermediates [47, 66, 39]. On the other hand, a structural and ultrafast probe has the potential to isolate charge transformation into a surface-bound catalytic intermediate, which is expected to occur very early in the reaction. Indeed, transient optical experiments at the n-type semiconductor/aqueous interface suggest holes are trapped at surface sites within picoseconds [16, 69].

Here, I employ in-situ ultrafast infrared spectroscopy of a single crystal n-SrTiO₃/aqueous interface under attenuated total reflection (ATR) to detect the oxyl radical, Ti – O•. Importantly and as shown previously [16], the n-SrTiO₃ single-crystal electrode can operate at high (90%) photon-to-O₂ efficiency even under ultrafast, pulsed laser irradiation (266 nm, 500 Hz, 150 fs). Ultrafast infrared spectroscopy can identify photo-induced molecular changes at the solid-gas interface [117], within the liquid [118] and, recently, in the condensed phase, OH stretches [102, 119, 120], but has not yet been applied to the identification of a catalytic intermediate formed under reaction conditions. The experiments described here, in combination with theoretical modeling and interpretation, provide the first molecular-scale detection of the transformation of charge into a nascent, catalytic intermediate at the solid-liquid interface. In doing so, they not only provide evidence for the oxyl radical, but reveal a new way to track a catalytic cycle in this setting.

Our hypothesis is that the oxyl radical causes the oxygen motion directly underneath it to de-couple from the rest of the oxygen sub-lattice, creating a localized sub-surface Ti-O stretch vibration unique to the radical site. Such a sub-surface vibration could be a distinctive infrared vibration of many catalytic intermediates, before a more stable bond has formed (such as the O-O bond or the surface-bound oxo, M=O). Importantly, once de-coupled from the phonon band structure of the SrTiO₃ substrate, the sub-surface Ti-O vibration couples to solvent dynamics (water librations) as shown by Fano line shapes. The vibration is truly interfacial since it remains coupled to the electron dynamics in the solid (plasmonic excitations).

Altogether, three handles for tracking intermediates within the catalytic cycle at a solid-liquid interface are proposed by these experiments: the sub-surface vibration itself, its coupling to solvent, and its coupling to electron dynamics. Importantly, the experiments show that a catalytic intermediate’s vibration is coupled to reactant (water) dynamics. This allows us to probe one aspect of the activation barrier for bond formation, specifically the contribution of reactant librations. Altogether, the identification of the oxyl radical through a sub-surface vibration at ultrafast time-scales and its interfacial coupling open the door to understanding a catalytic cycle dynamically and from the point of charge transfer at the solid-liquid interface.

5.3 Results

The perovskite SrTiO₃ (100) is shown with a water-adsorbed surface of the Ti-O layer in Figure 5.1a. Both the Ti-O and the Sr-O layer can be exposed, with a suggested

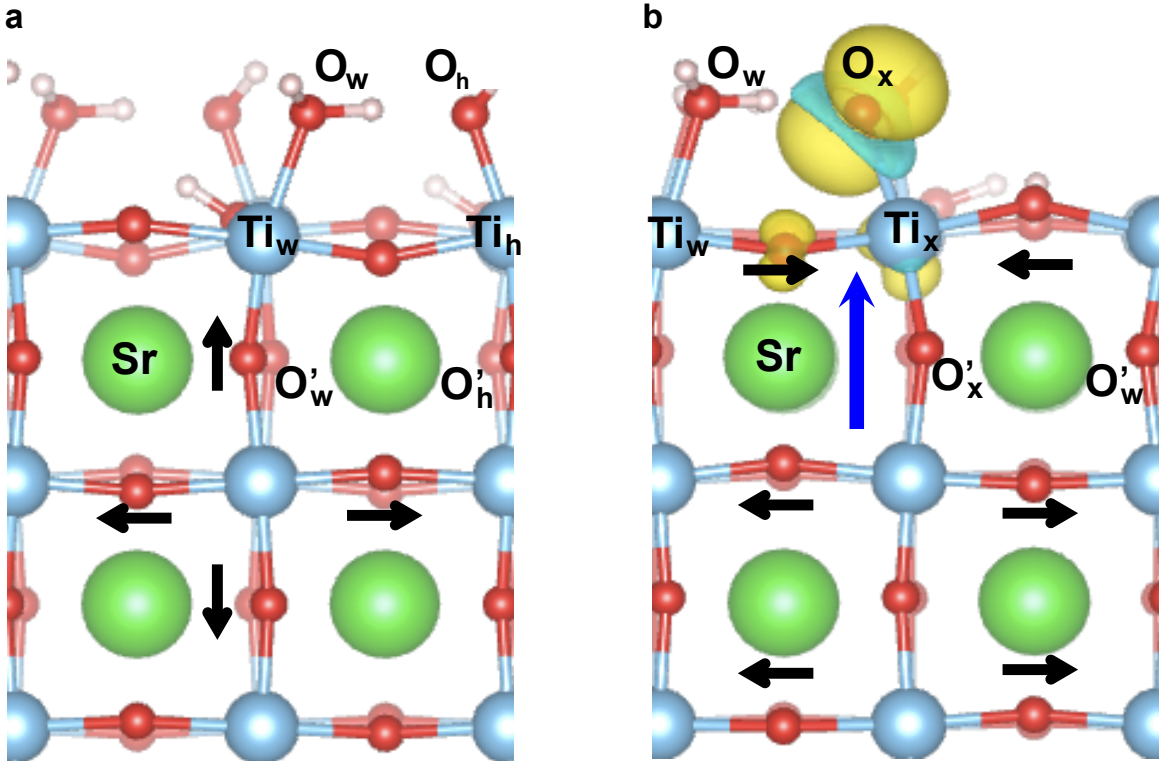


Figure 5.1: A representation of the water-adsorbed SrTiO_3 surface before and after illumination. **a**, The water-adsorbed SrTiO_3 surface. The mode shown is a bulk breathing motion present in the dark and IR-inactive. **b**, The water adsorbed SrTiO_3 after illumination. Changes in electron spin density (decrease – yellow, increase – cyan) indicative of hole capture to O_x results in a surface $\text{Ti}_x - \text{O}_x^\bullet$ termination. The presence of $\text{Ti}_x - \text{O}_x^\bullet$ generates a new, surface, IR active mode because of a large amplitude motion of O'_x that disrupts the original breathing mode.

ratio of 7(TiO):3(SrO) by surface sensitive x-ray diffraction [121]. The Ti-O surface is shown with all transition metal sites terminated by either water or hydroxyl groups, as expected for an ambient air or aqueous electrolyte interface [122]. Photo-excitation at the n-SrTiO₃ interface generates a hole that is trapped at a surface terminating oxygen site. The experiments and theoretical calculations described here provide evidence that the hole is trapped in an oxyl radical, Ti – O•, as shown in Figure 5.1b. First-principles density functional theory calculations indicate that producing the radical causes a bulk breathing mode (Figure 5.1a) to combine with other dark and infrared-active modes of the initial configuration. This new surface mode (Figure 5.1b) is infrared-active due to a large amplitude, Ti-O stretch motion of the O (labeled O_x') in the SrO layer right below the Ti – O• site; the assigned IR activity matches the bright surface mode observed by the ultrafast experiments. This bright surface mode, and the Fano line shapes that are sensitive to the electron plasma density and the electrolyte, is expected to report on the Ti-O oxyl species until a new bond is formed (e.g. the O-O peroxo species). It is shown that the bright mode occurs in a wide range of surface conditions, in air and electrolyte, through pH 2 – 14, with deuteration and for surface excitations between 0.5 - 30% of surface titanium atoms.

5.3.1 An Interfacial Ti-O Dipole that Reports on the Oxyl Radical

A New Infrared Mode

The spectrum of the photo-generated bright mode, probed by attenuated total reflectance, peaks at 795 cm⁻¹ (± 3 cm⁻¹), as shown in Figure 5.2a for the 0.1% Nb-doped n-SrTiO₃ sample. At these time scales, it is the only prominent transient signal seen in a wide spectral range (Figure 5.3, 700 – 1200 cm⁻¹). The narrow bandwidth of the photo-generated signal (35 cm⁻¹, 4 meV) and its appearance in the frequency range known for Ti-O stretches are strong evidence for a vibrational rather than an electronic transition. Moreover, the same narrow mode occurs over a wide range of doping (Nb 0.1% to 0.7%) and surface excitation (0.5% to 30%) that would necessarily modify the width of an electronic transition. The Fano lineshape fitting shows a consistent 30 – 45 cm⁻¹ spectral width across a range of doping (Figure 5.6) and surface excitation (Figure 5.5).

The photo-generated mode (Figure 5.2a) solely occurs in P-polarization of the infrared probe beam. Its exclusive appearance in P-polarization completes its identification as a molecular, surface localized vibration with a dipole perpendicular to the sample plane. While a bulk LO phonon also occurs near 800 cm⁻¹ in reflectivity measurements [123], it shows up in both P and S polarization in single crystal samples (Figure 5.4) and moreover, the interfacial reflectance measured by ATR is not sensitive to the bulk LO phonon at all (Figure 5.4). Other than a surface polariton (Figure 5.4) seen previously [124], which occurs as a broad mode centered at 700 cm⁻¹ and only at the air interface, no mode is observed by the evanescent infrared probe in the ATR cell in this frequency range without

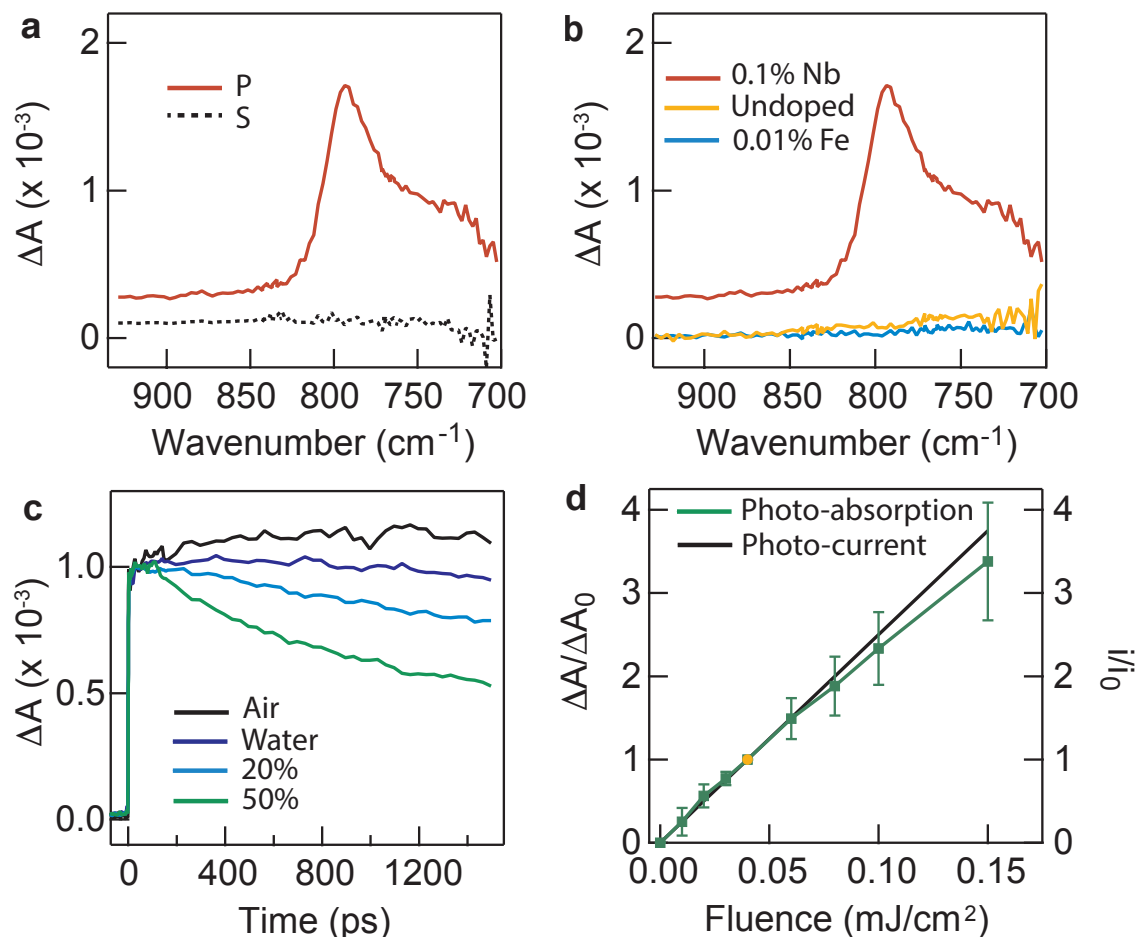


Figure 5.2: The photo-induced absorption of the oxyl radical is defined experimentally by its polarization, **a**, doping dependence, **b**, changes in its lifetime in different electrolytes, **c**, and its correlation with highly efficient O_2 evolution, **d**. The photo-induced absorption is shown, **a**, 700 ps after excitation. It is only observed using P (red) but not S (black, dashed) polarized light. **b**, The absorption only appears in 0.1% Nb doped (red) but not 0.01% Fe doped (blue), or undoped (yellow) SrTiO_3 . **c**, Kinetics of the transient response at 795 cm^{-1} for the 0.1% Nb n-doped sample in contact with air (black), water (blue), and 20% (cyan), 50% (green) methanol in water. **d**, The absorbance change (green, squares) at 795 cm^{-1} and the resulting steady-state photocurrent (black, line), measured in a three-electrode cell held at 0.0V vs Ag/AgCl at pH 14. Error bars in ΔA represent the standard error over three trials. The absorbance change and the current have been normalized to their respective value (solid yellow dot) at a fluence of 0.04 mJ/cm^2 (5% surface excitation).

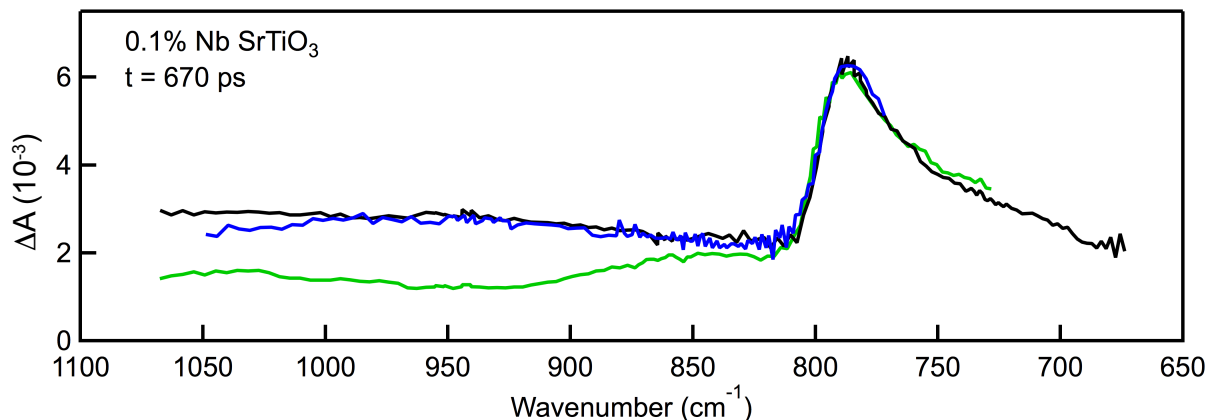


Figure 5.3: Transient Infrared Spectra from 675 – 1070 cm^{-1} . Traces were taken in air (green), open circuit in 1.0M NaOH electrolyte (black) and at closed circuit, 0V vs. Ag/AgCl (blue) with Pt counter electrode. This figure confirms that there are no additional features in the broader spectral range of 675 – 1070 cm^{-1} . The difference in the broad background absorption between air and electrolyte above 850 cm^{-1} was not reproducible.

photo-excitation. Therefore, the photo-generated mode is characteristic of a new transient species rather than a change in the dipole or occupation of a ground state mode. It is important to note that the sign of the transient species, when measured by ATR of the solid-liquid interface, cannot be interpreted via Beer's law and a new absorptive cross-section can appear as either a positive or negative differential signal; this is discussed in Section 5.3.2 and Figures 3.5, 5.8, and 5.9.

The photo-generated mode is attributed to a transient $\text{Ti} - \text{O}^\bullet$ species by: (1) its appearance only with photo-induced charge separation at the n-SrTiO₃ interface, (2) a long lifetime that decreases as a function of methanol concentration, and (3) its correlation with O₂ evolution. The photo-generated mode occurs exclusively in n-doped samples (Figure 5.2b), while it is completely absent in un-doped and p-doped samples that have low quantum efficiency for charge separation and O₂ evolution (< 1%). The lifetime of the signal at 795 cm^{-1} (Figure 5.2c) demonstrates a very long-lived vibration (> 1 ns). This long and fluence-independent lifetime (Figure 5.5b and 5.5e) excludes an assignment to a highly excited Ti-O surface mode of the ground state. Finally, the lifetime decreases substantially as a function of methanol concentration in water (Figure 5.2c), indicating that the photo-hole generated transient species occurs uniquely at the water-adsorbed surface and is quenched by a better hole acceptor.

Ground State Spectra of SrTiO₃

The differential absorption found at 795 cm^{-1} derives from a new mode at the photo-excited surface. Additionally, the fitting parameters chosen for this data set require that

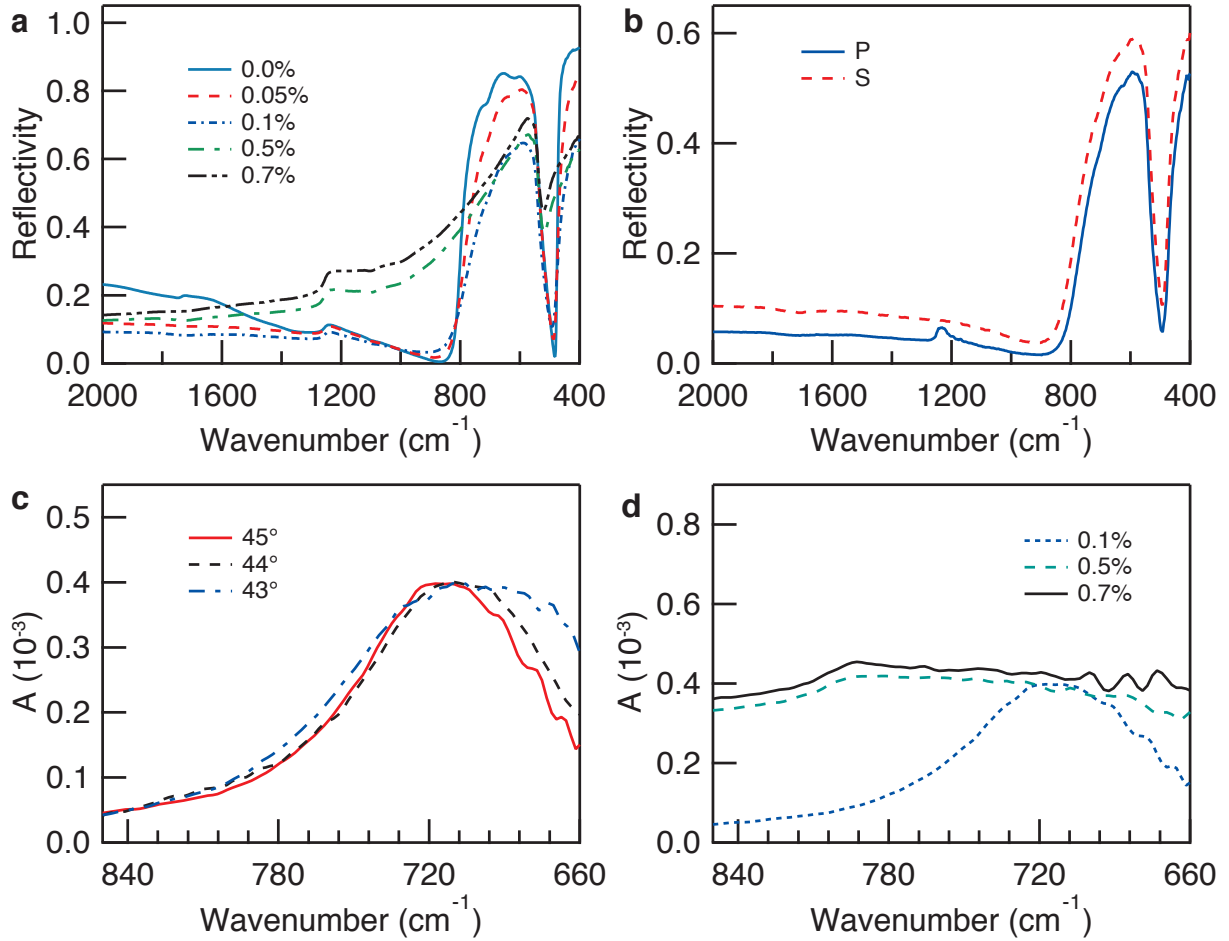


Figure 5.4: Specular reflectance and attenuated total reflection of SrTiO₃. **a**, Reflectance spectra of undoped and variously % Nb doped SrTiO₃. **b**, Static reflectance of 0.1% Nb doped SrTiO₃ sample for both S and P polarization. **c**, Static ATR of 0.1% Nb doped SrTiO₃ with different incident angles (P-polarization). **d**, Static ATR spectra of SrTiO₃ with different dopings (P-polarization).

the sign of the absorption is negative for the 0.5% and 0.7% Nb doped samples. Both of those statements are examined here. From the literature, two poles in the imaginary part of the dielectric constant, one at 530 cm^{-1} and one at 795 cm^{-1} , can be extracted using a Kramers-Kronig transform of the 0.1 % and undoped samples [125]. The 535 cm^{-1} peak is assigned to a transverse optical (TO) phonon and the 795 cm^{-1} peak is assigned to a longitudinal optical (LO) phonon. For higher doped samples (0.5% and 0.7%), the reflection spectra differ from that of the undoped and 0.1% doped samples due to the coupling of the LO phonon to the plasma density induced by higher doping. For spectra collected in the range of $600 - 1600\text{ cm}^{-1}$, the higher doped samples have significantly different n , κ than the lower doped sample (0.1%). This is likely why the Fano fits in Section 5.3.2 require that for the 0.5% and 0.7% samples the overall magnitude is negative, while for the 0.05% and 0.1% samples it is positive. Spectra of 0.1% Nb doped SrTiO_3 with S and P polarized light are shown in Figure 5.4b. For a single crystal sample, bulk LO phonons that propagate in the same direction as their electric field cannot be excited by light unless they couple to TO phonons or a transverse electron plasma. This is exemplified by the lack of a polarization dependence in reflectivity at 795 cm^{-1} where an LO phonon, with a dipole perpendicular to the sample plane, is expected. In contrast, a molecular and surface localized vibration will exhibit polarization dependence indicative of the direction of its dipole. The static attenuated total reflection spectra (in air) are shown in Figure 5.4c and Figure 5.4d. The peak in the spectrum found in Figure 5.4c is assigned to a surface LO polariton: a P-polarized light wave that propagates along the sample plane and couples to an in-plane surface vibration. The spectrum shows the center frequency of the peak at 710 cm^{-1} , but that shifts with incident angle, reproducing previous results [124]. As a result of coupling to the plasma density the surface polariton becomes much broader for the higher doped samples (Figure 5.4d) and moves to higher frequencies. This polariton, unlike the photo-hole generated mode, does not occur at the electrolyte interface. Importantly, whether in air or electrolyte and at any n-doping, the reflectivity measured by static ATR is not sensitive to the bulk LO phonon (at $\approx 800\text{ cm}^{-1}$). Based on this evidence, the photoinduced mode is assigned to a new mode with similar bond strength as the bulk LO phonon but derived from a new surface species.

Dependence on Excitation Fluence

To further explore the role this transient species may play as a photo-hole active site for water oxidation, the excitation fluence was varied across a range of 10 to $400\text{ }\mu\text{J}/\text{cm}^2$ (1.25% to 50% surface lattice site coverage). For this range of conditions, the magnitude of the absorbance change at closed circuit (conditions when a molecular oxygen evolves) was compared with O_2 evolution (inferred from the photo-current measured by a potentiostat). Varying the laser excitation fluence increases both the steady-state photocurrent and the observed signal magnitude, as shown in Figure 5.2d and Figure 5.5a. The O_2 evolution was measured by a potentiostat through the steady-state photocurrent reports on the photocurrent averaged over many laser shots. When the sample is positioned at

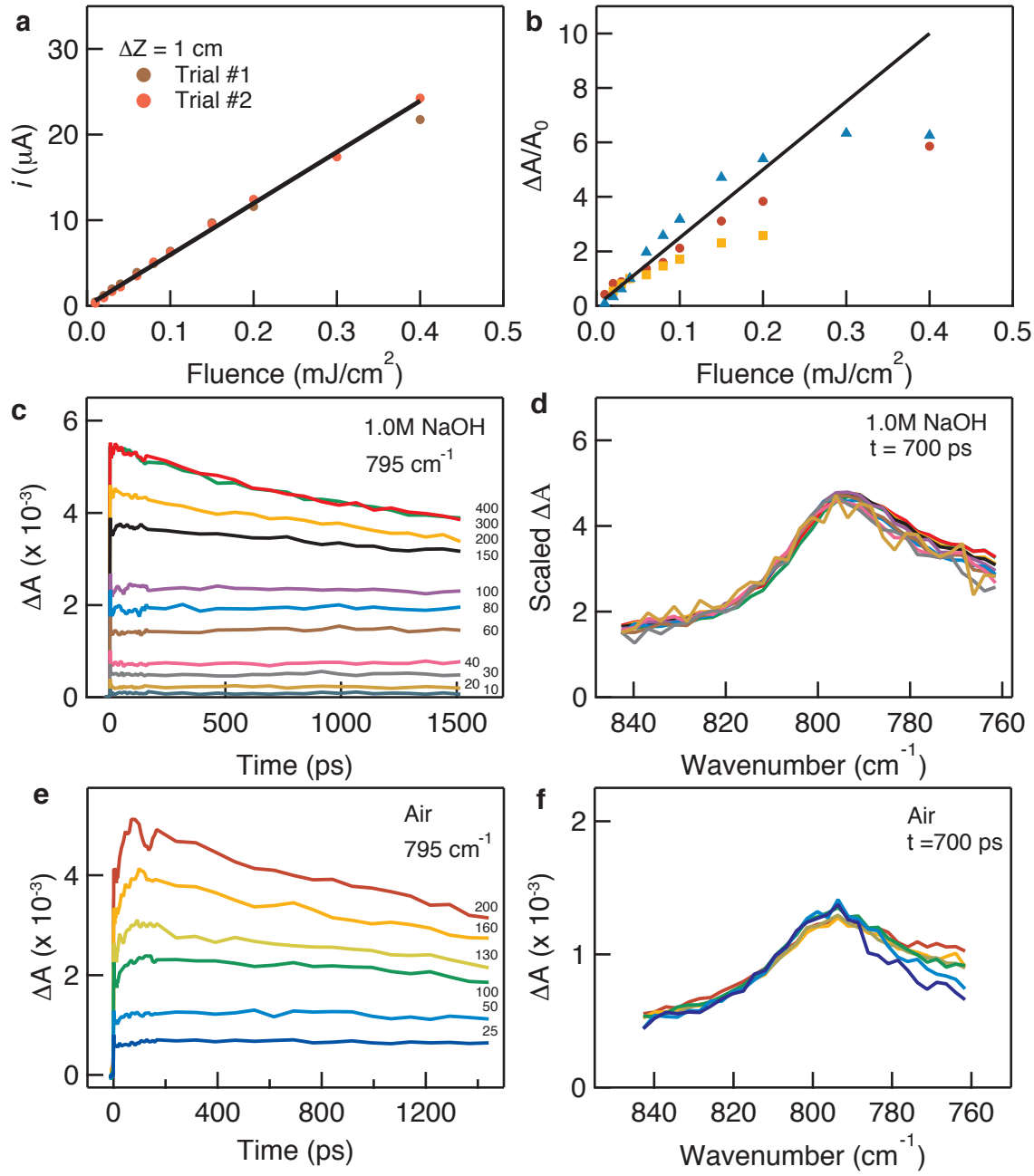


Figure 5.5: The 0.1% Nb doped SrTiO_3 sample was illuminated by the 266 nm laser while held at 0V vs. Ag/AgCl in pH 14 electrolyte. **a**, The photocurrent with the sample positioned such that diffusion is not limiting, with a linear fit. The photocurrent and photoinduced absorption at 795 cm^{-1} , **b**, are normalized to their respective values at $40 \mu\text{J}/\text{cm}^2$ and compared for three trials. Two where the fluence was increased from low to high, and one where it was decreased from high to low. The transient absorption kinetics at 795 cm^{-1} for a range of fluences are shown in electrolyte, **c**, and air, **d**. The scaled spectra at 700 ps are also shown (**e**, **f**, respectively). Fluences are in $\mu\text{J}/\text{cm}^2$.

the diamond surface ($\Delta Z \approx 1 \mu\text{m}$) to collect spectra, the narrow diffusion path between working electrode and bulk electrolyte causes the average photocurrent to become diffusion limited. This is identified by a lower photocurrent, equivalent to a Q.E. of 22% across the range of fluences tested. The photocurrent and Q.E. recover to 90% when the diffusion layer is made sufficiently large. Together with 100% Faradaic efficiency of O_2 evolution at the n-SrTiO₃/aqueous interface [126] (experimentally confirmed in Section 5.5), this high Q.E. means that almost all of the hole-activated sites at picosecond time scales are involved in the evolution of O_2 (as long as enough reactants are available). The photocurrent reports on the long-time-scale O_2 evolution, and is affected by long-time-scale processes such as diffusion. The photoinduced absorption, in contrast, is present within picoseconds and does not decay over the first 1.5 nanoseconds of its lifetime (Figure 5.5c, measured at closed circuit). As such, I present the photocurrent measured when the sample is pulled back from the diamond ($\Delta Z \approx 1 \text{ cm}$) as this reflects the conditions probed at early time scales, i.e. before diffusion plays a role. In order to correlate current (μA) with absorbance change (unit less) each is normalized to their respective values at a fluence of $40 \mu\text{J}/\text{cm}^2$ (5% surface site excitation). The correlation shown in Figure 5.5b reveals a linear relationship up to a fluence of around $200 \mu\text{J}/\text{cm}^2$ (25% surface site excitation), and a slight saturation of the absorption signal beyond that. This is understood as sample damage that occurs under high intensity, pulsed laser illumination. Briefly, this damage takes the form of a slowly dropping ΔA that is frequency independent, i.e. the spectra and traces recorded after c.a. 30 minutes, although smaller in magnitude, can be scaled by a single factor to recover results indistinguishable from those collected after one minute (i.e. without damage). Sample damage is only observed under closed-circuit conditions, is most significant at high fluences, and does not affect the photocurrent as significantly as the ΔA signal. To confirm that damage does not interfere with the correlation of $\Delta A/A_0$ with O_2 evolution in Figure 5.5, multiple trials were performed. In these trials, the fluence was both incremented decreasing from high-to-low and increasing from low-to-high. The results of Figure 5.5b show that $\Delta A/A_0$ scales similarly as $\Delta i/i_0$ with fluence for all the trials, although the high-to-low experiment exhibits the most quantitative agreement at high fluences. The trials where high-fluence points were collected after low-fluence points show the highest divergence, consistent with accumulated sample damage. These three trials are used to determine the error bars shown in Figure 5.5d. Based on the facts that the absorbance change (i) tracks a new transient species, (ii) has characteristics of a photo-hole at a water absorbed surface, (iii) is shown to be surface localized, and (iv) scales with highly efficient O_2 evolution, I propose the vibration is that of a $\text{Ti} - \text{O}^\bullet$ species active in the water oxidation reaction.

There is a final aspect of the signal fluence-dependence that is worth noting. The signal lifetime (Figure 5.5e) and spectrum (Figure 5.5f) in air does not change significantly within a range from $10 - 400 \mu\text{J}/\text{cm}^2$. The long ($\tau > 1.5 \text{ ns}$) lifetime indicates a new molecular species rather than a highly excited vibration inherent to the unperturbed system. The large amplitudes associated with highly excited vibrational wavepackets lead to large anharmonic coupling and associated fast decay kinetics. The wavepacket coupling would

be expected to decay faster for higher vibrational states (generated at higher fluences), which is not seen here. The frequency, linewidth, and lineshape of the species does not change across the fluence range considered, indicating the same species is probed at each fluence and that the species does not couple to photo-induced free carriers, as discussed in Section 5.3.2.

5.3.2 Line Shape Analysis Reports on Coupling Nearby Continua

Coupling to Electronic and Librational Continua

The Ti-O surface localized vibration, as shown by Fano line shapes, is coupled both to the electronic dynamics in the solid and solvent dynamics in the liquid, demonstrating the extent to which the mode is truly interfacial. In that it couples to the electron dynamics, the mode is similar to one of a small molecule (CO, methanol) adsorbed on a solid surface that exhibits Fano line shapes because of the solid-state continuum [127, 128]. On the other hand, the coupling of a molecular, surface localized vibration to solvent dynamics in the electrolyte is new. As will be shown, the solvent dynamics the Ti-O stretch couples to are water librations and in that sense, the coupling exemplifies what has been expected of a catalytic intermediate, but had not yet been detected molecularly—namely the interaction of its vibrations with reactant dynamics.

A Fano lineshape occurs whenever a discrete mode, such as a vibration, couples to a broad continuum of excitations whose spectral weight crosses the mode frequency, creating a resonance between the mode and the continuum. The lineshape is characterized by the coupling constant, Γ , of the mode to the continuum and an asymmetry factor, q , that in turn depends on the screening of the mode by the continuum and the continuum density of states at the resonant frequency. The Fano line shapes [129] and asymmetry factor q are defined rigorously by:

$$| \langle \Psi | T | i \rangle |^2 = A \left[\frac{(q + \epsilon)^2}{1 + \epsilon^2} \right] + Y_0 \quad (5.1)$$

$$q = \frac{\langle \Phi | T | i \rangle}{\pi V_E^* \langle \psi_E | T | i \rangle} \quad (5.2)$$

where $\epsilon = \frac{\omega - \omega_0}{2\Gamma}$ and ω_0 is the resonant frequency. $\langle \Psi | T | i \rangle$ represents the transition matrix element of the coupled vibration and continuum that is measured by the spectroscopy and separated by theory into transition matrix elements of the screened vibration, $\langle \Phi | T | i \rangle$, and of the continuum excitations, $\langle \psi | T | i \rangle$. The asymmetry factor q is the ratio of the screened vibrations over the continuum excitations at ω_0 . A represents solely the continuum excitations that are coupled to the mode ($|\langle \psi | T | i \rangle|^2$) and Y_0 represents the uncoupled continuum excitations.

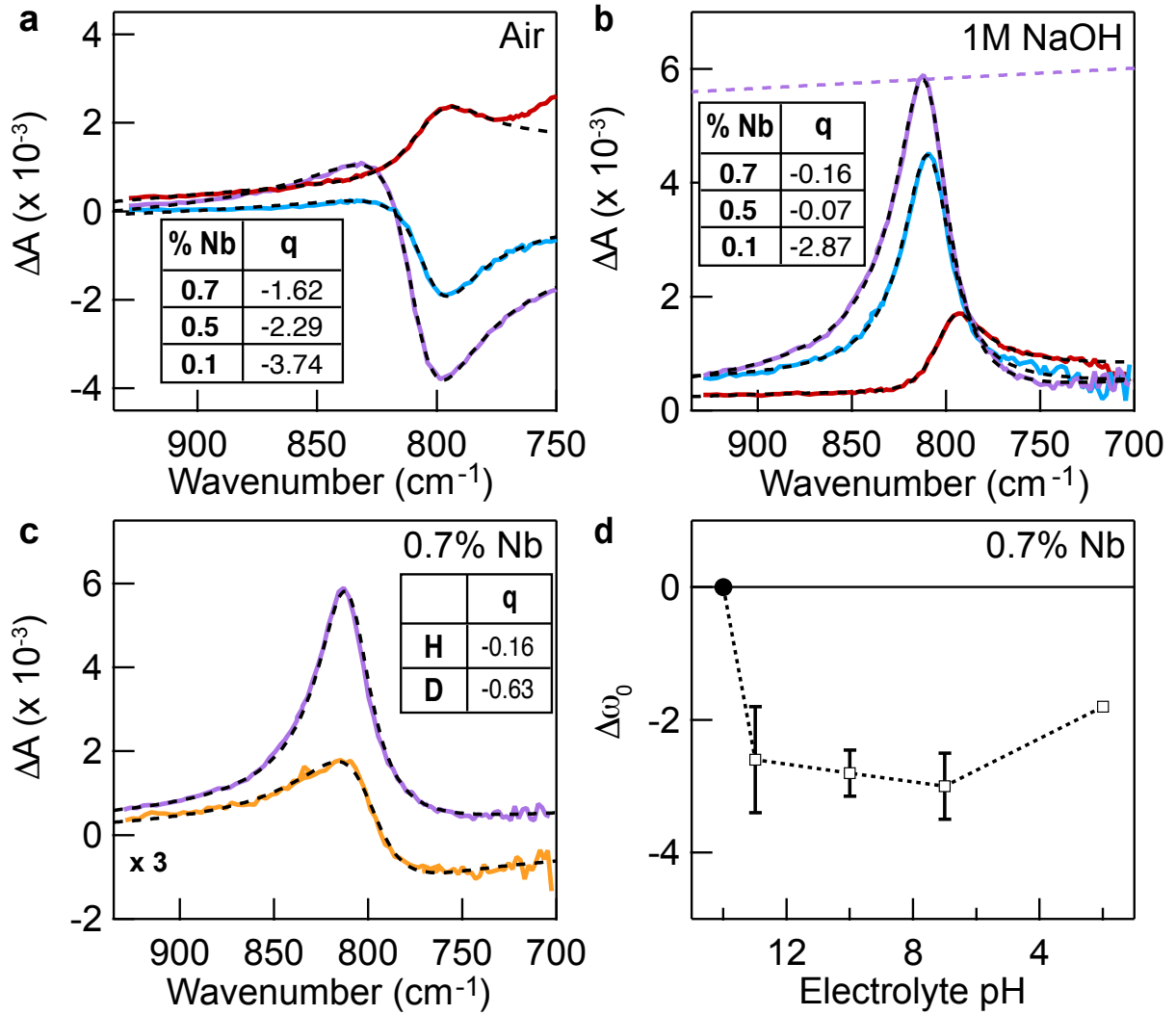


Figure 5.6: Fano line shapes describe the coupling of the discrete, surface localized mode to two separate continua. Modifying the n-doping tunes the Fano lineshape associated with coupling to the plasma continuum in the solid. Modifying the electrolyte conditions (air vs. electrolyte, H/D exchange, pH) tunes the Fano lineshape associated with coupling to water librations. Transient spectra at 700 ps of 0.1% (red), 0.5% (cyan) and 0.7% Nb (purple) doped SrTiO_3 in **a**, air, **b**, 1M NaOH in H_2O , and **c**, 1M NaOD in D_2O (yellow). The dotted purple line in **b** represents the uncoupled continuum for the 0.7% Nb sample. **d**, The underlying vibrational mode shows a consistent $\approx 3 \text{ cm}^{-1}$ redshift when the solution pH is less than 14. Error bars show standard error from 4 trials. Fano fits are shown in dotted lines and the q values are in the table insets.

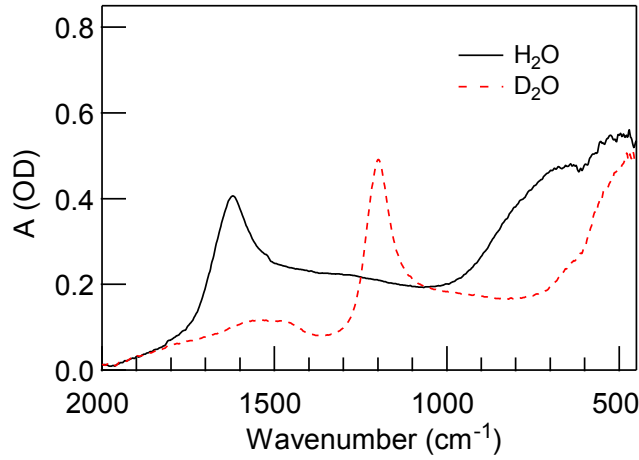


Figure 5.7: Attenuated total reflection of liquid H_2O and D_2O using a triple-bounce diamond internal reflection element, at 298 K and exposed to air. The librational frequency changes with deuterium exchange. For H_2O the librational frequencies center around 500 cm^{-1} and extend to 1000 cm^{-1} . In D_2O the librational frequencies red shift, resulting in an absorption centered below 500 cm^{-1} . The relative spectral weight in the region of the oxyl reporting mode (800 cm^{-1}) is lower for D_2O than H_2O .

The asymmetry of the spectral line-shape changes drastically with n-doping, pH, and H/D exchange, as shown in Figure 5.6. Remarkably, the variations in lineshape are all described by changes in the magnitude of the asymmetry factor, $|q|$, that occur when the experimental conditions modify the extent to which continuum excitations are involved. The three characteristics of the Fano lineshape fit by $|q|$ are a dip in spectral weight prior to the resonant frequency, followed by a steep rise near the resonant frequency, and then a more gradual decay following the resonance. The magnitude of the asymmetry factor decreases with increasing spectral weight of the continuum that crosses the resonant frequency, either through screening (decreasing Φ in the numerator, $|\langle\Phi|T|i\rangle|$) or through a larger density of states (increasing ψ in the denominator, $|\langle\psi|T|i\rangle|$). Accordingly, with higher doping at the air interface (Figure 5.6a), the asymmetry factor changes from -3.7 (0.1% Nb) to -1.5 (0.7% Nb). The doping induced electronic continua that cross the resonant frequency near 795 cm^{-1} are the electron plasma mode peaked at $400 - 500\text{ cm}^{-1}$ and the Drude free electron peak [130]. Interestingly, the resonant frequency of the mode increases from $798 - 800\text{ cm}^{-1}$ to $807 - 810\text{ cm}^{-1}$ in the more highly doped samples (Table 5.1), which reflects an increase in the plasma frequency in this doping range [130] and suggests that plasma excitations are primarily involved.

With the addition of electrolyte (Figure 5.6b), a second continuum is introduced by condensed phase molecular water librations in this frequency range [131] and as a result, the magnitude of the asymmetry factor decreases further. The most striking lineshape

change occurs for the Nb 0.5% and 0.7% doped samples. Here, continuum excitations due to both the electron plasma density and water librations have a large enough spectral weight at the resonant frequency that the vibration becomes a symmetric Lorentzian dip in the broad background of continuum excitations (this is the limit of $q \rightarrow 0$ for the Fano lineshape). As described by Fano’s theory [129], when two continua are involved in coupling to a single discrete mode, they introduce a significant, positive un-coupled background Y_0 (purple dotted line in Figure 5.6b); therefore, a true dip in spectral weight due to the vibration is only apparent after subtracting this un-coupled background. The asymmetry factor also significantly responds to shifts within the librational continuum obtained by pH and H/D exchange. Changes to the asymmetry are most readily accessed via the Lorentzian lineshape of the 0.7% doped sample in normal water. The change in the asymmetry factor from $q = -0.02$ in water to $q = -0.44$ in deuterated water (Figure 5.6c) is naturally explained by the librational frequency shift between H_2O and D_2O (Figure 5.7) resulting in less spectral weight at the resonant frequency [131]. While the lineshape changes drastically with H/D exchange, the resonant frequency does not (Table 5.2, Figure 5.9); this means that the interfacial Ti-O mode does not involve a proton. There is, however, a distinct effect of pH on the resonant frequency, red-shifting by $\approx 3 \text{ cm}^{-1}$ from pH 14 to pH’s lower than 13 (Figure 5.6d). Since only at pH 14 do surface hydroxyls dissociate to form a primarily $Ti - O^-$ terminated surface [111], this implies that the mode reporting on the $Ti - O^\bullet$ oxyl couples to librations that involve nearby adsorbed groups.

The full range of doping and electrolyte conditions fit with the Fano lineshape, and details of the fits are discussed with Figure 5.8, Figure 5.9 and Table 5.1, Table 5.2. The fact that the entire data set, despite the large changes in lineshape, can be fit with the expected modifications to the asymmetry factor demonstrates that the same Hamiltonian describing a localized, surface Ti-O vibration coupled to both the electron plasma density and water librations is involved throughout; the sign of the asymmetry factor is important in this consistency and arises in the context of continuum excitations that peak at lower energies than the mode, as described in Section 5.3.2. It is also important that the width of the transition, given by a similar coupling strength Γ ($30 - 45 \text{ cm}^{-1}$) across the data set, leads to a lifetime of $\approx 1 \text{ ps}$ for the coupled mode, which confirms that the measured nanosecond kinetics (Figure 5.2c) are that of a transient species rather than of a mode that decays into vibrational or electronic excitations. I will note that some of the transition width fit by the coupling strength is likely un-related directly to the Fano lineshape and can instead be attributed to anharmonic phonon coupling, polaronic behavior of the trapped hole, and surface heterogeneity.

While the Fano line shapes shown here primarily describe variations in the continuum spectral weight that couples to the mode (via q), they also have the potential to describe variations in the coupling strength (Γ) of the mode to solvent and electron dynamics, which are expected to occur especially as $Ti - O^\bullet$ evolves through a transition state and the O-O bond is formed.

Individual Fits and Fano Parameters

In this section the full details of the line shape fitting are presented. For the various experiments performed, the results were fit using Equation 5.1, reproduced here as Equation 5.3. Fano [129] addresses both the case of a single continua coupling with a discrete state and the present case, the interaction of multiple continua with a discrete state.

$$| \langle \Psi | T | i \rangle |^2 = A \left[\frac{\left(q + \frac{\omega - \omega_0}{\Gamma/2} \right)^2}{1 + \left(\frac{\omega - \omega_0}{\Gamma/2} \right)^2} \right] + Y_0 \quad (5.3)$$

In Equation 5.3, A represents the transition probability $|\langle \psi_{E_1} | T | i \rangle|^2$ to continua that interact with the discrete state transition, and Y_0 represents a transition probability $|\langle \psi_{E_2} | T | i \rangle|^2$ arising from continua that do not couple to the discrete state. Y_0 is a nearly energy independent offset (slope $< 0.004 \Delta A (\times 10^{-3}) / \text{cm}^{-1}$) identified by fitting a line to the region $850 - 950 \text{ cm}^{-1}$, where the discrete state contribution is minimal. Γ represents the coupling between the discrete state and the continuum. The factor q is defined (Equation 5.2) as the ratio of the transition matrix element of the initial state to the discrete state (modified by interaction with the continua), over the transition matrix element between the initial state and the continuum states (over a bandwidth given by Γ). Phenomenologically, the value of q is dictated by the asymmetry of the resulting lineshape (negating q is equivalent to reversing the abscissa axis). Finally ω_0 is the observed resonance energy corresponding to excitation to the discrete state modified by interaction with the continuum. The parameter values used in fitting results in air and electrolyte, as well as figures showing fits, are found in Table 5.1 and Figure 5.8 respectively. Γ (the continua/discrete state coupling) is roughly constant as a function of doping, and does not change appreciably in the presence of electrolyte. In contrast q changes with both doping and the presence of electrolyte. The resonant frequency ω_0 is consistently found to be $797 - 802 \text{ cm}^{-1}$ in air and electrolyte, although it increases to $807 - 810 \text{ cm}^{-1}$ for the 0.5% and 0.7% Nb doped samples. The coupled-continua transition probability (A) increases with doping and further with the presence of electrolyte. The Fano fits require that for the more highly doped samples (0.5%, 0.7%), A is negative, while for the less doped samples (0.05%, 0.1%), it is positive. Justification for this is that the plasma mode can significantly change the dielectric constants of reflectivity for the 0.5% and 0.7% doped samples in this wavenumber range (Figure 5.4) [130] and that differential reflectance, even if coming from an additional absorption, can appear either as a positive or negative absorbance change [132, 133] (see Equation 3.2 and further discussion in Appendix A). The fitting parameters for the hydrogen-deuterium exchange experiments are found in Table 5.2 and shown in Figure 5.9. Representative fits for the experiments supporting Figure 5.6d (pH-dependent frequency shift) are found in Figure 5.9.

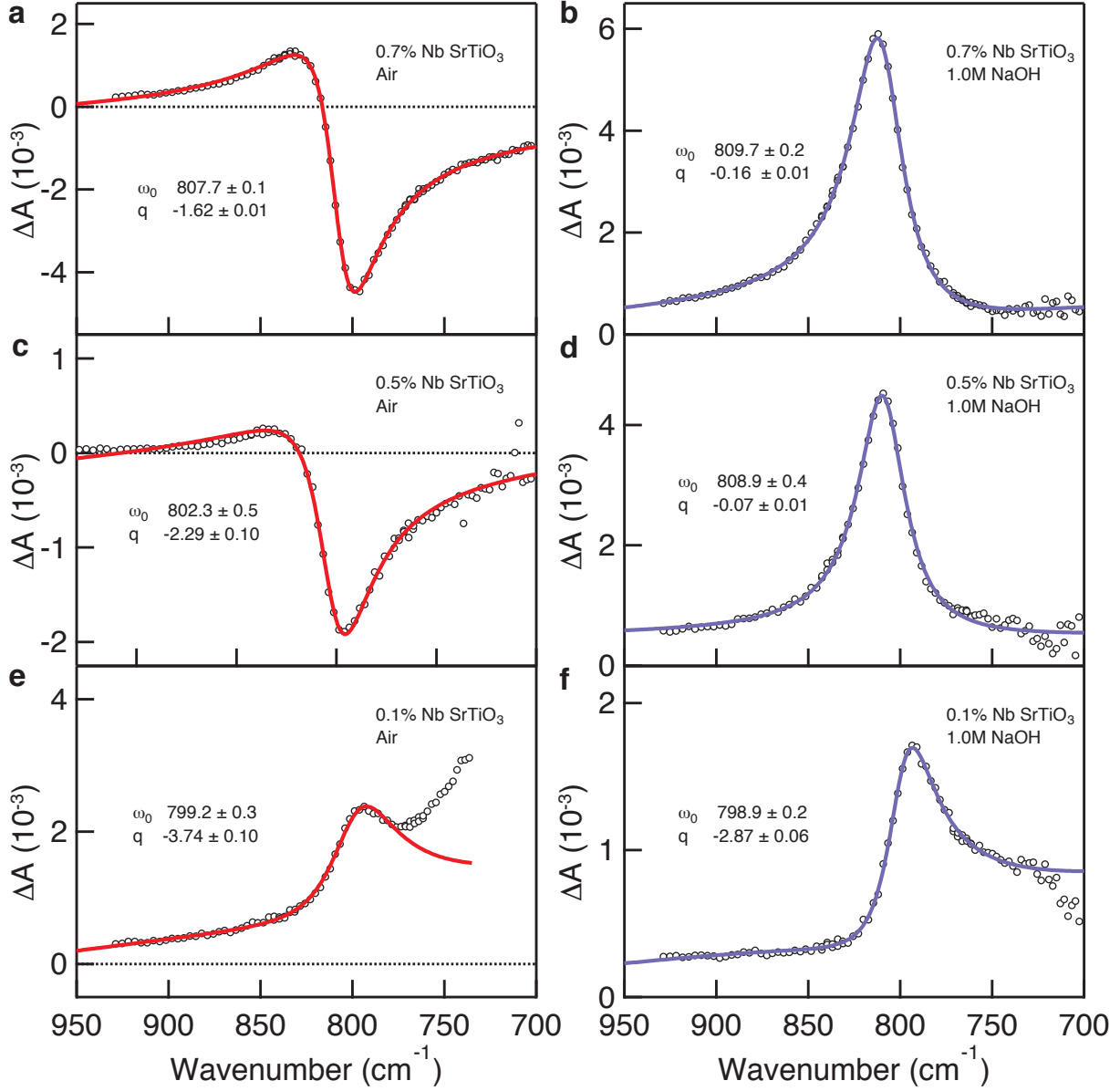


Figure 5.8: Full spectra of variously doped samples in air and electrolyte. Transient spectrum of doped SrTiO_3 in air and electrolyte with doping concentration **a**, **b**, 0.7% Nb, **c**, **d**, 0.5% Nb, **e**, **f**, 0.1% Nb. Spectra were fit with Equation 5.3 describing a Fano resonance. Full fitting parameters found in Table 5.1.

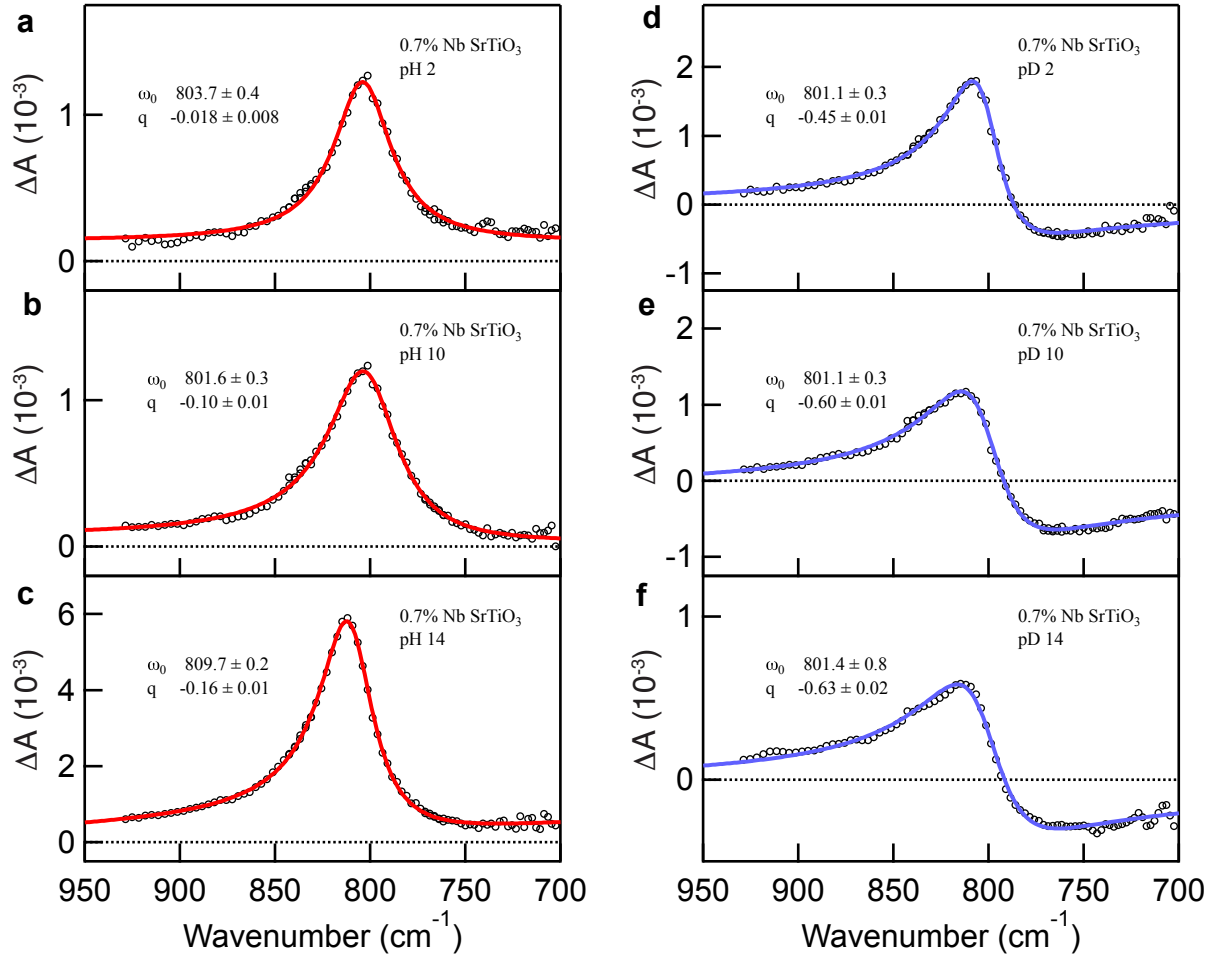


Figure 5.9: Full spectra in different pH and pD electrolyte. Transient spectrum of 0.7% doped SrTiO₃ in **a – c**, H₂O with different pH and **d – f**, D₂O with different pD. Spectra were fit with Equation 5.3 describing a Fano resonance. Full fitting parameters found in Table 5.2.

Condition	Doping	ω_0	q	A	Γ	Y_0	S
Air	0.7% Nb	807.7	-1.62	-1.58	29.6	1.25	120.41
	0.5% Nb	802.3	-2.29	-0.35	31.0	0.24	72.97
	0.05% Nb	797.6	-1.93	0.16	53.2	0.38	37.30
Electrolyte: 1M NaOH	0.7% Nb	809.7	-0.16	-5.34	34.5	5.60	281.60
	0.5% Nb	808.9	-0.07	-3.97	31.5	4.50	195.68
	0.05% Nb	797.9	-1.98	0.09	44.5	0.32	18.80

Table 5.1: Fano parameters obtained for different dopings.

Condition	pH	ω_0	q	A	Γ	Y_0	S
H ₂ O	14	809.7	-0.16	-5.34	34.5	5.60	281.60
	10	801.6	-0.10	-1.14	44.6	1.20	79.06
	2	803.7	-0.02	-1.09	36.8	1.23	61.24
D ₂ O	14	801.4	-0.63	-0.63	47.9	0.60	28.29
	10	801.2	-0.60	-1.33	44.0	1.18	58.83
	2	800.3	-0.45	-1.83	33.7	1.79	75.95

Table 5.2: Fano parameters obtained from H/D exchange in both acidic and basic conditions for the 0.7% Nb SrTiO₃ sample.

Negative q, Monotonic Changes in q, and Uncoupled Background

This section interprets the negative sign of q and the variations in $|q|$ in the context of a monotonic increase in the contributions of electronic and librational continua. The matrix elements that define q are:

$$q = \frac{\langle \phi | T | i \rangle}{(V_E + W_E) \langle \psi_E | T | i \rangle} + \frac{\int \frac{dE' ((V_{E'} + W_{E'}) \langle \psi_{E'} | T | i \rangle)}{E - E'}}{(V_E + W_E) \langle \psi_E | T | i \rangle} \quad (5.4)$$

Here V_E , W_E represent the coupling of the vibration (ϕ) to the electronic, librational continua respectively. E is the resonance energy, E' the energy that spans through both continua, and $\psi_{E'}$ represents both continua. Fano has shown that the presence of two continua does not change the form of the Fano equation, but only adds an additional smooth background, described further below. While the sign of the first term is due to the phases of the wave-functions involved, the sign of the second term is always positive for continua that peak at lower energy than E (when $(E - E') > 0$). Since the electron plasma density and the librations are the only continua that I know of that can extend to E and they become large for lower energies, the sign of q cannot be determined by the second, screening term. Therefore, the consistent negative values suggest that the first term is dominant and the phases of the wavefunctions make it negative. The first term could be dominant in many considerations of the Fano lineshape, since it involves the wavefunctions in the region near the resonance energy E . The relative phases of the wavefunctions cannot be predicted without more extensive calculations. From this starting point, the changes in the magnitude of q can be rationalized with the changes in the density of states of the two continua. As the electronic continuum increases with doping, magnitude of the first term (negative) is expected to decrease and the contribution of the screening term (positive) is expected to increase. This then results in a lower $|q|$ with doping, as exhibited in Table 5.1. In a similar manner, the addition of a librational continuum can explain why $|q|$, for a given doping, decreases in electrolyte. The contribution from the librational density of states will decrease upon H/D exchange. This explains why $|q|$, for the 0.7% doped sample in deuterated electrolyte, is lower than in air, but larger than in pH 14 electrolyte.

In the lower doped, 0.1% sample, the changes in q between air and electrolyte are not as pronounced and q doesn't change in deuterated electrolyte. The less pronounced effect of the librational continuum on q may have to do with the fact that the denominator in the first term is already small due to a much lower electronic continuum. Indeed, if a consistent relative phase of the wavefunctions determines the first term despite the presence of two continua, one of the continua – likely the electron doping – determines this phase. The relative importance of the continuum to the signal can also be seen in the differential signal amplitude (A in the table), representative of transitions within the continuum. As expected within this interpretation, the amplitude is highest in the case of the more highly doped samples in electrolyte. Finally, the presence of two continua also means that there will be a large, smooth background on top of the original Fano lineshape given by:

$$Y_0 = \sqrt{(V_E^2 + W_E^2)} |\langle \psi_E | T | i \rangle|^2 \quad (5.5)$$

We find that the 0.7% doped and 0.5% doped samples in electrolyte have a large uncoupled continuum, close to the magnitude of the Fano signal (see Table 5.1, Y_0). These are exactly the two cases when q changes significantly with the librational continuum, suggesting that two full continua are involved through V_E and W_E . The presence of this large uncoupled continuum is why the data look like Lorentzian peaks rather than Lorentzian dips within a coupled continuum, described by the $q \rightarrow 0$ limit of the Fano lineshape. A Lorentzian peak is associated with the $q \rightarrow \infty$ limit. However, the $q \rightarrow \infty$ limit means that a continuum is not significantly contributing ($A \rightarrow 0$), while experimentally the Lorentzian occurs when the electronic and librational continua are maximally involved. There is another solution set for the Fano fitting, if one explores the case when the differential signal amplitude (A) is positive for all dopings. In this case, one has to interpret the Lorentzian line shapes of 0.5% and 0.7% in the $q \rightarrow \infty$ limit. As described, this minimum is not physically matched with the experimental conditions. Furthermore, the fits require q to change sign and to span -2 to 15 non-monotonically with changes in the continuum density of states. The screening term would have to dominate some of the time and not in others. Finally, these fits also require a large uncoupled continuum (of the order the Fano signal) to be added to the 0.5% and 0.7% doped samples in air (rather than in electrolyte), where two clear continua do not exist. All of these considerations are made in the case where there is no direct coupling between the two continua, which is the first order effect considered by Fano.

5.3.3 Theory of Interfacial Ti – O[•] and its Surface Modes

Infrared Activity Overview

The data demonstrate that a transition dipole for a surface-localized, Ti-O vibration becomes bright whenever a hole sits at the surface. Therefore, we consider a water-adsorbed and undoped SrTiO₃/air interface with holes as the starting point for a more

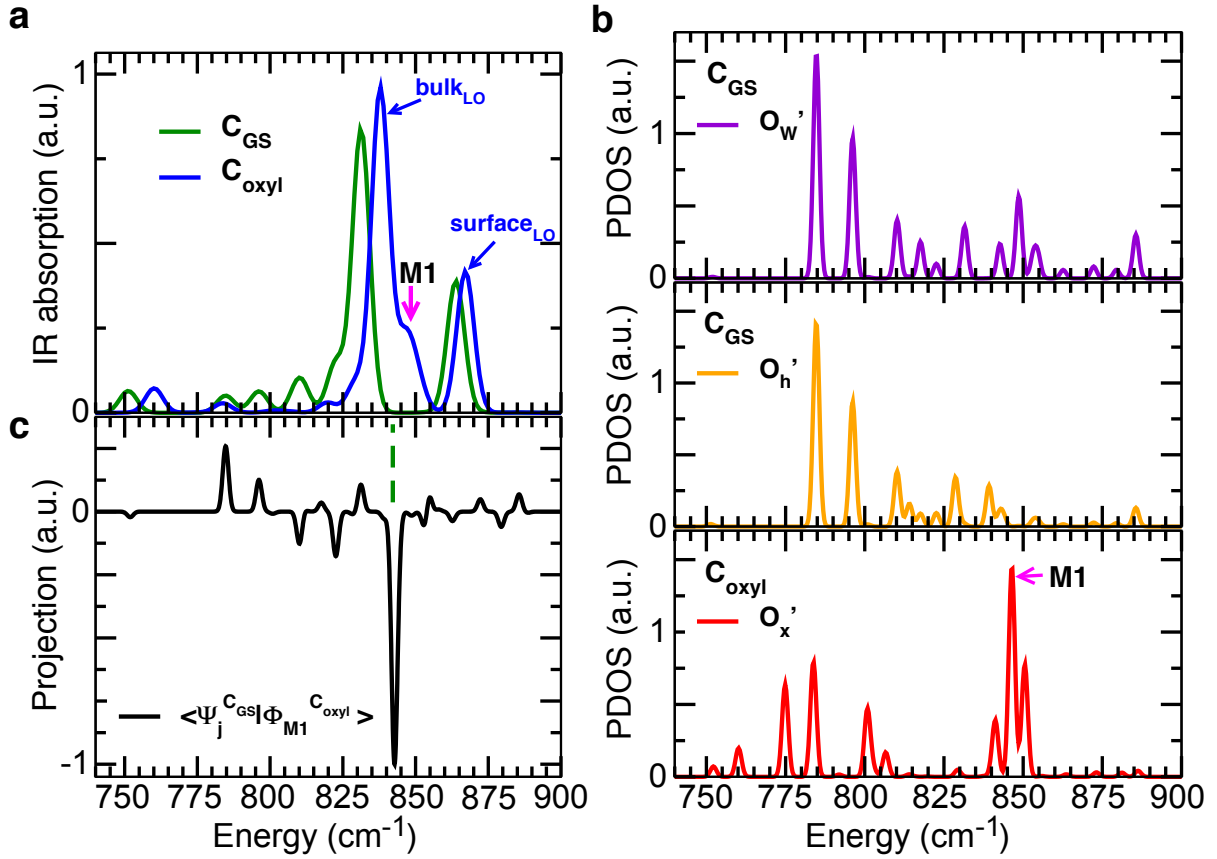


Figure 5.10: . Infrared activity of the ground state configuration (C_{GS}) and the oxyl configuration (C_{oxyl}) and associated phonon density of states for different surface related O sites (O_w' , O_h' , O_x') within the two configurations. **a**, Infrared activity of the slab for C_{GS} and C_{oxyl} where M1 indicates the new surface mode upon creating the oxyl. **b**, Partial density of states of O_w' sites in C_{GS} (top), O_h' in C_{GS} (middle) and O_x' in C_{oxyl} (bottom). **c**, Projection of the eigenvector of mode M1 in C_{oxyl} on the phonon eigenvectors of C_{GS} , where the primary contribution comes from a dark breathing mode at 843 cm^{-1} .

detailed, molecular description of the vibration and the associated transient species using first-principles theory. At equilibrium, we find a partially dissociated configuration (C_{GS}), wherein 50% of adsorbed water molecules lose an H atom to one of the lattice surface oxygen atoms and hydroxyl-water dimers form (Figure 5.1a). In the photo-excited configuration (C_{oxyl}), the hole is localized on an O adatom (O_x) and there are two hydroxyl groups on the surface TiO_2 layer (Figure 5.1b). O sites on the surface-terminating $Ti-O_2$ layer of the STO slab are henceforth referred to as lateral oxygen to distinguish them from the oxygen of adsorbed water or hydroxyl groups. These calculations indicate that the configuration in which the hole is localized at O_x is the lowest in energy by 0.46 eV. Furthermore, localizing the hole at a lateral oxygen surface site does not lead to P-polarized vibrations, as observed in experiment (see Section 5.3.3).

Phonon frequencies and eigenvectors for configurations C_{GS} , C_{oxyl} , and a pristine surface are calculated using a density functional finite difference approach, and associated infrared absorption oscillator strengths are obtained using an established methodology [134]. The dominant motion for the Ti-O modes observed in P-polarization (perpendicular to the surface) is related to either the O in SrO layers or the adsorbed atoms (O_w , O_h , O_x) defined in Figure 5.1. The vibrations of O sites within the SrO layers can be divided into bulk O modes ($O_{bulk-SrO}$), sub-surface O modes of the un-terminated layer ($O_{bottom-SrO}$), and the sub-surface O modes of the terminated layer (O'_h , O'_w , and O'_x). In both C_{GS} and C_{oxyl} , the bulk LO Ti-O mode occurs near 835 cm^{-1} (bulk LO in Figure 5.10a, see Supplementary Video 1). A surface infrared active LO Ti-O mode of $O_{bottom-SrO}$ occurs at 866 cm^{-1} (surface LO in Figure 5.10a, see Supplementary Video 2).

The significant difference in infrared activity between C_{GS} and C_{oxyl} appears at 846 cm^{-1} (Figure 5.10a) where O'_x is decoupled from the O'_h , O'_w motion and dominates the projected phonon density of states (PDOS) (Figure 5.10b and Figure 5.13). As can be seen from projecting the new eigenstate (M1 in Figure 5.10a) in C_{oxyl} on the C_{GS} eigenstates, the dominant contributor to M1 is an originally dark (infrared-inactive) mode in C_{GS} at the same energy and the remaining spectral weight is distributed among many (infrared active and dark) modes in C_{GS} (Figure 5.10c). The dark breathing motion in C_{GS} (Figure 5.1a, Supplementary Video 3) is disrupted by a new large amplitude motion on O'_x (Figure 5.1b, Supplementary Video 4). The origin of this infrared activity, along with the effects of ionic screening, are discussed in terms of the PDOS of both configurations (Figure 5.13, Section 5.3.3). M1 can be assigned to the Ti-O infrared activity seen experimentally because: (1) it occurs at a frequency $\approx 10\text{ cm}^{-1}$ above the bulk LO Ti-O mode; (2) it is associated with an oxyl radical, or a photo-hole active site; (3) it is associated with a completely new absorption cross-section not seen in the ground state; (4) it does not involve a proton; and (5) the infrared activity comes from a sub-surface layer whose motion is P-polarized and can readily couple to bulk and surface water librations (see Supplementary Video 4). Note that experiment does not observe an isotope shift upon O_{16}/O_{18} surface exchange and theory confirms this for M1 (Figure 5.14).

Furthermore, as shown in Figure 5.10a, M1 is the distinctive infrared mode associated with the oxyl radical. One might also expect to observe a beating mode of the surface

oxyl Ti-O_X bond itself, but only weak and spectrally broad IR activity is predicted for motions of Ti-O_X at the fully water-adsorbed surface (see Section 5.3.3); hydrogen bonding strongly hybridizes the motion of O_X with nearby surface-adsorbed water groups. Thus, a pure Ti-O_X beating mode is not expected to be a stable vibrational eigenstate of the oxyl radical.

First-Principles Computational Details

In order to investigate infrared active vibrational excitations at a SrTiO_3 (STO) surface, we employ atomistic models of functionalized STO (001) slabs consisting of 13 atomic layers and terminated on either side by a TiO_2 layer (see Figure 5.11). We do not consider SrO terminated slabs as it is expected that TiO_2 termination is dominant in the experimental samples. In the lateral dimension, the supercells considered include four formula units of STO every two atomic layers and periodic boundary conditions are imposed. In the longitudinal direction, the periodically repeated slabs are separated by at least 14 Å of vacuum. The goal of the theoretical simulations is to provide a microscopic model for the photo-induced 795 cm^{-1} mode observed experimentally in the transient ATR measurements. Since the experimental data unambiguously indicate that the photo-induced mode is observed only in the case of a p-polarized probe, we focus on estimating the infrared activity of the slab models for light polarized along the surface normal, which we set to lie along the z-axis. In the experimental setup, following illumination by the UV pump field, we expect hole carriers to migrate to the STO surface. As explained in Section 5.3.3, there is evidence correlating the appearance of the transient spectral feature at 795 cm^{-1} with hole trapping at the surface. Furthermore the transient signal observed is narrow and remains the same over a nanosecond suggesting that the species being observed is stable on the timescale of electro-nuclear dynamics. We therefore assume that the vibrational excitations being probed in the transient ATR measurement occur on the potential energy surface of a long-lived electronic excited state associated with localized holes at the STO surface. Hence we seek to calculate the infrared absorption functions of water adsorbed STO slabs without and with hole doping and identify spectral features that can be attributed to hole trapping at the surface.

Density functional theory (DFT) [135, 136] simulations are based on the first-principles electronic structure platform implemented in the Vienna Ab Initio Simulation Package [137, 138] (VASP). Wavefunctions are expanded in a plane wave basis set with an energy cutoff of 400 eV and the electron-ion interaction is described through Projected Augmented Wave [139] pseudo-potentials with the following valence electronic configurations $\text{Sr}:4s^24p^65s^2$, $\text{Ti}:3p^64s^23d^2$, $\text{O}:2s^22p^6$, $\text{H}:1s^1$. The Perdew-Burke-Ernzerhof [140] (PBE) generalized gradient approximation (GGA) to the exchange-correlation energy is used in conjunction with the DFT-D2 [141] approach for the treatment of dispersion forces. In order to mitigate some of the well-known shortcomings of semi-local GGA functionals in describing oxide materials, such as band-gap underestimation and excessive delocalization of the electron density [142], we employ the DFT+U [143] approach. A +U correction is

included on both the Ti-3d ($U_{\text{eff}}^{\text{3d}} = 4.36$ eV [144, 145]) as well as O 2p ($U_{\text{eff}}^{\text{2p}} = 8$ eV [146]) states within the rotationally invariant scheme due to Dudarev et al. [143]. A +U correction on the O 2p states is necessary to correctly describe hole polaron states [146, 147]. The Brillouin zone is sampled using the equivalent of an $8 \times 8 \times 8$ Γ -centered k-point grid for the primitive unit cell of cubic SrTiO₃ (STO) and in the slab calculations, a $4 \times 4 \times 1$ k-point grid is used, with the non-periodic direction along the z-axis. For all the systems presented, structural optimization is carried out until forces on all the atoms are smaller than 10^{-3} eV/Å. Since most of the slabs considered have a non-zero dipole moment, we apply self-consistent dipole corrections in all cases to the potential, total energy and forces using the approach of Neugebauer et al. [148] as implemented in VASP. Hole doping is treated using the "pseudo atom" approach of Sinai et al. [149] whereby pseudo-potentials with fractional nuclear charge are introduced so that a nominally neutral slab would have one electron less, thus mimicking hole doping. The unfunctionalized STO slabs in these calculation consist of 132 atoms and we found that including a net fractional charge of 0.008 on each Sr and 0.01 on each O nucleus is enough to produce a doping density of 0.998 holes per supercell. This corresponds to 25% surface excitation density. The advantage of this method based on the virtual crystal approximation is that the slabs are nominally neutral with the compensating charge distributed roughly uniformly throughout the material and no additional monopole image charge corrections are needed while dipole corrections can be applied as usual. We note that fractional nuclear charges are assigned only to the O and Sr sites within the 13 atomic layers of the STO slab and not to O atoms of adsorbed water molecules. Vibrational properties were calculated using the supercell finite differences or frozen phonon approach [150]. The phonopy code [151] was used to generate supercell displacements necessary for the finite difference calculations as well as to calculate the inter-atomic force constants, dynamical matrix and associated phonon Eigen energies and eigenvectors. Infrared (IR) absorption functions were obtained using the methodology proposed by Giustino et al. [134]. The Born effective charge tensor and static dielectric matrix for bulk STO supercells were obtained from the density functional perturbation theory (DFPT) approach [152, 153] implemented in VASP. For the slab geometries, lateral components of the Born effective charge tensors were obtained from DFPT while the longitudinal component for the field along the surface normal was obtained from finite differences by applying a saw-tooth potential across the slab. The IR spectrum corresponding to the longitudinal response of bulk STO was calculated using Equation 5.6 given in reference [134]:

$$I_t(\omega) = \frac{2\pi^2}{Ac} \sum_{I,J,\beta,\gamma,n} \frac{Z_{I,\alpha,\beta}^C \xi_{I,\beta}^{l,n}}{\sqrt{m_I}} \frac{Z_{J,\gamma}^C \xi_{J,\gamma}^{l,n}}{\sqrt{m_J}} \delta(\omega - \omega_{l,n}) \quad (5.6)$$

wherein the indices α, β, γ indicate coordinate directions, α being a longitudinal direction, $Z_{I,\alpha,\beta}^C$ are Callen charges with are related to Born effective charges $Z_{I,\alpha,\beta}^B$ by $Z_{I,\alpha,\beta}^C = \frac{z_{I,\alpha,\beta}^C}{\epsilon_\infty}$ through the electronic dielectric constant ϵ_∞ , $\xi_{I,\alpha}^{l,n}$ and $\omega_{l,n}$ are respectively the eigenvectors and Eigen frequencies calculated by including the non-analytical part

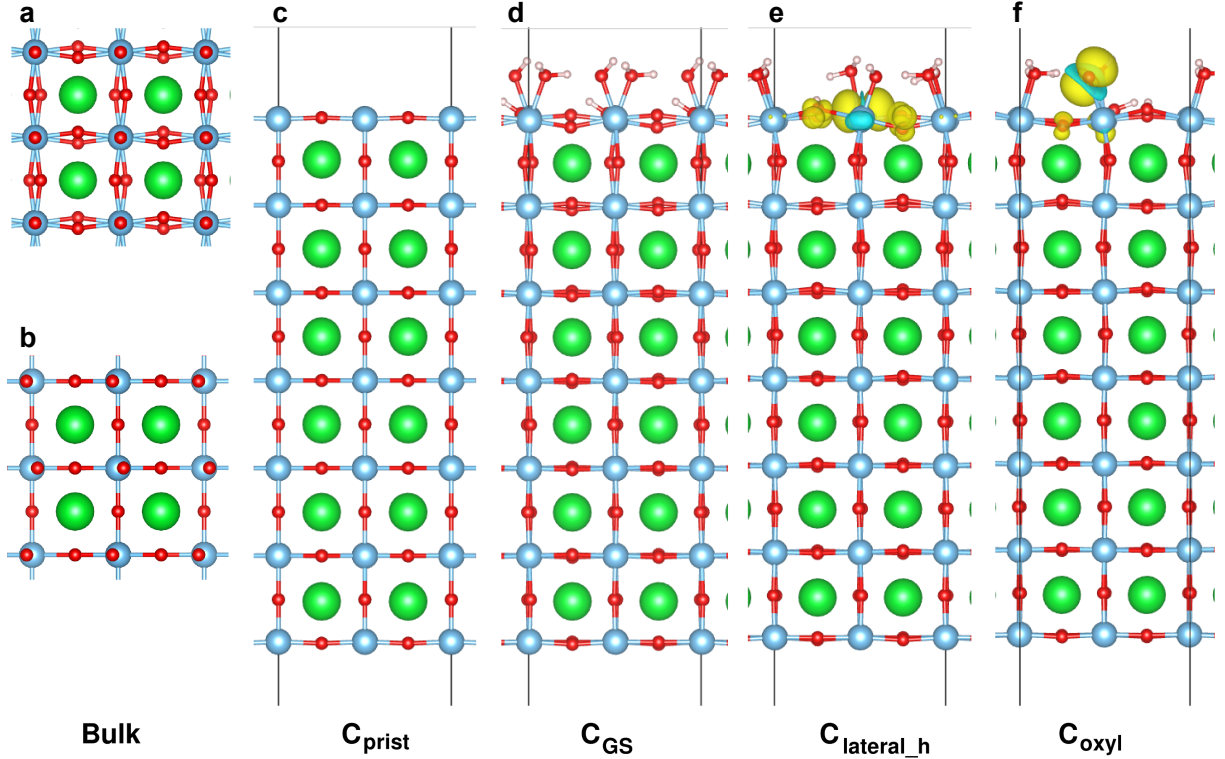


Figure 5.11: Bulk and slab geometries. **a**, **b**, Top view (down the c -axis) and side-view of bulk SrTiO_3 . **c** – **f**, Slab geometries of supercells featuring pristine (**c**), water absorbed (**d**), and hole doped water adsorbed (**e**, **f**) surfaces. Spin-density iso-surfaces depicting hole localization at the surface are also shown in **e** and **f**. The iso-surfaces of hole density are plotted at $\pm 5\%$ of their maximum positive value (positive surfaces: yellow, negative surfaces: cyan). Color code for atoms: Sr – green, Ti – light blue, O – red, H – beige. Iso-surface – yellow.

[134] in the dynamical matrix. For the response along the surface normal in the slab calculations a formally identical expression applies except that the additional non-analytical part is not included as the effect of the surface charge is automatically present in the finite slab setup.

The SrTiO_3 Bulk

We calculate electronic and vibrational properties based on the low temperature tetragonal antiferrodistortive (AFD) phase of STO [154] as opposed to the room-temperature cubic phase. This is because as has been widely studied [155, 156, 157], within 0K DFT calculations, the cubic phase exhibits soft phonon modes at the R point in the Brillouin zone [156] and is unstable. The stable low temperature AFD phase, with the space group ($I4/mcm - D_{4h}$ [149]) is characterized by a rotation of the TiO_6 octahedral and

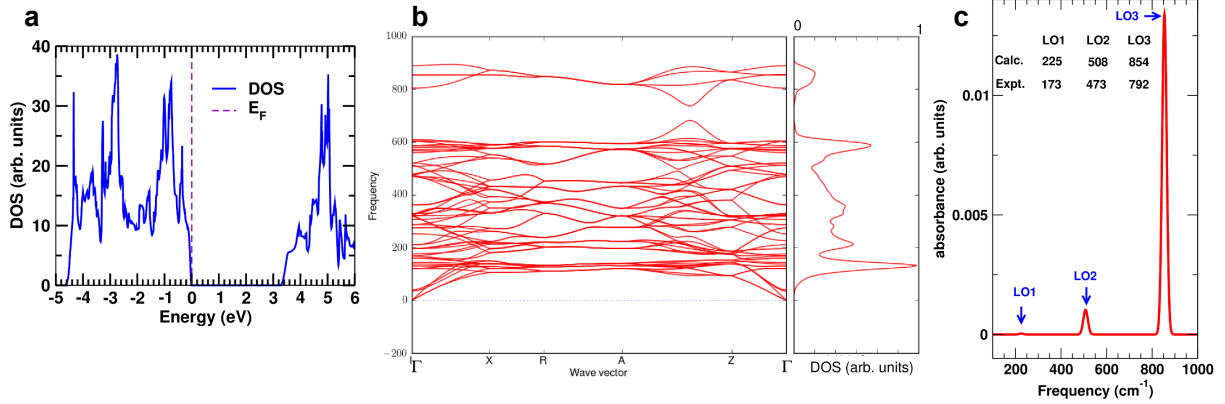


Figure 5.12: Calculated bulk electronic and vibrational properties. **a**, Electronic density of states of bulk SrTiO₃. **b**, Phonon band structure and density of states from an 80 atom bulk STO supercell. **c**, Calculated infrared absorbance with relevant peaks labeled LO₁, LO₂, and LO₃. Inset table: Comparison between theoretical and experimental frequencies in thin films of LO absorption features.

a tetragonal distortion whereby the c/a ratio increases [157]. In Table 5.3, we compare the experimental and calculated structural parameters for the AFD phase of bulk STO. A schematic of this bulk cell is shown in Figures 5.11a-b. We find that the PBE+U functional used in this study leads to a and c being underestimated by 1.2% and 0.4% respectively, and similarly to previous LDA, PBE and LDA+U calculations [157, 158], significantly overestimates the rotation angle Θ of the TiO₆ octahedra. This in turn results in more asymmetric Ti-O and Sr-O bonds with average bond lengths underestimated by 0.5% and 0.9% respectively. In spite of these structural differences the PBE+U method represents a satisfactory compromise since as we show below it significantly improves the electronic properties, essential for describing hole polarons in STO [142, 147, 146], and yields longitudinal IR response that is consistent with experimental measurements.

For the choice of +U parameters used in this study, PBE+U predicts a band gap of 3.2 eV for bulk AFD STO as seen from the calculated electronic density of states (DOS) shown in Figure 5.12a. This is in good agreement with experimental measurements [159]. The phonon band structure and phonon DOS calculated for an 80 atom bulk supercell are shown in Figure 5.12b. The phonon band structure does not show any imaginary modes and the longitudinal optical branch around 800 cm⁻¹ which involves Ti-O bond stretches is clearly separated from the rest of the band structure. The calculated longitudinal infrared absorption function for polarization along the c -axis is shown in Figure 5.12c. The calculated spectrum shows three features LO₁, LO₂ and LO₃ with progressively higher intensity which is consistent with experimental measurements on STO thin films [125] (see figure 2b of reference [125]). The calculated LO₁, LO₂ and LO₃ frequencies are compared to experiment within the table inset in Figure 5.12c. We find that the calculated frequencies are systematically blue-shifted by ≈ 50 cm⁻¹ primarily due to the fact that the

	a (Å)	c (Å)	θ (°)	$d_{\text{Ti-O}}$ (Å)	$d_{\text{Sr-O}}$ (Å)
Calculated	5.4432	7.7706	7.23	1.9399 [4]	2.5685 [2]
				1.9427 [2]	2.7216 [4]
				1.9408	2.9115 [2]
					2.7308
Experiment [153]	5.5134(10)	7.8072(20)	2.02(5)	1.9505(11) [4]	2.7104(9) [2]
				1.9518(5) [2]	2.7567(5) [4]
				1.9509	2.8074(9) [2]
					2.7578

Table 5.3: Calculated bulk SrTiO_3 structural parameters compared to experiment. $d_{\text{Ti-O}}$ and $d_{\text{Sr-O}}$ label Ti-O and Sr-O bond lengths respectively. The numbers in square brackets give the multiplicity of each bond while the numbers in bold indicate average bond lengths.

lattice constant and bond-lengths are slightly underestimated within PBE+U, however no additional absorption features not seen in experiment are predicted. Since the ATR experiments in the current study probe the energies between $700 - 900 \text{ cm}^{-1}$, we are primarily interested in the LO_3 mode, which at the zone center involves a concerted oscillation of the O sub-lattice against the Ti sub-lattice along the propagation direction. We note that in general, modes in this energy involve relative motion of O and Ti sites with most of the amplitude distributed on the O sites.

The SrTiO_3 Surface

We now analyze the infrared response, for polarization along the surface normal, of the series of STO slabs shown in Figures 5.11c-f. Parallel to surface normal, the slabs can be thought of as a set of alternating TiO_2 and SrO layers. In this geometry only along-the-bond Ti-O stretches involving O sites in the SrO layers lead to polarization parallel to the normal while those of O sites in the TiO_2 layers primarily lead to in-plane polarization. Therefore in analyzing the infrared activity of optical modes coupling to p-polarized light we primarily focus on the motions of O sites in the SrO layers. In the energy range $740 - 900 \text{ cm}^{-1}$, the zone-center projected phonon density of states (PDOS) averaged over selected O sites is shown Figure 5.13a for bulk STO and the slabs of Figures 5.11c-f. The corresponding IR absorbance is also shown in Figure 5.13b. Henceforth in discussing the PDOS and IR absorbance we refer to Figure 5.13. The PDOS of bulk STO (Figure 5.13, panel A1) shows peaks spread between $800 - 890 \text{ cm}^{-1}$. The O motions leading to the IR active LO_3 mode discussed earlier (now labeled LO_{bulk}), constitute the PDOS at 854 cm^{-1} while peaks within several tens of wavenumbers on either side correspond to fully or partially breathing modes of the TiO_6 octahedra and are IR inactive. The modes around 800 cm^{-1} constitute opposite phase Ti-O bond stretches in adjacent SrO layers and are also IR inactive. Thus the corresponding IR absorption function shown

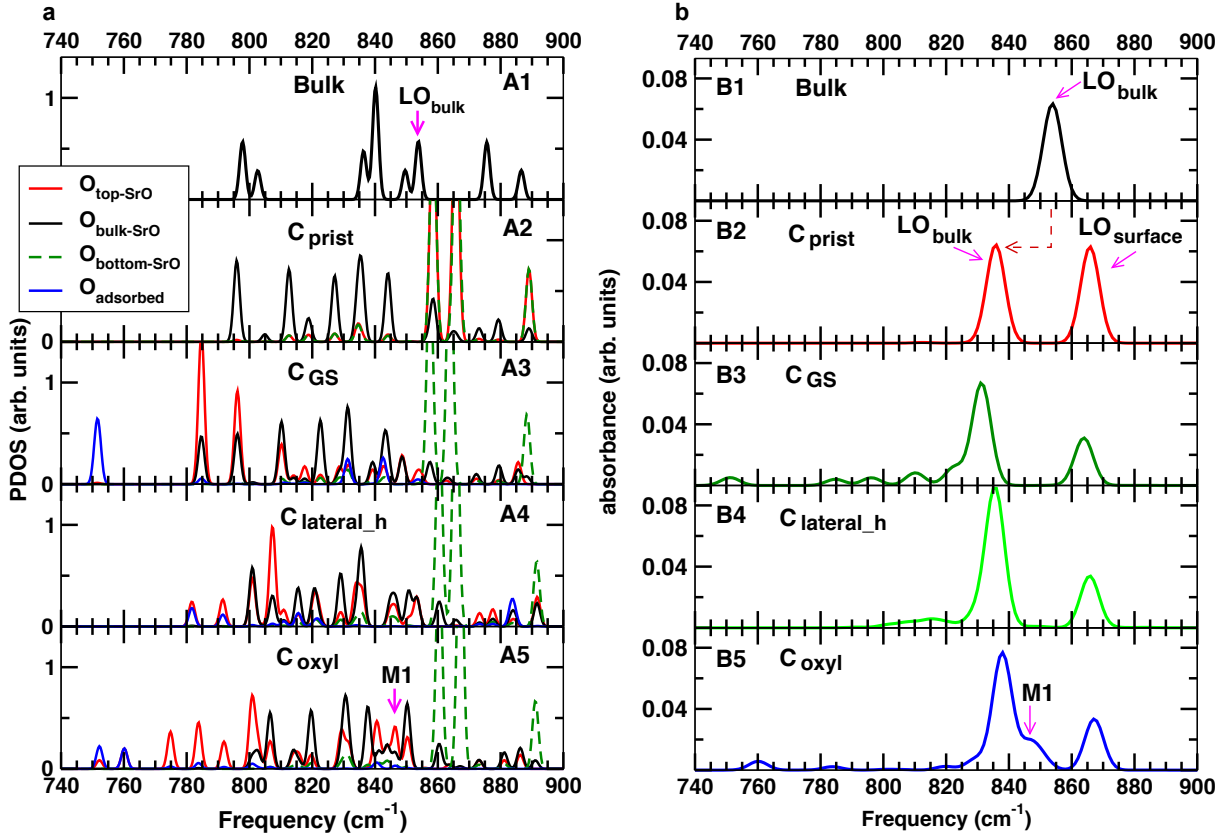


Figure 5.13: Projected densities of states and IR absorbance of slab configurations. **a**, Projected densities of states (PDOS) averaged over selected O sites from the bulk and slab geometries shown in Figure 5.11. O_{top-SrO}, O_{Bulk-SrO}, O_{Bottom-SrO}, O_{adsorbed} represent collective labels for O sites in the top-most SrO layer, middle four SrO layers, bottom SrO layer and surface adsorbed species, respectively. In particular, sites contained within O_{top-SrO} are individually labeled as O'_W, O'_h, O'_X etc. in Figure 5.10. **b**, Calculated IR absorbance corresponding to the configurations represented in **a**.

in Figure 5.13, panel B1 consists of only one feature at 854 cm^{-1} . Next we consider the case where two pristine surfaces are introduced by making an unfunctionalized STO slab (Figure 5.11c). We label this configuration C_{prist} . Structural relaxation at the surface causes a 3.4% shortening of the Ti-O bonds between the surface TiO_2 layer and sub-surface SrO layer while the separation between the top two TiO_2 layers is smaller by 1.2% relative to bulk. Furthermore, in the middle of the slab we find the Ti-O bonds along the normal are 0.5% longer compared to bulk. As a result of these two effects combined with the loss of translational symmetry along the normal direction, we find two IR active features in this case (see Figure 5.13, panel B2). The lower energy feature at 836 cm^{-1} arises from a mode with O motions resembling the LO_{bulk} phonon but with significant amplitude only on the O sites in the middle four SrO layers that constitute the bulk-like region of the slab (see Supplementary Video 1). We will henceforth refer to this mode which is red-shifted by 20 cm^{-1} relative to the LO_3 mode as the bulk LO mode within the slabs. We note that the red-shift is due to the finite size of the slab setup. The feature at 866 cm^{-1} is composed of two individual quasi-degenerate surface modes, each localized at one end of the slab such that the IR activity arises essentially from O motions in the top and bottom sub-surface SrO layers (see Supplementary Video 2). This picture is reflected in the calculated PDOS shown in Figure 5.13, panel A2. The PDOS averaged over the four O sites in the top and bottom SrO layers, which we will refer to as $\text{O}_{\text{top-SrO}}$ and $\text{O}_{\text{bottom-SrO}}$ respectively, are strongly peaked around $859 - 866\text{ cm}^{-1}$ while the PDOS averaged over the O sites in the four middle SrO layers (referred to as $\text{O}_{\text{bulk-SrO}}$) is primarily distributed in the $795 - 845\text{ cm}^{-1}$ range with relatively low weight in the 860 cm^{-1} range. Thus we infer that the bulk and surface LO motions decouple and occur at frequencies separated by $\approx 30\text{ cm}^{-1}$. Having analyzed the pristine surface, we consider the effect of functionalizing the STO surface with a monolayer of water molecules. As shown in Figure 5.11d, we place four water molecules, one per Ti site, on the top TiO_2 layer. During the course of the structural optimization, we find that two of the four water molecules lose a H to a lateral O site on the TiO_2 surface layer and as a result 50% of the Ti sites are decorated by water molecules while the other 50% by OH groups which share a hydrogen bond with a neighboring water. The PDOS and IR absorbance for this configuration, which we label CGS, are depicted in Figure 5.13, panels A3 and B3 respectively. Functionalizing the surface, significantly disrupts the local symmetry and leads to atomic rearrangements in the top layers that resemble rotations of TiO_6 octahedra (see Figure 5.11d). Completing the octahedral coordination structure around Ti sites in the top layer through the adsorbed water or OH groups leads to longer Ti-O bonds to the sub-surface SrO layer and restores the average separation between the top two TiO_2 layers to almost the bulk value. The net result of these perturbations is that the phonon DOS associated with $\text{O}_{\text{top-SrO}}$ is significantly red shifted and primarily peaked between $780 - 800\text{ cm}^{-1}$. In contrast the PDOS associated with $\text{O}_{\text{bottom-SrO}}$ on the unfunctionalized side shows little change and remains in the $855 - 865\text{ cm}^{-1}$ range as in the pristine slab. The PDOS averaged over O sites of the adsorbed water and OH groups, which we designate as $\text{O}_{\text{adsorbed}}$, is primarily peaked around 745 cm^{-1} and lower, although

some hybridization with $O_{\text{top-SrO}}$ and $O_{\text{bulk-SrO}}$ modes around $830 - 840 \text{ cm}^{-1}$ is apparent. From the corresponding IR absorbance we find that the bulk LO mode occurs at 831 cm^{-1} slightly red-shifted by 5 cm^{-1} relative to the pristine slab. Importantly, the intensity of the higher energy IR peak at 864 cm^{-1} is essentially halved relative to the pristine slab as only one mode involving $O_{\text{bottom-SrO}}$ motions now occurs at this frequency. In other words the 866 cm^{-1} IR active mode localized at the top SrO layer in the pristine slab is disrupted by functionalization. Instead, the lower symmetry near the functionalized surface leads to a number of IR active modes in the $780 - 830 \text{ cm}^{-1}$ range. Of these, two weak modes at 785 cm^{-1} and 796 cm^{-1} predominantly involve $O_{\text{top-SrO}}$ motions while the rest are dominated by $O_{\text{bulk-SrO}}$ motions. We now consider a water functionalized slab, introduce hole doping through the "pseudoatom" approach as outlined in the computational details, and re-optimize the cell geometry by introducing a bond distortion in the functionalized top TiO_2 layer so that a hole is trapped at one of the lateral O sites. This configuration which we label $C_{\text{lateral_h}}$, is shown in Figure 5.11e. Trapping of the hole at a lateral O site involves a polaronic distortion where by the O moves slightly out of the TiO_2 plane and has Ti-O bonds with neighboring in-plane Ti sites that are $\approx 6\%$ longer compared to bulk. In the relaxed geometry, we find that one of the water molecules loses an H to another lateral O site so that we have three water and one OH decorating the Ti sites on the top surface. The hole sits on an O site next to the OH adsorbed Ti site. Introducing a localized hole at the surface leads to a screening response within the slab, which in the equilibrium geometry includes an ionic displacement that resembles a frozen bulk LO mode and involves a small concerted shift of the electron rich O sites of the slab towards the top surface resulting in asymmetric Ti-O bond lengths along the z-axis. We find that within each SrO layer, the O-Ti bond to the TiO_2 layer above it is on average shorter by $\approx 2\%$ while that to the one below it is longer by $\approx 2\%$ compared to the configuration with no hole. In particular in the top SrO layer, O-Ti bonds to the surface TiO_2 layer are shorter by $\approx 3\%$. The combined effect of the surface rearrangements and screening response is to blue-shift the $O_{\text{top-SrO}}$ PDOS which is now peaked between $800 - 815 \text{ cm}^{-1}$ and shows increased hybridization with $O_{\text{bulk-SrO}}$ PDOS in the $830 - 855 \text{ cm}^{-1}$ range. Modes between $800 - 810 \text{ cm}^{-1}$ have strong $O_{\text{top-SrO}}$ character but do not show significant IR activity as seen from Figure 5.13, panel B4. Instead, some enhancement of the infrared absorbance around the bulk LO frequency is found due to increased hybridization between $O_{\text{top-SrO}}$ and $O_{\text{bulk-SrO}}$ motions. Thus introducing hole doping at the surface effectively increases the coupling between surface and bulk ionic motions. Finally we investigate the geometry where the hole is now localized on an oxyl moiety forming a charged radical. This configuration, which we label C_{oxyl} can be thought of as being connected to the previous $C_{\text{lateral_h}}$ configuration through a single proton-coupled electron transfer process. The total energy of the oxyl radical configuration is found to be lower by 0.46 eV compared with the hole on the lateral O site. In the equilibrium geometry, there are three water molecules and one oxyl radical decorating the four Ti sites on the top layer and we find that the oxyl radical forms hydrogen bonds with two neighboring water molecules. As in the $C_{\text{lateral_h}}$ case, an ionic screening response extending through the slab is also seen in this

case and O-Ti bond lengths exhibit a similar asymmetry along the z-axis. Additionally however, since the Ti-O bond of the oxyl radical is relatively weak, as evidenced by a bond length of 2.14 Å, the bond between the oxyl Ti site and the sub-surface O underneath (site O'_X in Figure 5.1) is strengthened and exhibits a bond length of 1.86 Å. On the other hand, the $Ti_w - O'_w$ bond (see labeling in Figure 5.1) that was adjacent to the hole in the $C_{lateral_h}$ configuration is now $\approx 1.5\%$ longer as no hole is present next to it. These effects combine to give rise to an interesting bifurcation whereby some portions of the $O_{top-SrO}$ PDOS are red-shifted while others are blue-shifted compared to $C_{lateral_h}$ (see Figure 5.13, panel A5). The red-shifted fraction is spread over $775 - 805 \text{ cm}^{-1}$ while the blue-shifted one is spread over $825 - 855 \text{ cm}^{-1}$. Crucially, the PDOS associated with the O'_X site is sharply peaked in the $840 - 855 \text{ cm}^{-1}$ as shown in Figure 5.10a. From the corresponding IR absorbance (Figure 5.13, panel B5), we see that modes in the $775 - 805 \text{ cm}^{-1}$ range with strong $O_{top-SrO}$ character lead to little new IR activity. In contrast the blue-shifted frequencies give rise to significant absorption at 846 cm^{-1} involving a new mode labeled M1 which has a strong amplitude on $Ti_X - O'_X$ bond stretches (see Supplementary Video 4). By projecting the Eigen function of mode M1 onto a basis composed of the Eigen modes of C_{GS} (see Figure 5.10b), we see that the mode is a superposition of an originally dark breathing mode around 843 cm^{-1} (see Supplementary Video 3) and a number of lower frequency modes involving $O_{top-SrO}$ motions. Importantly the mode M1 derives its IR activity primarily from the motion of O'_X whose vibrational properties are determined through its bond to the oxyl radical. This is one of the key differences with respect to the $C_{lateral_h}$ configuration wherein we find increased IR activity around 835 cm^{-1} from a few predominantly bulk-like modes but those modes with dominant surface $O_{top-SrO}$ character are only weakly IR active. Interestingly, while the sub-surface $Ti - O'_X$ bond reports on the oxyl radical through mode M1, we find only weak IR activity from modes with significant weight on the $Ti - O_X$ bond itself. Motions involving the O_X site are strongly coupled to neighboring adsorbed waters through hydrogen bonds and this hybridization leads to several modes in the $684 - 1142 \text{ cm}^{-1}$ range with some O_X character. Among these, the modes at 1142 cm^{-1} and 752 cm^{-1} have the most O_X PDOS, with the former exhibiting roughly a third of the IR activity of mode M1 while the latter is virtually dark.

Electrolyte Isotope Effect

We investigate the effect of O^{16}/O^{18} isotope substitution within the adsorbed water layer, on the infrared absorbance of the C_{oxyl} slab configuration. To this end we change the masses of the $O_{adsorbed}$ sites while the rest of the atomic masses remain unchanged and recalculate the dynamical matrix, phonon frequencies, Eigen modes and infrared absorption functions. The IR spectra calculated for the O^{16} and O^{18} cases are compared in Figure 5.14. We find very small changes in the frequency and IR intensity of the modes in the $740 - 900 \text{ cm}^{-1}$ range. The mode at 760 cm^{-1} which is primarily derived from motions of $O_{adsorbed}$ is red-shifted by 0.6 cm^{-1} while its intensity is unchanged. The weakly IR active mode at 784 cm^{-1} primarily composed of $O_{top-SrO}$ motions and some

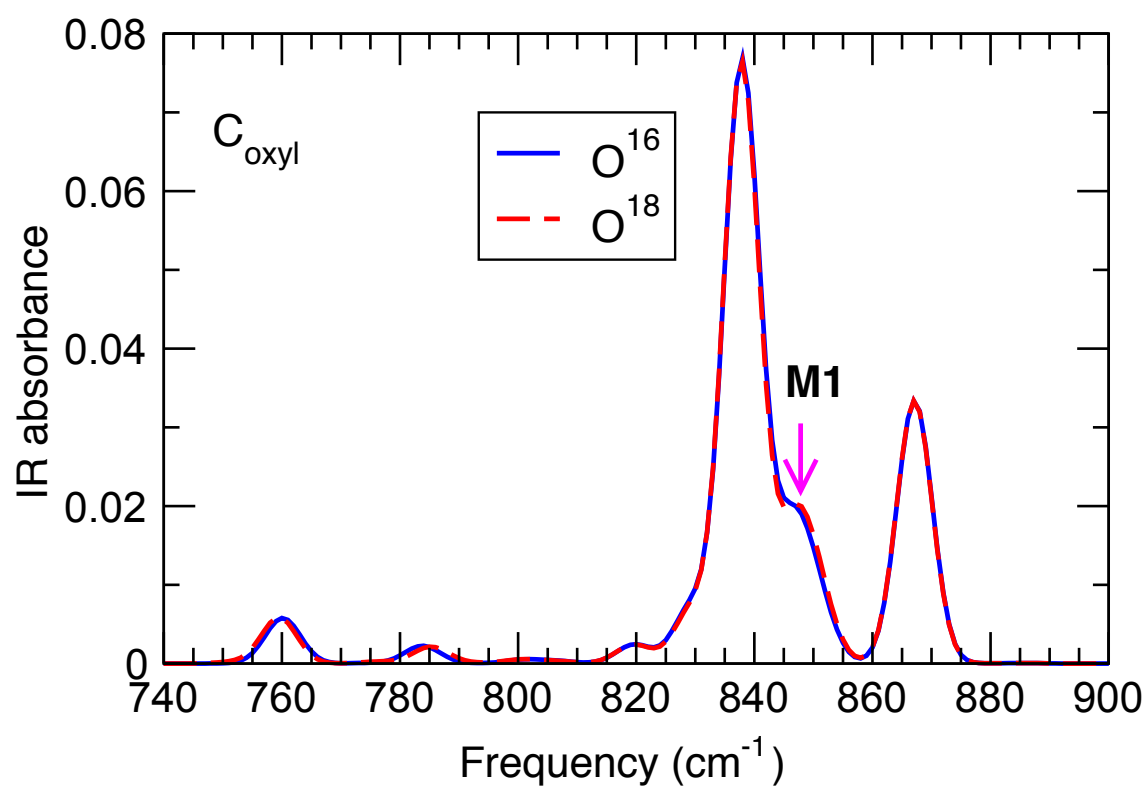


Figure 5.14: Theory Calculations of the Effect of O¹⁶/O¹⁸. Isotope Exchange on IR Absorbance. Calculated IR absorbance for the C_{oxyl} configuration with and without O¹⁸ isotope exchange within the surface adsorbed species.

rocking motion of water molecules blue-shifts by 1 cm^{-1} . The mode M1 is slightly blue-shifted by 0.3 cm^{-1} and its intensity is virtually unchanged. These findings are in line with the experimental observation that $\text{O}^{16}/\text{O}^{18}$ isotope substitution has little effect on the mode near 795 cm^{-1} .

Origin of Hole Related IR Activity

We identify two mechanisms that lead to higher infrared activity in the hole doped slab calculations: the first is a long range screening effect in the solid and the second is a new molecular mode at the surface. The former is related to the ionic screening response of the slab composed primarily of a displacement of the O sub-lattice towards the hole doped surface layer leading to asymmetric Ti-O bond lengths on either side of the SrO layers within the slab. This manifests in the IR absorbance as both a small frequency blue-shift and an intensity enhancement of the bulk LO mode (see Figure 5.10b and Figure 5.13 B3, B4) relative to the undoped case. This picture is similar for both lateral hole trapping and the oxyl radical at the surface. However detecting this change requires sensitivity to the bulk LO mode statically; the static ATR measurement only sees the surface polariton (see Figure 5.4) and therefore we do not expect the transient enhancement to be detectable. More generally, we expect the magnitude of the screening response to scale with the hole density at the surface and therefore that both the frequency and the IR activity of this mode will increase with hole density. Referring to Figure 5.5, experimentally we find that the mode frequency is exactly the same for fluences between $20 - 200\text{ }\mu\text{J}/\text{cm}^2$, which increases the surface hole density by an order of magnitude. Finally, we expect this screening response to last as long as there is surface charge, somewhat independent of the exact intermediate that traps it. Experimentally, we find that the infrared signature of surface hole capture disappears with % methanol concentration. With 100% methanol, it fully disappears for the entire time window when surface charge is still expected. All of the above exclude an increased amplitude of the bulk LO mode near the surface from being assigned to the transient infrared activity seen. In the case of the oxyl radical, we find a truly molecular effect, namely the weakening of the Ti-O bond of the oxyl and the concomitant strengthening of the bond to the sub-surface O below it which leads to a new mode with strong IR activity. This mode, M1, has a large amplitude on the sub-surface O below the oxyl and derives its IR activity primarily from this motion although it exhibits hybridization with an IR inactive bulk breathing mode. This motion is specific to the oxyl, in contrast to other modifications of the IR activity theoretically found at lower frequencies in the range of $740 - 800\text{ cm}^{-1}$. Modes at $740 - 760\text{ cm}^{-1}$ are related to motions of the adsorbed water oxygens and the modes in the $770 - 800\text{ cm}^{-1}$ range are related to sub-surface O motions. All of them are sensitive to the distribution of the adsorbed molecular species rather than specific to the oxyl, since their IR activity derives from all the oxygens in a given layer (either the adsorbed or sub-surface O). These modes are not observed experimentally likely because their IR activity is relatively weak. Further, since they involve the adsorbed oxygen, the strongest of them (between $740 - 760\text{ cm}^{-1}$)

likely decay quickly into the librational motion of the electrolyte. Interestingly, hydrogen bonding in the water layer at the surface prevents the appearance of any IR active mode with a clear Ti-O beating motion of the oxyl radical even in these calculations that have a single absorbed water layer. This means that at the solid-liquid interface, the distinctive molecular and infrared signature of the oxyl radical is the motion of the sub-surface O site right below it.

5.4 Discussion

Together, experiment and theory molecularly detect the transformation of charge into a $\text{Ti} - \text{O}^\bullet$ oxyl radical through a well-defined sub-surface vibration of the O directly below it. The oxyl radical is formed within picoseconds, i.e. at the point of charge transfer, and remains present for at least nanosecond time scales. This means changes in this sub-surface vibration over time can be used to track the formation of later time scale intermediates of the water oxidation cycle at a transition metal oxide surface. While some of the molecular intermediates of the cycle can be followed by the new bonds that are created on the surface, as done in other laboratories, the de-coupling of the sub-surface vibration from the lattice could be the distinctive vibrational mode of the transformation of charge into a catalytic intermediate prior to bond formation, not only for the oxyl radical, but more generally. The vibration of the adsorbed atom involved in creating the new bond is likely well-hybridized with reactants, as is the case for the $\text{Ti} - \text{O}_x$ beating mode. While the sub-surface vibration has the integrity of a spectrally defined mode, I have discovered that it still couples the oxyl radical to its immediate surroundings. Both the coupling strength (Γ) and the involvement of the continuum excitations (q), through Fano line shapes, describe how the sub-surface vibration couples to solvent and electron dynamics. This coupling opens up opportunities for tracking and influencing the dynamics of the reaction pathway directly through the local electrolyte environment and the electronic plasma density in the solid. In particular, coupling of the vibrations of the oxyl radical to different local electrolyte environments could strongly alter the dynamics of how it transforms into the O-O bond. Broadly speaking, the methods shown here to study nascent catalytic intermediates and how they interact with the solid-liquid interface open up a new field of investigating catalytic dynamics from the point of charge transfer and then successively through the molecular intermediates of the cycle.

5.5 Sample Characterization

Samples

0.7%, 0.5%, 0.08% and 0.05% Nb-doped SrTiO_3 by weight (henceforth 0.08% is referred to as 0.1%), as well as undoped and 0.01% Fe-doped SrTiO_3 single crystals with crystallographic orientation (100) were obtained from MTI Corp. (Richmond, CA). The

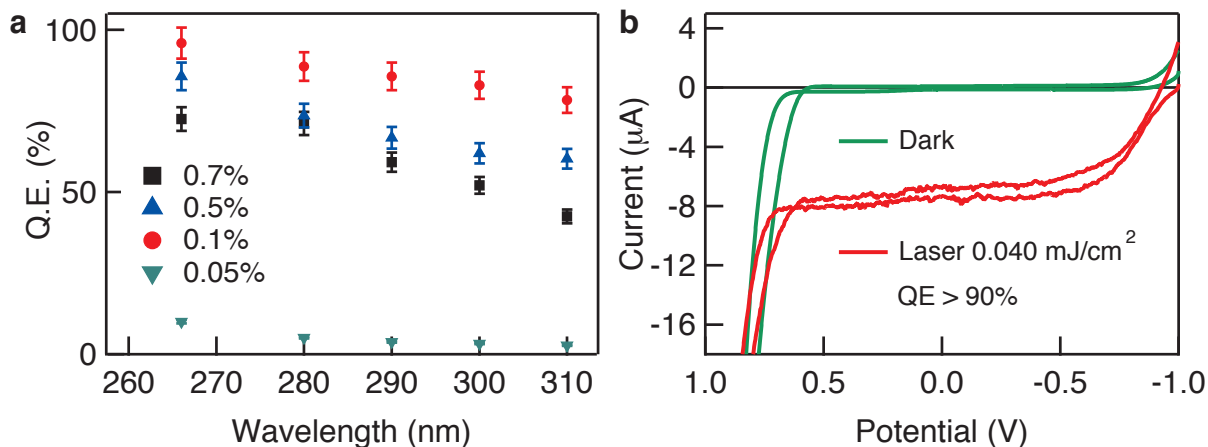


Figure 5.15: SrTiO₃ quantum efficiency is high even under pulsed laser irradiation. **a**, The absorbed-photon-to-photocurrent quantum efficiency (Q.E.) for a variously Nb doped SrTiO₃ sample illuminated by the monochromatized output of a Xenon lamp. **b**, Cyclic voltammetry (CV) of the 0.1% Nb doped SrTiO₃ sample in the dark and illuminated by 266 nm, 500 Hz, 150 fs pulsed laser excitation.

crystals were 0.5 mm thick with polished front sides ($R_a < 5 \text{ \AA}$) and unpolished back sides. All spectroscopic measurements were performed on the polished front sides.

Reflectivity Measurements

Static infrared spectra of the samples were measured by specular reflectance (45° incident angle) and attenuated total internal reflection (40° incident angle) using a Fourier transform IR spectrometer (Bruker Vertex 70v). For static specular reflectance measurements a protected gold mirror was used as reference. For static ATR measurements the internal reflection in air (i.e. without a sample present) was used as a reference. The spectra were taken in the mid-IR region of $400 - 1000 \text{ cm}^{-1}$. A DTGS detector and KBr beam splitter were used within the spectrometer. A KRS5 wire-grid polarizer placed across the IR beam path selected the incident light polarization. External reflection spectra (unpolarized) of doped and undoped SrTiO₃ are shown in Figure 5.4a. The results are consistent with those previously reported in the literature for both undoped and doped SrTiO₃.

Quantum Efficiency of Photocatalytic Oxygen Evolution

The quantum efficiency reported is the absorbed-photon-to-photocurrent quantum efficiency. This is the ratio of the number of electrons generated as a photocurrent to the number of incident photons (correcting for sample reflectivity, 27% at 266 nm). Only sufficiently doped n-SrTiO₃ samples show a high Q.E. under steady-state illumination

(Figure 5.15a), specifically 0.1% Nb doped (Q.E. > 90%), 0.5% Nb doped (Q.E. > 80%) and 0.7% Nb doped (Q.E. > 70%) samples. The Q.E. measurements were performed in a home-built Teflon electrochemical cell with CaF_2 optical windows. The electrolyte is a 1M aqueous solution of sodium hydroxide. A potentiostat (CH Instruments 1140B) controlled the applied bias and measured the current in a three-electrode setup, with the n-SrTiO₃ sample as the working electrode, a platinum wire as the counter electrode and a 3M Ag/AgCl electrode as the reference electrode. The potential was held at 0V vs Ag/AgCl and the sample was illuminated with the monochromatized output of a Xe lamp (Newport Model 67005) from 310 nm to 266 nm. Samples with lower n-doping (e.g. 0.05% Nb) show significantly lower Q.E. ($\approx 10\%$), and also showed a smaller photoinduced absorption relative to the sample with high Q.E.. The undoped and p-doped (0.01% Fe) samples showed no measurable photocurrent (Q.E. < 1%), and no photoinduced absorption. The 0.1% Nb doped sample was also characterized using cyclic voltammetry (CV), where the potential was swept from -1.0V to +1.0V and back, and the resulting current is recorded. The CV was performed under the same laser illumination as in the transient infrared experiments (266 nm, 500 Hz repetition rate, 150 fs pulse length) as well as in the dark. The CV sampling rate was slower (10 Hz) than the laser frequency, so the current recorded under laser irradiation corresponds to the average photocurrent over many laser shots. The sample still exhibits a high Q.E. under pulsed 266 nm laser excitation, > 90%. Here, the laser power was attenuated to 50 μW , corresponding to an energy density (fluence) of 40 $\mu\text{J}/\text{cm}^2$ per pulse or a surface excitation density of 5%. The surface excitation (%) is calculated by dividing the photon density by the surface site density. Using a lattice constant of 3.905 Å, the surface site density is calculated to be 6.56×10^{14} sites/ cm^2 . A CV of the sample mounted in the experimental configuration but pulled back from the diamond crystal was performed with platinum counter and 3M Ag/AgCl reference electrodes (Figure 5.15a). The CV was performed in the dark and under laser illumination equivalent to 5% surface excitation. The illuminated sample generates a consistent photocurrent from -0.85V to 0.6V (vs. Ag/AgCl). Below the onset potential the applied bias flattens the built-in band bending, preventing the electron-hole separation required to drive water oxidation. Here the $\approx 50 \mu\text{W}$ of pulsed laser illumination gives rise to a $8 \approx \mu\text{A}$ photocurrent, which after accounting for 28% sample reflectivity at 266 nm corresponds to an absorbed-photon-to-current quantum efficiency of 100%. The expected Q.E. for this system under steady-state illumination is 80-100%.

Quantum Yield of Photocatalytic Oxygen Evolution

The high quantum efficiency of n-SrTiO₃ indicates that nearly all absorbed photons contribute to sustained photochemistry. To confirm that all of the measured photocurrent corresponds to the oxygen evolution reaction of interest the quantity of O₂ evolved by the sample must be compared to that expected based on the photocurrent. A 5 x 5 mm sample of 0.1% Nb-doped SrTiO₃ was enclosed in a two-electrode spectroelectrochemical cell with Pt wire counter electrode and 1.0M NaOH electrolyte. The polished side of the sam-

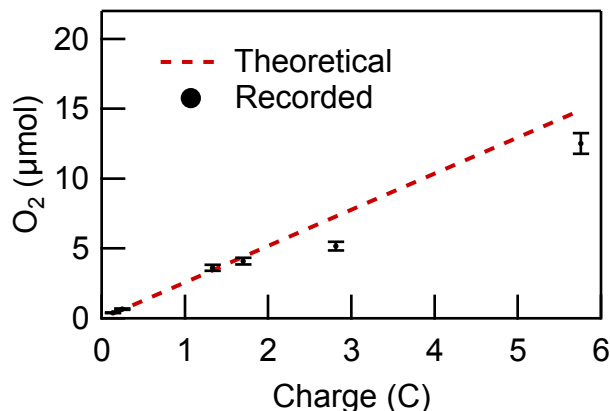


Figure 5.16: Direct Observation of O_2 Evolution. The theoretical (100% Faradaic efficiency) and observed oxygen evolution at the $SrTiO_3$ single crystal are nearly identical. Deviation in longer experiments is attributed to O_2 leaks into the oxygen-free environment.

ple was irradiated with UV light from a 300W Xe lamp with IR-cut filter. A potentiostat was used to measure the charge passed, and an electrochemical O_2 gas sensor (RapidOx 1100L, Cambridge Sensotec, Cambridge, UK) with built in circulation pump and temperature/pressure correction capability recorded the partial pressure of molecular oxygen with ppb resolution. After correcting for oxygen dissolved in the electrolyte (10 mL) the partial pressure was converted to moles using the ideal gas law (144 mL headspace, 1.05 atm, 298K). The entire experiment was performed in a pressure-controlled dry-nitrogen glove box ($O_2 < 1$ ppb). Figure 5.16 shows the theoretical and measured quantity of O_2 as a function of passed charge. The slight deviation from 100% Faradaic efficiency in the longest experiments (17 hours, 5.8 C) is attributed to loss of O_2 due to leakage into the oxygen-free glove box.

5.6 Acknowledgements

Dr. Tanja Cuk conceived the project and wrote the manuscript with input from all authors. David M. Herlihy and Dr. Matthias M. Waegle constructed the transient setup, collected transient data and prepared samples. Xihan Chen collected and analyzed the static reflectance measurements and characterized sample quantum efficiency. Dr. Tanja Cuk and David M. Herlihy analyzed the transient data. Dr. Sri Das Pemmaraju and Dr. David Prendergast were responsible for the theoretical calculations.

This material is based upon work supported by the Air Force Office of Scientific Research under AFOSR Award No. FA9550-12-1-0337, which supplied the 64-element infrared array detector and partially supported a postdoctoral fellow, and by the Department of Energy Office of Basic Energy Sciences, under the CPIMS program KC030102

(FWP No. CH12CUK1), which supported two graduate students. The theory work of C.D.P. and D.P. was supported through a User Project at The Molecular Foundry (TMF), LBNL with calculations performed on its computing resources, Nano and Vulcan, managed by the High Performance Computing Services Group of LBNL, and on the Cray XE6 Hopper computer at the National Energy Research Scientific Computing Center (NERSC), LBNL. Both TMF and NERSC are DOE Office of Science User Facilities supported by the Office of Science of the US Department of Energy under Contract No. DE-AC02-05CH11231.

Chapter 6

Surface State Dynamics at the Aqueous Electrolyte / Strontium Titanate Interface

6.1 Introduction

Holes at the surface localize in a number of surface states, including a terminal-oxygen (oxyl) radical. Experimental evidence discussed in the preceding chapters indicates a number of signatures that evolve at unique timescales. The 800 nm signal rises within the instrument response function (150 – 300 fs) and evolves to reveal both an absorption and a bleach feature, each at different timescales and with independent responses to applied bias. As examined later in this chapter the bleach feature is minimized without photo-electrochemical surface roughening, while the absorption remains present regardless of surface treatment. The 795 cm^{-1} absorption identified as the terminal oxyl radical appears over a slower (picoseconds) relative window and decays with a time constant well beyond the 1.6 ns window regardless of surface treatment. The lineshape of the oxyl radical signature likewise evolves over the initial appearance of the oscillator strength. Together, the variety of characteristics and time constants suggest a multifaceted reaction surface involving a number of dynamically involved states.

Although more work remains to be done, a preliminary understanding of the dynamic surface states has emerged, and is examined here. The dynamics of the oxyl radical are revealed through analysis of the 795 cm^{-1} signature’s line-shape evolution in different environments. The dynamics of the voltage dependent states are examined through their electronic transitions at 800 nm and through modulation of the experiment probe polarization, electrolyte pH, excitation fluence, surface roughening, electrolyte H-D exchange, and applied bias.

Taken together the ultrafast dynamics here paint a picture of a multi-state surface with holes present as a minimum of three distinct states (the valence band edge, the 800 nm absorption; lateral oxygen radical, the 800 nm negative absorption; and the terminal oxyl radical, observed at 795 cm^{-1}). The dynamics of the identified states suggest a reaction pathway involving a steady-state population of quickly formed and easily de-trapped surface oxyl radicals interacting with other surface radicals whose formation is applied-bias dependent. The overall population of holes is significant at the valence band edge which maintains the steady-state population of oxyl radicals. These steps precede the O-O bond formation seen at longer timescales which is thought to be rate limiting and bias independent, in keeping with the bias independence shown previously for the overall four hole-transfer reaction. The decay of the 800 nm absorption (VBE holes) and appearance of the polarized bleach species then primarily reports on the species (lateral oxygen radical) whose rate of production is kinetically slower than the oxyl radical, but subsequently reacts to form the first reactant O-O bond. As previously suggested by Frei and coworker [43] regarding the reaction following oxyl-radical formation on titanium dioxide: “the subsequent slow process might be the formation of a $\text{TiO}(\text{h}+)\text{Ti}$ site” i.e. a multiply-bound oxygen atom at a defect site.

6.2 Results

6.2.1 Polarization Dependence

Previously, the oxyl radical signature at 795 cm^{-1} was shown to be entirely oriented perpendicular to the sample plane. This helped identify the interfacial origin of the signal, as well as inform on molecular characteristics of its origin. To follow up on those experiments, the spectroscopic signature at 800 nm identified in Chapter 4 was investigated by varying the polarization of the pump and probe light. The results, found in Figure 6.1, show the observed signal is pump-polarization independent, but probe polarization dependent. The independence from pump-polarization is consistent with the understanding that excitation occurs to well beyond the conduction/valence band edge and the excited electron and hole populations thermalize into band-edge states after thermalizing with the lattice. Instead, the probe polarization dependence arises from the character of the observed transition involving the surface-states that are occupied after thermalization to the band-edge. At all applied biases and open circuit the signal rise-time is in the range of $150 - 300\text{ fs}$. At more negative applied bias and open circuit the lifetime extends 3 ns , qualitatively similar to the results found in Chapter 4. At more positive applied biases the absorption feature decays and a bleach feature appears. The bleach component shows a significant polarization dependence. In the experimental geometry used here (identical to that of Chapter 4) and assuming an electronic transition is being probed based on the wavelength used, a transition with a dipole perpendicular to the surface would interact only with a P-polarized light wave. In contrast, a dipole oriented within the plane of the sample surface would appear in both S and P polarized probes, but with twice the amplitude in S than in P. An isotropic signal would appear in both polarizations with equal weight.

Given that all biases and all polarizations find an identical rise time to an absorption feature of similar amplitude, I hypothesize that the initial absorption component derives from holes thermalized at the band edge that are generated regardless of applied bias and whose intra-band absorptions should be isotropic. Even at open circuit, this valence band hole population is expected to decay due to recombination, trapping and interfacial charge transfer. In fact, at open circuit the signal does decay slightly, and with the extremely long time constant expected of a photocatalyst such as SrTiO_3 with such a high quantum efficiency. At positive applied biases a new surface state is generated, here identified by its associated bleach of (or stimulated emission corresponding to) an in-plane transition. As discussed in Chapter 5, for an isotropic material such as strontium titanate in contact with a disordered liquid, a polarization sensitive signature can only arise from the interface. The lifetimes of each of the two components are obscured by the dynamics of the other state.

In Figure 6.1d I present linear combinations of the collected data to visualize the unpolarized and in-plane modes without the other component. The linear combination 2P-S corresponds to an unpolarized transition without any contribution from the uniquely

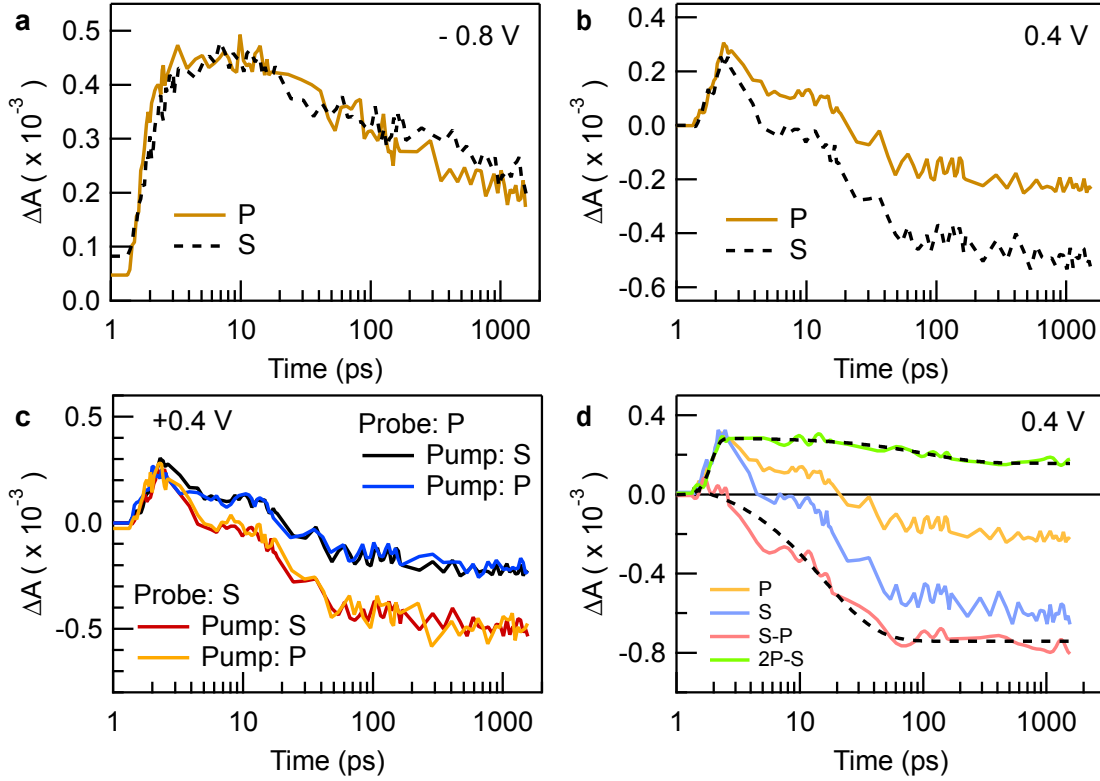


Figure 6.1: Time traces of the transient 800 nm signal from a reflection experiment similar to the one described in Chapter 4. The polarization dependence at **a** an applied bias of -0.8 V and **b** +0.4 V indicate the positive absorption component is unpolarized but the bias-dependent negative absorption has in-plane character. By changing the pump polarization **c** polarization anisotropy can be ruled out, indicating the polarization arises from separate components with different selection rules. **d** A linear combination of each polarization signal reveals the dynamics of the unpolarized component (green, 2P-S) and the in-plane component (Red, S-P). The experiments were conducted in 0.1 M NaOH electrolyte on a 0.1% Nb doped SrTiO₃ sample.

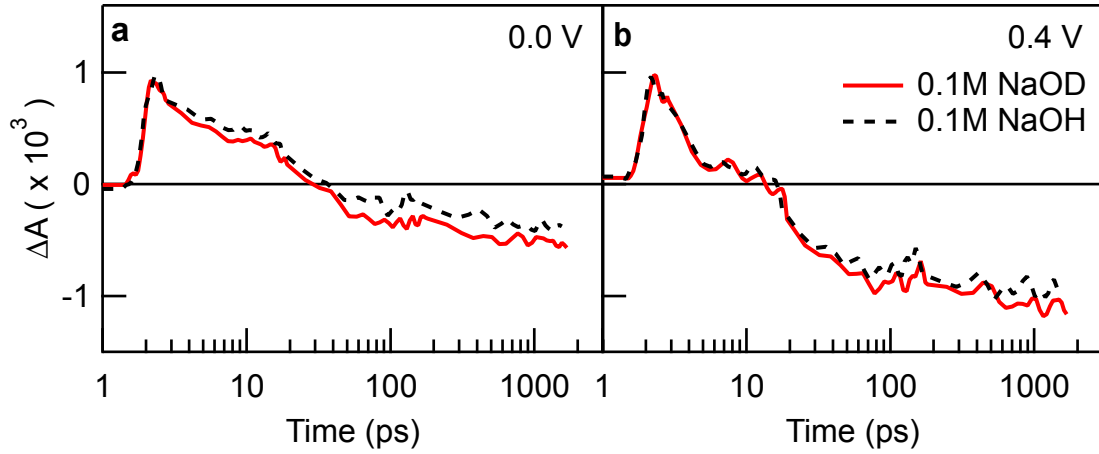


Figure 6.2: The effect of electrolyte isotope exchange on the dynamics of the 800 nm signal. Traces corresponding to the deuterated (red, solid) and hydrogenated (black, dashed) conditions are shown at an applied bias of **a** 0.0 V and **b** 0.4 V. The results are identical for both cases, indicating neither the positive nor the negative absorption components have any isotope effects. The experiment was conducted in 0.1 M NaOH(D) in (99.9% deuterated) water on a 0.1% Nb doped SrTiO₃ sample.

in-plane mode. The linear combination S-P corresponds to the in-plane transition with any unpolarized signal contribution subtracted out. Within this model-dependent presentation, the data reveals the valence band hole lifetime is multi-exponential, with one lifetime of 102 ps and one well beyond the 1.5 ns observation window of the experiment. Consistent with transient photocurrent measurements previously completed on titanium dioxide [68], catalytically active surface states can be expected to have occupancy lifetimes even beyond the millisecond regime. The bleach-like component (S-P) shows an exponential rise with a time constant of 15 ps and a voltage-dependent magnitude.

6.2.2 H-D Electrolyte Exchange

The dynamics revealed in Section 6.2.1 have time constants ranging from 15 ps to 102 ps and beyond the nanosecond window of the optical delay stage. I find it worthwhile to attempt an understanding of the interplay between the solvent dynamics and the charge dynamics as the two meet at the interface. To interrogate this interplay, the aqueous electrolyte was prepared in both deuterated form and both the near- and far-infrared experiments were repeated. The results for the near-infrared transition are shown at representative potentials in Figure 6.2a and Figure 6.2b. It is apparent that neither the absorption dynamics nor the bleach-like dynamics are affected by the deuteration of the solvent. Given the significant difference between vibrational and rotational anisotropy lifetimes of the two isotopes of water, the dynamics of both the surface state and the

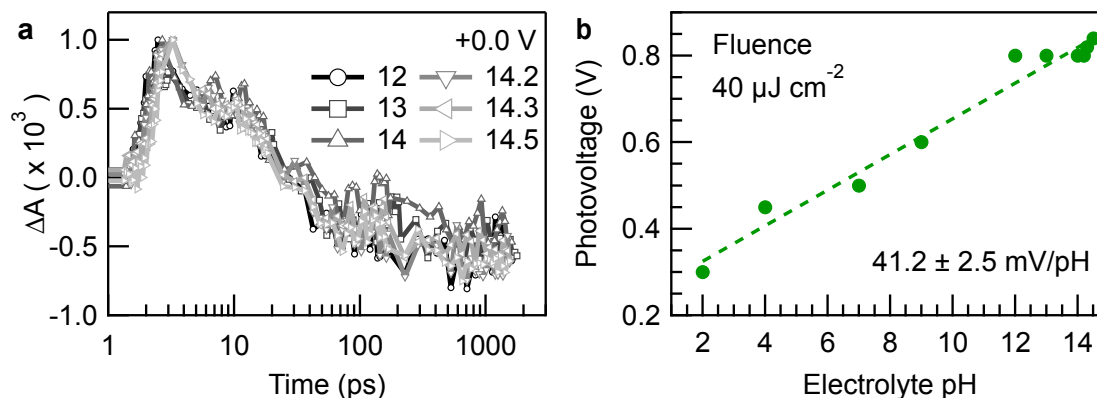


Figure 6.3: The effect of electrolyte pH on **a** the dynamics of the 800 nm signal and **b** the open circuit photovoltage. The pH range investigated was limited by stability of the sample cell materials. The results indicate the reaction rate is zero order with respect to hydroxide concentration. This could be due the rate-limiting low density of reactive defect sites. Both experiments were conducted on a 0.1% Nb SrTiO₃ sample.

valence-band edge carriers are not limited by the solvent dynamics. Shown in Figure 6.2c, repetition of these experiments across the full accessible range of applied potentials revealed no change in the magnitude or dynamics of the positive and negative absorption components. The lack of a kinetic isotope effect imply both these species are not involved in a rate-determining proton transfer step [160, 161, 162].

As a secondary probe of the role of protons at the surface on the species evolution as well as for the sake of completeness, the electrolyte pH was varied by the addition of sodium hydroxide and the reflection experiments were repeated. The results are shown in Figure 6.3a, and reveal that both the free-carrier and lateral-hole signals' decay rate are zero-order in hydroxide concentration in a range of pH 12 – 14.5. This is within the range of values expected for surface hydroxide de-protonation. Meanwhile the photo-voltage increases at 59 mV/pH as expected. It should be pointed out that work by Fayer [163] found that the behavior of water at an interface was not affected by the polar, non-polar, or formally charged nature of nearby interfaces, so the changing charge of the surface at different pH values would not have been expected to change solvent dynamics appreciably.

Time resolved studies of the oxyl radical evolution are presented as spectra at regular time intervals (in H₂O: Figure 6.4a, in D₂O: Figure 6.4b) and as time-traces of each fitting parameter of the Fano line shape. The oscillator evolution as well as the contributions of the coupled and uncoupled continua and the line-width for the oxyl radical are all completely independent of solvent H-D exchange. The only affected parameters are the central frequency (shifted by 5 cm^{-1} with a resolution of 0.88 cm^{-1} achieved from averaging) and the asymmetry factor, as expected and discussed previously in Chapter 5. The oxyl radical therefore interacts with the solvent librational modes on the liquid side of the

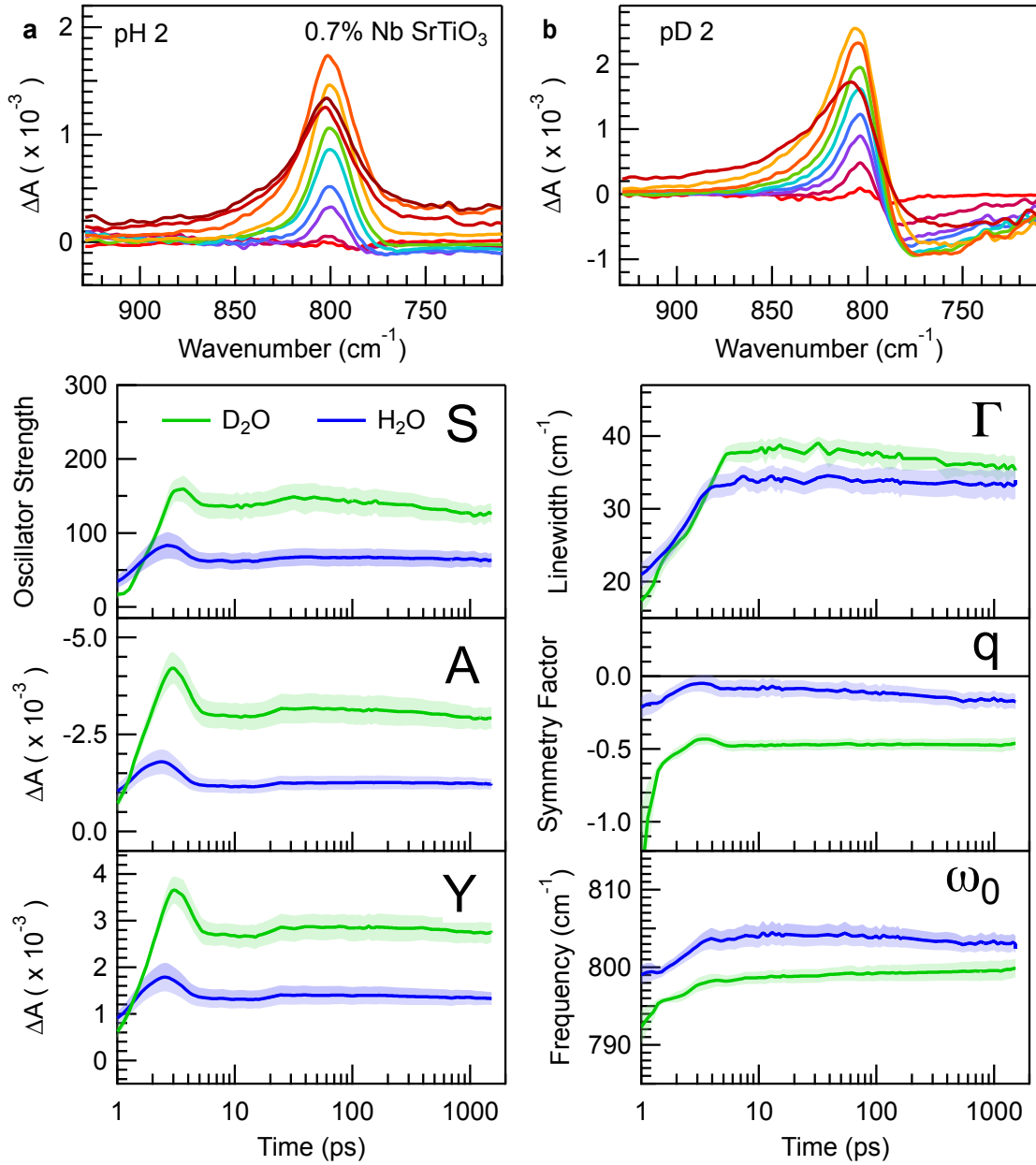


Figure 6.4: The spectrum of the oxyl radical sub-surface vibration is shown for representative time points (-1.0, -0.5, 0, 0.5, 1.0, 4.0, 8.0, 12 and 1500 ps) in **a** hydrogenated and **b** deuterated electrolyte. The data were collected in 150 fs resolution at early timescales and in larger increments at longer time scales. Every spectrum was fit with a Fano equation and the parameter evolutions plotted as traces. As discussed in extensively in Chapter 5 the Fano parameters represent **S**: Oscillator strength, **A**: Coupled-Continua, **Y**: Uncoupled-Continua, **Γ** : Line-Width (Coupling Strength), **q**: asymmetry factor, and **ω_0** : The coupled-mode frequency. Error bars show standard error from 3-5 trials. The data was collected using a 0.7% Nb doped SrTiO₃ sample in pH(D) 2 (deuterated) electrolyte.

interface, but the species formation and reaction rates, like those of the valence band holes and lateral oxygen radical, are not affected by solvent dynamics. Since the theoretical calculations addressed in Section 5.3.3 of Chapter 5 suggest that formation of the oxyl radical requires proton transfer from the terminal to lateral oxygen sites this result may be surprising. However, the mechanism of the underlying proton-coupled electron transfer, and whether it is sequential or concerted, is not resolved by the DFT calculations. These results would suggest the transfer is sequential rather than concerted [160, 161, 162], and the proton-transfer step is not rate limiting.

6.2.3 Fluence and Roughening

Traces taken at a range of excitation fluences (i.e. hole concentrations) were performed at open circuit. The traces and fits are shown for a sample measured immediately after delivery from the manufacturer (a “pristine” sample) and after 30 minutes of sustained photoelectrochemical water oxidation under steady state illumination by a xenon lamp (a “roughened” sample) in Figure 6.5a and Figure 6.5b, respectively. Figure 6.5c shows the signal magnitude grows linearly with excitation fluence (hole density) for both samples. However, the rate of decay (Figure 6.5d) is fluence independent for the photoelectrochemically roughened sample and the pristine sample at higher fluences. This reveals a rate-equation that is zero-order with respect to holes, consistent with a saturated surface even at the lowest fluences (5% surface sites). Given the low excitation density, this suggests defect-site driven kinetics. Since the pristine sample lifetimes reverted to the same lifetime as the “roughened” sample at sufficient light intensity, it seems likely that illumination of the sample surface can introduce these defects. Careful inspection of the open circuit lifetimes in Figure 6.5d reveal that the “pristine” samples indeed show a longer lifetime (slower kinetics) and higher signal amplitude, both consistent with increased reactive site density. At fluences below $200 \frac{\text{mJ}}{\text{cm}^2}$ (25% surface excitation) the lifetime before surface roughening is extended from c.a. 1 – 3 ns to 5 – 10 ns.

At various closed-circuit conditions the observed kinetics are also found to be independent of excitation fluence. Repeating experiments across the full range of potentials found in Chapter 4 with a “pristine” sample shows a longer lifetime (i.e. slower dynamics) at all potentials for the same fluence. This results in a transfer coefficient value of 0.11 ± 0.05 rather than 0.25 ± 0.05 , consistent within fitting error across all measured fluences. This insensitivity matches the observations taken at open circuit. These closed circuit results are also explained by a rate limiting surface site density. Figure 6.6 shows that the $\log(k)$ slopes are identical with respect to potential for three fluences: 50, 100, and $150 \mu\text{J}/\text{cm}^2$. This is remarkable not least because the potential drop over the Helmholtz layer should be dependent on the excitation fluence. While this could suggest the transfer coefficient is insensitive to excitation fluence, an alternative explanation, consistent with the full data set, is that the observed rate is limited by the surface site density. Since both bleach and absorption components are unaffected by fluence, the defect site must also mediate the formation of the state giving rise to the bleach-like component. The order of the rate

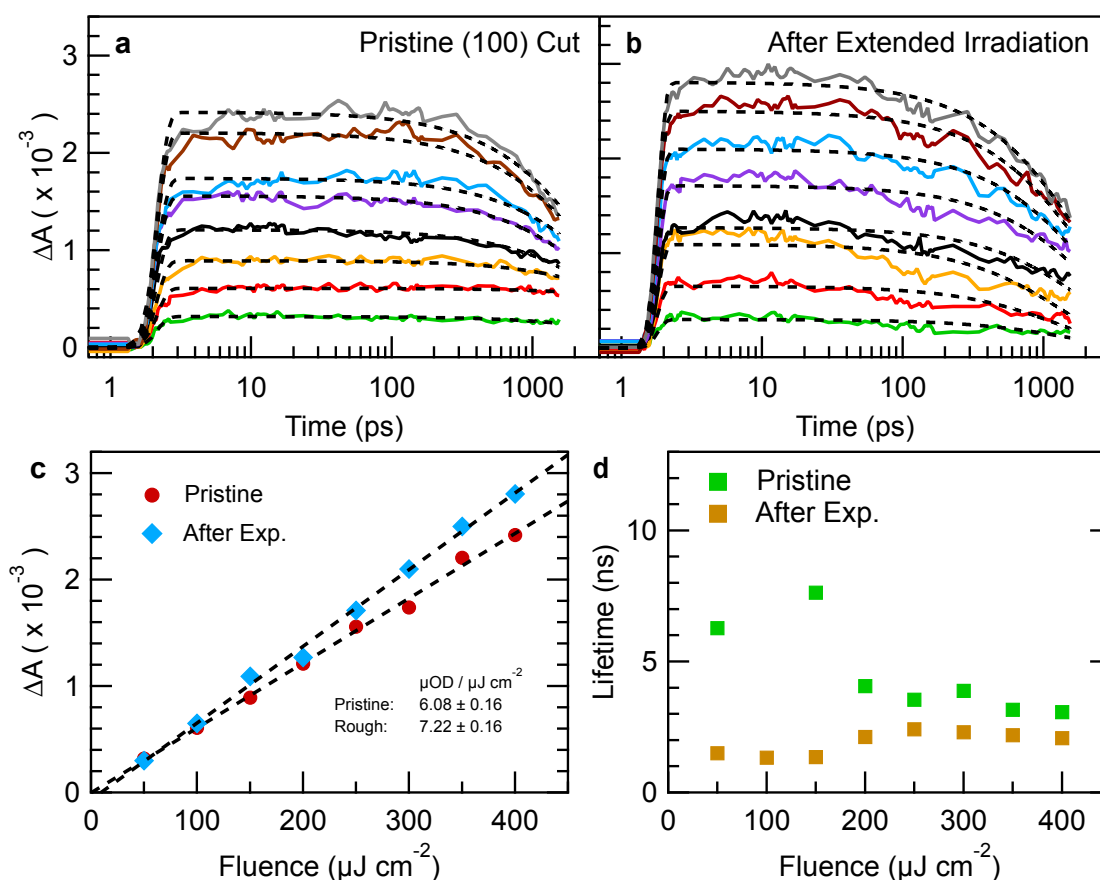


Figure 6.5: The effect of increased hole concentration on the dynamics of the 800 nm signal. The experimental traces are shown for **a** an “as-delivered” sample not previously exposed to electrolyte or photo-irradiation under closed circuit conditions and **b** the same sample after extended irradiation under photocatalytic conditions. The signal amplitude, **c**, is linear for both samples but larger for the electrochemically “roughened” sample. The transient absorption lifetimes, **d**, reveal a zero-order dependence of the decay rate with respect to hole concentration. The data were collected at open circuit on a 0.1% Nb doped SrTiO_3 sample in 0.1M NaOH electrolyte.

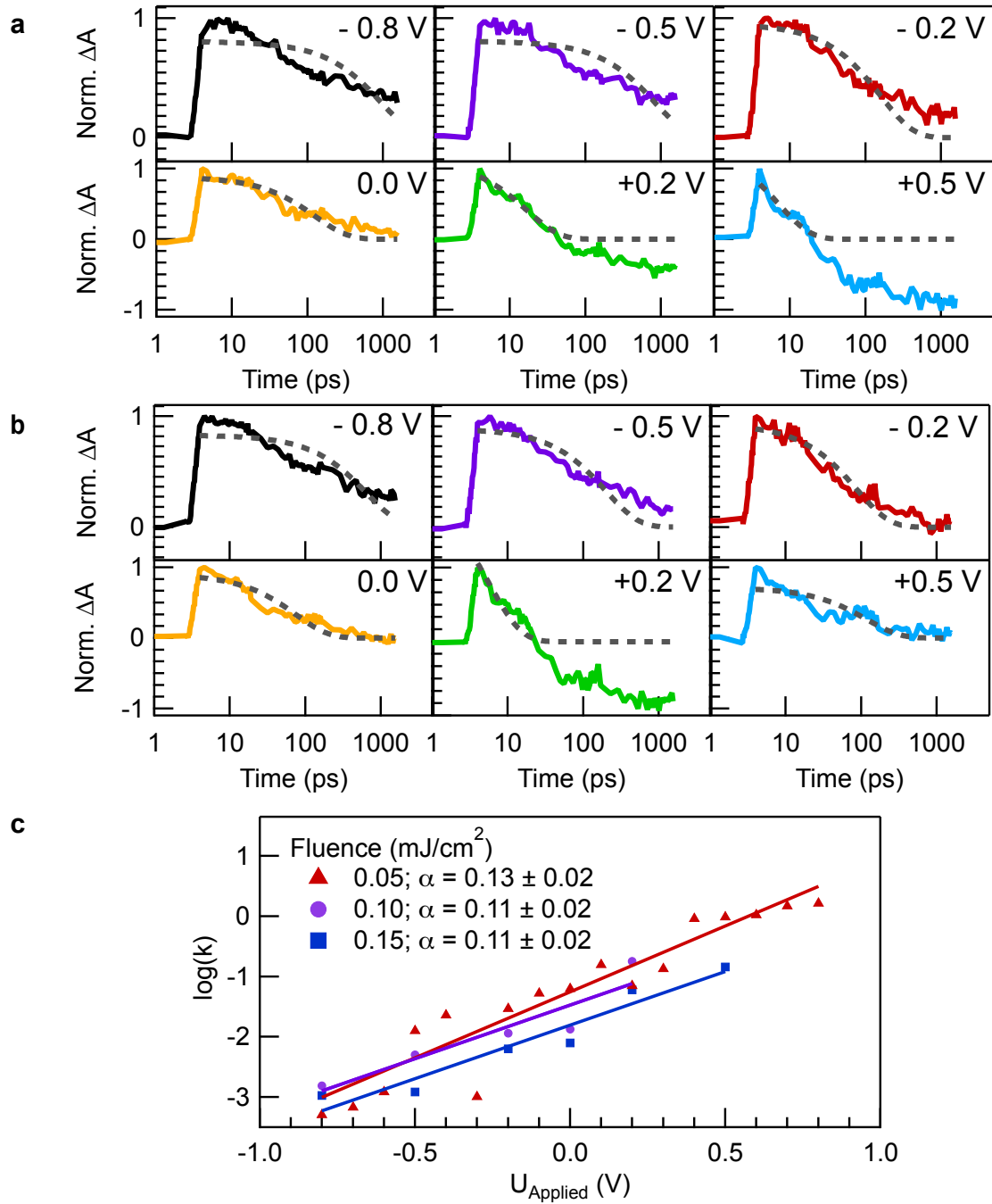


Figure 6.6: The experiments of Chapter 4 were repeated on a pristine sample with increased photoexcited hole concentrations. The experiments were conducted at closed circuit conditions across a range of applied biases. Representative fits, using the published methodology, to data at excitation power densities of **a** $150 \mu\text{J}/\text{cm}^2$ and **b** $100 \mu\text{J}/\text{cm}^2$ are presented. **c** The $\log(k)$ vs. applied bias plot reveals identical bias-dependence at all three fluences. The experiments were conducted on 0.1% Nb doped SrTiO_3 samples as received from the manufacturer, and in 0.1 M NaOH electrolyte.

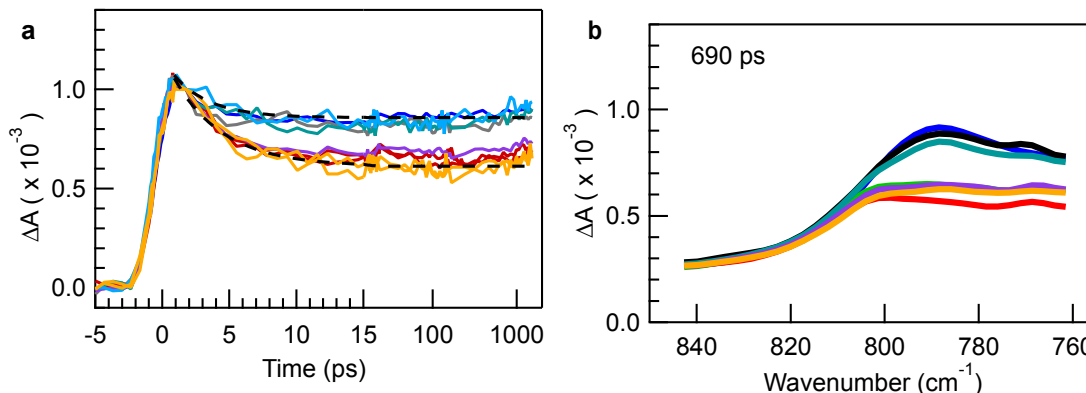


Figure 6.7: The oxyl radical signature was tracked from inception for 1.5 ns with sub-picosecond resolution. Comparing the open circuit and closed circuit **a** traces and **b** spectra reveals no affect on the rise-time of the oxyl radical signature. However, there is a fast decay component that does respond to applied bias that changes from 2.7 ± 0.7 ps at open circuit (blue-grey traces) to 3.7 ± 0.4 ps at closed circuit: (Yellow: $+0.5\text{V}$, Purple: -0.5V , and Red and Pink: 0.0V). Spectra are conserved during the signal rise however at longer time scales the Fano peak is “flattened”. The experiment was conducted in 1.0 M NaOH electrolyte and with a 0.1% Nb SrTiO₃ sample.

constant with respect to defect site density has not been determined due to the difficulty in quantifying the defect-site density at the surface.

Finally, to ensure that the increase of active sites at the surface comes about through surface reorganization and not photodecomposition of the electrode, the electrolyte was checked for the presence of strontium and titanium ions after extended operation of the photoelectrochemical cell. As discussed in Section 6.5, Sample Characterization, ICP-AES analysis confirms that the roughening process does not involve stoichiometric photodecomposition of the catalyst itself.

6.2.4 Oxyl Radical Potential Dependence

As further evidence of surface changes that occur during sustained water oxidation, repeated experiments show a fast flattening of the oxyl-radical spectrum at closed circuit conditions that is not present at open circuit conditions. Although preliminary, these results provide direction for future experiments. Providing molecular-level details of the surface species that evolve as a result of photocatalysis is clearly achievable using this technique.

6.3 Discussion

There are three clear signatures detected in the infrared spectrum corresponding to vibrational and electronic signatures of surface holes. The first is identified from an unpolarized positive absorption that appears within 300 fs of photoexcitation. Although the probe IRF has been measured to be less than 200 fs, the ultraviolet excitation pulse goes through several transmissive optics before reaching the sample. As such, it is likely that the unpolarized signal rises faster than the instrument response function (estimated at 300 fs). Characteristic rise times for free carriers in semiconductors fall below 300 of femtoseconds [164, 165]. The unpolarized signal shows a fast decay (45% spectral weight) on the order of 102 ps, and a second lifetime estimated to be on the order of 400 microseconds at open circuit. The reaction rate constant of these valence band holes is zero-order with respect to holes, consistent with the interpretation that these holes react through a limiting number of surface states. The very low fluences achieved in this work place an upper bound on the density of reactive sites on the surface, i.e. well below 5% of the surface sites. The observed rate constant is increased by sustained photocatalytic water oxidation, further implicating surface states as the rate limiting reactive species.

There is also an in-plane bleach-like component that grows in with an exponential rise time on the order of 15 ps, significantly slower than the oxyl radical (≈ 2 ps). The signal amplitude and lifetime show strong dependence on applied potential. While this signal dominates at positive applied biases, it is nearly absent at open circuit and negative biases. This suggests the state is inaccessible at the resting valence band position, but likely shifts into relevance at sufficient overpotential. The molecular character of this site has not been conclusively determined from these experiments, however it is tentatively assigned to a “lateral-oxygen” radical state similar to the one identified in DFT calculations performed initially as part of the work described in Chapter 5. The previously identified state cannot suffice as a full description since the lateral oxygen state was calculated from a defect-free slab model, inconsistent with the evidence presented in this chapter. However, the state is positioned similarly from an energetic standpoint and for the sake of simplicity the unknown state is referred to as a lateral oxygen in this work. Conclusive characterization of the molecular details, the monitored transition, and the catalytic relevance of the state are left as future work. The lateral-oxygen state is estimated to lie 0.3 – 1.0 eV below the oxyl radical state. While inaccessible by valence band holes below at least 3576 K, applied bias in the range of 1 V would be sufficient to reach the lower bounds of that range. For future work, the distinct in-plane polarization of the transition should serve as a physical observable to assist more detailed DFT calculations to identify the specific transition and molecular species being detected.

Finally, the oxyl radical shows a rise time of approximately 1.5 – 2 ps, with no dependence on deuteration of the reactant water. In fact, none of the observed hole states: valence band edge holes, lateral oxygen radicals, or oxyl radicals - show any dependence on electrolyte isotope exchange. This leads to the perhaps surprising conclusion that neither the formation nor subsequent consumption of these species involves a concerted proton-

coupled electron-transfer step. Likewise none of these populations show any change in dynamics with hydroxide concentration, even in the range expected to change the surface population from hydroxyl groups to oxide anions. This would imply that none involve charge transfer to a hydroxide ion in solution or at the surface. To explain the insensitivity of the oxyl radical rise time (which must involve a surface hydroxide) I am forced to conclude that even at pH 14.5 the majority of surface hydroxide groups remained protonated. Attempts to perform the spectroscopic experiments beyond a pH of 14.5 to clarify this point resulted in rapid degradation of epoxy used to secure the sample within the reaction cell and so could not be completed.

6.4 Conclusions

Spectroscopic interrogation of the transition metal oxide catalyst surface *in-operando* has revealed a minimum of three hole states present within the first nanosecond following photoexcitation. While the four-hole character of the water oxidation reaction always implied there would be multiple states at play on the catalyst surface, the slow overall rate combined with the rapid appearance of these states suggests that even at the earliest time scales, a minimum of three types of holes are present at the interface. This chapter, and in general this thesis, provide some of the first work on the water oxidation reaction from its inception. Other workers in the field [166, 35, 110, 71, 46, 167, 58, 78, 42, 168, 169, 60, 59] are studying the critical O-O bond formation and other steps in-between, e.g. the metal-oxo formation. The time scales and reaction steps being elucidated in this field will need to be connected and reconciled, but completing that work holds the promise of opening the way for a full artificial synthetic device, supported by a water oxidation catalyst that meets all characteristics required to meet commercial viability. The multiple states identified here show little evolution between the first tens of picoseconds and early nanoseconds. This is consistent with the high quantum efficiency associated with strontium titanate as a water oxidation catalyst, however in other materials with more attractive properties (e.g. α -hematite) hole dynamics at early times play an important role in influencing reactivity and quantum efficiency [59, 42, 170, 171, 58]. A full mechanistic understanding of the water oxidation reaction on metal oxide catalysts will enable their intelligent design, whether that includes increased defect site density (of the right kind to drive charge transfer rather than recombination), morphological adaptations at the nanoscale to enable synergistic interactions between different phases, or surface treatment to maximize the chance of molecular diffusion of radicals. The work here identifies three key state where holes reside, at the surface, in a material where the quantum efficiency exceeds 80%. Along with further details on these time scales, future studies will have to take the next step and connect early time scales, like this work, with the insights and discoveries being made on the microsecond, millisecond and second timescales.

6.5 Sample Characterization

Inductively Coupled Plasma Atomic Emission Spectroscopy (ICP-AES) analysis was performed on deionized water, a 2 ppm calibration solution of the metal ion of interest, and on electrolyte both before and after experiments. The Sr^{2+} ion and Ti^{4+} ion concentrations were tracked using their 407.78 nm and 335.12 nm fluorescence lines, respectively. A 0.1% Nb doped SrTiO_3 sample was laser excited at 266 nm with a fluence of $40 \mu\text{J}/\text{cm}^2$, while held at 0.0 V in approximately 5 mL of electrolyte. Analysis of the Sr^{2+} emission line found 8 ppb (0.8%) of Sr^{2+} ions, and < 0.1 ppb Ti^{4+} ions in the electrolyte after irradiation. The faradaic efficiency for Sr^{2+} ion generation under experimental conditions is therefore $0.0018\% \pm 0.0001\%$. The faradaic efficiency for Ti^{4+} ion generation is zero within experimental uncertainty ($0.0001\% \pm 0.0001\%$).

6.6 Acknowledgements

Dr. Tanja Cuk conceived the original projects. David M. Herlihy and Dr. Matthias M. Waagele constructed the transient mid-infrared (800 cm^{-1} probe) instruments, collected transient mid-infrared data and prepared samples. David M. Herlihy and Xihan Chen constructed the transient spectroscopy instrument and collected data for the near-infrared (800 nm probe) experiments. David M. Herlihy and Xihan Chen analyzed the transient data. Dr. Sri Das Pemmaraju and Dr. David Prendergast were responsible for the theoretical calculations. The project was also pushed forward with the help of Dr. Daniel Aschaffenburg and Dr. Stephanie Choing. Further experiments are being pursued by remaining members of the group, including Xihan Chen and Dr. Dan Aschaffenburg.

Mid-Infrared work in this chapter is based upon work supported by the Air Force Office of Scientific Research under AFOSR Award No. FA9550-12-1-0337, which supplied the 64-element infrared array detector and partially supported a postdoctoral fellow, and by the Department of Energy Office of Basic Energy Sciences, under the CPIMS program KC030102 (FWP No. CH12CUK1), which supported two graduate students. The theory work of C.D.P. and D.P. was supported through a User Project at The Molecular Foundry (TMF), LBNL with calculations performed on its computing resources, Nano and Vulcan, managed by the High Performance Computing Services Group of LBNL, and on the Cray XE6 Hopper computer at the National Energy Research Scientific Computing Center (NERSC), LBNL. Both TMF and NERSC are DOE Office of Science User Facilities supported by the Office of Science of the US Department of Energy under Contract No. DE-AC02-05CH11231.

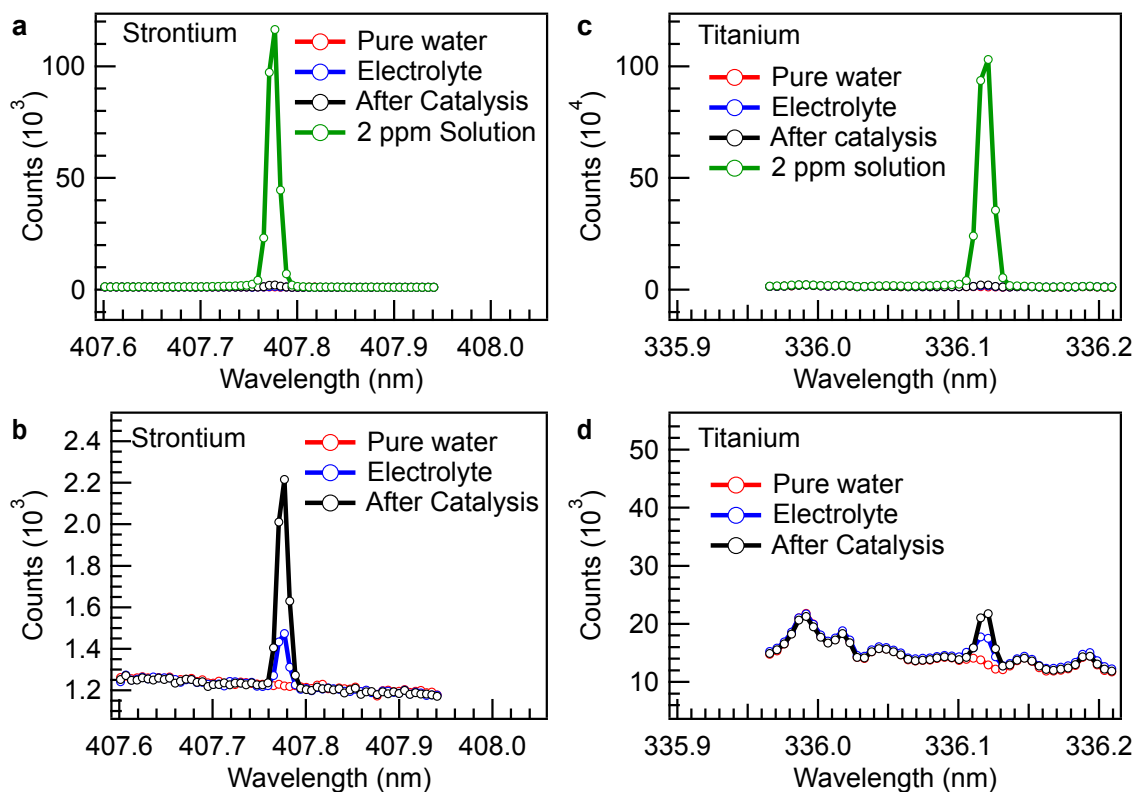


Figure 6.8: The bias dependence of the positive and negative absorption features observed at 800 nm is affected by prolonged photo-electrochemistry. Anecdotally, visual and SEM inspection reveals a darkened surface after irradiation under photocatalytic conditions. One possible explanation is photodecomposition of the SrTiO_3 lattice. To test for this process, electrolyte was tested before and after irradiation of a sample at closed circuit, as was deionized water and a reference solution of each ion at 2ppb for calibration. The results for both Sr^{2+} and Ti^{4+} ions indicates faradaic efficiency of photodecomposition well below 0.01%.

Chapter 7

Spectroscopic Elucidation of Energy Transfer in Hybrid Inorganic-Biological Organisms for Solar-to-Chemical Production

7.1 Original Publication

The work presented in this chapter has been published previously as: Nikolay Kornienko¹, Kelsey K. Sakimoto¹, David M. Herlihy², Son C. Nguyen², A. Paul Alivisatos, Charles. B. Harris, Adam M. Schwartzberg, and Peidong Yang, *Proceedings of the National Academy of Sciences*, **2016** (in press).

¹N.K and K.K.S contributed equally to this work.

²D.M.H and S.C.N. performed the time-resolved infrared experiments.

7.2 Introduction

The final chapter of this dissertation addresses the reduction half reaction of artificial photosynthesis. While in previous chapters the reduction half reaction involved hydrogen evolution by a platinum wire electrode, the commercial use of hydrogen gas as a chemical fuel does not carry the same benefits as would a drop-in liquid fuel. To that end, the work presented in this chapter attempts to shed light on the mechanism of a particularly promising artificial photosynthetic system developed by my collaborators on this project.

The sluggish transduction of solar energy into chemical bonds through natural photosynthesis has strangled our efforts to harvest the full bounty of the sun's energy [172]. We have temporarily sidestepped this limitation by tapping into large reserves of carbonaceous energy to drive an exponential growth in manufacturing, agriculture, urbanization and population. However, the growing scarcity of petrochemicals has called for a return to photosynthesis - rather a new form of photosynthesis capable of keeping pace with modern society [173, 174]. As a sign of progress, inorganic semiconductor light harvesters now routinely surpass the efficiency of plants [29]. In contrast, synthetic catalysts still struggle to replicate the complex C-C bond formation of biology [175, ?]. Significant strides towards comprehensive solar-to-chemical production have been demonstrated through several inorganic-biological hybrid systems combining inorganic semiconductor light harvesters with microbial CO₂ reduction [18, ?, ?]. Recently, we have reported the self-photosensitized hybrid bacterium, *M. thermoacetica*-CdS, that photosynthesizes acetic acid from CO₂ via bio-precipitated CdS nanoparticles [19]. Though e⁻ transfer from electrodes to bacteria has been demonstrated across several genera, the mechanism remains in contention [?]. Spectroscopic investigations of bacterium-to-electrode anodic e⁻ transfer in electrogenic microbial fuel cells have implicated cytochrome mediated mechanisms [?]. However, analogous studies of semiconductor-to-bacterium cathodic e⁻ transfer in electrotrophic organisms have remained sparse. Electron transfer first to membrane bound or extracellular H₂ase to generate molecular H₂ as an intermediate followed by uptake into the native acetogenic Wood-Ljungdahl pathway (WLP) has been speculated or inferred [?, ?, 176]. Still, detailed spectroscopic characterization has remained elusive due to the difficulty of adapting previous techniques to solid electrode platforms. In contrast, our model system, *M. thermoacetica*-CdS, as a translucent colloidal suspension in

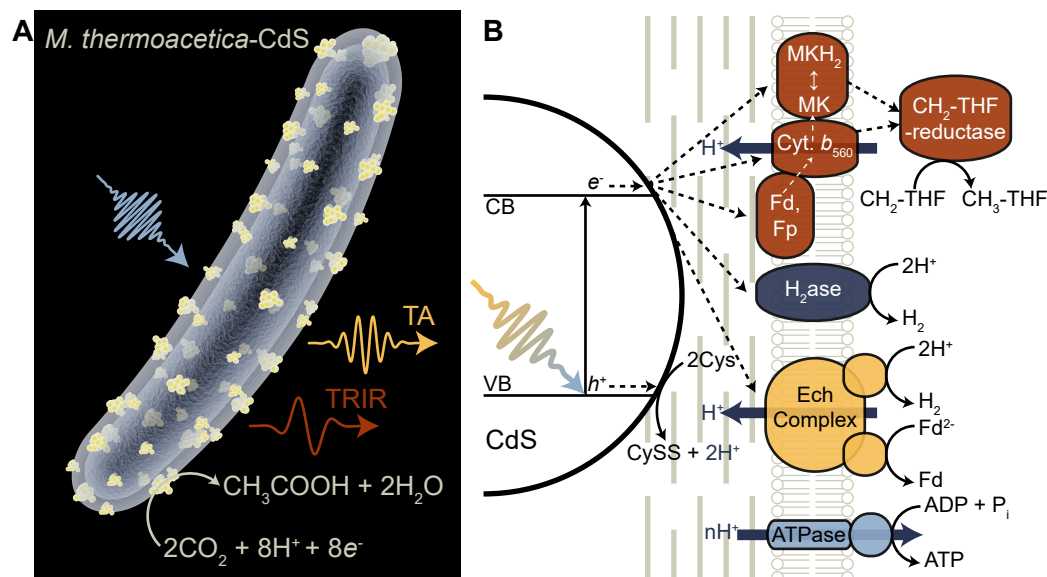


Figure 7.1: Schematic of *M. thermoacetica*-CdS Photosynthetic Charge Transfer. (A) Visible light excitation of optically addressable CdS photosensitizing nanoparticles enables photosynthetic acetic acid production from CO_2 , as well as characterization by TA and TRIR spectroscopy. (B) Potential e^- pathways in *M. thermoacetica*-CdS.

which an optically addressable CdS nanoparticle generates photoelectrons, eliminates the need for opaque electrodes, thereby enabling existing transmittance based spectroscopies in uncovering the molecular basis of this charge transfer mechanism (Figure 7.1A). Here, we present TA and TRIR spectroscopies correlated with biochemical activity to propose a model of the dynamics of inorganic-biological charge and energy transfer. Upon photoexcitation of CdS, cysteine (Cys) oxidation to cystine (CySS) and H^+ quenches the valence band h^+ , while the conduction band e^- may transfer to membrane bound proteins or soluble e^- acceptors. Genomic mining, enzymology, and thermodynamic comparison of protein redox potentials have proposed several viable e^- transfer pathways (Figure 7.1B) [?, ?, ?, ?]. Membrane bound NiFe H_2ases may play a significant role as H_2 directly feeds into the WLP. Demonstrations of direct e^- transfer between metal chalcogenide nanoparticles and purified H_2ases in vitro lend credibility to this pathway's existence in complex whole cells [?, 177, 178]. Alternative pathways have implicated e^- transfer first to membrane bound cytochromes, ferredoxin (Fd), flavoproteins (Fp) and menaquinones (MK) [?, ?]. While these pathways generate reducing equivalents, implicitly, they must also couple to the formation of a H^+ gradient to facilitate ATP synthesis by ATPase. The generation of this proton motive force, either through the transmembrane Ech complex or simply through surface proximal Cys oxidation, may be crucial to electrotrophic behavior, as a related acetogen, *A. woodii*, which instead utilizes a Na^+ motive force, notably cannot engage in electrotrophy [?, 179].

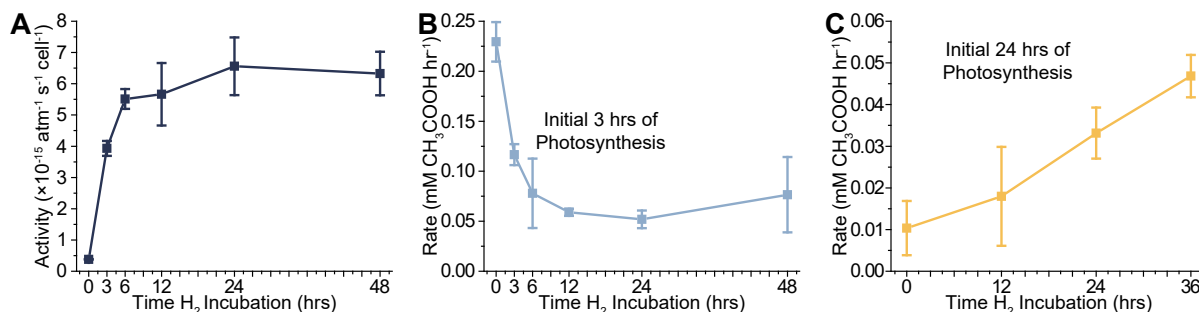


Figure 7.2: Biochemical Assays of *M. thermoacetica*-CdS. (A) H₂ase activity with varying incubation time under H₂. See Methods for details of quantification. (B) CO₂-to-acetic acid conversion rates averaged over the first 3 hrs of photosynthesis show a decreasing trend with increasing H₂ incubation time. For comparison, 24 hrs glucose grown cells had a measured rate of 0.47 ± 0.15 mM hr⁻¹. (C) CO₂-to-acetic acid conversion rates averaged over the first 24 hrs of photosynthesis show an increasing trend with increasing H₂ incubation time. Error bars represent the standard deviation obtained from triplicate experiments.

7.3 Results and Discussion

7.3.1 Biochemical Characterization

To investigate the possibility of H₂ase mediated e⁻ transfer, *M. thermoacetica*-CdS was incubated from 0-48 hrs on H₂ (H₂:CO₂), 80:20, henceforth referred to as H₂ incubated) or glucose (25 mM) to vary the expression and activity of H₂ase. Activity was assayed photometrically by standard benzyl viologen (BV) reduction in the presence of H₂ (Figure 7.2A, 7.3) [180, 181]. Consistent with previous characterizations of *M. thermoacetica*, H₂ oxidation-BV reduction activity increased under increasing H₂ incubation time, presumably through increased H₂ase expression. Comparison of *M. thermoacetica*-CdS incubated for 24 hrs under glucose and H₂ showed H₂ase activity of $6.56 \pm 0.92 \times 10^{-15}$ (atm s cell)⁻¹ and $1.85 \pm 8.39 \times 10^{-17}$ (atm s cell)⁻¹, respectively. To correlate enzyme activity with photosynthetic performance, the same samples were subjected to simulated solar illumination (0.5% sun, AM1.5G) and analyzed for acetic acid production. During the initial 3 hrs of photosynthesis, the rate of CO₂ reduction anti-correlated with H₂ase activity, with the 0 hrs (previously grown on glucose only) incubated sample showing the highest activity (0.23 ± 0.02 mM hr⁻¹). The 24 hrs glucose incubated sample produced acetic acid at 0.47 ± 0.15 mM hr⁻¹, one order of magnitude faster than that of the 24 hrs H₂ incubated sample (0.052 ± 0.009 mM hr⁻¹). However, at longer illumination times, H₂ incubated samples demonstrated the opposite trend. When averaged over 24 hrs of illumination, photosynthesis rates increased with increasing incubation time in H₂ from 0.010 ± 0.001 mM hr⁻¹ ($7.1 \pm 4.5\%$ quantum yield of photons above CdS band-gap) at 0 hrs H₂ incubation to 0.047 ± 0.005 mM hr⁻¹ ($32 \pm 4\%$ quantum yield) at 36 hrs H₂ incu-

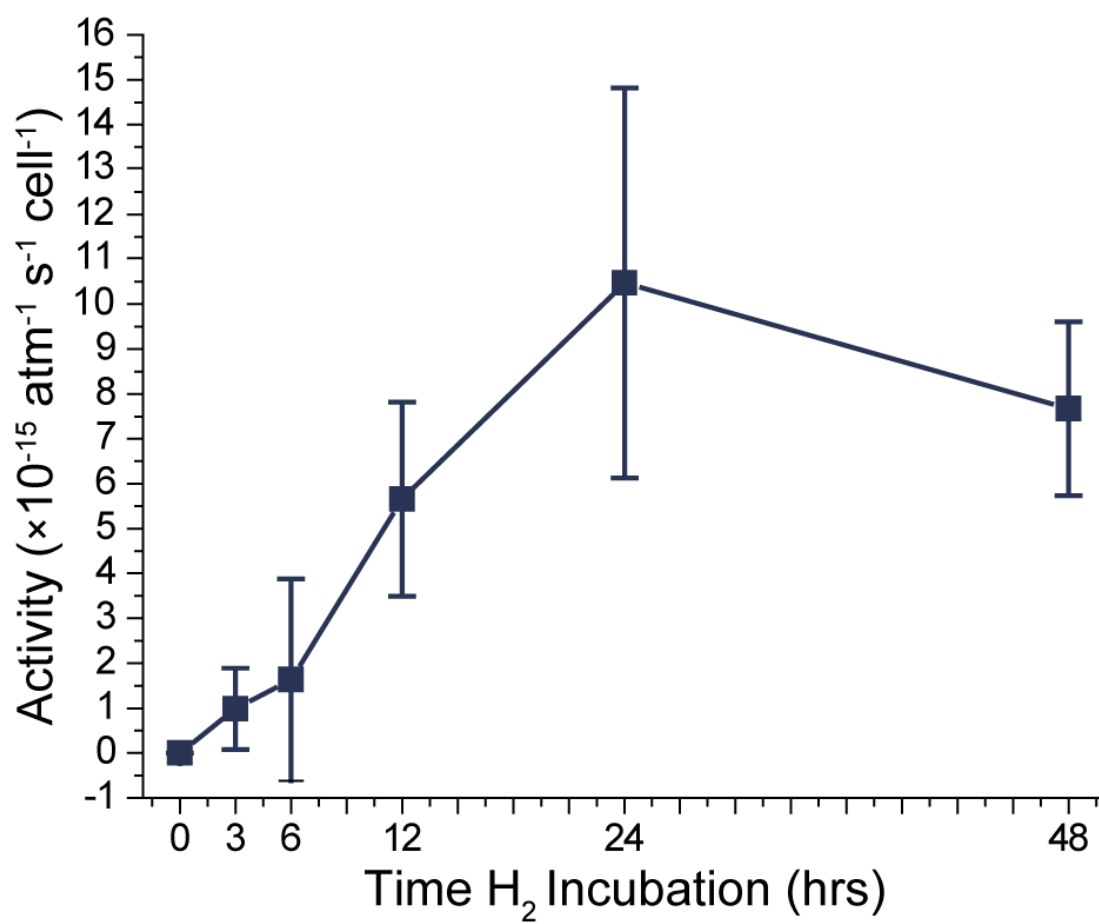


Figure 7.3: H₂ase Activity of *M. thermoacetica*-CdS with Varying [H₂]. H₂ase activity was determined by variation of H₂ partial pressure with a fixed [BV].

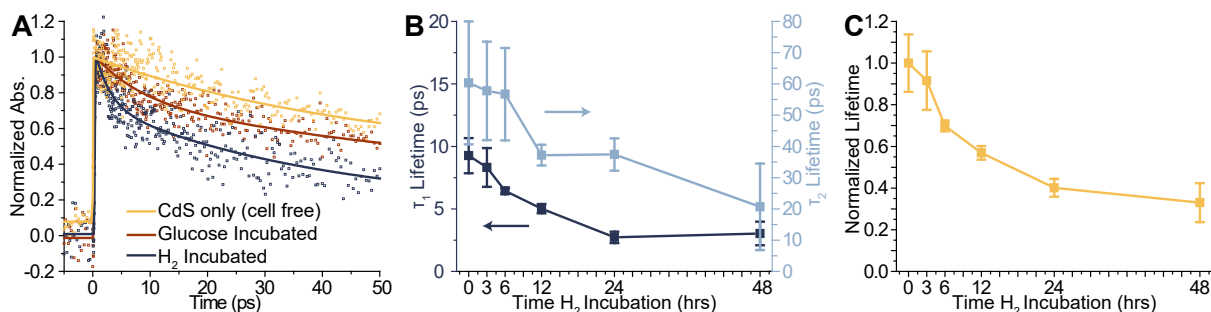


Figure 7.4: TA Spectroscopy of *M. thermoacetica*-CdS. (A) TA plots of CdS only (cell-free), 24 hrs glucose incubated, and 24 hrs H₂ incubated. (B) Trends of exponential τ_1 and τ_2 lifetimes with increasing incubation time under H₂. (C) Weighted averages of the normalized τ_1 and τ_2 lifetimes with increasing incubation time under H₂. Error bars represent the standard error associated with the exponential fitting.

bation (Figure 7.2C). We do note that the rate of acetic acid generation is within the first 3 hrs than the 24 hrs average. The 3 hrs rates are also not stoichiometric (e.g. 0 hrs H₂ sample has an apparent quantum yield of $160 \pm 10\%$), suggesting that despite extensive washing and removal of residual glucose and H₂, some reduced intermediate carries over from the pre-incubation period. The observed trend indicates that lower H₂ase activity cells more effectively transfer CdS e⁻ to terminally reduce these intermediates, perhaps through a later set of enzymes in the WLP. In contrast, the 24 hrs averaged data agrees in quantum yield with previous reports showing no such residual intermediates [19]. These contrasting results suggest two competing charge transfer mechanisms: a non-H₂ase mediated pathway dominant at short time scales (<3 hrs) and a H₂ase mediated pathway dominant at long time scales (~24 hrs).

7.3.2 TA Spectroscopy

To delve deeper into the molecular basis of these two mechanisms, we turned to time-resolved spectroscopic techniques for a dynamic understanding of the activity trends. TA decay kinetics followed the rate of photogenerated e⁻ leaving CdS for various preparations of *M. thermoacetica*-CdS (Figure 7.4, 7.5A). A transient bleach from 440-490 nm matched typical spectra observed with CdS e⁻ acceptor systems and was not observed in CdS-free *M. thermoacetica*. The spectrum of chemically precipitated CdS alone decayed much slower than *M. thermoacetica*-CdS indicating that rapid quenching may result from a proximal e⁻ acceptor. The H₂ incubated *M. thermoacetica*-CdS displayed even faster decay kinetics than the glucose analogue, correlating well with the higher H₂ase activity. These observations point to likely either faster e⁻ transfer to an acceptor site or more e⁻ acceptors available in H₂ incubated bacteria [178]. Fitting each of the TA data sets to a tri-exponential decay revealed three lifetimes: a fast component in the range of 2-10

H ₂ Incubation Time (hrs)	τ_1 (ps)	τ_2 (ps)	τ_3 (ps)	A_1	A_2	A_3
0	9.26 ± 1.41	60.33 ± 19.66	1246.90 ± 249.33	0.27 ± 0.04	0.41 ± 0.07	0.32 ± 0.07
3	8.32 ± 1.55	57.77 ± 15.75	701.67 ± 23.99	0.29 ± 0.04	0.37 ± 0.06	0.34 ± 0.09
6	6.44 ± 0.24	56.72 ± 14.79	757.67 ± 39.38	0.39 ± 0.01	0.37 ± 0.07	0.24 ± 0.04
12	5.02 ± 0.37	37.22 ± 3.32	355.70 ± 17.81	0.30 ± 0.04	0.43 ± 0.04	0.27 ± 0.05
24	2.73 ± 0.46	37.41 ± 5.17	377.10 ± 40.30	0.30 ± 0.02	0.50 ± 0.03	0.20 ± 0.04
48	3.03 ± 0.95	20.68 ± 13.85	645.07 ± 407.55	0.21 ± 0.07	0.49 ± 0.07	0.29 ± 0.10

Table 7.1: TA spectra were fit to a tri-exponential function of the form $f(t) = A_1 \exp(t/\tau_1) + A_2 \exp(t/\tau_2) + A_3 \exp(t/\tau_3)$. Values indicated represent the value and standard error associated with the tri-exponential regression.

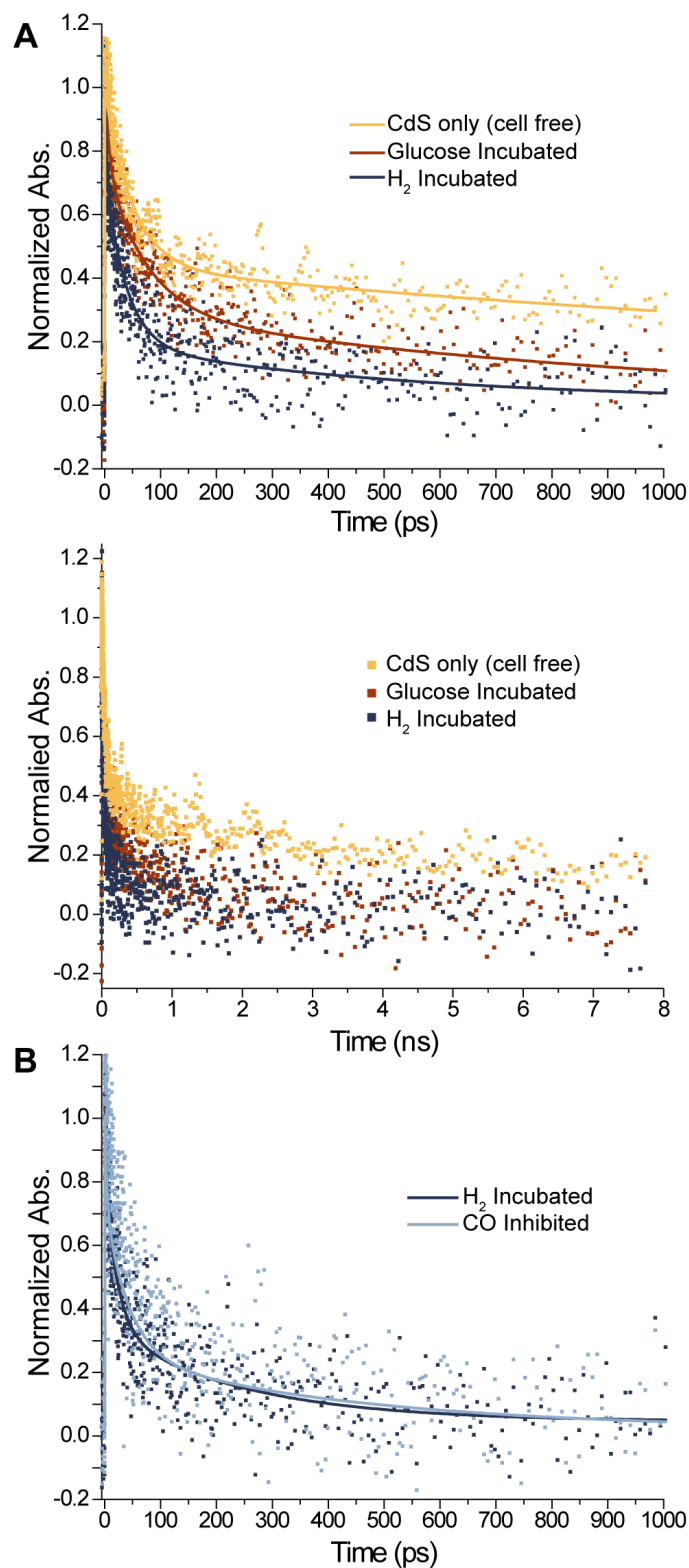


Figure 7.5: TAS Spectra of *M. thermoacetica*-CdS. (A) Expanded time scale of spectrum presented in Figure 7.4A. (B) Comparison of H₂ incubated and CO inhibited spectra.

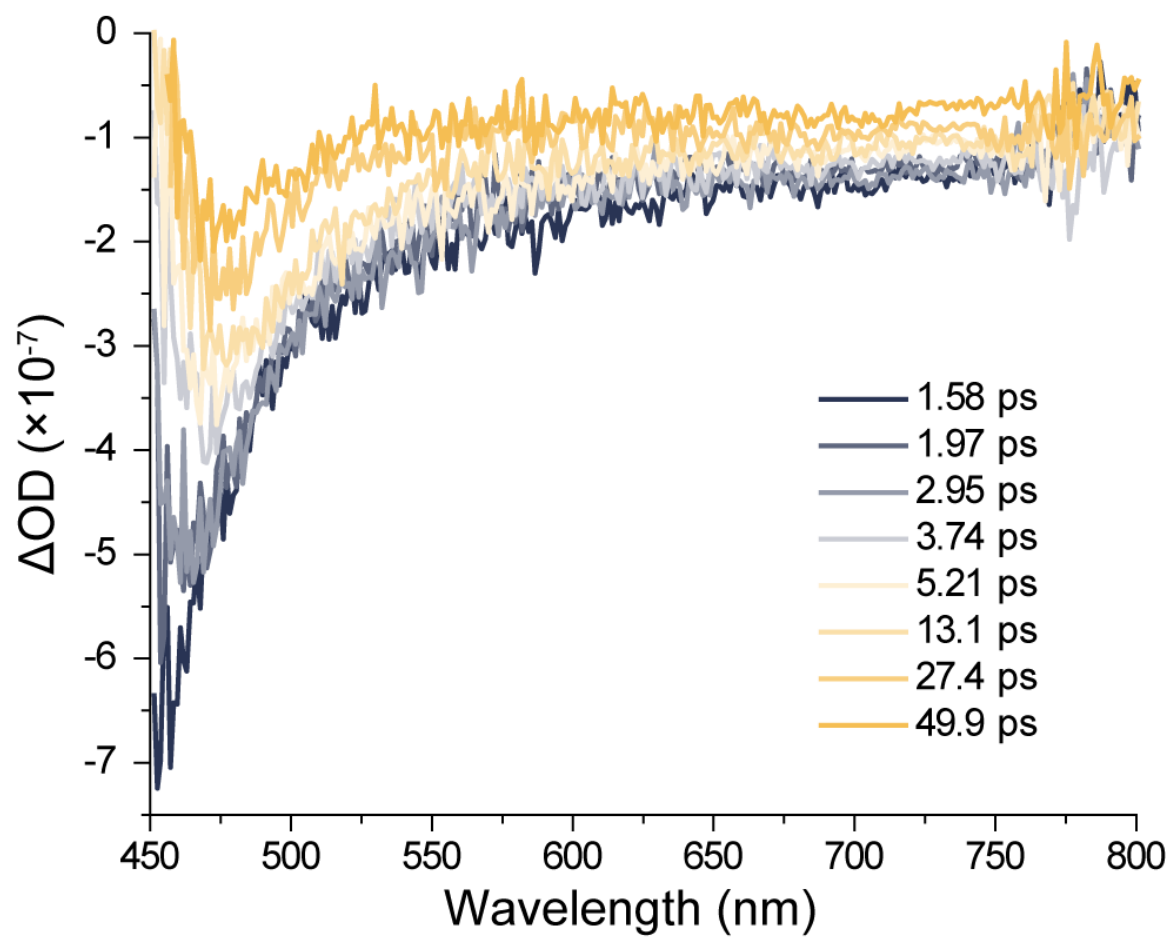


Figure 7.6: TA Spectra. Typical series of TA spectra, show from 1.5 to 50 ps of a 6 hrs H₂ incubated sample.

ps (τ_1), a longer component in the range of 20-80 ps (τ_2) and an even longer component in the range of several 100 ps (τ_3) (Table 7.1). A multi-exponential decay unsurprisingly indicates several processes at play in the complex *M. thermoacetica*-CdS hybrids. Rapid picosecond decays were previously measured with colloidal CdS that featured molecular acceptors with fast e^- transfer behavior [182, 183, 184]. As hot e^- relaxation in Cd-chalcogenide quantum dots occurs in the sub-picosecond regime, this process does not likely contribute to the TA kinetics in the measured timescale [185]. However, previous studies of FeFe H₂ase-CdS constructs reported TA lifetimes in the range of 100 ns, significantly longer than the data presented here [177, 178]. The discrepancy may be attributed to the presence of surface ligands (not present in *M. thermoacetica*-CdS) which present a charge transfer barrier, differences in CdS-H₂ase spatial proximity, solvent effects and reorganization energies, H-bonding networks, and the relatively impaired functionality of purified enzymes under in vitro vs. in vivo conditions [186, 187, 188]. A molecular carrier may also be at play, accepting charge and subsequently transferring it to H₂ase, amongst other potential charge transfer pathways. The differences in lifetimes between cell-free CdS, H₂ incubated, and glucose incubated cells suggests the importance of H₂ase expression in e^- transfer kinetics. To correlate with the above H₂ase activity (Figure 7.2A), the TA lifetimes of the H₂ incubated time series were measured (Figure 7.4B, C). Both the fast τ_1 , τ_2 and their weighted average showed decreasing lifetimes with increasing H₂ase activity, suggesting that the fast e^- transfer kinetics were due to an increase in H₂ase e^- acceptor sites or molecular carriers whose appearance is correlated with H₂ase expression. Inhibition of the H₂ase active site (H-cluster) with CO did not significantly change the TA kinetics, similar to previous works, in which e^- transfer initially proceeds through the FeS cluster chain rather than directly to the NiFe active site (Figure 7.5B) [178, 189, 190].

7.3.3 TRIR Spectroscopy

While kinetically efficient e^- transfer to membrane bound H₂ase may explain the increasing photosynthesis rates at long time scales (Figure 7.2C), TRIR helped determine the basis of the decreasing rates seen at short time scales (Figure 7.2B). We observed changes in the 1760 – 1880 cm⁻¹ spectral window, roughly corresponding to the vibrational range of CO and CN double and triple bonds, among other IR active modes characteristic of amino acid residues (Figure 7.7) [191, 192, 193]. The peaks decayed on the same timescale as the TA signal (Figure. 7.9, 7.10), giving further evidence that the picosecond e^- transfer resulted from a molecular, rather than purely physical, process. No significant changes in the 1900 – 2100 cm⁻¹ spectral window associated with the catalytic cycle of the NiFe H₂ase H-cluster were observed, indicating that a significant quantity of photo-generated e^- were not transferred to the active site within this timeframe [?, 194, 195]. While the complexity of the whole cell *M. thermoacetica*-CdS system renders unambiguous peak assignment beyond the scope of these initial results, careful construction of controls yielded valuable insight into the nature of these vibrational changes. H₂ and glucose incubated samples yielded different TRIR spectral responses. While several bleach

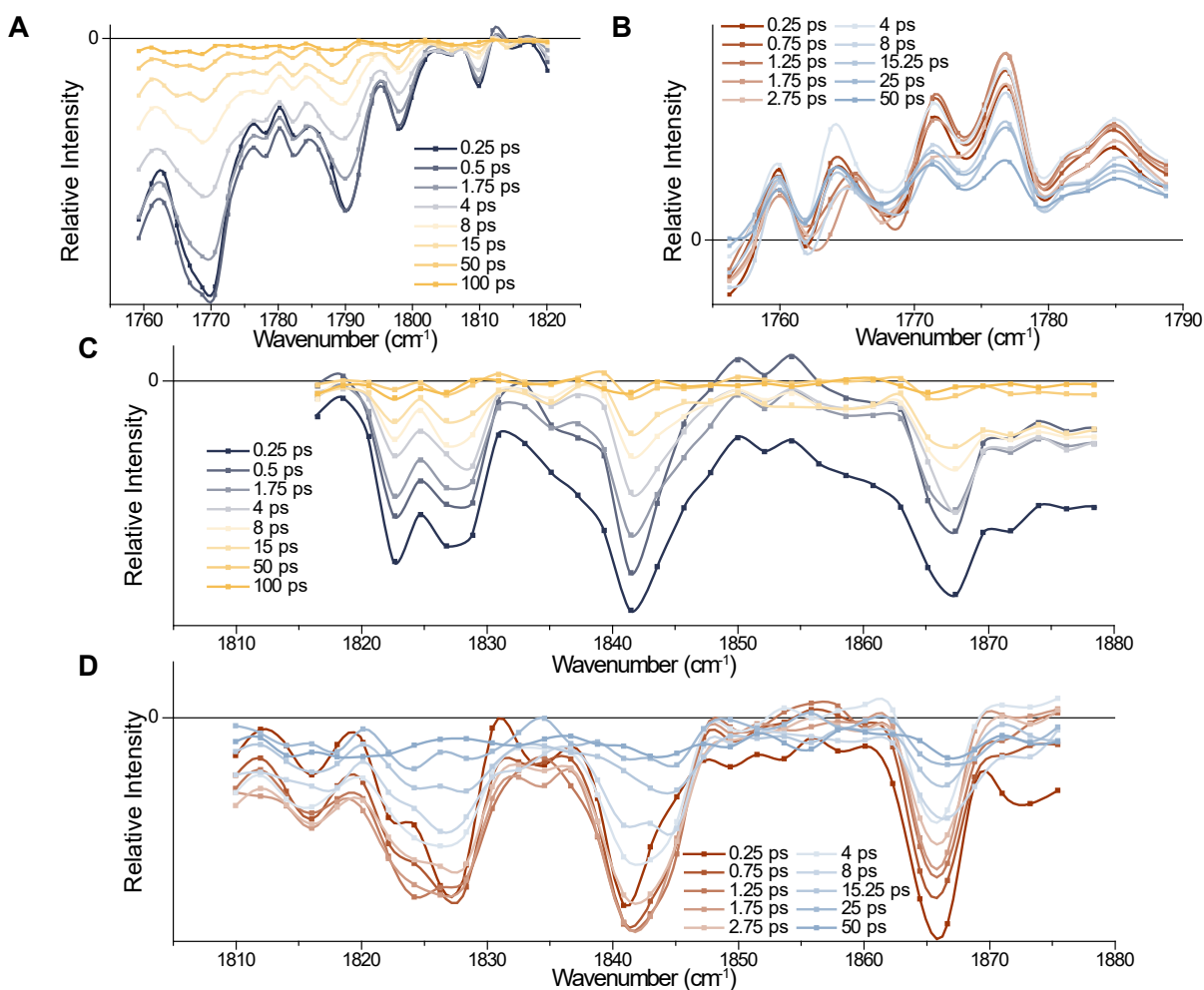


Figure 7.7: TRIR Spectra of *M. thermoacetica*-CdS. (A,C) TRIR of 24 hrs H₂ incubated *M. thermoacetica*-CdS showing bleaching of several peaks in the region of C, N, O double and triple bonds. (B,D) TRIR of 24 hrs glucose incubated *M. thermoacetica*-CdS.

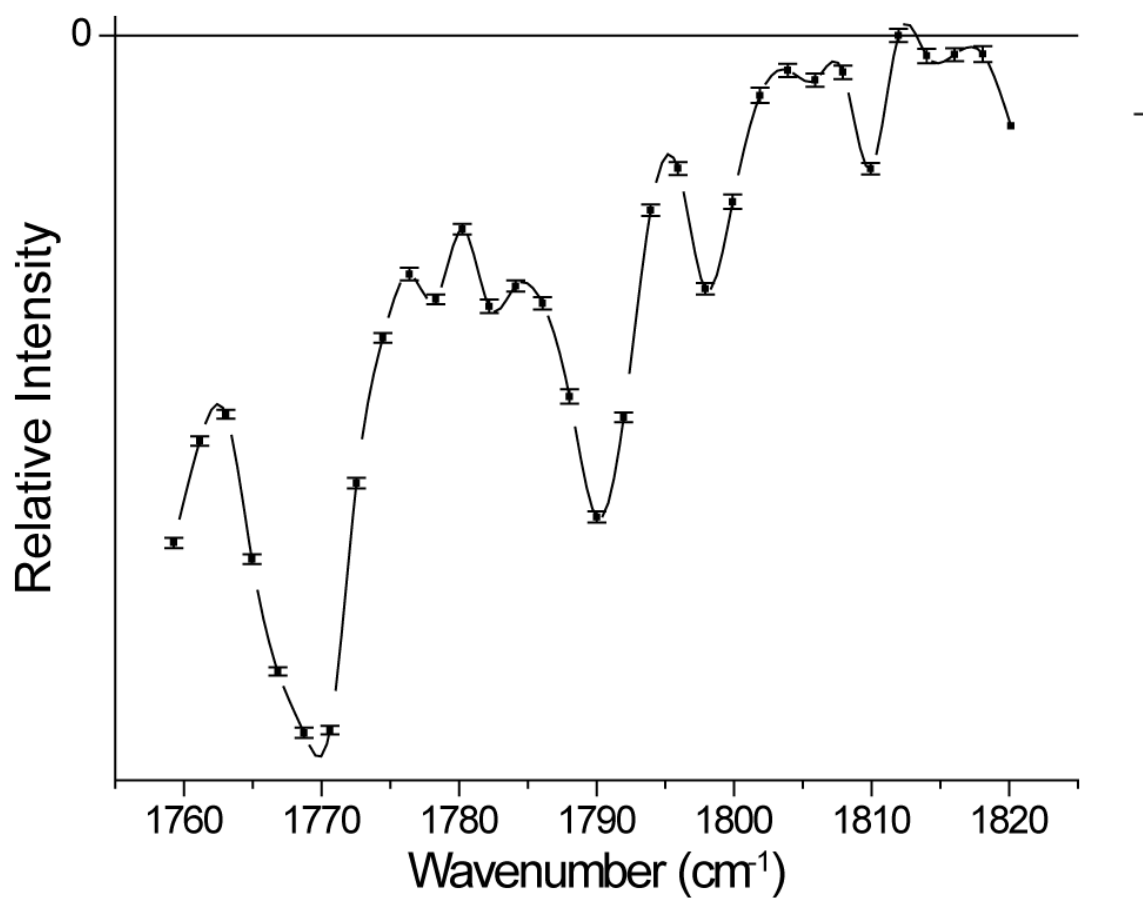


Figure 7.8: Standard Error of TRIR Spectra. Standard error associated with the 24 H₂ incubated sample at 0.25 ps.

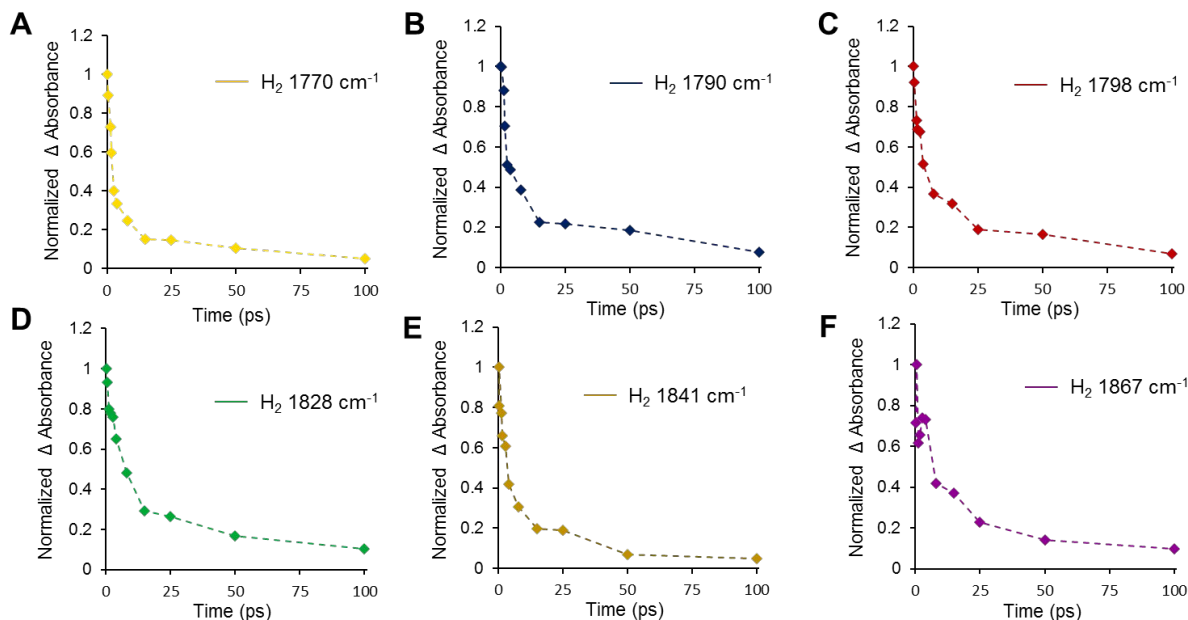


Figure 7.9: TRIR Kinetic Data. Intensities vs. time for several features in the TRIR spectral traces for the 24 hrs H_2 incubated *M. thermoacetica*-CdS.

features in the range of 1760 – 1820 cm^{-1} on the picosecond time regime appeared for the H_2 incubated sample (Figure 7.7A, 7.8), in the same spectral window, glucose incubated samples showed long lived peak growth (Figure 7.7B). These features may indicate H_2 ase mediated charge transfer, with the differential response seen in glucose potentially representing an alternate pathway. In the region of 1810 – 1880 cm^{-1} , signal bleaches of similar time scales appeared in both H_2 and glucose incubated samples, implicating a similar e^- transfer pathway in both systems (Figure 7.7C, D). However, differences in their kinetic evolution point towards different utilization of this shared mechanism. While the pair of bands at 1823 and 1827 cm^{-1} retained a roughly 1:1 ratio for the H_2 incubated sample, in the glucose incubated sample, the 1823 cm^{-1} feature did not grow in until 1-2 ps after the pump excitation, and decayed back to zero faster than the 1827 cm^{-1} feature. We conclude that these spectral responses point towards different predominant e^- transfer pathways in H_2 vs. glucose incubated samples. Further elucidation of the e^- transfer pathways can be accomplished through fluorescent labeling studies, 2D electron spectroscopy, and synthetic biology [196, 197, 198].

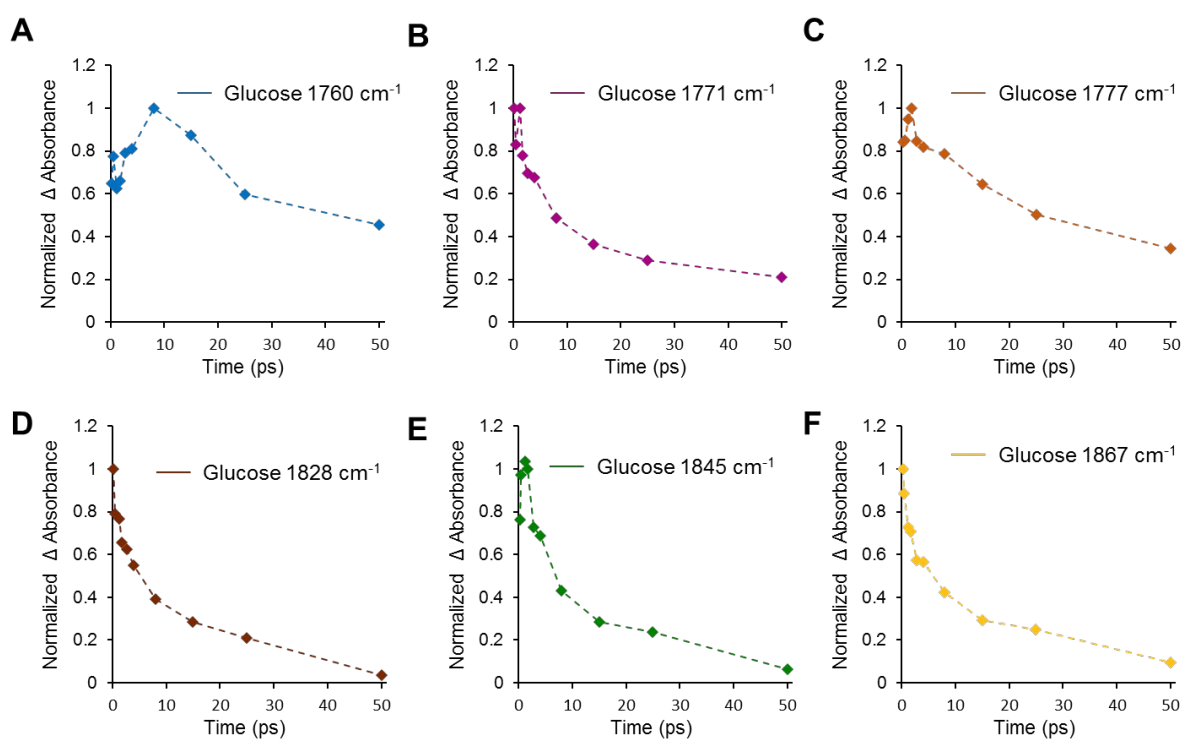


Figure 7.10: TRIR Kinetic Data. Intensities vs. time for several features in the TRIR spectral traces for the 24 hrsH₂ incubated *M. thermoacetica*-CdS.

7.4 Discussion

7.4.1 Proposed e^- Transfer Mechanism of *M. thermoacetica*-CdS

Taken together, the biochemical, TAS and TRIR data suggest two competing pathways for e^- transfer within *M. thermoacetica*-CdS (Figure 7.11). Initially, low H_2 ase expression likely favors e^- injection to a membrane bound e^- acceptor (Fd, Fp, cytochrome, MK) that generates a proton motive force for ATP generation, as well as potentially directly reduces $CH_2 - THF$ for the final stages of the WLP, using up any accumulated intermediates. However, slower charge transfer leads to poorer quantum efficiency, likely due to e^- - h^+ recombination losses. Additionally, this pathway cannot generate high energy reducing equivalents (H_2 , NAD(P)H, Fd) needed for the first reductive steps of the full WLP. As H_2 ase expression increases, charge transfer kinetics favors e^- transfer to a membrane bound H_2 ase to generate molecular H_2 . The possibility also exists of electron transfer to a molecular acceptor, which subsequently transfers an electron to H_2 ase. While this H_2 ase mediated pathway may display higher quantum efficiency, the higher photosynthetic rates only kick in once a significant concentration of extra(intra)cellular H_2 accumulates. This results in lower photosynthetic rates in the first 3 hrs with increasing H_2 ase activity (e^- diverted from the non- H_2 ase pathway), but eventually higher rates after 24 hrs. This H_2 then likely enters the normal WLP via oxidation by the HydABC complex generating both ATP and reducing equivalents [?]. Interestingly, the presence of CdS on *M. thermoacetica* may also induce novel, yet highly functional electron transfer pathways, different from what occurs naturally.

7.5 Conclusions

In conclusion, the work here represents an initial experimental probe into the photosynthetic, electrotrophic behavior of *M. thermoacetica*-CdS. With the careful construction of controls and mild, bio-compatible probing conditions, complex biological behaviors can be studied through conventional spectroscopic techniques. Increasing H_2 ase activity correlated with more efficient long term photosynthetic rates of acetic acid generation. Evidence provided by TA and TRIR likewise supported the existence of a charge transfer pathway that correlated with results from biochemical characterization. Our proposed two-pathway mechanism bears further investigation to probe more acutely the molecular and enzymatic basis of this biotic-abiotic charge transfer. Such insights will ultimately lead to a deeper understanding of the burgeoning complex nexus of inorganic materials and biological systems, and provide a rational framework for the optimization and design of next generation solar-to-chemical systems.

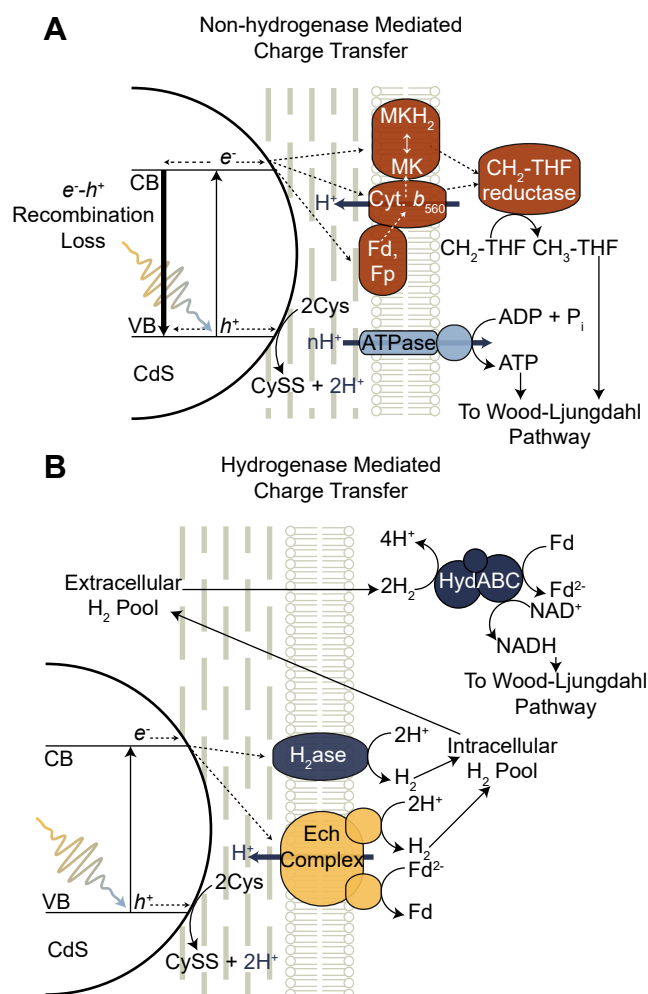


Figure 7.11: Proposed Dual Pathway of Charge and Energy Transfer in *M. thermoacetica*-CdS. (A) The proposed non- H_2 ase mediated pathway predominant in glucose incubated cells, transiently faster during the initial 3 hrs of photosynthesis. (B) Membrane bound H_2 ase mediated pathway dominant in H_2 incubated cells and photosynthetically faster at long time intervals.

7.6 Methods and Materials

7.6.1 Preparation and Biochemical Characterization of *M. thermoacetica*-CdS

M. thermoacetica-CdS was prepared and assayed as previously described with modifications noted below [19]. After full growth, *M. thermoacetica*-CdS was centrifuged under N₂ and resuspended in 20% of the original volume of defined photosynthesis media (DPM) with 0.1 wt% Cys-HCl and 2.5 atm H₂ : CO₂ (80:20) or 25 mM glucose. At various time points, aliquots of *M. thermoacetica*-CdS were sampled and stored at 4°C under N₂ : CO₂ (80:20). BV reduction assays were conducted in a modified procedure as previously described [180]. In short, 0.1 mL of *M. thermoacetica*-CdS was added to 5 mL of 50 mM PIPES buffer (pH 7) with [BV dichloride] ranging from 0.5 mM to 8 mM under a 2.5 atm H₂ : CO₂ head space in a Hungate tube (Chemglass, Inc.). For varying [H₂ : CO₂], volumes of H₂ : CO₂ were syringe injected into an N₂ : CO₂ headspace with [BV] = 4 mM. Kinetics of BV reduction were monitored by at 578 nm (Shimadzu UV3101PC UV-Vis-NIR Spectrophotometer with an integrating sphere) for the initial 30 s. Rates were cell normalized by OD600 correlated with manual cell counting. H₂ase activity was calculated assuming pseudo-first order kinetics (constant [BV] or [H₂]). The activity is thus defined as mM BV formed (mM benzyl viologen)⁻¹ (atm H₂)⁻¹ s⁻¹ cell⁻¹. For photosynthesis measurements, 1 mL of *M. thermoacetica*-CdS was diluted into 4 mL of DPM with 0.1 wt% Cys-HCl. The suspension was illuminated by a filtered 75 W Xenon lamp (Newport Corp., AM1.5G, 0.5% sun) with heating and stirring (55°C, 150 rpm) under a 2.5 atm 80:20 N₂ : CO₂ atmosphere. Time points were centrifuged to remove cells and nanoparticles and assayed by ¹H-qNMR.

7.6.2 TA Spectroscopy

Broadband TA spectra were obtained using an Ultrafast Systems Helios TA system with a Coherent Libra amplified Ti:Sapphire laser system and Coherent OPerA optical parametric amplifier (OPA) pump/probe source. Briefly, the samples were excited with ~50 fs laser pulses generated by the OPA at a repetition rate of 1 kHz. TA spectra were obtained by time delaying a broadband supercontinuum probe pulse that is overlapped in time and space with the femtosecond pump pulse. The supercontinuum is produced by focusing a small portion of the amplified laser fundamental into a sapphire plate. Multi-wavelength TA spectra were recorded using dual spectrometers (signal and reference) equipped with fast Si array detectors. In all experiments, the fluence value was held constant at 0.6 μJ/cm² to rule out effects from exciton-exciton annihilation as a result of high power excitation. TA data were fit to a multi-exponential decay.

7.6.3 TRIR Spectroscopy

The TRIR spectroscopy was performed with a home-built setup described previously in a publication [199]. This setup is different from the one described in Chapter 3 however the operating principles are the same. A 400 nm pump pulse was utilized and the spectral region of $1700 - 2800 \text{ cm}^{-1}$ was probed. The sample was circulated in a N_2 purged and sealed flow cell through two IR-transparent CaF_2 windows spaced 150 or $75 \mu\text{m}$ apart. To exclude the contributions of hot e^- in the conduction band to the IR spectrum at early time scales as a broad positive absorbance, TRIR data were baseline-normalized by utilizing a flat, featureless area of the TRIR spectrum as the baseline.

7.7 Acknowledgements

This work was supported by the Office of Science, Office of Basic Energy Sciences, of the U.S. Department of Energy, under Contract No. DE-AC02-05CH11231 (pchem). Solar-to-chemical production experiments were supported by the NSF under grant DMR-1507914. TA measurements were performed in the Molecular Foundry. Work at the Molecular Foundry was supported by the Office of Science, Office of Basic Energy Sciences of the U.S. Department of Energy under Contract No. DE-AC02-05CH11231.

Bibliography

- [1] Ookie Ma, Steve Capanna, Fred Joseck, et al. 2014 Renewable Energy Data Book. *National Renewable Energy Laboratory*, 2014.
- [2] Energy Information Administration. Energy Use for Transportation - Energy Information Administration, 2014.
- [3] FAO: Agriculture and Consumer Protection. Renewable Biological Systems for Alternative Sustainable Energy Production, 1997.
- [4] The National Renewable Energy Center. Photovoltaics Efficiency Chart, 2016.
- [5] William Shockley and Hans J. Queisser. Detailed balance limit of efficiency of p-n junction solar cells. *Journal of Applied Physics*, 32(3):510–519, 1961.
- [6] Brian D. James, George N. Baum, Julie Perez, and Kevin N. Baum. Technoeconomic Analysis of Photoelectrochemical (PEC) Hydrogen Production. Technical Report December, 2009.
- [7] Blaise A Pinaud, Jesse D Benck, Linsey C Seitz, et al. Technical and economic feasibility of centralized facilities for solar hydrogen production via photocatalysis and photoelectrochemistry. *Energy & Environmental Science*, 6(7):1983–2002, 2013.
- [8] Ken Ichi Ishibashi, Akira Fujishima, Toshiya Watanabe, and Kazuhito Hashimoto. Detection of active oxidative species in TiO₂ photocatalysis using the fluorescence technique. *Electrochemistry Communications*, 2(3):207–210, 2000.
- [9] C S Turchi and D F Ollis. Photocatalytic Degradation of Organic-Water Contaminants - Mechanisms Involving Hydroxyl Radical Attack. *Journal of Catalysis*, 122:178, 1990.
- [10] Peter F. Schwarz, Peter F. Schwarz, Nicholas J. Turro, et al. A New Method To Determine the Generation of Hydroxyl Radicals in Illuminated TiO₂ Suspensions. *The Journal of Physical Chemistry B*, 101(36):7127–7134, 1997.
- [11] D. Lawless, N. Serpone, and D. Meisel. Role of OH Radicals and Trapped Holes in Photocatalysis. A Pulse Radiolysis Study. *J. Phys. Chem.*, 95(13):5166–5170, 1991.

- [12] Yukihiro Nakabayashi and Yoshio Nosaka. OH radical formation at distinct faces of rutile TiO₂ crystal in the procedure of photoelectrochemical water oxidation. *Journal of Physical Chemistry C*, 117(45):23832–23839, 2013.
- [13] Javier J Concepcion, Jonah W Jurss, Joseph L Templeton, and Thomas J Meyer. One site is enough. Catalytic water oxidation by [Ru(tpy)(bpm)(OH₂)]²⁺ and [Ru(tpy)(bpz)(OH₂)]²⁺. *Journal of the American Chemical Society*, 130(49):16462–16463, 2008.
- [14] Robert C Weast, Melvin J Astle, and William H Beyer. *CRC handbook of chemistry and physics*, volume 69. CRC press Boca Raton, FL, 64th editi edition, 1988.
- [15] R A Marcus. On the Theory of Electron Transfer Reactions. VI. Unified Treatment for Homogeneous and Electrode Reactions. *J. Chem. Phys*, 43(2):679–701, 1965.
- [16] Matthias M. Waegle, Xihan Chen, David M. Herlihy, and Tanja Cuk. How Surface Potential Determines the Kinetics of the First Hole Transfer of Photocatalytic Water Oxidation. *Journal of the American Chemical Society*, 136(30):10632–10639, 2014.
- [17] David M Herlihy, Matthias M Waegle, Xihan Chen, et al. Detecting the oxyl radical of photocatalytic water oxidation at an n-SrTiO₃/aqueous interface through its subsurface vibration. *Nat Chem*, 8(6):549–555, jun 2016.
- [18] Chong Liu, Joseph J. Gallagher, Kelsey K. Sakimoto, et al. Nanowire-bacteria hybrids for unassisted solar carbon dioxide fixation to value-added chemicals. *Nano Letters*, 15(5):3634–3639, 2015.
- [19] K.K. Sakimoto, A.B. Wong, and P. Yang. Self-photosensitization of nonphotosynthetic bacteria for solar-to-chemical production. *Science*, 351(6268):74–77, 2016.
- [20] Allen J Bard and Larry R Faulkner. *Electrochemical Methods: Fundamentals and Applications, 2nd Edition*. Wiley: Hoboken, NJ, 2000.
- [21] Charles Kittel. *Introduction to Solid State Physics*. Wiley, 2005.
- [22] H P R Frederikse. *Electronic Structures in Solids: The Electronic Band Structure of Strontium Titanate: Theory and Experiment*. Springer US, New York, New York, 1 edition, 1968.
- [23] David A. Muller, Naoyuki Nakagawa, Akiri Ohtomo, John L. Grazul, and Harold Y. Hwang. Atomic-scale imaging of nanoengineered oxygen vacancy profiles in SrTiO₃. *Nature*, 430(August):657–661, 2004.
- [24] H Reiss. The Fermi Level and the Redox Potential. *Journal of Physical Chemistry*, 89(18):3783–3791, 1985.

- [25] Rüdiger Memming. Electrochemical Decomposition of Semiconductors. In *Semiconductor Electrochemistry*, pages 332–367. Wiley-VCH Verlag GmbH, 2000.
- [26] Roel Van De Krol and Michael Grätzel. *Photoelectrochemical Hydrogen Production*, volume 102 of *Electronic Materials: Science & Technology*. Springer US, Boston, MA, 2012.
- [27] J. O'M ' M Bockris and Z. Nagy. Symmetry factor and transfer coefficient. A source of confusion in electrode kinetics. *Journal of Chemical Education*, 50(12):839, 1973.
- [28] Jenny Nelson. *The physics of solar cells*, volume 1. World Scientific, 2003.
- [29] Robert E Blankenship, David M Tiede, James Barber, et al. Comparing photosynthetic and photovoltaic efficiencies and recognizing the potential for improvement. *Science (New York, N.Y.)*, 332(6031):805–9, 2011.
- [30] a Fujishima and K Honda. Electrochemical photolysis of water at a semiconductor electrode. *Nature*, 238(5358):37–38, 1972.
- [31] César Clavero. Plasmon-induced hot-electron generation at nanoparticle/metal-oxide interfaces for photovoltaic and photocatalytic devices. *Nature Photonics*, 8(2):95–103, 2014.
- [32] Holger Dau, Christian Limberg, Tobias Reier, et al. The Mechanism of Water Oxidation: From Electrolysis via Homogeneous to Biological Catalysis. *ChemCatChem*, 2(7):724–761, 2010.
- [33] Yasuhiro Tachibana, Lionel Vayssieres, and James R. Durrant. Artificial photosynthesis for solar water-splitting. *Nature Photonics*, 6(8):511–518, 2012.
- [34] Junwang Tang, James R. Durrant, and David R. Klug. Mechanism of photocatalytic water splitting in TiO₂. Reaction of water with photoholes, importance of charge carrier dynamics, and evidence for four-hole chemistry. *Journal of the American Chemical Society*, 130(42):13885–13891, 2008.
- [35] Alexander J Cowan, Christopher J Barnett, Stephanie R Pendlebury, et al. Activation Energies for the Rate-Limiting Step in Water Photooxidation by Nanostructured α -Fe₂O₃ and TiO₂. *J. Am. Chem. Soc.*, 133(26):10134–10140, 2011.
- [36] Tiffany Charbouillot, Marcello Brigante, Gilles Mailhot, et al. Performance and selectivity of the terephthalic acid probe for radical OH as a function of temperature, pH and composition of atmospherically relevant aqueous media. *Journal of Photochemistry and Photobiology A: Chemistry*, 222(1):70–76, 2011.

- [37] Kelley M. H. Young, Benjamin M. Klahr, Omid Zandi, and Thomas W. Hamann. Photocatalytic water oxidation with hematite electrodes. *Catalysis Science & Technology*, 3(7):1660, 2013.
- [38] Derek J Wasylenko, Ryan D Palmer, and Curtis P Berlinguette. Homogeneous water oxidation catalysts containing a single metal site. *Chemical communications (Cambridge, England)*, 49(3):218–27, 2013.
- [39] Narayanappa Sivasankar, Walter W Weare, and Heinz Frei. Direct Observation of a Hydroperoxide Surface Intermediate upon Visible Light-Driven Water Oxidation at an Ir Oxide Nanocluster Catalyst by Rapid-Scan FT-IR Spectroscopy. *J. Am. Chem. Soc.*, 133(33):12976–12979, 2011.
- [40] Hernan G Sanchez Casalongue, May Ling Ng, Sarp Kaya, et al. In-Situ Observation of Surface Species on Iridium Oxide Nanoparticles during the Oxygen Evolution Reaction. *Angewandte Chemie (International Edition)*, 53(28):7169–72, 2014.
- [41] Julio Lloret Fillol, Zoel Codolà, Isaac Garcia-Bosch, et al. Efficient water oxidation catalysts based on readily available iron coordination complexes. *Nature chemistry*, 3(10):807–13, 2011.
- [42] Benjamin Klahr and Thomas Hamann. Water Oxidation on Hematite Photoelectrodes: Insight into the Nature of Surface States through In Situ Spectroelectrochemistry, 2014.
- [43] Miao Zhang and Heinz Frei. Towards a molecular level understanding of the multi-electron catalysis of water oxidation on metal oxide surfaces. *Catalysis Letters*, 145(1):420–435, 2015.
- [44] Yogesh Surendranath, Matthew W Kanan, and Daniel G Nocera. Mechanistic Studies of the Oxygen Evolution Reaction by a Cobalt-Phosphate Catalyst at Neutral pH. *J. Am. Chem. Soc.*, 132(46):16501–16509, 2010.
- [45] J Gregory McAlpin, Yogesh Surendranath, Mircea Dinc\ua, et al. EPR Evidence for Co(IV) Species Produced During Water Oxidation at Neutral pH. *J. Am. Chem. Soc.*, 132(20):6882–6883, 2010.
- [46] Matthew W Kanan, Junko Yano, Yogesh Surendranath, et al. Structure and Valency of a Cobalt-Phosphate Water Oxidation Catalyst Determined by in Situ X-ray Spectroscopy. *Journal of the American Chemical Society*, 132(39):13692–13701, 2010.
- [47] Miao Zhang, Moreno de Respinis, and Heinz Frei. Time-resolved observations of water oxidation intermediates on a cobalt oxide nanoparticle catalyst. *Nat. Chem.*, 6(4):362–367, 2014.

- [48] Hieu H. Pham, Mu-Jeng Cheng, Heinz Frei, and Lin-Wang Wang. Surface Proton Hopping and Fast-Kinetics Pathway of Water Oxidation on Co_3O_4 (001) Surface. *ACS Catalysis*, 4(001):5610–5617, 2016.
- [49] K Van Benthem, C Elsässer, and R H French. Bulk electronic structure of SrTiO_3 : Experiment and theory. 6156(2001), 2013.
- [50] J Ringling and F Noack. Efficient generation of subpicosecond seed pulses at 193 nm for amplification in ArF gain modules by frequency mixing in nonlinear optical crystals. 17(24):1794–1796, 1992.
- [51] J Ringling, F Noack, G Korn, and J Squier. Tunable femtosecond pulses in the near vacuum ultraviolet generated by frequency conversion of amplified Ti : sapphire laser pulses. 18(23):2035–2037, 1993.
- [52] G A Rines, H H Zenzie, R A Schwarz, Y Isyanova, and P F Moulton. Nonlinear conversion of Ti:sapphire laser wavelengths. *Selected Topics in Quantum Electronics, IEEE Journal of*, 1(1):50–57, 1995.
- [53] V. Petrov, F. Rotermund, F. Noack, et al. Frequency conversion of Ti:sapphire-based femtosecond laser systems to the 200-nm spectral region using nonlinear optical crystals. *IEEE Journal of Selected Topics in Quantum Electronics*, 5(6):1532–1542, 1999.
- [54] Y R Shen. *The principles of nonlinear optics*. Wiley classics library. Wiley-Interscience, 2003.
- [55] John G Power and Chunguang Jing. Temporal Laser Pulse Shaping for RF Photocathode Guns : The Cheap and Easy way using UV Birefringent Crystals View online : <http://dx.doi.org/10.1063/1.3080991> View Table of Contents :. 689, 2009.
- [56] Milan Milosevic. *Internal Reflection and ATR Spectroscopy*, volume 262. John Wiley & Sons, 2012.
- [57] Ryuhei Nakamura, Tomoaki Okamura, Naomichi Ohashi, Akihito Imanishi, and Yoshihiro Nakato. Molecular Mechanisms of Photoinduced Oxygen Evolution, PL Emission, and Surface Roughening at Atomically Smooth (110) and (100) n - TiO_2 (Rutile) Surfaces in Aqueous Acidic Solutions. *Journal of the American Chemical Society*, 127(37):12975–12983, sep 2005.
- [58] M Barroso, S R Pendlebury, A J Cowan, and J R Durrant. Charge carrier trapping, recombination and transfer in hematite ($\alpha\text{-Fe}_2\text{O}_3$) water splitting photoanodes. *Chemical Science*, 4(7):2724–2734, 2013.

- [59] Benjamin Klahr, Sixto Gimenez, Francisco Fabregat-santiago, Thomas Hamann, and Juan Bisquert. Water Oxidation at Hematite Photoelectrodes: The Role of Surface States. 2012.
- [60] Omid Zandi and Thomas W Hamann. Determination of Water Oxidation Intermediates on Haematite Electrode Surfaces using Operando Infrared Spectroscopy. *Nature Chemistry*, (July), 2016.
- [61] Anthony Harriman, Ingrid J Pickering, John M Thomas, and Paul A Christensen. Metal oxides as heterogeneous catalysts for oxygen evolution under photochemical conditions. *J. Chem. Soc., Faraday Trans. 1*, 84(8):2795–2806, 1988.
- [62] Xiangsong Lin, Xiangqian Hu, Javier J Concepcion, et al. Theoretical study of catalytic mechanism for single-site water oxidation process. *Proc. Natl. Acad. Sci. U.S.A.*, 109(39):15669–15672, 2012.
- [63] D Kwabena Bediako, Yogesh Surendranath, and Daniel G Nocera. Mechanistic Studies of the Oxygen Evolution Reaction Mediated by a Nickel Borate Thin Film Electrocatalyst. *J. Am. Chem. Soc.*, 135(9):3662–3674, 2013.
- [64] D Kwabena Bediako, Cyrille Costentin, Evan C Jones, Daniel G Nocera, and Jean-Michel Savéant. Proton-Electron Transport and Transfer in Electrocatalytic Films. Application to a Cobalt-Based O₂-Evolution Catalyst. *Journal of the American Chemical Society*, 135(28):10492–10502, 2013.
- [65] John Newman and Karen E Thomas-Alyea. *Electrochemical Systems, 3rd Edition*. Wiley: Hoboken, NJ, 2004.
- [66] Ryuhei Nakamura and Yoshihiro Nakato. Primary Intermediates of Oxygen Photoevolution Reaction on TiO₂ (Rutile) Particles, Revealed by in Situ FTIR Absorption and Photoluminescence Measurements. *J. Am. Chem. Soc.*, 126(4):1290–1298, 2004.
- [67] Calvin D Jaeger and Allen J Bard. Spin trapping and electron spin resonance detection of radical intermediates in the photodecomposition of water at titanium dioxide particulate systems. *J. Phys. Chem*, 83(24):3146–3152, 1979.
- [68] Alexandra P Norton, Steven L Bernasek, and Andrew B Bocarsly. Mechanistic aspects of the photooxidation of water at the n-titania/aqueous interface: optically induced transients as a kinetic probe. *J. Phys. Chem*, 92(21):6009–6016, 1988.
- [69] J J Kasinski, L A Gomez-Jahn, K J Faran, et al. Picosecond dynamics of surface electron transfer processes: Surface restricted transient grating studies of the n-TiO₂/H₂O interface. *The Journal of chemical physics*, 90(2):1253–1269, 1989.

- [70] Juliette M Lantz and Robert M Corn. Time-Resolved Optical Second Harmonic Generation Measurements of Picosecond Band Flattening Processes at Single Crystal TiO₂ Electrodes. *J. Phys. Chem.*, 98(38):9387–9390, 1994.
- [71] Zhuangqun Huang, Yongjing Lin, Xu Xiang, et al. In Situ Probe of Photocarrier Dynamics in Water-Splitting Hematite Electrodes. *Energy Environ. Sci.*, 5(10):8923–8926, 2012.
- [72] Mino Green. Electrochemistry of the Semiconductor-Electrolyte Electrode. I. The Electrical Double Layer. *The Journal of Chemical Physics*, 31(1):200, aug 1959.
- [73] R De Gryse, W P Gomes, F Cardon, and J Vennik. On the Interpretation of Mott-Schottky Plots Determined at Semiconductor/Electrolyte Systems. *J. Electrochem. Soc.*, 122(5):711–712, 1975.
- [74] Kohei Uosaki and Hideaki Kita. Effects of the Helmholtz Layer Capacitance on the Potential Distribution at Semiconductor/Electrolyte Interface and the Linearity of the Mott-Schottky Plot. *J. Electrochem. Soc.*, 130(4):895–897, 1983.
- [75] Gerald Cooper, John A Turner, Bruce A Parkinson, and Arthur J Nozik. Hot carrier injection of photogenerated electrons at indium phosphide/electrolyte interfaces. *J. Appl. Phys.*, 54:6463–6473, 1983.
- [76] Roel van de Krol and Michael Grätzel. *Photoelectrochemical Hydrogen Production*, vol. 102, p. 13-67. Springer: New York, NY, 2012.
- [77] J A Turner, J Manassen, and A J Nozik. Photoelectrochemistry with p-Si electrodes: Effects of inversion. *Appl. Phys. Lett.*, 37:488–491, 1980.
- [78] Chun Du, Xiaogang Yang, Matthew T Mayer, et al. Hematite-Based Water Splitting with Low Turn-On Voltages. *Angew. Chem. Int. Ed.*, 52(48):12692–12695, 2013.
- [79] Allen J Bard, Andrew B Bocarsly, Fu Ren F Fan, Erick G Walton, and Mark S Wrighton. The concept of Fermi level pinning at semiconductor/liquid junctions. Consequences for energy conversion efficiency and selection of useful solution redox couples in solar devices. *J. Am. Chem. Soc.*, 102(11):3671–3677, 1980.
- [80] John. O’ M Bockris and Shahed. U M Khan. *Surface Electrochemistry*, chap. 2, p. 59-202. Springer: New York, NY, 1993.
- [81] Yong Xu and Martin A.A. Schoonen. The absolute energy positions of conduction and valence bands of selected semiconducting minerals. *American Mineralogist*, 85(3-4):543–556, mar 2000.
- [82] Simon M. Sze and Ming-Kwei Lee. *Semiconductor Devices Physics and Technology*. Wiley, New York, NY, 1985.

- [83] O N Tufte and P W Chapman. Electron mobility in semiconducting strontium titanate. *Physical Review*, 155(3):796, 1967.
- [84] Peter Wardman. Reduction Potentials of One-Electron Couples Involving Free Radicals in Aqueous Solution. *J. Phys. Chem. Ref. Data*, 18(4):1637–1755, 1989.
- [85] Yasuhiro Yamada, Hideki Yasuda, Takeshi Tayagaki, and Yoshihiko Kanemitsu. Photocarrier recombination dynamics in highly excited SrTiO₃ studied by transient absorption and photoluminescence spectroscopy. *Appl. Phys. Lett.*, 95:121112, 2009.
- [86] W H Koppenol and Joel F Liebman. The oxidizing nature of the hydroxyl radical. A comparison with the ferryl ion (FeO₂⁺). *J. Phys. Chem.*, 88(1):99–101, 1984.
- [87] James P Hoare. *Standard Potentials in Aqueous Solution*, p. 49-63; Bard, A. J. and Parsons, R., Eds. IUPAC: New York, NY, 1985.
- [88] Jun Cheng, Marialore Sulpizi, Joost VandeVondele, and Michiel Sprik. Hole Localization and Thermochemistry of Oxidative Dehydrogenation of Aqueous Rutile TiO₂(110). *ChemCatChem*, 4(5):636–640, 2012.
- [89] Boon Siang Yeo and Alexis T Bell. Enhanced Activity of Gold-Supported Cobalt Oxide for the Electrochemical Evolution of Oxygen. *J. Am. Chem. Soc.*, 133(14):5587–5593, 2011.
- [90] Hai-Yan Su, Yelena Gorlin, Isabela C Man, et al. Identifying active surface phases for metal oxide electrocatalysts: a study of manganese oxide bi-functional catalysts for oxygen reduction and water oxidation catalysis. *Phys. Chem. Chem. Phys.*, 14(40):14010–14022, 2012.
- [91] Peilin Liao, John A Keith, and Emily A Carter. Water Oxidation on Pure and Doped Hematite (0001) Surfaces: Prediction of Co and Ni as Effective Dopants for Electrocatalysis. *J. Am. Chem. Soc.*, 134(32):13296–13309, 2012.
- [92] Michal Bajdich, Mónica García-Mota, Aleksandra Vojvodic, Jens K Nørskov, and Alexis T Bell. Theoretical Investigation of the Activity of Cobalt Oxides for the Electrochemical Oxidation of Water. *J. Am. Chem. Soc.*, 135(36):13521–13530, 2013.
- [93] Feng Liu, Javier J Concepcion, Jonah W Jurss, et al. Mechanisms of Water Oxidation from the Blue Dimer to Photosystem II. *Inorg. Chem.*, 47(6):1727–1752, 2008.
- [94] Leila Alibabaei, M Kyle Brennaman, Michael R Norris, et al. Solar water splitting in a molecular photoelectrochemical cell. *Proc. Natl. Acad. Sci. U.S.A.*, 110(50):20008–20013, 2013.

- [95] R Stoian, A Rosenfeld, D Ashkenasi, et al. Surface Charging and Impulsive Ion Ejection during Ultrashort Pulsed Laser Ablation. *Phys. Rev. Lett.*, 88(9):97603, feb 2002.
- [96] W. G. Roeterdink, L. B. F. Juurlink, O. P. H. Vaughan, et al. Coulomb Explosion in Femtosecond Laser Ablation of Si(111). *Appl. Phys. Lett.*, 82(23):4190, apr 2003.
- [97] Andrew B Bocarsly, Jeffrey M Bolts, Phillip G Cummins, and Mark S Wrighton. Photoelectrolysis of water at high current density: Use of ultraviolet laser excitation. *Appl. Phys. Lett.*, 31(9), 1977.
- [98] C W de Kreuk, J L B de Groot, and A Mackor. Photocorrosion of strontium titanate photoanode. *Sol. Energ. Mater*, 5(4):437–444, oct 1981.
- [99] S Licht, B Wang, S Mukerji, et al. Efficient Solar Water Splitting, Exemplified by RuO₂-Catalyzed AlGaAs/Si Photoelectrolysis. *The Journal of Physical Chemistry B*, 104(38):8920–8924, 2000.
- [100] Michael G Walter, Emily L Warren, James R McKone, et al. Solar Water Splitting Cells. *Chemical reviews*, 110(11):6446–6473, 2010.
- [101] R Eisenberg and H B Gray. Preface on Making Oxygen. *Inorganic chemistry*, 47(6):1697–1699, 2008.
- [102] Krupa Ramasesha, Luigi De Marco, Aritra Mandal, and Andrei Tokmakoff. Water vibrations have strongly mixed intra- and intermolecular character. *Nat Chem*, 5(11):935–940, 2013.
- [103] Gernot Renger. Light induced oxidative water splitting in photosynthesis: Energetics, kinetics and mechanism. *Journal of Photochemistry and Photobiology B: Biology*, 104(1-2):35–43, 2011.
- [104] J Yano and V K Yachandra. Where Water Is Oxidized to Dioxygen: Structure of the Photosynthetic Mn₄Ca Cluster from X-ray Spectroscopy. *Inorganic chemistry*, 47(6):1711–1726, 2008.
- [105] R Tagore, R H Crabtree, and G W Brudvig. Oxygen Evolution Catalysis by a Dimanganese Complex and Its Relation to Photosynthetic Water Oxidation. *Inorganic chemistry*, 47(6):1815–1823, 2008.
- [106] Per E M Siegbahn. Theoretical Studies of O-O Bond Formation in Photosystem II. *Inorganic chemistry*, 47(6):1779–1786, 2008.
- [107] Marie Louise Groot, Natalia P Pawlowicz, Luuk J G W van Wilderen, et al. Initial electron donor and acceptor in isolated Photosystem II reaction centers identified with femtosecond mid-IR spectroscopy. *Proceedings of the National Academy of Sciences of the United States of America*, 102(37):13087–13092, 2005.

- [108] R David Britt, Kristy A Campbell, Jeffrey M Peloquin, et al. Recent pulsed EPR studies of the photosystem II oxygen-evolving complex: implications as to water oxidation mechanisms. *Biochimica et biophysica acta*, 1655(1-3):158–71, apr 2004.
- [109] Jan Kern, Rosalie Tran, Roberto Alonso-Mori, et al. Taking snapshots of photosynthetic water oxidation using femtosecond X-ray diffraction and spectroscopy. *Nat Commun*, 5, 2014.
- [110] Charles Y Cummings, Frank Marken, Laurence M Peter, K G Upul Wijayantha, and Asif A Tahir. New Insights into Water Splitting at Mesoporous α -Fe₂O₃ Films: A Study by Modulated Transmittance and Impedance Spectroscopies, 2012.
- [111] Akihito Imanishi, Tomoaki Okamura, Naomichi Ohashi, Ryuhei Nakamura, and Y Nakato. Mechanism of Water Photooxidation Reaction at Atomically Flat TiO₂ (Rutile) (110) and (100) Surfaces: Dependence on Solution pH. *Journal of the American Chemical Society*, 129(37):11569–11578, 2007.
- [112] Olga I. Micic, Yuenian Zhang, Keith R. Cromack, Alexander D. Trifunac, and Marion C. Thurnauer. Trapped holes on titania colloids studied by electron paramagnetic resonance. *The Journal of Physical Chemistry*, 97(28):7277–7283, jul 1993.
- [113] J Gregory McAlpin, Troy A Stich, C Andre Ohlin, et al. Electronic Structure Description of a [Co(III)₃Co(IV)O₄] Cluster: A Model for the Paramagnetic Intermediate in Cobalt-Catalyzed Water Oxidation. *Journal of the American Chemical Society*, 133(39):15444–15452, 2011.
- [114] Michael Huynh, D Kwabena Bediako, and Daniel G Nocera. A Functionally Stable Manganese Oxide Oxygen Evolution Catalyst in Acid. *Journal of the American Chemical Society*, 136(16):6002–6010, 2014.
- [115] Hikmet Sezen, Maria Buchholz, Alexei Nefedov, et al. Probing electrons in TiO₂ polaronic trap states by IR-absorption: Evidence for the existence of hydrogenic states. *Sci.Rep.*, 4, 2014.
- [116] Hikmet Sezen, Honghui Shang, Fabian Bebensee, et al. Evidence for photogenerated intermediate hole polarons in ZnO. *Nat.Comm.*, 6, 2015.
- [117] Ian M Lane, David A King, Zhi-Pan Liu, and Heike Arnolds. Real-Time Observation of Nonadiabatic Surface Dynamics: The First Picosecond in the Dissociation of NO on Iridium. *Physical Review Letters*, 97(18):186105, 2006.
- [118] G Haran, W D Sun, K Wynne, and R M Hochstrasser. Femtosecond far-infrared pump-probe spectroscopy: A new tool for studying low-frequency vibrational dynamics in molecular condensed phases. *Chemical Physics Letters*, 274(4):365–371, 1997.

- [119] Sean T Roberts, Krupa Ramasesha, Poul B Petersen, Aritra Mandal, and Andrei Tokmakoff. Proton Transfer in Concentrated Aqueous Hydroxide Visualized Using Ultrafast Infrared Spectroscopy, 2011.
- [120] H J Bakker, M Bonn, and M D Fayer. Femtosecond Vibrational Spectroscopy of Aqueous Systems. *Ultrafast Infrared Vibrational Spectroscopy; Fayer, MD, Ed.; CRC Press: Boca Raton, FL*, page 99–148, 2013.
- [121] H Hussain, X Torrelles, P Rajput, et al. A Quantitative Structural Investigation of the 0.1 wt % Nb-SrTiO₃(001)/H₂O Interface. *The Journal of Physical Chemistry C*, 118(20):10980–10988, 2014.
- [122] Guido Ketteler, Susumu Yamamoto, Hendrik Bluhm, et al. The Nature of Water Nucleation Sites on TiO₂(110) Surfaces Revealed by Ambient Pressure X-ray Photoelectron Spectroscopy. *The Journal of Physical Chemistry C*, 111(23):8278–8282, 2007.
- [123] A S Barker. Temperature Dependence of the Transverse and Longitudinal Optic Mode Frequencies and Charges in SrTiO₃ and BaTiO₃. *Physical Review*, 145(2):391–399, 1966.
- [124] B Fischer, D Bäuerle, and W J Buckel. Surface polaritons in KTaO₃ and SrTiO₃. *Solid State Communications*, 14(3):291–294, 1974.
- [125] S S A Seo, H N Lee, and T W Noh. Infrared spectroscopy of CaTiO₃, SrTiO₃, BaTiO₃, Ba_{0.5}Sr_{0.5}TiO₃ thin films, and (BaTiO₃)/(SrTiO₃) superlattice grown on SrRuO₃/SrTiO₃(001) substrates. *Thin Solid Films*, 486(1-2):94–97, aug 2005.
- [126] Mark S Wrighton, Arthur B Ellis, Peter T Wolczanski, et al. Strontium titanate photoelectrodes. Efficient photoassisted electrolysis of water at zero applied potential. *Journal of the American Chemical Society*, 98(10):2774–2779, 1976.
- [127] Yimin Zhu, Hiroyuki Uchida, and Masahiro Watanabe. Oxidation of Carbon Monoxide at a Platinum Film Electrode Studied by Fourier Transform Infrared Spectroscopy with Attenuated Total Reflection Technique. *Langmuir*, 15(25):8757–8764, 1999.
- [128] Yimin Zhu, Hiroyuki Uchida, Takahiro Yajima, and Masahiro Watanabe. Attenuated Total Reflection-Fourier Transform Infrared Study of Methanol Oxidation on Sputtered Pt Film Electrode. *Langmuir*, 17(1):146–154, 2001.
- [129] U Fano. Effects of Configuration Interaction on Intensities and Phase-shifts. *Physical Review*, 124(6):1866–1878, 1961.

- [130] F Gervais, J Servoin, A Baratoff, J G Bednorz, and G Binnig. Temperature dependence of plasmons in Nb-doped SrTiO₃. *Physical Review B*, 47(13):8187–8194, 1993.
- [131] Paul A Giguère and K B Harvey. On the infrared absorption of water and heavy water in condensed states. *Canadian Journal of Chemistry*, 34(6):798–808, 1956.
- [132] Matthias M Waegle, Hoang Q Doan, and Tanja Cuk. Long-Lived Photoexcited Carrier Dynamics of d-d Excitations in Spinel Ordered Co₃O₄. *The Journal of Physical Chemistry C*, 118(7):3426–3432, 2014.
- [133] J D E McIntyre and David E Aspnes. Differential reflection spectroscopy of very thin surface films. *Surface Science*, 24(2):417–434, 1971.
- [134] Feliciano Giustino and Alfredo Pasquarello. Infrared Spectra at Surfaces and Interfaces from First Principles: Evolution of the Spectra across the Si(100)\SiO₂ Interface. *Physical Review Letters*, 95(18):187402, oct 2005.
- [135] P Hohenberg and W Kohn. Inhomogeneous Electron Gas. *Physical Review*, 136(3B):B864–B871, nov 1964.
- [136] W Kohn and L J Sham. Self-Consistent Equations Including Exchange and Correlation Effects. *Physical Review*, 140(4A):A1133–A1138, nov 1965.
- [137] G. Kresse and J. Furthmüller. Efficiency of ab-initio total energy calculations for metals and semiconductors using a plane-wave basis set. *Computational Materials Science*, 6(1):15–50, jul 1996.
- [138] G. Kresse. Efficient iterative schemes for ab initio total-energy calculations using a plane-wave basis set. *Physical Review B*, 54(16):11169–11186, oct 1996.
- [139] P E Blöchl. Projector augmented-wave method. *Physical Review B*, 50(24):17953–17979, dec 1994.
- [140] John P Perdew, Kieron Burke, and Matthias Ernzerhof. Generalized Gradient Approximation Made Simple. *Physical Review Letters*, 77(18):3865–3868, oct 1996.
- [141] Stefan Grimme. Semiempirical GGA-type density functional constructed with a long-range dispersion correction. *Journal of Computational Chemistry*, 27(15):1787–1799, nov 2006.
- [142] Stephan Lany and Alex Zunger. Accurate prediction of defect properties in density functional supercell calculations. *Modelling and Simulation in Materials Science and Engineering*, 17(8):84002, dec 2009.

- [143] S L Dudarev, S Y Savrasov, C J Humphreys, et al. Electron-energy-loss spectra and the structural stability of nickel oxide: An LSDA+U study. *Physical Review B*, 57(3):1505–1509, jan 1998.
- [144] Satoshi Okamoto, Andrew J Millis, and Nicola A Spaldin. Lattice Relaxation in Oxide Heterostructures: LaTiO₃/SrTiO₃ Superlattices. *Physical Review Letters*, 97(5):56802, jul 2006.
- [145] Minseok Choi, Fumiyasu Oba, and Isao Tanaka. Role of Ti Antisitelike Defects in SrTiO₃. *Physical Review Letters*, 103(18):185502, oct 2009.
- [146] Paul Erhart, Andreas Klein, Daniel Åberg, and Babak Sadigh. Efficacy of the DFT + U formalism for modeling hole polarons in perovskite oxides. *Physical Review B*, 90(3):35204, jul 2014.
- [147] A Droghetti, C D Pemmaraju, and S Sanvito. Polaronic distortion and vacancy-induced magnetism in MgO. *Physical Review B*, 81(9):92403, mar 2010.
- [148] Jörg Neugebauer and Matthias Scheffler. Adsorbate-substrate and adsorbate-adsorbate interactions of Na and K adlayers on Al(111). *Physical Review B*, 46(24):16067–16080, dec 1992.
- [149] Ofer Sinai and Leeor Kronik. Simulated doping of Si from first principles using pseudoatoms. *Physical Review B*, 87(23):235305, jun 2013.
- [150] K Parlinski, Z Q Li, and Y Kawazoe. First-Principles Determination of the Soft Mode in Cubic ZrO₂. *Physical Review Letters*, 78(21):4063–4066, may 1997.
- [151] Atsushi Togo, Fumiyasu Oba, and Isao Tanaka. First-principles calculations of the ferroelastic transition between rutile-type and CaCl₂-type SiO₂ at high pressures. *Physical Review B*, 78(13):134106, oct 2008.
- [152] Stefano Baroni and Raffaele Resta. Ab initio calculation of the macroscopic dielectric constant in silicon. *Physical Review B*, 33(10):7017–7021, may 1986.
- [153] M Gajdoš, K Hummer, G Kresse, et al. Linear optical properties in the projector-augmented wave methodology. *Physical Review B*, 73(4):45112, jan 2006.
- [154] J M Kiat and Thierry Roisnel. Rietveld analysis of strontium titanate in the Muller state. *Journal of Physics: Condensed Matter*, 8(19):3471–3475, may 1996.
- [155] Roman Wahl, Doris Vogtenhuber, and Georg Kresse. SrTiO₃ and BaTiO₃ revisited using the projector augmented wave method: Performance of hybrid and semilocal functionals. *Physical Review B*, 78(10):104116, sep 2008.

- [156] Robert A Evarestov, Evgeny Blokhin, Denis Gryaznov, Eugene A Kotomin, and Joachim Maier. Phonon calculations in cubic and tetragonal phases of SrTiO₃: A comparative LCAO and plane-wave study. *Physical Review B*, 83(13):134108, apr 2011.
- [157] Fedwa El-Mellouhi, Edward N Brothers, Melissa J Lucero, and Gustavo E Scuseria. Modeling of the cubic and antiferrodistortive phases of SrTiO₃ with screened hybrid density functional theory. *Physical Review B*, 84(11):115122, sep 2011.
- [158] James M Rondinelli and Nicola A Spaldin. Substrate coherency driven octahedral rotations in perovskite oxide films. *Physical Review B*, 82(11):113402, sep 2010.
- [159] T Hasegawa, M Shirai, and K Tanaka. Localizing nature of photo-excited states in SrTiO₃. *Journal of Luminescence*, 87-89:1217–1219, may 2000.
- [160] Robert A Binstead and Thomas J Meyer. Hydrogen-atom transfer between metal complex ions in solution. *Journal of the American Chemical Society*, 109(11):3287–3297, may 1987.
- [161] Estelle L Lebeau, Robert A Binstead, and Thomas J Meyer. Mechanistic Implications of Proton Transfer Coupled to Electron Transfer. *Journal of the American Chemical Society*, 123(43):10535–10544, oct 2001.
- [162] Robert I Cukier and Daniel G Nocera. Proton-coupled electron transfer. *Annual review of physical chemistry*, 49(1):337–369, 1998.
- [163] Michael D Fayer. Dynamics of Water Interacting with Interfaces, Molecules, and Ions. *Accounts of Chemical Research*, 45(1):3–14, jan 2012.
- [164] K E Myers, Q Wang, and S L Dexheimer. Ultrafast carrier dynamics in nanocrystalline silicon. *Physical Review B*, 64(16):161309, 2001.
- [165] G C Cho, W Kütt, and H Kurz. Subpicosecond time-resolved coherent-phonon oscillations in GaAs. *Physical Review Letters*, 65(6):764–766, aug 1990.
- [166] Alexander J Cowan. Intermediate identification. *Nature Publishing Group*, 8(8):740–741, 2016.
- [167] T A Betley, Q Wu, T Van Voorhis, and D G Nocera. Electronic Design Criteria for O-O Bond Formation via Metal-Oxo Complexes. *Inorganic chemistry*, 47(6):1849–1861, 2008.
- [168] S Pendlebury R., X Wang, F Le Formal, et al. Ultrafast Charge Carrier Recombination and Trapping in Hematite Photoanodes under Applied Bias. *Journal of the American Chemical Society*, 136(28):9854–9857, 2014.

- [169] Florian Le Formal, Ernest Pastor, S David Tilley, et al. Rate Law Analysis of Water Oxidation on a Hematite Surface, 2015.
- [170] Jesse W Ondersma and Thomas W Hamann. Measurements and Modeling of Recombination from Nanoparticle TiO₂ Electrodes. pages 8264–8271, 2011.
- [171] Monica Barroso, Camilo A Mesa, Stephanie R Pendlebury, et al. Dynamics of photogenerated holes in surface modified α - Fe₂O₃ photoanodes for solar water splitting. *Proceedings of the National Academy of Sciences of the United States of America*, 109(39):15640–15645, 2012.
- [172] A. W D Larkum. Limitations and prospects of natural photosynthesis for bioenergy production. *Current Opinion in Biotechnology*, 21(3):271–276, 2010.
- [173] Donald R. Ort, Sabeeha S. Merchant, Jean Alric, et al. Redesigning photosynthesis to sustainably meet global food and bioenergy demand. *Proceedings of the National Academy of Sciences*, 112(28):1–8, 2015.
- [174] Thomas a. Faunce, Wolfgang Lubitz, a. W. (Bill) Rutherford, et al. Energy and environment policy case for a global project on artificial photosynthesis. *Energy & Environmental Science*, 6(3):695, 2013.
- [175] Dohyung Kim, Kelsey K. Sakimoto, Dachao Hong, and Peidong Yang. Artificial photosynthesis for sustainable fuel and chemical production. *Angewandte Chemie - International Edition*, 54(11):3259–3266, 2015.
- [176] Jörg S. Deutzmann, Merve Sahin, and Alfred M. Spormann. Extracellular Enzymes Facilitate Electron Uptake in Biocorrosion and Bioelectrosynthesis. *mBio*, 6(2):e00496–15, may 2015.
- [177] James K Utterback, Molly B Wilker, Katherine a Brown, et al. Competition between electron transfer, trapping, and recombination in CdS nanorod-hydrogenase complexes. *Physical chemistry chemical physics : PCCP*, 17:5538–42, 2015.
- [178] Molly B Wilker, Katherine E Shinopoulos, Katherine A Brown, et al. Electron Transfer Kinetics in CdS Nanorod - [FeFe]-Hydrogenase Complexes and Implications for Photochemical H₂ Generation. *J. Am. Chem. Soc.*, 2013.
- [179] Kelly P. Nevin, Sarah A. Hensley, Ashley E. Franks, et al. Electrosynthesis of organic compounds from carbon dioxide is catalyzed by a diversity of acetogenic microorganisms. *Applied and Environmental Microbiology*, 77(9):2882–2886, 2011.
- [180] H. L. Drake. Demonstration of hydrogenase in extracts of the homoacetate-fermenting bacterium *Clostridium thermoaceticum*. *Journal of Bacteriology*, 150(2):702–709, 1982.

- [181] S L Daniel, T Hsu, S I Dean, and H L Drake. Characterization Of The H-2-Dependent And Co-Dependent Chemolithotrophic Potentials Of The Acetogens *Clostridium-Thermoaceticum* And *Acetogenium-Kivui*. *Journal of Bacteriology*, 172(8):4464–4471, 1990.
- [182] Huan Wei Tseng, Molly B. Wilker, Niels H. Damrauer, and Gordana Dukovic. Charge transfer dynamics between photoexcited CdS nanorods and mononuclear Ru Water-oxidation catalysts. *Journal of the American Chemical Society*, 135(9):3383–3386, 2013.
- [183] Yoshio Nosaka, Hajime Miyama, Mamoru Terauchi, and Takayoshi Kobayashi. Photoinduced Electron Transfer from Colloidal Cadmium Sulfide to Methylviologen: A Picosecond Transient Absorption Study. *J Phys Chem*, 255(7):6521–6522, 1988.
- [184] Yuval Ben-Shahar, Francesco Scotognella, Ilka Kriegel, et al. Optimal metal domain size for photocatalysis with hybrid semiconductor-metal nanorods. *Nature Communications*, 7:10413, 2016.
- [185] Patanjali Kambhampati. Unraveling the Structure and Dynamics of Excitons in Semiconductor Quantum Dots. *Accounts of Chemical Research*, 44(1):1–13, 2011.
- [186] Paul W King. Designing interfaces of hydrogenase - nanomaterial hybrids for efficient solar conversion. *BBA - Bioenergetics*, 1827(8-9):949–957, 2013.
- [187] H B Gray and J R Winkler. Electron Transfer in Proteins. *Annual review of biochemistry*, 65:537–561, 1996.
- [188] Harry B Gray and Jay R Winkler. Long-range electron transfer. *Proceedings of the National Academy of Sciences of the United States of America*, 102(10):3534–9, 2005.
- [189] Simone Morra, Francesca Valetti, Sheila J. Sadeghi, et al. Direct electrochemistry of an [FeFe]-hydrogenase on a TiO₂ Electrode. *Chemical Communications*, 47:10566, 2011.
- [190] Lindsey A Flanagan and Alison Parkin. Electrochemical insights into the mechanism of NiFe membrane-bound hydrogenases. *Biochemical Society transactions*, 44(1):315–28, 2016.
- [191] Antonio L. De Lacey, Victor M. Fernández, Marc Rousset, and Richard Cammack. Activation and inactivation of hydrogenase function and the catalytic cycle: Spectroelectrochemical studies. *Chemical Reviews*, 107(10):4304–4330, 2007.
- [192] Jilie Kong and Shaoning Yu. Fourier transform infrared spectroscopic analysis of protein secondary structures. *Acta Biochimica et Biophysica Sinica*, 39(8):549–559, 2007.

- [193] S Y Venyaminov and N N Kalnin. Quantitative Ir Spectrophotometry of Peptide Compounds in Water (H₂O) Solutions .1. Spectral Parameters of Amino-Acid Residue Absorption-Bands. *Biopolymers*, 30(13-14):1243–1257, 1990.
- [194] Maria Eirini Pandelia, Hideaki Ogata, Leslie J. Currell, Marco Flores, and Wolfgang Lubitz. Probing intermediates in the activation cycle of [NiFe] hydrogenase by infrared spectroscopy: The Ni-SIr state and its light sensitivity. *Journal of Biological Inorganic Chemistry*, 14(8):1227–1241, 2009.
- [195] Antonio J Pierik, Winfried Roseboom, Randolph P Happe, Kimberly A Bagley, and Simon P J Albracht. Carbon Monoxide and Cyanide as Intrinsic Ligands to Iron in the Active Site of [NiFe]-Hydrogenases. *The Journal of Biological Chemistry*, 274(6):3331–3337, 1999.
- [196] Moira L. Flanagan, Phillip D. Long, Peter D. Dahlberg, et al. Mutations to R. sphaeroides Reaction Center Perturb Energy Levels and Vibronic Coupling but Not Observed Energy Transfer Rates. *Journal of Physical Chemistry A*, 120(9):1479–1487, 2016.
- [197] Duangkhae Srikun, Aaron E. Albers, Christine I. Nam, Anthony T. Iavarone, and Christopher J. Chang. Organelle-targetable fluorescent probes for imaging hydrogen peroxide in living cells via SNAP-Tag protein labeling. *Journal of the American Chemical Society*, 132(12):4455–4465, 2010.
- [198] Brooks B Bond-Watts, Robert J Bellerose, and Michelle C Y Chang. Enzyme mechanism as a kinetic control element for designing synthetic biofuel pathways. *Nature chemical biology*, 7(april):222–7, 2011.
- [199] Son C. Nguyen, Justin P. Lomont, Matthew C. Zoerb, et al. Chemistry of the triplet 14-electron complex Fe(CO)₃ in solution studied by ultrafast time-resolved IR spectroscopy. *Organometallics*, 31(10):3980–3984, 2012.
- [200] Justin; Ware Peatross Peatross. Physics of Light and Optics. pages 1–341, 2008.
- [201] Wilford N. Hansen. Expanded formulas for attenuated total reflection and the derivation of absorption rules for single and multiple ATR spectrometer cells. *Spectrochimica Acta*, 21(4):815–833, apr 1965.
- [202] J. P Goudonnet L. Salomon, F. De Fornel. Sample-tip coupling efficiencies of the photon-scanning tunneling microscope. *Journal Optical Society of America A*, 8(12):2009–2015, 2009.
- [203] Max Born and Emil Wolf. *Principles of optics: electromagnetic theory of propagation, interference and diffraction of light*. CUP Archive, 2000.

- [204] a J Meixner, M a Bopp, and G Tarrach. Direct measurement of standing evanescent waves with a photon-scanning tunneling microscope. *Applied optics*, 33(34):7995–8000, 1994.
- [205] P. Dore, G. Marzi, and a. Paolone. Refractive indices of SrTiO₃ in the infrared region. *International Journal of Infrared and Millimeter Waves*, 18(L):125–138, 1997.
- [206] F De Fornel, E Lesniewska, L Salomon, and J P Goudonnet. First images obtained in the near infrared spectrum with the photon scanning tunneling microscope. *Optics Commun.*, 102(1, 2):1–5, 1993.
- [207] Neil W Ashcroft and N David Mermin. Solid state phys. *Saunders, Philadelphia*, 293, 1976.
- [208] J. Fahrenfort and W.M. Visser. On the determination of optical constants in the infrared by attenuated total reflection. *Spectrochimica Acta*, 18(698):1103–1116, 1962.

Appendix A

Derivation of Attenuated Total Reflection Signals

The multi-layered sample configuration probed in these experiments require a more nuanced understanding of the physics of light-matter interaction at the the Internal Reflecting Element (IRE) - electrolyte interface than is traditionally given in IR spectroscopy textbooks addressing ATR of solutions.

One new source of complexity, addressed in Section A.1 is the multiple material indices at play. These include the diamond IRE, the electrolyte-occupied gap (aqueous solution) of variable thickness, thin film over-layers that can differ from the bulk (e.g. surface states), and finally the underlying charge injection electrode (bulk SrTiO₃).

A second source of complexity, addressed in Section A.2, is how to relate the differential signal to photo-induced changes in the material, understood through the indices of refraction, dielectric constants and absorption cross section. In transmission spectroscopy this is done using Beer's law. In Subsection A.2.5 on page 155 a Beer's law type relation is identified for this method.

A.1 Evanescent Fields at Multiple Interfaces

A.1.1 Internal Reflection Equations

In an ATR probe geometry with a sample positioned within the volume of the evanescent wave at the IRE | electrolyte interface, R is the intensity of light transmitted through the IRE and recorded by a detector, e.g. an MCT detector, that records the intensity (electric field squared) of the reflected probe beam. The straightforward application of Maxwell's equations to the conditions of total internal reflection gives Equations A.1 and A.2 for S- and P-polarized light, respectively. For a non-absorbing IRE, I set $\hat{n}_1 = n_1$ (i.e. real) and represent the sample complex index of refraction as $\hat{n}_2 = n_2 + i\kappa_2$:

$$R_S = |r_{12}^S|^2 = \left| \frac{n_1 \cos(\theta) - i\sqrt{n_1^2 \sin^2(\theta) - \hat{n}_2^2}}{n_1 \cos(\theta) + i\sqrt{n_1^2 \sin^2(\theta) - \hat{n}_2^2}} \right|^2 \quad (\text{A.1})$$

$$R_P = |r_{12}^P|^2 = \left| \frac{\hat{n}_2^2 \cos(\theta) - in_1 \sqrt{n_1^2 \sin^2(\theta) - \hat{n}_2^2}}{\hat{n}_2^2 \cos(\theta) + in_1 \sqrt{n_1^2 \sin^2(\theta) - \hat{n}_2^2}} \right|^2 \quad (\text{A.2})$$

For a weakly absorbing material Equations A.1 and A.2 can be expanded to first order in the imaginary component of the sample index of refraction, κ , as Equation A.3. The derivation is available in several textbooks [56, 200]. Further expansion, as far as fourth order in κ , have been published [201]:

$$\frac{R}{I_0} = 1 - \frac{P_{\text{Absorbed}}}{P_{\text{Incident}}} = 1 - \frac{\frac{Dc}{\cos\theta} |t_{12}|^2 |E_0|^2 \int_0^\infty n_2(z) \kappa_2(z) k \exp\left(\frac{-2z}{d_p}\right) dz}{\frac{|E_0|^2}{4\pi} c n_1 D} \quad (\text{A.3})$$

$$d_P = \frac{\lambda}{2\pi\sqrt{n_1^2 \sin^2(\theta) - \hat{n}_2^2}} \quad (\text{A.4})$$

where $|t_{12}|^2$ is the Fresnel transmission coefficient for the appropriate polarization component, $|E_0|^2$ is the incident light intensity, D is the illuminated area, θ is the incident angle and d_P (Equation A.4) is the electric field $1/e$ penetration depth.

For a homogenous, thick sample material (e.g. solutions, or a solid crystal pressed directly to the IRE) the refractive index is a constant with respect to distance from the interface (i.e. $n_2(z) = n_2$; $\kappa_2(z) = \kappa_2$). In this case Equation A.3 reduces to Equation A.5:

$$\frac{R_{ATR}}{I_0} = 1 - \frac{n_2 \kappa_2 |t_{12}|^2}{n_1 \cos \theta \sqrt{n_1^2 \sin^2 \theta - n_2^2}} \quad (\text{A.5})$$

For a homogenous, thick sample that is displaced a distance z_0 from the internal reflecting surface, the probed index of refraction is described by a piece-wise function dealing with first the gap (typically air or water) and second the absorbing sample. Assuming a non-absorbing material in the gap, Equation A.3 reduces to Equation A.6:

$$\frac{R_{ATR}}{I_0} = 1 - \frac{n_2 \kappa_2 |t_{12}|^2}{n_1 \cos \theta \sqrt{n_1^2 \sin^2 \theta - n_2^2}} \exp\left(\frac{-2z_0}{d_P}\right) \quad (\text{A.6})$$

For an absorbing sample of thickness t that is displaced a distance z_0 from the interface, the indices of refraction can be approximated by a top-hat function of width t . This reduces to a signal dependence (Equation A.7) coincidentally similar to a transmission measurement, where the “transmitted” intensity is exponentially dependent on the thickness of the sample:

$$\frac{R_{ATR}}{I_0} = 1 - \frac{n_2 \kappa_2 |t_{12}|^2}{n_1 \cos \theta \sqrt{n_1^2 \sin^2 \theta - n_2^2}} \exp\left(\frac{-2z_0}{d_P}\right) \left(1 - \exp\left(\frac{-2t}{d_P}\right)\right) \quad (\text{A.7})$$

As a check on the consistency of these equations, consider that Equation A.7 reduces to Equation A.6 for a sample much thicker than the evanescent probe depth as expected if the “back” of the sample is effectively beyond the range of the probe depth. Also as expected, the signal reduces to zero for an infinitely thin sample.

A.1.2 Equations for Multiple Absorbing Interfaces

In our diamond IRE - aqueous electrolyte - SrTiO_3 configuration (Figure A.1) the third material (SrTiO_3) has indices of refraction such that a propagating wave can be stimulated at the second interface. In this case the the evanescent wave is only present

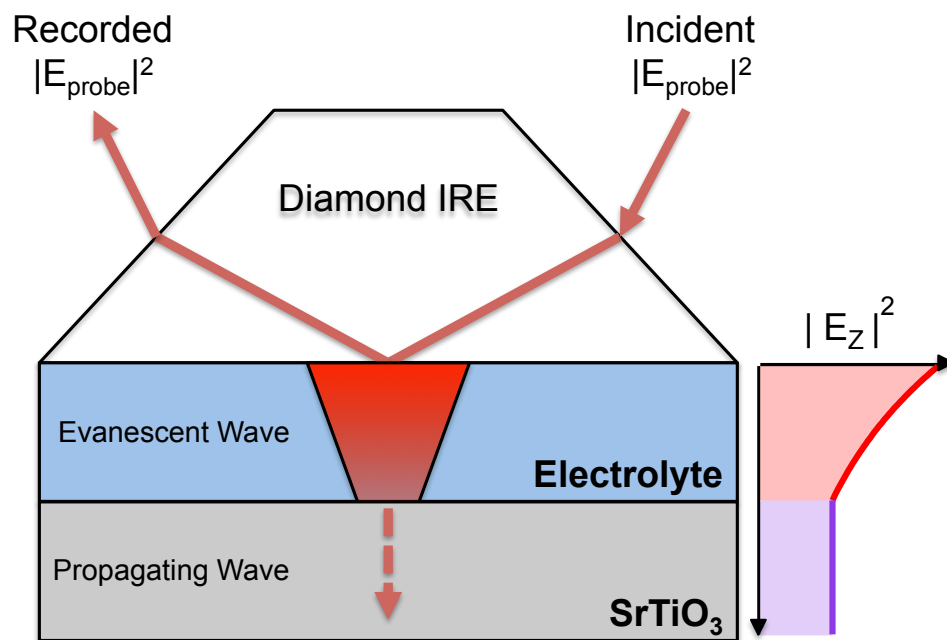


Figure A.1: Experimental setup where the evanescent wave reaches a second material (here, SrTiO₃) that supports a propagating wave. The collected reflection intensity now carries absorptions from within the evanescent wave (an “attenuated total internal reflection” signal) as well as power loss from the re-propagating component in the second material (a “frustrated total internal reflection” signal). Note that the electric field intensity graphed at right is for non-absorbing sample and electrolyte.

in the electrolyte region, and a propagating wave is reformed within the SrTiO₃ sample. This process is referred to as “Photon Tunneling” or “Frustrated Total Internal Reflection” (F-TIR). Equation A.8 [200, (Sec. 4.3)] describes the power loss arising from F-TIR by the SrTiO₃ sample:

$$T = \frac{n_2 \cos \theta_2}{n_0 \cos \theta_0} |t^{tot}|^2 = \frac{n_2 \cos \theta_2}{n_0 \cos \theta_0} \frac{|t_{01}|^2 |t_{12}|^2}{|e^{-ik_1 d \cos \theta_1} - r_{10} r_{12} e^{ik_1 d \cos \theta_1}|^2} \quad (\text{A.8})$$

Where t_{ij} and r_{ij} represent the Fresnel coefficients at the interface between materials i and j . The indices 0, 1, and 2 correspond to the IRE, the electrolyte layer, and the SrTiO₃ sample, respectively. The thickness of material 1 is given by d and the wavevector in material 1 is represented by $k_1 = \hat{y} \sin \theta_1 + \hat{x} \cos \theta_1$. We can replace $\sin \theta_1$ and $\cos \theta_1$ using Snell’s law as in Equation A.9 and A.10 below:

$$\sin \theta_1 = \frac{n_0}{n_1} \sin \theta_0 \quad (\text{A.9})$$

$$\cos \theta_1 = i \sqrt{\sin^2 \theta_1 - 1} \quad (\text{A.10})$$

Conceptually, the existence of frustrated total internal reflection implies that the “absorption” measured by the experimental probe is a combination of two mechanisms [202]. First, power loss from the evanescent wave in the first material as described by Equation A.3, i.e. ATR. Second, power lost to the propagating wave formed in the second material as described by Equation A.8, i.e. F-TIR. The second component is essentially that of the transmitted portion of an incident wave at an IRE-sample interface (0th and 2nd materials), modified by the evanescent wave decay in the intervening medium (1st material, i.e. electrolyte). Note that the maximum power lost through the second mechanism is limited by the power that reaches the second interface, so if the evanescent wave decays (or is absorbed) before reaching the second interface then the frustrated-TIR contribution is zero. Whether the signal observed in Chapter 5 originates from a region where the indices of refraction allow for an evanescent wave (i.e. the electrolyte) or a propagating wave (SrTiO₃) is not certain. The answer to that question would indicate which equations should be used to interpret the observed signal quantitatively.

In the case where the second material does not support a propagating wave, the evanescent wave continues into the second material. The rate of decay is now defined by the IRE and the new material indices as is the electric field amplitude [56, 200, 203]. However, as in the case of the frustrated total internal reflection, the maximum amplitude is restricted to the that of the power reaching the second material through the intervening layer [202, 204, 203, 200]. The electric field strength that reaches the second interface is dictated both by the natural (non-absorbing) decay of the evanescent wave away from the generating interface, as well as by power loss to any absorbing species present in the region.

A.2 Differential Measurements Using ATR

A.2.1 General Equations

Starting from our description of the light reflected from an ATR probe, I can use the equations derived in Section A.1.1 to investigate our pump-probe signal. The transient signal is given by the difference between the photo-excited and ground state reflectance. I use the decadic log as is convention in chemistry literature for reporting absorbance:

$$\Delta A = -\log \left(\frac{R^{ON}}{R^{OFF}} \right) \quad (\text{A.11})$$

$$\Delta A = -\log \left[\frac{\left| \frac{n_1 \cos(\theta) - i\sqrt{n_1^2 \sin^2(\theta) - (\hat{n}_2^{ON})^2}}{n_1 \cos(\theta) + i\sqrt{n_1^2 \sin^2(\theta) - (\hat{n}_2^{ON})^2}} \right|^2}{\left| \frac{n_1 \cos(\theta) - i\sqrt{n_1^2 \sin^2(\theta) - (\hat{n}_2^{OFF})^2}}{n_1 \cos(\theta) + i\sqrt{n_1^2 \sin^2(\theta) - (\hat{n}_2^{OFF})^2}} \right|^2} \right] \quad (\text{A.12})$$

A.2.2 Weak Absorption Approximation

To attempt to reach an understanding the relationship between ΔA and Δk , I use the weak-absorption equations arrived at in Section A.1 to evaluate the differential signal of an infinitely deep electrode displaced from the ATR surface by a distance z_0 , beginning with Equation A.13. For other sample configurations, a different equation describing the reflective intensity is required (e.g. Equations A.6 and A.7):

$$\Delta A = -\log \left[\frac{I_0 - I_0 \left(\frac{n_2^{ON} \kappa_2^{ON} |t_{12}|^2}{n_1 \cos \theta \sqrt{n_1^2 \sin^2 \theta - (n_2^{ON} + i\kappa_2^{ON})^2}} \exp \left(\frac{-2z_0}{d_P} \right) \right)}{I_0 - I_0 \left(\frac{n_2^{OFF} \kappa_2^{OFF} |t_{12}|^2}{n_1 \cos \theta \sqrt{n_1^2 \sin^2 \theta - (n_2^{OFF} + i\kappa_2^{OFF})^2}} \exp \left(\frac{-2z_0}{d_P} \right) \right)} \right] \quad (\text{A.13})$$

Representing the term in parenthesis of Equation A.13 as A^{ON} or A^{OFF} for the excited and ground state respectively, I use the first order Taylor expansion $\log(1 - x) \approx -x$ in Equation A.14 to report that the result is linear in Δn and $\Delta \kappa$. While this result may be expected from a first-order expansion, it is not tautological as I could have found that the signal was zero-order in the indices of refraction:

$$\Delta A = -\log \left(\frac{1 - A^{ON}}{1 - A^{OFF}} \right) = -\log(1 - A^{ON}) + \log(1 - A^{OFF}) \approx A^{ON} - A^{OFF} \quad (\text{A.14})$$

This linearity is an important result, indicating the differential absorbance measured using the internally reflected light returns a signal proportional to the change in material indices between light on and light off conditions. This is strictly only shown for weakly

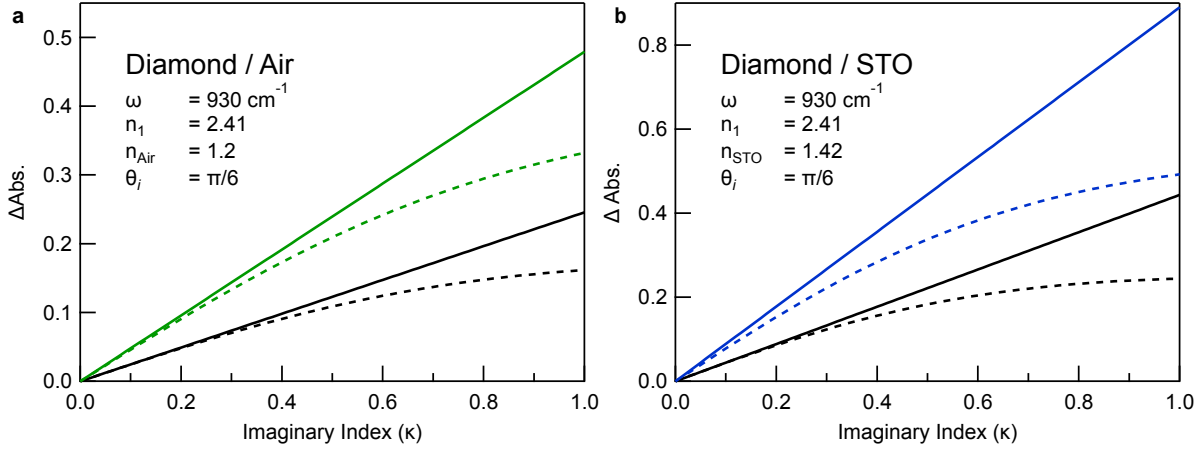


Figure A.2: Differential absorbance for ATR spectroscopy calculated from Equations A.1-A.2 (dashed), and Equation A.14 (solid), the exact and linearized equations respectively. The accuracy of the linearized form is demonstrated for the (a) diamond-air and (b) diamond-SrTiO₃ interfaces. S-polarized (black) and P-polarized (colored) probes are shown independently.

absorbing samples, which allows me to drop κ^2 and higher terms, and to use the first-order Taylor expansion. This approximation has its limits. The deviation of the linearized equations from the exact equations of ΔA for the diamond-sample interface are demonstrated in Figure A.2, A.2. The actual value of κ for SrTiO₃ around 800 cm⁻¹ is roughly 0.4[205], suggesting linearization overestimates the observed absorption intensity by $\approx 20\%$ and the error is polarization dependent.

A.2.3 Evanescent Wave Decay

I can identify an important (first order) characteristic of differential ATR spectroscopy by approximating the absorbance with a linearization of the reflectivity. Inspection of A_0^{ON} and A_0^{OFF} reveals that both carry a term $\exp\left(\frac{-2z_0}{d_P}\right)$. Factoring this out as in Equations A.15 - A.17, I find that in ATR-based pump-probe experiments there is an explicit, exponential dependence of the differential absorption magnitude on the position at which the sample is placed.

$$\Delta A = -\log\left(1 - A_0^{ON} \exp\left(\frac{-2z_0}{d_P}\right)\right) + \log\left(1 - A_0^{OFF} \exp\left(\frac{-2z_0}{d_P}\right)\right) \quad (\text{A.15})$$

$$\Delta A \approx A_0^{ON} \exp\left(\frac{-2z_0}{d_P}\right) - A_0^{OFF} \exp\left(\frac{-2z_0}{d_P}\right) \quad (\text{A.16})$$

$$\Delta A \approx (A_0^{ON} - A_0^{OFF}) \exp\left(\frac{-2z_0}{d_P}\right) \quad (\text{A.17})$$

This matches intuitively with the concept that the reflected light intensity should not depend on material changes outside of the evanescent probe-volume. Photon scanning-tunneling microscopy utilizes a similar experimental setup, and researchers in that field have demonstrated experimentally [206] that the magnitude of the evanescent wave reaching the sample (either for ATR or for F-TIR) is affected by the evanescent wave decay within the electrolyte region.

In addition to the displacement-dependence identified above, the different evanescent wave intensities for S- and P-polarized light imply that even an isotropic transition dipole should show some polarization dependence [202]. It is important to point out this does not interfere with any conclusion in Chapter 5 where the oxyl-radical orientation is identified from polarization data. The ratio $|E_P|^2/|E_S|^2$ is maximally 2, and so this effect cannot fully obscure another mode if it is otherwise present.

A.2.4 Surface Sensitivity

I am primarily concerned with the photo-induced chemistry that occurs at the interface of the electrode and electrolyte. The sample-displacement dependence of the signal suggests that there could be a particular displacement that maximizes the surface contribution to our signal with respect to the bulk-electrode contribution. Consider within the volume of the evanescent wave, the power attenuation (signal) by a single absorbing monolayer located at a distance z_0 from the ATR interface, represented by $\kappa(z) = \kappa^{ML} \times \delta(z - z_0)$. The intervening region (air, electrolyte) is assumed to be non-absorbing, and the region beyond z_0 (the bulk electrode) is represented by a Heaviside step function $\kappa = \kappa^{Bulk} \times \Theta(z - z_0)$. The relative signal contribution of surface to bulk is given by Equation A.18:

$$Surface\ Ratio = \frac{S_{Surface}}{S_{Total}} = \frac{S_{Surface}}{S_{Surface} + S_{Bulk}} \quad (\text{A.18})$$

Plugging in Equation A.6 for a displaced sample and solving for the surface (Equation A.19) and bulk (Equation A.20) contributions, I demonstrate that the surface-to-bulk-signal ratio (Equation A.21) has no dependence on z_0 . This implies the surface-fraction contribution to the transient signal is independent of the sample position.

$$S_{Surface} = \int_0^{\inf} \kappa^{ML} \times \delta(z - z_0) \times \exp\left(\frac{-2z}{d_P}\right) dz = \kappa^{ML} \times \exp\left(\frac{-2z_0}{d_P}\right) \quad (\text{A.19})$$

$$S_{Bulk} = \int_0^{\inf} \kappa_0 \times \Theta(z - z_0) \times \exp\left(\frac{-2z}{d_P}\right) dz = \kappa_0 \left[\exp\left(\frac{-2z}{d_P}\right) \times \frac{d_P}{2} \right] \Bigg|_{z_0}^{\inf}$$

$$S_{Bulk} = \kappa_0 \frac{d_P}{-2} \times \left[\exp\left(\frac{-2 \times \inf}{d_P}\right) - \exp\left(\frac{-2z_0}{d_P}\right) \right] = \kappa_0 \frac{d_P}{2} \times \exp\left(\frac{-2z_0}{d_P}\right) \quad (\text{A.20})$$

Combining Equation A.18, A.19, and A.20 gives Equation A.21:

$$Surface\ Ratio = \frac{S_{Surface}}{S_{Surface} + S_{Bulk}} = \frac{\kappa^{ML}}{\kappa^{ML} + \kappa_0 \frac{d_P}{2}} \quad (\text{A.21})$$

As shown in Section A.2.2, all signal magnitudes decay exponentially with displacement. However, Equation A.21 clarifies that the relative fraction of the overall signal that arises from the surface, i.e. the “surface sensitivity” of the technique, is independent of the sample position. The surface sensitivity does depend on d_P and therefore on the probe angle of incidence and IRE material chosen.

A.2.5 Quantitative Determination of Changes of κ and n

In transmission spectroscopy the Lambert-Beer law (Equation A.22) is used to express the linear relationship between absorbance measurements and the path length (l), concentration (C), and molar absorptivity (ϵ) of a homogenous sample. Here the relation $\epsilon = \frac{4\pi n}{\lambda} \kappa$ is used to relate ΔA to κ .

$$A = -\log\left(\frac{I_{Sample}}{I_0}\right) = -\log\left(\frac{I_0 \exp(-\epsilon Cl)}{I_0}\right) = \frac{4\pi n C}{\lambda} \kappa \quad (\text{A.22})$$

There is no equivalent justification for the application of Beer’s law (i.e. a negative absorbance transform) to ATR spectra, since the relationship between reflected light intensity and the sample absorption is not exponentially dependent on these parameters. The very concept of a “path length” for ATR spectroscopy can be misleading as the probe does not interact equally with all parts of the probe volume. Even the evanescent wave propagation depth d_P has a dependence on κ , so the path length is effectively lengthened for a sample that is more absorbing. As a result, the linearized relationship between differential absorption and κ (Equation A.3) is only strictly valid for a non-absorbing sample, and deviates from the actual absorption as explored in Section A.2.2. Strictly, measurement of the sample κ requires modeling of the measured absorption with the full equation for reflection at the interface. The linear relationship explored here is most useful to explore the relationship between the observed signal and various experimental parameters that otherwise are difficult to identify by inspection.

To identify any Beer’s law-like relationship between absorption index and absorbance, I start with A_0 from Equation A.17. This results in an expression for $(A_0^{ON} - A_0^{OFF})$ in Equation A.24, below:

$$\Delta A \approx \frac{2\pi |t_{12}|^2 d_P}{n_1 \cos \theta \ 2\lambda} \left(n_2^{ON} \kappa_2^{ON} - n_2^{OFF} \kappa_2^{OFF} \right) \quad (\text{A.23})$$

$$\Delta A \approx \frac{|t_{12}|^2}{n_1 \cos \theta \sqrt{n_1^2 \sin^2 \theta - n_2^2}} \left(n_2^{ON} \kappa_2^{ON} - n_2^{OFF} \kappa_2^{OFF} \right) \quad (\text{A.24})$$

The prefactor in Equation A.24 represents the power density of the evanescent probe:

$$\frac{|t_{12}|^2}{n_1 \cos \theta \sqrt{n_1^2 \sin^2 \theta - n_2^2}}$$

on the sample side of the interface. The latter term highlights the fact that the observed signal is a convolution of any changes in both real and imaginary components of the sample index of refraction. To deconvolute the independent contributions from n and κ either they must be related through a Kramers-Kronig transformation [207], or multiple angles of incidence must be used and the resulting spectra compared [208]. The Kramers-Kronig method requires absorption measurements across a wide range of frequencies, some of them not experimentally accessible due to the difficulty of generating the appropriate far-infrared ultrafast pulses. If a full separation of the real and imaginary components is desired, the two-angle method is generally more experimentally accessible. Finally, the change of the real component of the refractive index can be assumed to be negligible (as in Chapter 5) based on the line-shapes resolved in these experiments that are well described by the change of a single component of the refractive index.